UNIVERSIDAD AUTÓNOMA DE QUERÉTARO

FACULTAD DE QUÍMICA

“INGENIERÍA DE LA DINÁMICA DE TRANSPORTE DE CARGA EN CELDAS SOLARES EMERGENTES DE $Sb_2(S,Se)_3$ UTILIZANDO CAPAS TRANSPORTADORAS DE HUECOS BASADAS EN TRIAZATRUXENO, $SrTiO_3$ COMO CAPA TRANSPORTADORA DE ELECTRONES Y NITRURO DE CARBONO GRÁFICO COMO CAPA INTERFACIAL”

TESIS

QUE COMO PARTE DE LOS REQUISITOS PARA OBTENER EL GRADO DE

DOCTORADO EN CIENCIAS DE LA ENERGÍA

PRESENTA

VALENTINA SNEHA GEORGE

DIRIGIDO POR

Dra. LATHA MARASAMY

SANTIAGO DE QUERÉTARO, QUERÉTARO, NOVIEMBRE 2025.

REPOSITORIO INSTITUCIONAL DGBSDI-UAQ

La presente obra está bajo la licencia:
https://creativecommons.org/licenses/by-nc-nd/4.0/deed.es

CC BY-NC-ND 4.0 DEED

Atribución-NoComercial-SinDerivadas 4.0 Internacional

Usted es libre de:

Compartir — copiar y redistribuir el material en cualquier medio o formato

La licenciante no puede revocar estas libertades en tanto usted siga los términos de la licencia

Bajo los siguientes términos:

Atribución — Usted debe dar crédito de manera adecuada , brindar un enlace a la licencia, e indicar si se han realizado cambios . Puede hacerlo en cualquier forma razonable, pero no de forma tal que sugiera que usted o su uso tienen el apoyo de la licenciante.

NoComercial — Usted no puede hacer uso del material con propósitos comerciales .

SinDerivadas — Si remezcla, transforma o crea a partir del material, no podrá distribuir el material modificado.

No hay restricciones adicionales — No puede aplicar términos legales ni medidas tecnológicas que restrinjan legalmente a otras a hacer cualquier uso permitido por la licencia.

Avisos:

No tiene que cumplir con la licencia para elementos del material en el dominio público o cuando su uso esté permitido por una excepción o limitación aplicable.

No se dan garantías. La licencia podría no darle todos los permisos que necesita para el uso que tenga previsto. Por ejemplo, otros derechos como publicidad, privacidad, o derechos morales pueden limitar la forma en que utilice el material.

UNIVERSIDAD AUTÓNOMA DE QUERÉTARO

FACULTAD DE QUÍMICA

DOCTORADO EN CIENCIAS DE LA ENERGÍA

“INGENIERÍA DE LA DINÁMICA DE TRANSPORTE DE CARGA EN CELDAS SOLARES EMERGENTES DE $Sb_2(S,Se)_3$ UTILIZANDO CAPAS TRANSPORTADORAS DE HUECOS BASADAS EN TRIAZATRUXENO, $SrTiO_3$ COMO CAPA TRANSPORTADORA DE ELECTRONES Y NITRURO DE CARBONO GRÁFICO COMO CAPA INTERFACIAL”

TESIS

QUE COMO PARTE DE LOS REQUISITOS PARA OBTENER EL GRADO DE

PRESENTA

VALENTINA SNEHA GEORGE

DIRIGIDO POR

Dra. LATHA MARASAMY

SINODALES

Dra. Latha Marasamy

Presidente

Dr. José Santos Cruz

Secretario

Dr. Francisco Javier de Moure Flores

Vocal

Dra. Aruna Devi Rasu Chettiar

Suplente

Dr. José Álvaro Chávez Carvayar

Suplente

Centro Universitario, Querétaro, Qro.
Noviembre, 2025
México

Contents

List of Figures

List of Tables

Resumen

El $Sb_2(S,Se)_3$ es un material absorbedor emergente, abundante en la tierra y no tóxico, con un ancho de banda ajustable (1.3–1.7 eV), alto coeficiente de absorción y buena estabilidad, convirtiéndose en un candidato prometedor para celdas solares de película delgada. Su eficiencia se limita por el uso de HTLs costosas e inestables, la toxicidad e interdifusión del Cd y el desajuste estructural y electrónico en la interfaz $CdS/Sb_2(S,Se)_3$, que provocan perdidas en V_{OC} y el FF. Esta tesis explora el desempeño de celdas solares $Sb_2(S,Se)_3$ mediante tres estrategias complementarias, abarcando un total de 838 configuraciones simuladas en SCAPS-1D. En el primer enfoque, se validó un dispositivo base $FTO/CdS/Sb_2(S,Se)_3$/Spiro-OMeTAD/Au frente a la eficiencia experimental (~10.75%). La sustitución de Spiro-OMeTAD por HTLs derivadas de triazatruxeno (CI-B2, CI-B3, TAT-H, TAT-TY1 y TAT-TY2) mejoró notablemente la PCE, alcanzando valores superiores al 23% para TAT-TY1, atribuida a un alineamiento óptimo de bandas (CBO = +1.8 eV; VBO = −0.06 eV) que favoreció el transporte selectivo de cargas y redujo la recombinación ($\sim 3\times10^{18}$ $cm^{-3}.s^{-1}$). En el segundo enfoque, se reemplazó la capa CdS por $SrTiO_3$ como ETL libre de Cd. Los dispositivos optimizados mostraron una mayor generación de portadores (3.21×10^{21} $cm^{-3}.s^{-1}$), una densidad de corriente J_{SC} de 27.52 mA/cm^2 y una absorción superior al 70%, reduciendo la pérdida de V_{OC} (~0.39 V) y alcanzando una PCE de 21.91%. Finalmente, en el tercer enfoque, se sintetizó nitruro de carbono grafítico (GCN) mediante polimerización térmica de urea, caracterizado por un ancho de banda de 2.8 eV, permitividad dieléctrica de 7.01 y afinidad electrónica de 3.6 eV. Incorporado como capa interfacial entre CdS y $Sb_2(S,Se)_3$, el GCN mejoró el potencial incorporado (V_{bi} = 0.8 V), redujo las resistencias R_{CT} (~401 $\Omega.cm^2$) y R_s (~3.5 $\Omega.cm^2$), aumentando el FF a 76.07% y la PCE a 27.42%. En conjunto, los resultados demuestran que el uso de HTLs de bajo costo, ETLs libres de Cd y capas interfaciales de GCN puede optimizar sinérgicamente el transporte de carga, la estabilidad y la eficiencia, posicionando al $Sb_2(S,Se)_3$ como un absorbedor fotovoltaico de alto desempeño y sustentable.

Palabras Clave: SCAPS-1D, absorbedor $Sb_2(S,Se)_3$, resistencia a la recombinación, ingeniería de interfaz.

Abstract

Emerging $Sb_2(S,Se)_3$ is an earth-abundant, non-toxic absorber for thin-film photovoltaics, with a tunable bandgap (1.3-1.7 eV), high absorption coefficient, and stability. However, its efficiency is limited by costly and unstable HTL, Cd toxicity and interdiffusion from CdS ETL, and structural/electronic mismatch at the CdS/$Sb_2(S,Se)_3$ interface, resulting in significant losses in V_{OC} and FF. This thesis investigates $Sb_2(S,Se)_3$ solar cells in three approaches, comprising a total of 838 device configurations simulated using SCAPS-1D. The impact of thickness, carrier densities, and operating conditions was systematically evaluated. In the first approach, a baseline FTO/CdS/$Sb_2(S,Se)_3$/Spiro-OMeTAD/Au device was replicated to validate the simulation against experimental efficiency (~10.75%). Replacing Spiro-OMeTAD with triazatruxene-based HTLs (CI-B2, CI-B3, TAT-H, TAT-TY1, TAT-TY2) enhanced the PCEs, attaining maximum efficiency of >23% for TAT-TY1 device. Its superior performance is attributed to favorable HTL/absorber band alignment (CBO = +1.8 eV, VBO = -0.06 eV), which promotes selective carrier transport and suppresses recombination to ~3×10^{18} $cm^{-3}.s^{-1}$. The second approach employed $SrTiO_3$ as an alternative Cd-free ETL. Optimized devices exhibited enhanced carrier generation (3.21×10^{21} $cm^{-3}.s^{-1}$) and a high J_{SC} of 27.52 mA/cm^2. These improvements resulted from enhanced absorption (>70%) and minimized V_{OC} loss (~0.39 V), collectively boosting PCE to 21.91%. In the third approach, graphene carbon nitride (GCN) was synthesized via urea-based thermal polymerization and characterized using XRD, XPS, FESEM, EDS, and UV–Vis to extract the bandgap (2.8 eV), dielectric permittivity (7.01), and electron affinity (3.6 eV) values. These experimental properties of GCN were incorporated as input parameters to study its role as an interfacial layer between CdS and $Sb_2(S,Se)_3$. Subsequent optimization improved the built-in potential (V_{bi}) of 0.8 V, reduced charge transfer (R_{CT}) and series (R_s) resistances to ~401.3 $\Omega.cm^2$ and 3.5 $\Omega.cm^2$, which enhanced FF to 76.07%, and increased PCE to 27.42%. These studies demonstrate that cost-effective HTLs, Cd-free ETLs, and interface-engineered GCN layers can synergistically enhance charge transport, suppress recombination, improve absorption, and strengthen stability, establishing $Sb_2(S,Se)_3$ as a high-performance, environmentally sustainable photovoltaic absorber.

Keywords: SCAPS-1D, $Sb_2(S,Se)_3$ absorber, Recombination resistance, interfacial engineering.

Student Statement of Responsibility

I declare that the data obtained in this research were generated during the development of my thesis work in an ethical manner, and I report the necessary details so that the results of this thesis can be reproduced in future research.

Finally, this thesis is an original work in which any collaboration or direct citation presented in the document has been properly declared and acknowledged.

Valentina Sneha George

Dedication

This work is humbly dedicated to everyone who has shaped my journey, to those whose love, faith, and guidance have been the unseen hands leading me through every challenge and triumph.

Above all, my deepest gratitude belongs to ***my Lord and Savior, Jesus Christ****, whose divine grace has been my anchor and my light. In moments of silence and uncertainty, His presence became my peace. Every step forward, every moment of perseverance, was strengthened by His mercy and unfailing love.*

My dear mother, ***Mrs. Emilda Poonguzhali****, stands at the heart of this journey. Her unwavering strength, sacrifices, and enduring faith have been the foundation of my life. She taught me what resilience truly means to stand tall amid adversity, to love deeply, and to hold on to goodness no matter how difficult the path becomes. Every achievement I hold today reflects her prayers, her values, and her unending courage.*

My father, ***Mr. George Francis Cardoza****, whose steadfast support provided the foundation for our lives. Through his hard work and sense of responsibility, he ensured that I had the means and stability to pursue my education and dreams, for which I remain deeply grateful.*

My sister, ***Evanjalin Kaviya****, has been a companion in both laughter and learning. Her warmth, insight, and faith in me have often been my comfort during long, uncertain days. She has been more than family a friend whose strength and affection constantly reminded me that love, in its truest form, is patient, understanding, and unconditional.*

To my family and dear ones, particularly ***Denis Charles****, whose presence turned uncertainty into calm. You listened when my thoughts were tangled, stood beside me when exhaustion blurred my vision, and believed in my abilities when I hesitated to. Your patience and understanding became my grounding force, your encouragement my quiet motivation and your family's kindness will always be remembered with gratitude.*

I owe special appreciation to ***Dr. Sownthari****, my professor during my master's degree, whose thoughtful guidance and faith in me opened the doors to this remarkable opportunity. It was her encouragement and recommendation that led me here, and I remain deeply grateful for her belief in my potential and her role in shaping the beginnings of this academic path.*

Words will always fall short when I speak of my heartfelt gratitude to my thesis supervisor, ***Dr. Latha Marasamy****. Among all the people who shaped this journey, none has left a deeper*

imprint on my heart and mind than ***Dr. Latha Marasamy****. From the very first day, she was not only my supervisor but the compass that quietly guided me when the path seemed uncertain. What began as a professional relationship soon evolved into a mentorship that shaped my entire perspective on research, on perseverance, and on believing in possibilities I once thought were beyond me. When I first stepped into this journey, I carried both hope and hesitation. It was* ***Dr. Marasamy*** *who transformed that uncertainty into courage. She saw promise even in my rough beginnings and, through her quiet confidence, helped me see it too. Her patience knew no limits each question answered, each doubt clarified, each failure turned into a lesson. She never allowed me to lose faith, even when my own conviction wavered. There were times when the research felt overwhelming when setbacks stretched longer than expected, and progress seemed like a distant dream. In those moments, her steady voice, her reassuring words, and her tireless guidance became the strength I leaned on. She never just supervised, she walked alongside. Whether it was late-night manuscript corrections, detailed discussions over experiments, or those simple gestures of kindness that reminded me I was never alone, each act spoke of her extraordinary generosity and care.* ***Dr. Marasamy's*** *influence extended far beyond the boundaries of academia. She taught me what it means to be resilient, to stay true to integrity, and to approach science with both intellect and heart. Her discipline, clarity, and passion have left an indelible mark not just on this thesis but on the person I have become. She showed me that excellence is not a moment of achievement but a journey of persistence and humility. Even outside the lab, her compassion and warmth created a sense of belonging that made foreign soil feel like home. I will always remember her open-door conversations, her thoughtful check-ins, and the comfort of her encouragement when I needed it most. Through her guidance, I didn't just complete a Ph.D. I found direction, strength, and the quiet confidence to stand on my own.* ***Dr. Latha Marasamy****, you are far more than a mentor, you are the foundation on which this work was built, the light that guided every uncertain step, and the reason this journey found its meaning. My gratitude to you is endless. This thesis, and every achievement it represents, stands as a reflection of your unwavering faith in me and the lessons you have so selflessly imparted.*

Finally, to my dearest friends, ***Evangeline Linda, Kaviya Tracy, Dhineshkumar, Eupsy Navis, Vairamuthu, and Roshini,*** *your companionship has been my greatest comfort through every phase of this long and demanding path.*

This thesis is a reflection of all these beautiful souls. Every page bears the imprint of your support, and I dedicate this work to each of you with profound gratitude and affection.

Acknowledgement

I am sincerely grateful to the **National Council of Humanities, Science and Technology (CONAHCyT)** for their generous funding and support, which made this research possible. I also extend my heartfelt thanks to the **Autonomous University of Querétaro (UAQ)** and the **Faculty of Chemistry** for providing the essential infrastructure, academic guidance, and personal support throughout this journey.

I am profoundly thankful to my thesis supervisor, **Dr. Latha Marasamy**, whose expert guidance, encouragement, and steadfast support have been invaluable throughout my doctoral research. Her deep knowledge, insightful advice, and dedicated mentorship have not only shaped this thesis but have also contributed significantly to my personal and professional growth.

I am deeply appreciative of the members of my examination committee and mentors **Dra. Aruna Devi Rasu Chettiar, Dr. José Álvaro Chávez Carvayar, Dr. Francisco de Moure Flores, Dr. José Santos Cruz, and Dra. Claudia Elena Pérez García** for their invaluable insights, thoughtful suggestions, and contributions to this work.

Finally, I wish to express my sincere gratitude to **Prof. Marc Burgelman** from **ELSI, University of Gent, Belgium**, for kindly providing access to the SCAPS-1D simulation software, which played a crucial role in this research.

Published works

- **Valentina Sneha George**, Aruna-Devi Rasu Chettiar, Saravanan Rajendran, Hichem Bencherif, P. Sasikumar, and Latha Marasamy. "Modelling Insights of $Sb_2(S,Se)_3$ Solar Cells Using Triazatruxene Hole Transport Layers." **Advanced Theory and Simulations**, 8, no. 10 (2025): e00487**, https://doi.org/10.1002/adts.202500487.**
- Evangeline Linda, Aruna-Devi Rasu Chettiar, **Valentina Sneha George**, Ravichandran Manisekaran, Dhineshkumar Srinivasan, Abigail Barcenas Martínez, M. Khalid Hossain, Md. Ferdous Rahman, José Álvaro Chávez Carvayar, Sergio Armando Tomás, Ángeles Mantilla, Latha Marasamy, "Exploring the physical properties of pristine γ-In2S3 and its influence on Ba doping for photocatalytic degradation of 2,4-D herbicide", **Journal of Photochemistry and Photobiology A: Chemistry,** 456 (2024) 115831**, https://doi.org/10.1016/j.jphotochem.2024.115831.**

Accepted for publication

- **Valentina Sneha George**, Aruna-Devi Rasu Chettiar, Claudia Elena Pérez García, Latha Marasamy, "Numerical simulation of Cd-free Strontium Titanate Electron Transport Layer in $Sb_2(S,Se)_3$ solar cell"**, in 22nd International Conference on Electrical Engineering, Computing Science and Automatic Control (CCE), 2025.**

Submitted work

- **Valentina Sneha George**, Aruna-Devi Rasu Chettiar, Saravanan Rajendran, Hichem Bencherif, P. Sasikumar, Jeyakumar Ramanujam, Latha Marasamy, "Exploring Interfacial Charge Dynamics in $Sb_2(S,Se)_3$ Solar Cells with Graphitic Carbon Nitride: Experimental Parameters Applied in SCAPS-1D Modeling", **Journal of Alloys and Compounds**.

1. Introduction

1.1.Global Energy Demands and Solar PV

Renewable energy has become the pillar of global strategy towards achieving a sustainable low-carbon future, as nations experience the dual challenge of rising energy demand and growing climate change impacts. As global energy consumption is projected to exceed 27 TW in 2050, driven by rapidly increasing populations and industrialization, fossil-fuel consumption continues to be one of the principal reasons for ruinous environmental damage, from greenhouse-gas emissions, air contamination, to ocean acidification [1,2]. To counteract these effects, clean energy technologies such as solar, wind, hydroelectricity, geothermal, and biomass are increasingly making strides because they are naturally recharged and lead to lower pollution than fossil fuels [3]. Renewables expanded to over 38 % of global electricity generation by the end of 2024, larger than coal as a single form of new power generation, the International Energy Agency (IEA) reports [4]. Solar photovoltaic (PV) technology, in particular, has emerged as one of the fastest-growing and transforming clean-energy sources, due to its scalability, modularity, and falling costs. IEA's Electricity Market Report 2025 highlights that global solar generation rose by 29 % in 2024, aggregating approximately 40 % of electricity demand growth for the year and over 2,260 GW of installed capacity cumulatively worldwide [4]. Moreover, the International Renewable Energy Agency (IRENA) reported that solar energy currently provides nearly 6 % of global electricity, marking the biggest single-year growth in capacity for any source of power [5]. These trends are being financed through unprecedented improvements in PV efficiency, reductions in levelized cost of electricity (LCOE), and the integration of hybrid systems combining PV and battery storage, which together enhance the robustness and diversity of solar energy [6,7]. Although solar energy deployment is expanding worldwide, the rate of development varies considerably across regions, with countries possessing high solar irradiation and well-established policy frameworks demonstrating the most rapid advancements. For example, Mexico situated within the world’s solar belt, exemplifies this potential receiving an average solar irradiance between 4.5 and 6.5 kWh/m^2/day, ranking among the top ten nations for solar resources [8]. Over the past decade, the solar PV installed capacity in Mexico has increased to approximately 12 GW as of 2024, dominated by large-scale plants in Sonora, Chihuahua, and Durango, and by distributed generation systems that comprised more than 1 GW in 2024 [9]. These achievements position Mexico as one of Latin America's leading producers of solar energy, yet its potential remains much from the point of saturation, creating enormous opportunity for

future expansion through continued investment, grid upgrades, and policy reforms supporting both utility-scale and distributed PV systems. [3]. Therefore, solar PV is not only a global leader of the shift to renewable energy but also an opportunity for global nations to attain their energy autonomy, become carbon-neutral, and be a critical player in the global effort against climate change.

1.2.Evolution of Thin Film PV Technology

Photovoltaic cells, commonly known as solar cells, convert sunlight directly into electricity through the PV effect, which was first discovered by Edmond Becquerel in 1839 [10]. The first practical silicon solar cells were developed in 1954 at Bell Laboratories by Gerald Pearson, Daryl Chapin, and Calvin Fuller, marking the beginning of modern solar energy technology [11]. Solar cells are typically classified according to the materials used in their light-absorbing layers and their generational development. The first generation consists of wafer-based crystalline silicon (c-Si) solar cells, which dominate the market due to their high efficiency and stability [12]. Despite their advantages, c-Si cells require high-purity silicon and thick wafers (typically 150–200 μm) because silicon has an indirect bandgap, resulting in higher energy consumption during production and increased manufacturing cost [13]. Modern c-Si modules have achieved record efficiencies of 26.8% under laboratory conditions [14].

The second generation of solar cells was introduced to reduce material usage and production costs while maintaining reasonable efficiency. These thin-film PV technologies use polycrystalline or amorphous semiconductors with high absorption coefficients, allowing significantly thinner absorber layers (1–3 μm) [15]. Key examples include cadmium telluride (CdTe), copper indium gallium selenide/sulfide (CIGS), and amorphous silicon (a-Si: H). CdTe solar cells have reached efficiencies up to 22.1% and are widely commercialized due to their low cost and fast energy payback time [16]. CIGS cells have demonstrated efficiencies of up to 22.6% while offering flexibility in applications, although they rely on scarce elements such as In and Ga [17]. Amorphous Si is less efficient (~10.2%) but remains relevant for lightweight, flexible, or building-integrated applications [18]. Thin-film solar cells thus represent a compromise between efficiency, cost, and material usage compared to first-generation crystalline Si technologies.

Third-generation solar cells aim to surpass the efficiency limits of second-generation thin films while retaining cost advantages. These emerging technologies include dye-sensitized solar

cells (DSSCs), perovskite solar cells (PSCs), organic PV cells (OPVs), and quantum-dot-based PVs [20]. PSCs have seen remarkable efficiency improvements from less than 4% in 2009 to over 26% in 2025 for single-junction devices, and up to 33.9% for tandem configurations combined with silicon, highlighting their potential for commercial deployment. DSSCs, OPVs, and quantum-dot solar cells offer additional pathways for flexible, low-cost, and tunable PV systems, although challenges remain regarding long-term stability, toxicity, and large-scale manufacturability [19].

Kesterite materials such as CZTS and CZTSSe have been pursued as more sustainable alternatives, using earth-abundant Cu, Zn, and Sn instead of In and Ga [13]. They offer direct bandgaps in the ~1.0 - 1.5 eV range and high absorption coefficients, but they also experience a pronounced open-circuit voltage (V_{OC}) deficit primarily due to intrinsic cation (Cu/Zn/Sn) disorder and deep defect states that enable non-radiative recombination. Consequently, while kesterites remain promising from a materials-abundance perspective, achieving their full theoretical potential remains elusive [20]. Other emerging absorber families, such as quantum-dot/nanocrystal solar cells, organic/DSSC devices, and binary chalcogenides like SnS, FeS_2, and Cu_2O, are also under heavy investigation. While these systems offer appealing features (e.g., ultra-light weight, indoor PV suitability, and very low-cost precursor methods), their current limitations include low photovoltages, poor long-term stability, complex ligand or interface chemistries (in QDs and organics), and short carrier lifetimes or unfavorable band alignments (in some binary chalcogenides)[21–25]. These persistent issues make it difficult for many researchers to bridge the gap from laboratory demonstration to commercial viability.

Beyond these, various eco-friendly semiconductors were also being investigated, including ternary II–IV–N_2 nitrides (e.g., $MgSnN_2$, $ZnSnN_2$) [26,27], binary halides (InI, BiI_3), and complex chalcogenide compounds such as $AgBiS_3$, $NaBiS_2$, $NaSbS_2$, BiOI, BiSI, SbSI, SbSeI, $Sn_2SbS_2I_3$, and Cu_2FeSnS_4 [28–31]. These materials contain earth-abundant and environmentally benign elements, offering significant advantages in long-term sustainability and large-scale manufacturability. However, their current power conversion efficiencies (PCE) remain below 6%, primarily due to non-radiative recombination, high defect densities, and morphological imperfections that limit carrier transport. Continued progress requires improved crystal quality, defect passivation, and optimized device architectures to unlock their theoretical performance potential [32,33].

Within this scope, antimony chalcogenides of the form Sb_2X_3 (X=S, Se, S/Se) have emerged as an effective and practical solution, as these materials are composed of abundant, low-toxicity elements, have very high absorption coefficients, and often possess simpler binary (or ternary) stoichiometries that ease precursor chemistry and device fabrication. Initially, Sb_2S_3 (antimony trisulfide) and Sb_2Se_3 (antimony triselenide) have attracted interest because they combine favorable optical bandgaps, strong absorption, and a quasi-one-dimensional, ribbon-like crystal structure whose anisotropic transport properties can be exploited by appropriate film growth and orientation control [34–36]. The practical appeal of antimony chalcogenides derives from several converging factors: (1) elemental abundance and lower toxicity compared with Cd- or Pb-containing absorbers; (2) optical bandgaps that lie in the useful range for single-junction and tandem cells ($Sb_2S_3 \approx$ 1.6 -1.7 eV and $Sb_2Se_3 \approx$ 1.0 - 1.2 eV) [36,37], enabling spectral tailoring; (3) extremely high absorption coefficients, allowing efficient light capture in sub-micron absorber layers; and (4) process flexibility. For example, Sb chalcogenides can be grown by evaporation, sputtering, chalcogenization, chemical bath deposition, spray pyrolysis, or hydrothermal routes [38,39]. These combined properties explain why antimony chalcogenides have risen rapidly in recent PV research.

A critical advantage of antimony chalcogenides is their bandgap tunability when S and Se are alloyed to form antimony selenosulfide ($Sb_2(S,Se)_3$) that allows continuous tuning between the wider bandgap Sb_2S_3 and the narrower bandgap Sb_2Se_3, which is attractive for designing standalone single-junction devices with optimal current–voltage trade-offs or for integrating Sb alloys into tandem stacks [40]. Because the Sb-chalcogenide family offers favorable transport, optical, and processing properties, it provides a strategic pathway to thin-film PVs with fewer of the limitations faced by other emerging families. For example, while perovskites struggle with long-term stability, and kesterites struggle with defect-related losses, Sb_2X_3 absorbers exhibit strong optical absorption, robust composition, process flexibility, and benign defect physics, making them a timely platform for further optimization [41]. Among mixed S–Se compositions, $Sb_2(S,Se)_3$ enables continuous bandgap tuning between $\approx$ 1.1 and 1.7 eV, and recent experimental reports include planar devices with efficiencies near 10%. In less than a decade, $Sb_2(S,Se)_3$ solar cells achieved a champion efficiency of ~10.75% using hydrothermal synthesis, which is the highest reported PCE in the Sb chalcogenide family [42]. These incremental but steady advances demonstrate the growing potential of the $Sb_2(S,Se)_3$ as a game-changing solar cell absorber.

In summary, the evolution of thin-film PV materials has progressed from Si wafers to mature thin films (CdTe, CIGS) and onward to a broad spectrum of emerging absorber families, each with unique strengths and persistent challenges. Among these, antimony chalcogenide, particularly $Sb_2(S,Se)_3$ stands out for its combination of environmental safety, elemental abundance, strong light absorption, and tunable electronic properties that make $Sb_2(S,Se)_3$ one of the most compelling next-generation absorbers for sustainable thin-film PVs.

1.3.Research Gaps and Problem Statement

Antimony sulfoselenide ($Sb_2(S,Se)_3$) has attracted significant attention as a thin-film PV absorber because it combines earth-abundant, non-toxic elements with a high absorption coefficient exceeding 10^5 cm^{-1} and a tunable bandgap close to the Shockley–Queisser (SQ) limit for single-junction solar cells. In spite of these advances in deposition methods, including hydrothermal and solvent-assisted growth, record devices still fall short of their theoretical performance, with notable deficits in V_{OC} and fill factor (FF) [43,44]. These challenges remain a barrier to unlocking the full potential of $Sb_2(S,Se)_3$ in attaining maximum conversion efficiency.

Extensive experimental and simulation studies suggest that nonradiative recombination at interfaces is the leading cause of these losses. Interface defects arising from under-coordinated atoms, dangling bonds, chemical reactions, and grain-boundary states form strong Shockley–Read–Hall (SRH) centers that pin quasi-Fermi levels and reduce V_{OC}. Both the front interface between the electron-transport layer (ETL) and absorber, as well as the rear interface at the absorber/back contact, are implicated. Deep defects caused by elemental diffusion, such as Cd from CdS buffer layers, or poorly designed back contacts, can introduce deep recombination centers, shortening carrier lifetimes even when the absorber has good bulk crystallinity [45–47]. The prevalence and impact of these interfacial defects are highlighted by studies showing that diffusion-blocking and surface-passivation strategies can potentially enhance device performance.

Band alignment between the absorber and hole transport layers (HTL) adds another layer of complexity. Even small mismatches in conduction or valence band positions can dramatically influence device operation. A negative conduction-band offset, often termed a “cliff,” can increase interfacial recombination, while an excessive positive offset, or “spike,” can impede electron extraction. Similarly, misalignment at the valence band edge can slow hole transfer and exacerbate recombination losses at the HTL/absorber interface. Research indicates that

fine-tuning band offsets, for example, through ultrathin dipole or passivation layers, can further mitigate V_{OC} losses. Yet, many commonly used ETLs and HTLs lack the necessary chemical flexibility or tunable energy levels to achieve ideal alignment with $Sb_2(S,Se)_3$ [47,48].

The choice of transport layers and their processing conditions also strongly affect performance. CdS has historically been favored for its consistent coverage and beneficial offsets, but suffers from toxicity, parasitic absorption in the blue spectrum, and interdiffusion that can produce buried homojunctions. Oxide ETLs such as TiO_2, SnO_2, and ZnO are chemically stable and transparent but often form weak bonds with chalcogenide absorbers, leave under-coordinated atoms or oxygen vacancies, or require high processing temperatures that can degrade the absorber [49–52]. On the hole-transport side, Spiro-OMeTAD initially provides good performance but relies on hygroscopic dopants that compromise stability and introduce ionic effects[53,54]. Alternative organic HTLs like PTAA and P3HT, as well as inorganic candidates such as NiO, CuSCN, and Cu_2O, have been explored; each, however, presents trade-offs in mobility, work-function matching, or interfacial compatibility [55–57]. These challenges underscore the pressing need for high-mobility, dopant-free HTLs and tunable, low-defect ETLs that are chemically compatible with Sb chalcogenides.

Microstructure and optical design further influence device efficiency. A quasi-one-dimensional crystal structure $Sb_2(S,Se)_3$ reveals that preferential [001] grain orientation and minimal grain-boundary defects are critical for long carrier diffusion lengths. Increasing absorber thickness can improve current generation by capturing more light, but it can also amplify bulk and grain-boundary recombination and increase the carrier transport paths, ultimately reducing PV performance [58]. Various theoretical studies emphasize the need to find an optimal thickness that balances generation and recombination. Additionally, parasitic optical losses in transport layers and non-optimized series or shunt resistances can depress FF even when interfaces are partially passivated [47].

Practical challenges related to the rear contact, device stability, and scalable processing further complicate performance improvements. Inefficient back contacts and the absence of hole-selective layers can lead to recombination and collection losses that cannot be offset by front-side enhancements alone. Long-term stability tests reveal that dopant migration, moisture sensitivity, thermal cycling, and chemical interdiffusion interact in complex ways, reducing device lifetime [59,60].

Addressing these issues requires systematic screening of novel HTLs, ETLs, and ultrathin interfacial layers capable of providing proper band alignment, chemical passivation, and diffusion blocking, while offering high intrinsic mobility and compatibility with $Sb_2(S,Se)_3$ fabrication processes. This thesis work employs SCAPS-1D simulations, informed by experimentally reported material parameters and novel candidate materials, to identify promising layer combinations that satisfy these requirements and support scalable device fabrication.

1.4.Justification

From the preceding discussion, it is clear that the persistent performance gap in $Sb_2(S,Se)_3$ solar cells primarily originates from interfacial recombination, unfavorable energy-band alignments, dopant-induced instability in transport layers, and chemical incompatibilities that limit charge extraction. Thus, addressing these issues requires an integrated material strategy capable of simultaneously improving charge selectivity, suppressing recombination, and maintaining chemical stability. In this context, the present study proposes a systematic combination of triazatruxene-based HTLs, namely AT-H, TAT-TY1, TAT-TY2, CI-B2, and CI-B3, strontium titanate (denoted as $SrTiO_3$ or STO) as the ETL, and graphitic carbon nitride (denoted as g-C_3N_4 or GCN) as a passivating interfacial modifier to overcome the limitations highlighted in the problem statement.

The first major issue identified in existing $Sb_2(S,Se)_3$ solar cells is inefficient hole extraction and dopant-related instability associated with conventional HTLs such as Spiro-OMeTAD and PTAA. These layers, although effective in PSCs, contain hygroscopic dopants (LiTFSI, tBP) that introduce trap states, induce ionic migration, and accelerate device degradation [53,54]. To mitigate these problems, in this work, we adopted triazatruxene-based HTLs, which offer inherently high hole mobility, chemical stability, and dopant-free operation. The star-shaped π-conjugated framework of triazatruxene facilitates ordered molecular stacking and efficient charge transport, while its tunable HOMO levels enable better valence-band alignment with $Sb_2(S,Se)_3$, thereby minimizing potential barriers for hole extraction. To be specific, these derivatives exhibit favorable HOMO energies around –5.1 eV, closely matching the valence band of $Sb_2(S,Se)_3$ positioned around –5.2 eV, which helps suppress interfacial recombination and enhances V_{OC}. Moreover, their dopant-free nature prevents moisture-induced degradation and enhances operational stability [44]. Therefore, the use of triazatruxene HTLs directly

addresses the problems of low hole mobility, poor band alignment, and dopant instability that have restricted $Sb_2(S,Se)_3$ device performance .

The second major issue is front-interface recombination and band misalignment between $Sb_2(S,Se)_3$ and traditional ETLs like CdS or TiO_2. CdS introduces Cd toxicity, high parasitic absorption, and interdiffusion at the interface, while TiO_2 suffers from oxygen vacancies and requires high-temperature processing. These limitations necessitate a non-toxic, stable, and electronically compatible ETL. STO fulfills these criteria owing to its wide bandgap (~3.2 eV), high dielectric constant, and excellent thermal and chemical stability. Its conduction band minimum (~ - 4.0 eV) provides a small positive conduction band offset with $Sb_2(S,Se)_3$ (~ - 4.1 eV), ensuring efficient electron extraction without forming a recombination-prone cliff. Additionally, the high dielectric constant of STO effectively screens interface charge, reducing the recombination velocity and stabilizing band bending at the junction [61]. By optimizing material properties, STO can significantly enhance charge selectivity and mitigate the front-interface recombination losses that dominate current $Sb_2(S,Se)_3$ devices.

Another critical issue highlighted in the literature is the persistence of interface trap states and elemental interdiffusion, which continue to limit device efficiency even when optimized ETLs and HTLs are used. To address this, the present study introduces an ultrathin GCN interlayer between ETL and absorber. The N-rich surface of GCN contains abundant lone pairs capable of coordinating with under-coordinated Sb or Se atoms, effectively passivating dangling bonds and defect states. This chemical passivation reduces SRH recombination centers and enhances carrier lifetime. Moreover, GCN acts as a diffusion barrier that suppresses intermixing between the oxide and chalcogenide layers, improving interface stability during thermal cycling. Its moderate bandgap (~2.8 eV) allows it to function as a selective contact that facilitates carrier transport rather than impeding it. Consequently, GCN resolves one of the most stubborn problems in $Sb_2(S,Se)_3$ PVs i.e., interface trap-assisted recombination, while simultaneously contributing to improved performance and long-term device reliability [62,63].

Overall, the exploration of a high-mobility organic HTL and a wide-bandgap oxide ETL ensures efficient charge extraction on both sides of the absorber, thereby reducing series resistance and improving carrier selectivity. Further, the inclusion of GCN provides enhanced interface passivation, thereby mitigating both front and back interface recombination. These modifications also contribute to reduced hysteresis, enhanced photostability, and better

tolerance to interface defect factors that have been consistently reported as performance bottlenecks in experimental and simulated $Sb_2(S,Se)_3$ studies.

Hence, the proposed architectures with triazatruxene HTLs, STO ETL, and GCN interlayer are not an arbitrary material substitution but a strategic, problem-driven framework that directly tackles the fundamental issues summarized in the problem statement. By systematically analyzing the impact of each layer through SCAPS-1D simulations, this thesis aims to demonstrate a marked improvement in PV parameters while ensuring environmental compatibility and long-term stability. Therefore, the selected material system provides a rational justification for advancing $Sb_2(S,Se)_3$ PVs toward high-efficiency, non-toxic, and industrially scalable solar technologies.

2. Antecedents/Background

2.1.Photovoltaic Effect and Solar Cell Function

Solar cells directly convert solar radiation into electrical energy by the photovoltaic effect, in which photons of sufficient energy create electron–hole pairs that are separated and collected to generate current and voltage. A p–n junction, formed by an n-type semiconductor (where electrons are the majority carriers) and a p-type semiconductor (with holes as the majority carriers), is the fundamental structure [64]. **Fig. 1** illustrates the p–n junction and its working principle, with electrons (yellow) and holes (purple) diffusing under concentration gradients, recombining near the junction, and being separated by a built-in electric field (red arrow).

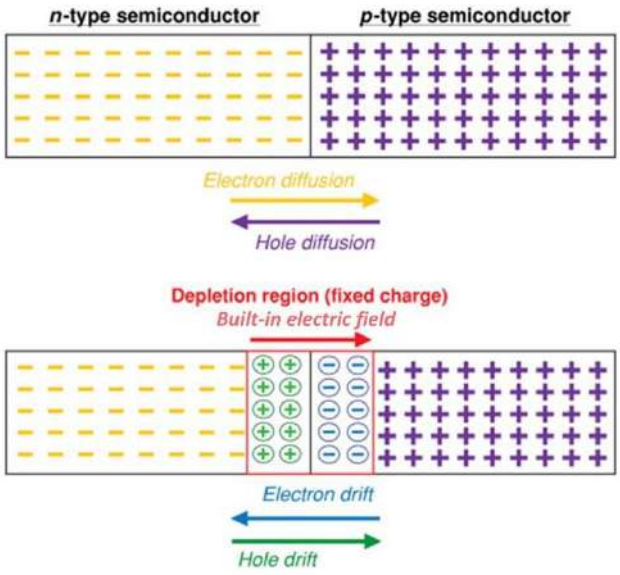

Fig. 1. p–n junction and its working principle (carrier diffusion, depletion region, built-in electric field) [65].

When these n-type and p-type regions are placed in contact, electrons diffuse from the n-region into the p-region while holes diffuse from p into n. In the region near the interface, recombination leaves behind ionized donors and acceptors, leading to a depletion region depleted of mobile carriers. The immobile ion charges establish a built-in electric field oriented from n to p, which opposes further diffusion and defines equilibrium [64].

Upon illumination, photons with energy ≥ the semiconductor bandgap excite electrons from the valence band maximum (VBM) to the conduction band minimum (CBM), leaving holes behind. Those photogenerated carriers that diffuse into the depletion zone (or are generated within it) are swept apart by the built-in field: electrons drift toward the n-side (or towards the electron-collecting contact) and holes drift toward the p-side (or the hole-collecting contact). This separation produces a photovoltage, and when the cell is connected to an external load, a photocurrent flows [12].

In thin-film solar cells (e.g. p–i–n or n–i–p architectures), an intrinsic or lightly doped absorber layer is sandwiched between ETL and HTLs. The differences in Fermi levels of adjacent layers cause band bending and the formation of heterojunctions, which assist in directing electrons toward the ETL and holes toward the HTL. This layered arrangement enhances carrier extraction and reduces recombination at interfaces [66]. The thin-film devices in this thesis all rely on the same underlying PV mechanism.

2.2. Key PV Performance Metrics

One of the essential performance parameters is the external quantum efficiency (EQE), defined at each wavelength λ as:

$$\mathrm{EQE}(\lambda) = \frac{n_e(\lambda)}{n_{\mathrm{ph}}(\lambda)} \quad (1)$$

where n_e (λ) is the number of collected charges and n_{ph} (λ)is the number of incident photons. **Fig. 2** shows a representative EQE spectrum. In an ideal device, EQE could reach 100 %, but real devices incur losses from reflection, transmission (i.e., photons not absorbed), recombination (bulk and interface), and incomplete collection, especially in the blue and red spectral regions. Thus, the EQE curve is a diagnostic tool to identify wavelength-dependent loss mechanisms [66].

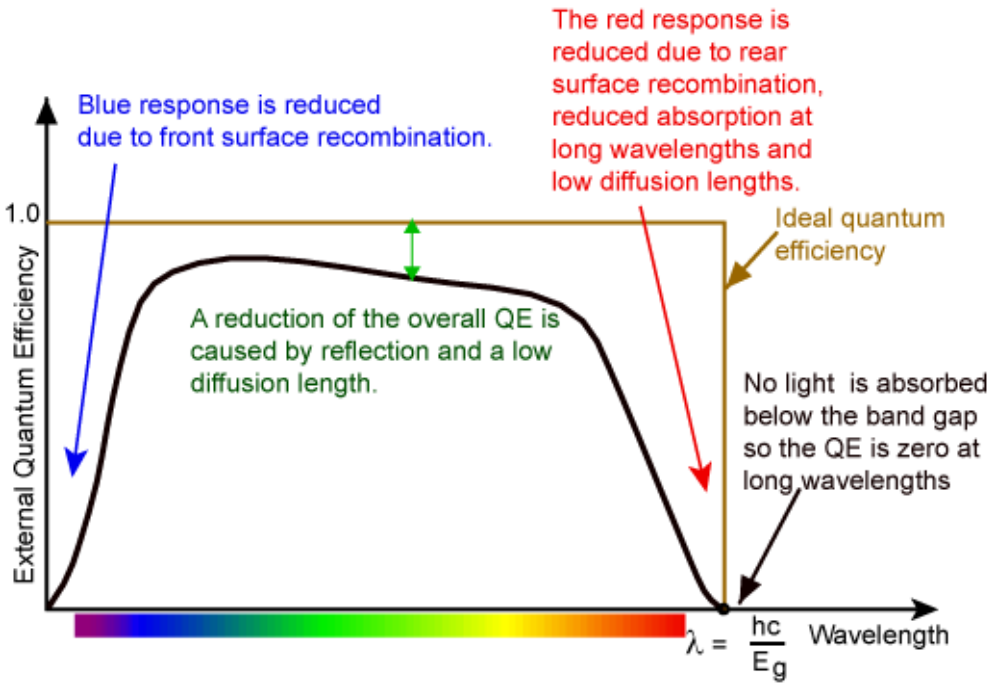

Fig. 2. Representative external quantum efficiency (EQE) spectrum [67].

Because the number of photons incident on a solar cell varies with irradiance, atmospheric conditions, geometry, and time, one uses a standard spectrum for consistent evaluation. The widely adopted standard is AM 1.5G (Air Mass 1.5 global), which corresponds to ~1000 Wm^{-2} at 25°C under terrestrial conditions. The AM parameter describes the effective atmospheric path length: for instance, AM 1.5 implies sunlight traverses 1.5 times the vertical thickness of the atmosphere.

By normalizing the current to the device area, one defines the photocurrent density J_{ph}. In well-designed cells, the short-circuit current density (J_{SC}) (i.e., at voltage $V = 0$) approximates J_{ph}, given by:

$$J_{SC} = J_{\text{ph}} = q \int \text{EQE}\,(\lambda)\, b_S(\lambda)\, d\lambda \tag{2}$$

where q is the elementary charge and b_S (λ)is the incident photon flux per wavelength. Thus, the measured J_{SC} links directly to how well photons are converted to usable carriers [12,66].

In the absence of light, the device behaves as a diode governed by the Shockley equation:

$$J_{\text{dark}} = J_0(e^{\frac{qV}{nkT}} - 1) \tag{3}$$

where J_0 is the reverse saturation current density, n is the ideality factor, k is Boltzmann's constant, q is the elementary charge and T is the temperature. Under illumination, the total current density J(V) is approximated by:

$$J(V) = J_{\text{ph}} - J_{\text{dark}} \tag{4}$$

This relation is standard in solar cell device theory [12,64,66].

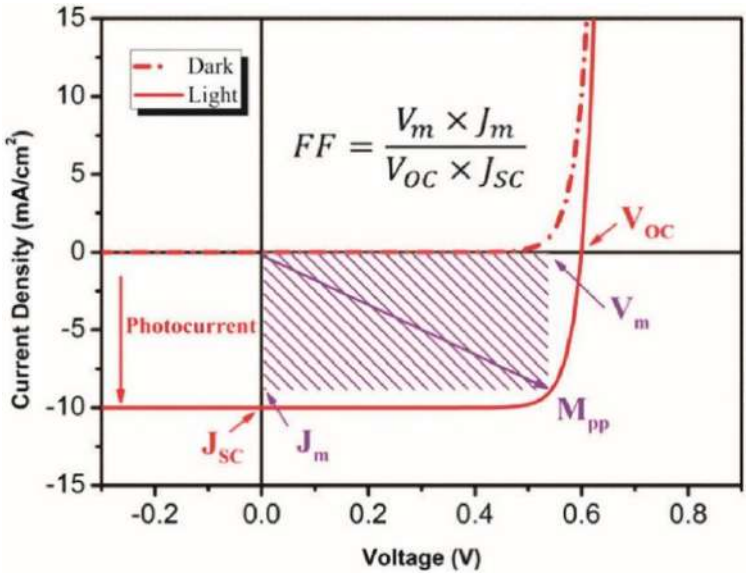

Fig. 3. J–V characteristic curve under illumination and in the dark [68].

The functional relationship between voltage (V) and current (I) under a given set of operating conditions, such as illumination and temperature, is commonly represented by the current–voltage (J–V) characteristics curve. **Fig. 3** illustrates the J–V characteristics of a solar cell both in the dark and under illumination. The operational states of a solar cell can be categorized into three key conditions: open circuit, short circuit, and the maximum power point (M_{PP}) during loading. Under short-circuit conditions, the terminal voltage is zero ($V = 0$) while the current reaches its maximum value where J = J_{SC}. Conversely, in the open-circuit state, the current is zero ($J = 0$) and the voltage attains its maximum value to be V= V_{OC}. Under ideal assumptions, the short-circuit current corresponds to the photogenerated current ($J_{SC} = J_{ph}$), and the V_{OC} can be expressed analytically as:

$$V_{\text{OC}} \approx \frac{nkT}{q} \ln\left(\frac{J_{SC}}{J_0} + 1\right) \tag{5}$$

where n is the diode ideality factor, k is the Boltzmann constant, T is the absolute temperature, q is the elementary charge, and is the diode saturation current. Eq. (2) and (5) collectively

indicate that both J_{SC} and V_{OC} are strongly dependent not only on the intrinsic properties of the PV material but also on external environmental conditions such as irradiance and temperature. To ensure consistency and comparability of measurements, a standard testing condition (STC) is employed, where the incident irradiance is set to 1000 $W.m^{-2}$ using the AM 1.5G solar spectrum and the temperature is maintained at 25 °C.

In addition to J_{SC} and V_{OC}, the FF is another crucial parameter that quantifies the squareness of the J–V curve and reflects how effectively the solar cell can convert generated charge carriers into usable power FF is defined as:

$$\mathrm{FF} = \frac{J_M V_M}{J_{\mathrm{SC}} V_{\mathrm{OC}}} \tag{6}$$

where J_M and V_M are the current and voltage at the M_{PP}, the point on the J–V curve where the product of current and voltage is maximized, as depicted in **Fig. 3**. The PCE, which serves as a comprehensive measure of the solar cell's ability to convert incident solar energy into electrical energy, is calculated based on the relation:

$$PCE = \frac{P_M}{P_{in}} = \frac{J_{SC} V_{OC} FF}{P_{in}} \tag{7}$$

where P_M is the maximum output power at the M_{PP} and P_{in} is the incident power per unit area, specified as 1000 $W.m^{-2}$ according to AM 1.5G standards. Together, the parameters J_{SC}, V_{OC}, FF and PCE provide a complete description of the PV performance and are essential for assessing the effectiveness of solar cell designs under practical operating conditions [12,69].

In practical solar cells, resistance is unavoidable due to material properties and device architecture. Series resistance (R_s) arises from resistive components in the contacts, interfaces, and bulk materials, whereas shunt resistance (R_{sh}) originates from defects in the depletion region, edge recombination, or leakage paths. Consequently, the resulting current density is expressed by the modified diode equation:

$$J = J_0 \left[\exp\left(\frac{q(V+JR_s)}{nkT}\right) - 1\right] + \frac{V+JR_s}{R_{sh}} - J_{ph} \tag{8}$$

An increase in R_s typically leads to a nonlinear reduction in J_{SC} and FF, while V_{OC} remains relatively unaffected. In contrast, a higher R_{sh} significantly enhances FF, with only minor changes to V_{OC}. Therefore, achieving high-efficiency solar cells requires careful design to

maintain a low ideality factor, minimal R_s, and maximal R_{sh}, alongside minimizing recombination and optical losses [12,64].

2.3.Conventional $Sb_2(S,Se)_3$ Solar Cell Structure and Functional Layers

2.3.1. Baseline Device and Band Alignment

The standard thin-film $Sb_2(S,Se)_3$ solar cell used in the present work adopts the planar heterojunction architecture FTO/CdS/$Sb_2(S,Se)_3$/Spiro-OMeTAD/Au, a stack that has become a suitable baseline because it combines a transparent conductive oxide electrode and a compact chalcogenide absorber with a well-studied n-type buffer and an organic hole transporter that reliably extracts holes to the metal back contact. The conventional base device structure is shown in **Fig. 4**. In this architecture, FTO functions as the transparent conductive oxide (TCO) through which light passes and reaches the $Sb_2(S,Se)_3$ layer, which serves as the absorber material, and Au serves as the back contact. CdS is employed as the ETL, while Spiro-OMeTAD functions as HTL [44]. Good extraction requires favorable band offsets at both interfaces: the CdS conduction band must lie below (or be well aligned with) the $Sb_2(S,Se)_3$ conduction band minimum to accept electrons with minimal barrier, and the HOMO of the HTL should align with the valence band maximum of the absorber to collect holes efficiently and suppress recombination. Practical device performance is governed by the absorber quality (defect density, grain orientation and thickness), the presence of interface recombination centers at the CdS/absorber and absorber/HTL contacts, the energy band alignment (spike vs cliff), and the transport and contact resistances of the charge-selective layers [60,70]. In the baseline architecture, $Sb_2(S,Se)_3$ acts as a p-type (or mildly p-type) narrow-gap absorber with a composition-tunable direct/indirect bandgap in the ~1.3 - 1.6 eV range depending on the S/Se ratio and processing, which places it in an ideal spectral region for single-junction PVs [71]. CdS, the conventional buffer, is a wide bandgap (≈2.4 - 2.5 eV) n-type material that forms the electron-collecting contact with FTO. In many devices, CdS produces a near-flat or mildly cliff-type conduction-band offset at the buffer/absorber interface, which can either help or hinder electron extraction depending on interface defect chemistry and buffer stoichiometry [70,72]. Spiro-OMeTAD is widely used as HTL because its HOMO (≈ −5.2 eV vs vacuum) and large transport gap allow efficient hole extraction and blocking of electrons, but Spiro's cost, the need for dopants to reach high conductivity, and its relative instability under some conditions motivate alternatives [44]. At the electrodes, commercial FTO provides a stable, transparent bottom contact (work function commonly reported near ~5.0 eV depending on

surface treatment) while Au serves as a high-work-function back contact (≈5.1 eV), forming an effective hole collection electrode when the HTL energy levels are matched [73,74]. Thus, a working device requires careful tuning of absorber thickness, buffer composition and interface passivation to realize high Voc and FF by minimizing interface recombination and band misalignment losses.

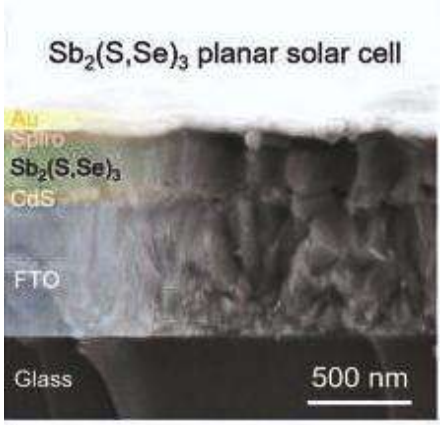

Fig. 4. Experimental high performance $Sb_2(S,Se)_3$ solar cell device structure.

2.3.2. $Sb_2(S,Se)_3$ Absorber Layer

$Sb_2(S,Se)_3$ is a quasi-one-dimensional (Q-1D) antimony chalcogenide semiconductor possessing an orthorhombic crystal structure with *Pbnm* symmetry. Its framework is composed of covalently bonded $[Sb_4(S,Se)_6]_n$ ribbons extending along the [001] direction, while weak van der Waals interactions connect adjacent chains along the [100] and [010] axes. This anisotropic configuration not only generates direction-dependent electronic and optical behavior but also minimizes defect-induced recombination because the grain boundaries are naturally terminated by non-dangling bonds when ribbons are vertically aligned [75,76]. The presence of Sb $5s^2$ lone-pair electrons provides additional structural flexibility, allowing the material to self-heal broken bonds and suppress deep trap states by minor lattice distortions that stabilize the crystal configuration [77]. Such self-passivating properties, combined with its benign grain boundaries, make $Sb_2(S,Se)_3$ particularly attractive for high-performance thin-film PVs.

The unique electronic structure of $Sb_2(S,Se)_3$ arises from strong hybridization between Sb 5s and 5p orbitals and the chalcogen p states. Density functional theory (DFT) analyses show that CBM primarily originates from Sb 5p and S(Se) p antibonding orbitals, while the VBM is dominated by Sb 5s and S(Se) p hybrid states [78,79]. Its nearly direct bandgap, with a difference between direct and indirect transitions smaller than 0.1 eV, facilitates efficient light

absorption and low recombination loss. The optical bandgap is tunable between 1.1 and 1.7 eV depending on the S/Se composition, as increasing Se content shifts the absorption edge from ~720 nm to ~1100 nm [80,81]. Moreover, its high absorption coefficient (10^4-10^5 cm^{-1}) enables nearly complete light harvesting in absorber layers only a few hundred nanometers thick, ensuring efficient utilization of solar energy while reducing material costs. Electrical and transport properties of $Sb_2(S,Se)_3$ are highly anisotropic due to its Q-1D nature. Carriers move preferentially along the ribbon axis, resulting in superior mobility and reduced interface recombination when grains are oriented perpendicular to the substrate [76,82]. Proper control of composition and selenization allows precise modulation of electrical conductivity and carrier type. The defect tolerance and benign nature of grain boundaries are further improved by the lone-pair electrons of Sb, which alleviate strain and facilitate spontaneous reconstruction. However, antisite and vacancy-type defects can still contribute to non-radiative recombination and V_{OC} losses, necessitating additive engineering or compositional optimization to mitigate deep-level trap formation [44,83].

The PV performance of $Sb_2(S,Se)_3$ has significantly advanced in recent years due to improved synthesis strategies. Early single-step CBD films achieved 2.5% efficiency [84], which later increased to 6.6% through controlled interdiffusion of S and Se layers [85]. The introduction of hydrothermal synthesis marked a breakthrough, where bandgap tuning via S/Se ratio adjustment enhanced carrier lifetime and minimized trap states, resulting in a certified 10% PCE [86]. Further optimization through ethylenediaminetetraacetic acid (EDTA) complexation enlarged the grain size and improved film uniformity, yielding 10.5% PCE [87]. Subsequently, alkaline metal fluoride-assisted hydrothermal post-treatment engineered a favorable S/Se gradient, booisting the performance to a record 10.7% PCE [88]. The latest report by Tao Chen and co-workers pushed this further to 10.75% through refined hydrothermal control and surface passivation, representing the current highest efficiency for $Sb_2(S,Se)_3$ solar cells [42]. Alongside hydrothermal processes, vacuum-based deposition methods such as vapor transport deposition, dual-source evaporation, and co-sublimation have also yielded PCEs in the range of 7-9% [40,89]. These approaches allow precise control of film composition and bandgap gradient formation, promoting dense crystallization and favorable ribbon orientation. Recent developments incorporating gradient band alignment and CsI-assisted defect passivation have further improved V_{OC} and device stability. Environmentally, $Sb_2(S,Se)_3$ remains an earth-abundant and non-toxic alternative to Pb- and Cd-based absorbers [90]. With continued advances in texture control, defect passivation, and bandgap engineering, the theoretical PCE

of $Sb_2(S,Se)_3$-based solar cells is projected to exceed 20% under optimized device architectures.

2.3.3. Conventional Inorganic ETLs

In $Sb_2(S,Se)_3$ solar cells, the ETL plays a decisive role in extracting electrons and blocking holes while ensuring minimal optical loss and ideal band alignment with the absorber. Because light first passes through the ETL, it must have a wide bandgap, high electron mobility, and excellent interface quality to suppress recombination. TiO_2 is among the most employed ETLs owing to its transparency, stability, and ease of fabrication. Its anatase (101) surface promotes parallel orientation of Sb-chalcogenide ribbons, while controlled annealing introduces oxygen vacancies that enhance epitaxial alignment and V_{OC} [91]. However, its low electron mobility (~1 $cm^2\ V^{-1}\ s^{-1}$) causes recombination, which has been mitigated by dopants such as Ba, Cs, Li, and Zn [92–95]. CdS remains the most successful ETL in achieving high efficiency (up to 10.75% PCE) because of its good band alignment and high mobility (~350 $cm^2\ V^{-1}\ s^{-1}$). Yet, its narrow bandgap (2.4 eV) leads to parasitic absorption, and Cd diffusion at the interface degrades stability. These drawbacks have encouraged partial Zn substitution ($Cd_{0.75}Zn_{0.25}S$), CdS thinning or double-buffer configurations, and oxygen incorporation (CdS:O) to broaden the bandgap and suppress Cd migration [36].

To replace CdS, Cd-free ETLs such as ZnO, Zn(O,S), and SnO_2 have been actively pursued. Spray-pyrolyzed ZnO exhibits tunable orientation, which influences $Sb_2(S,Se)_3$ ribbon alignment and ensures remarkable device stability under damp-heat and light-soaking tests [71]. SnO_2, another wide-bandgap material with high mobility, suffers from interface degradation at high annealing temperatures, but solution and spray processes with dopants (e.g., $LaCl_3$, $CdCl_2$) have improved compatibility [96–98]. Overall, TiO_2 and CdS remain benchmark ETLs, while ZnO, Zn(O,S), and SnO_2 based systems represent the most promising non-toxic alternatives, capable of sustaining efficient charge transport and stability through optimized doping and interface engineering. However, in terms of performance, they still lag behind the expected SQ limit, necessitating the new ETL exploration.

2.3.4. Organic and Inorganic HTLs

In $Sb_2(S,Se)_3$ solar cells, HTL is crucial for efficiently extracting holes from the absorber while minimizing interfacial recombination. Organic HTLs, such as spiro-OMeTAD and P3HT, are widely employed due to their excellent solubility, uniform thin-film formation via spin coating, and good band alignment with $Sb_2(S,Se)_3$ [83]. P3HT, though inexpensive and easy to process, suffers from low hole mobility in its amorphous form (~10^{-5} $cm^2\ V^{-1}\ s^{-1}$), limiting charge

transport, and only self-assembled nanofibrils achieve higher mobility (~0.1 cm^2 V^{-1} s^{-1}) through strong π–π interactions [99]. Spiro-OMeTAD, doped with LiTFSI and tBP, remains the most effective organic HTL, enabling high-efficiency $Sb_2(S,Se)_3$ solar cells due to superior hole extraction and interface passivation [86,88].

Inorganic HTLs offer higher stability against moisture, oxygen, and thermal stress, along with moderately high hole mobility (0.1-1 cm^2 V^{-1} s^{-1}). CuSCN, NiO_x, V_2O_5, MoS_3, and WO_3 have all been applied in Sb chalcogenides based solar cells. CuSCN, while initially promising, exhibits weak hole extraction (~5.9×10^8 s^{-1}), leading to defect accumulation and recombination. NiO_x, V_2O_5 have been deposited via spin coating and post-treatment, yielding moderate PCE (~3–5%) [167, 168], whereas quantum dot PbS and MoS_3 films enhance hole transport and improve PCE to ~6.8–7.1% [100–105]. Despite their superior stability, inorganic HTLs have yet to match the efficiency of spiro-OMeTAD-based devices, primarily due to suboptimal interface quality and hole extraction. This highlights the ongoing need for non-toxic, stable HTLs that maintain excellent PV performance in $Sb_2(S,Se)_3$ solar cells.

2.3.5. Front and Back Contacts

In reported $Sb_2(S,Se)_3$ solar cell devices, the front TCO layer almost universally employs FTO (fluorine-doped tin oxide) as the base substrate. FTO's advantages include excellent visible/near-IR transparency, low sheet resistance, and crucially, high thermal and chemical stability during hydrothermal growth, selenization, and annealing processes, which are essential to form high-quality $Sb_2(S,Se)_3$ films with good ribbon alignment and low defect densities [42,86]. Many reports on high-efficiency $Sb_2(S,Se)_3$ devices start with Glass/FTO /compact SnO_2 (or CdS)/absorber stacks, highlighting that the FTO with compact ETL supports favorable nucleation, orientation control, and interface passivation [106]. In contrast, alternative TCOs such as ITO and AZO have seen very limited use in $Sb_2(S,Se)_3$, generally only in semitransparent or bifacial device configurations where lower-temperature processing is possible; they are less chemically robust during harsh absorber processing, which limits their adoption in the bulk of high-performance $Sb_2(S,Se)_3$ solar cells [106].

For the back contact, gold (Au) remains the benchmark in $Sb_2(S,Se)_3$ solar cells because its high and stable work function (~5.1 eV) aligns well with the VB of $Sb_2(S,Se)_3$, enabling efficient hole extraction with minimal back-barrier losses and avoiding diffusion or chemical reaction with the absorber [42]. However, novel back electrodes have been explored in $Sb_2(S,Se)_3$ devices. A notable example is the use of MXene ($Ti_3C_2T_x$) as a back electrode in the

architecture FTO/CdS/$Sb_2(S,Se)_3$/MXene, which achieved competitive performance and illustrated that non-noble, conductive, low-reflectance materials can replace Au under proper interface engineering [107].

2.4.Evaluation of the Proposed Transport Layers

2.4.1. Triazatruxene HTLs

Triazatruxene derivatives exhibit remarkable physicochemical and electronic features that make them excellent candidates for HTLs in PV applications. Their planar C_3-symmetric π-extended core enables strong π–π stacking, forming uniform, pinhole-free films with low surface roughness and high morphological stability [108]. These materials demonstrate high hole mobilities in the range of 10^{-4}-10^{-3} cm^2 V^{-1} s^{-1}, deep HOMO levels between -5.1 and -5.3 eV that ensure favorable band alignment with common absorbers, and excellent thermal stability with decomposition temperatures above 300 °C . Moreover, the nitrogen-rich indole framework stabilizes oxidized species, enhances electrochemical robustness, and suppresses trap formation, leading to superior operational stability in devices [44].

Unlike Spiro-OMeTAD, they function efficiently without dopants, addressing stability issues from hygroscopic dopants and lithium-ion diffusion [44]. These HTLs have been widely applied in PSCs. For instance, in 2015, Rakstys et al. synthesized star-shaped HTLs with methoxybenzene groups, achieving up to 18.3% efficiency [109]. Later, Connel et al. applied triazatruxene derivatives featuring hexyl side chains in PSCs, reaching 20.3% efficiency [110]. Apart from this, various studies have also explored triazatruxene derivatives with different structures and properties, subsequently applied them in PSCs [111–117]. Recent studies have shown, dopant-free HTLs using donor–π–acceptor (D–π–A) architectures [118,119] and star-shaped triazatruxene derivatives, synthesized via Suzuki–Miyaura cross-coupling, show pinhole-free films, reducing recombination losses [120]. Additionally, structural modifications, such as incorporating electron-rich donor units (such as phenyl carbazole and N-hexyl carbazole) and π-bridging groups (terthiophene), optimize HOMO–LUMO levels, improve charge mobility, and enhance stability [108,121]. Moreover, HTLs with D–π–A architecture even achieved PCE twice as high as that of undoped Spiro-OMeTAD, underscoring their potential as a versatile alternative to Spiro-OMeTAD [122]. While these HTLs have been successful in PSCs, there are no experimental or theoretical reports on the use of these HTLs in $Sb_2(S,Se)_3$ solar cells. Therefore, for the first time, we propose the use of triazatruxene-based HTLs as an alternative for Spiro-OMeTAD in $Sb_2(S,Se)_3$ solar. Hence, this thesis investigates the potential of triazatruxene derivatives with D–π–A architectures, such as N-ethyl rhodamine

and dicyanovinylene N-ethyl rhodamine-modified triazatruxenes (CI-B2,CI-B3), and star-shaped 5,10,15-trihexyl-10,15-dihydro-5H-diindolo[3,2-a:3′,2′-c]carbazole (TAT-H), 3,8,13-tris(4-(8a,9a-dihydro-9H-carbazol-9-yl)phenyl)-5,10,15-trihexyl-10,15-dihydro-5H-diindolo[3,2-a:3′,2′-c]carbazole (TAT-TY1), and 3,8,13-tris(4-(8a,9a-dihydro-9H-carbazol-9-yl)phenyl)-5,10,15-trihexyl-10,15-dihydro-5H-diindolo[3,2-a:3′,2′-c]carbazole (TAT-TY2) derivatives, as a substitute for the conventional Spiro-OMeTAD HTL in $Sb_2(S,Se)_3$ solar cells using SCAPS-1D simulations.

2.4.2. $SrTiO_3$ ETL

$SrTiO_3$ is a cubic perovskite oxide (ideal ABO_3 structure) that is a wide-bandgap semiconductor (indirect $E_g \approx 3.2$-3.25 eV; direct $E_g \approx 3.7$–3.75 eV) with an electronic structure dominated by O-2p states at the VB and Ti-3d states at the CB edge. Its large static dielectric constant and strong polarizability provide superior charge screening compared with conventional oxide ETLs (e.g., TiO_2). Further, its reduced coulombic trapping can lower interfacial recombination velocities, which is a desirable property when coupling to a chalcogenide absorber such as $Sb_2(S,Se)_3$ where interface traps can limit V_{OC}. Pristine STO is insulating at room temperature, but controlled n-type conductivity is routinely achieved by aliovalent doping (e.g., Nb^{5+} to Ti^{4+}) or by engineering oxygen vacancies [123–125]. These approaches raise carrier concentration and electronic conductivity to levels suitable for ETL use while preserving the wide optical gap that prevents parasitic absorption of visible light. Importantly for $Sb_2(S,Se)_3$, the CB edge of STO is positioned at a higher energy relative to TiO_2 in many reports, which favors stronger electron extraction and can increase V_{OC} when properly aligned with the absorber CB. In solar cell device this effect has been shown to yield higher Voc and enhanced stability versus TiO_2 ETLs . Finally, STO films and nanoparticle inks can be deposited by a range of techniques (low-temperature solution/sol-gel, sputtering, pulsed laser deposition, spray pyrolysis, and nanoparticle paste processing), and nanoscale or mesoporous morphologies provide percolating electron pathways when the intrinsic conductivity is enhanced [61,126–128]. This flexibility in processing is valuable when integrating a novel ETL into an $Sb_2(S,Se)_3$ stack that may require specific thermal or chemical compatibility.

Experimentally, STO has been applied as an ETL in PSCs and colloidal quantum-dot devices, showing promising results: Bera et al. reported meso-STO ETLs in $CH_3NH_3PbI_{3-x}Cl_x$ devices with V_{OC} improvement of ~25% compared to TiO_2 controls [129], and De Bastiani et al. achieved ~19% PCE in PSCs with low-temperature processed STO ETLs and demonstrated enhanced device stability (~80 % of initial efficiency after 1000 h illumination) [61]. Although

STO has not yet been reported as an ETL in $Sb_2(S,Se)_3$ devices, these results strongly support its candidacy. Implementing STO in $Sb_2(S,Se)_3$ solar cells could leverage improved band alignment, optical transparency, and stability while reducing reliance on Cd-based ETLs (such as CdS). Key tasks will include verifying STO/$Sb_2(S,Se)_3$ band offsets, ensuring STO conductivity (e.g., via doping or nanoparticle films), and optimizing interface engineering to suppress recombination at STO/absorber boundaries.

2.4.3. g-C_3N_4 Interfacial Layer

g-C_3N_4 is a layered polymeric semiconductor composed of tri-s-triazine (heptazine) units connected through planar tertiary N linkages, forming a sp^2-hybridized conjugated π-system that enables charge delocalization along the 2D plane. It crystallizes in a pseudo-graphitic structure with an interlayer spacing of ~0.326 nm and exhibits a moderate bandgap of 2.6–2.8 eV, allowing visible-light absorption up to ~460 nm [130,131]. The CBM −4.1 eV and VBM −6.7 eV make it energetically compatible with typical n-type and p-type semiconductors for efficient electron extraction [132]. Despite its intrinsically low conductivity (~10^{-8} S cm^{-1}) and limited electron mobility (10^{-3}-10^{-2} cm^2 V^{-1} s^{-1}) due to strong electron–phonon coupling, these parameters can be enhanced by heteroatom doping (O, S, P, B), metal incorporation (Zn, Ag, Ni), or nanostructuring into nanosheets and quantum dots, which introduce mid-gap states and improve carrier delocalization [131]. The presence of surface amino and imide groups provides abundant Lewis base sites capable of coordinating metal cations or interacting with adjacent oxides and chalcogenides, enabling effective interface dipole formation and trap-state passivation. Furthermore, the high thermal stability (up to ~600 °C), chemical inertness, and tunable work function (4.1- 4.4 eV) make g-C_3N_4 a robust interfacial material for PV devices [130].

Recent studies have successfully incorporated g-C_3N_4 as an electron transport or buffer layer in various solar cell architectures owing to its favorable band alignment and passivation chemistry. In PSCs, introducing g-C_3N_4 nanosheets or quantum dots between the SnO_2/perovskite or TiO_2/perovskite interfaces markedly reduced interfacial recombination and improved carrier extraction, achieving PCEs exceeding 22%. The hybridization of SnO_2 with ultrathin g-C_3N_4 layers enhanced film conductivity and suppressed oxygen vacancies, facilitating faster interfacial electron transfer and higher V_{OC}. Similarly, in organic and DSSCs, g-C_3N_4-based ETLs have demonstrated improved charge collection and device stability through enhanced electron mobility and barrier-free energy alignment [133–135]. These results underline its multifunctional ability to act simultaneously as an electronic bridge and defect-

healing interface. Given its suitable CB position (close to CdS), strong adhesion through surface N sites, and capacity to inhibit interdiffusion, an ultrathin g-C_3N_4 layer between CdS and $Sb_2(S,Se)_3$ could effectively reduce interface recombination, minimize Cd–S/Se alloying, and tune the CB offset for optimized electron flow. Such integration could thus be a promising strategy for achieving higher Voc and overall device efficiency in $Sb_2(S,Se)_3$ thin-film solar cells.

2.5.Overview of SCAPS-1D Simulation

SCAPS-1D, short for Solar Cell Capacitance Simulator in One Dimension, was developed by Prof. Marc Burgelman and his research group at Ghent University, Belgium, and has since evolved into one of the most accessible simulation tool in PV research [136]. Originally designed to study thin-film heterojunction devices, SCAPS-1D has grown into a versatile modeling tool that bridges theoretical understanding and experimental design. Its wide acceptance stems from its ability to accurately reproduce experimental trends while maintaining simplicity and computational efficiency, making it suitable for both academic exploration and pre-fabrication analysis. Unlike complex multidimensional modeling platforms, SCAPS-1D focuses on vertical carrier transport within multilayer structures, which is often the dominant process in thin-film solar cells [44]. It numerically solves the coupled Poisson and continuity equations for electrons and holes, enabling the detailed simulation of fundamental device processes such as charge transport, recombination, and electrostatic potential distribution. From these solutions, it generates key electrical characteristics including current–voltage (J–V) curves, capacitance–voltage (C–V) behavior, quantum efficiency (QE) spectra, and transient responses, offering deep insight into the internal physics of the device.

One of greatest advantages of SCAPS-1D lies in its computational efficiency and intuitive interface, which allow researchers to perform rapid simulations without the need for advanced hardware or programming expertise [44]. It permits fine control over material and structural parameters such as doping density, defect concentration, bandgap, mobility, and layer thickness facilitating systematic optimization of PV performance. Despite being one-dimensional, SCAPS-1D has proven capable of reliably predicting device behavior and correlating well with experimental outcomes, which underpins its sustained importance in PV modeling. Although higher-dimensional tools like COMSOL Multiphysics or Sentaurus TCAD can model complex geometries and lateral effects, they typically require substantial computational power and costly licenses. In contrast, SCAPS-1D remains freely available, well-validated, and highly

adaptable, supporting features like interface modeling, defect analysis, and multilayer structures [137]. This combination of simplicity, accuracy, and accessibility has established SCAPS-1D as an indispensable tool for understanding and optimizing the performance of emerging thin-film solar cells.

3. Hypothesis

The emerging chalcogenide absorber $Sb_2(S,Se)_3$, known for its tunable direct bandgap, high optical density, and low effective carrier mass, can enhance solar cell performance when integrated with various transport layers and interfacial engineering strategies that modulate band offsets, improve photocurrent generation, and restrict ion interdiffusion, while minimizing open circuit voltage and fill factor losses.

4. Objectives

4.1.General Objective

To investigate the performance and charge carrier dynamics of $Sb_2(S,Se)_3$ solar cells through systematic studies of hole transport layers, electron transport layers, and interfacial modifications, aiming to enhance photocurrent, energy band alignment, and overall device efficiency.

4.2.Specific Objectives

1. To perform SCAPS-1D simulations of $Sb_2(S,Se)_3$ solar cells by reproducing the baseline FTO/CdS/$Sb_2(S,Se)_3$/Spiro-OMeTAD/Au device, introducing triazatruxene-based HTLs (CI-B2, CI-B3, TAT-H, TAT-TY1, TAT-TY2) as cost-effective alternatives, and optimizing HTL, ETL, and absorber parameters to improve PV characteristics and overall PCE.
2. To investigate the interface properties and optimized device performance by examining J-V, QE, Electric field, Nyquist plots, Generation and recombination profile, and energy band alignment, and to assess the effects of temperature and illumination intensity on device operation.
3. To explore the role of $SrTiO_3$ as a Cd-free electron transport layer in $Sb_2(S,Se)_3$ solar cells through SCAPS-1D numerical simulations, emphasizing its influence on charge transport and device efficiency.
4. To synthesize and characterize urea-derived graphitic carbon nitride (GCN) and study its structural, optical and electrical properties using various characterization techniques such as XRD, UV-Vis, FESEM-EDS and XPS.

5. To incorporate experimentally derived properties of GCN into device simulations and elucidate its effect on interfacial charge transport, accumulation capacitance, built-in potential, and charge transfer resistances for enhanced device performance of $Sb_2(S,Se)_3$.

4.3.Overview of the Objectives

Objectives 1 and 2: A comprehensive analysis pertaining to objectives 1 and 2, as detailed in **Sections 5.1 and 6.1**. Our investigation focused on evaluating the potential of triazatruxene-based HTLs as alternatives to the conventional Spiro-OMeTAD in $Sb_2(S,Se)_3$ solar cells. Initially, we successfully replicated the baseline device configuration of FTO/CdS/$Sb_2(S,Se)_3$/Spiro-OMeTAD/Au, which enabled us to reproduce the previously reported experimental results. Subsequently, we introduced a range of triazatruxene-based HTLs, specifically CI-B2, CI-B3, TAT-H, TAT-TY1, and TAT-TY2, which were selected due to their cost-effectiveness and thermal stability. These HTLs were chosen based on their high hole mobility, favorable energy level alignment, and superior molecular ordering, all of which contribute to enhanced charge extraction and reduced recombination losses. The optimization process entailed adjusting the thickness and doping concentrations of the HTL, ETL, and absorber layers, in addition to minimizing interface defect densities. This approach aimed to improve overall charge transport and device stability. We conducted detailed simulation analyses to examine the J-V characteristics, QE, Nyquist plots, electric field distribution, and generation-recombination profiles, along with the corresponding energy band alignments at the interfaces. The results indicated that optimized triazatruxene-based HTLs significantly enhanced device performance, achieving a PCE in the range of 21-23%. Among the HTLs investigated, TAT-TY1 and TAT-TY2 demonstrated superior band alignment and interfacial charge transfer, attaining the highest efficiencies of 23.24% and 23.11%, respectively. Additionally, we evaluated the influence of temperature (ranging from 280–400 K) and illumination intensity (ranging from 100 – 1000 W/m^2) on the optimized devices to assess their operational stability under realistic conditions. Overall, this study establishes triazatruxene-based HTLs as viable, low-cost, and stable alternatives to Spiro-OMeTAD, offering enhanced charge transport, reduced recombination, and improved device reliability in $Sb_2(S,Se)_3$ solar cells. The findings of this research have been published in **Advanced Theory and Simulations**, **Wiley, 2025** (https://doi.org/10.1002/adts.202500487).

Objective 3: A comprehensive investigation addressing Objective 3 is detailed in **Sections 5.2 and 6.2**. In this phase of the study, we conducted a numerical evaluation of the potential for a Cd-free $Sb_2(S,Se)_3$ solar cell utilizing strontium titanate (STO) as the ETL through the SCAPS-

1D simulation platform. The device was designed with the configuration FTO/STO/$Sb_2(S,Se)_3$/Spiro-OMeTAD/Au, with the intention of mitigating interface recombination losses typically observed in structures based on CdS and TiO_2. We initiated our work by constructing a baseline device, and to our surprise, the initial simulation yielded a PCE of 14.4%. Subsequently, we optimized the ETL parameters by varying the thickness of STO from 0.01 µm to 0.1 µm and the ND from 10^{12} cm^{-3} to 10^{20} cm^{-3}. This optimization aimed to achieve uniform interface coverage, reduce resistive losses, enhance carrier transport, and minimize recombination. Following these optimizations, the device efficiency increased to 21.91%, yielding a V_{OC} of 1.04 V, a J_{SC} of 27.52 mA/cm^2, and a FF of 76.29%. Moreover, we examined the energy band alignment and the generation-recombination behavior at the STO/$Sb_2(S,Se)_3$ interface after optimization to confirm the effectiveness of STO in promoting efficient electron extraction and in preventing hole backflow. To further evaluate the operational reliability of the proposed structure, we systematically investigated the effects of temperature and illumination intensity on device performance. These simulations aimed to capture the temperature-dependent variations in V_{OC}, J_{SC}, FF, and PCE, along with the illumination-induced behavior in carrier generation and quasi-Fermi level splitting. Overall, the optimized STO-based solar cell demonstrated superior performance and stability compared to CdS-based counterparts, establishing STO as a promising, non-toxic ETL capable of achieving high efficiency in $Sb_2(S,Se)_3$ solar cells. The findings from this objective have been accepted for publication in the **22nd International Conference on Electrical Engineering, Computing Science and Automatic Control (CCE), 2025.**

Objectives 4 and 5: A comprehensive analysis addressing Objectives 4 and 5 is provided in Sections 5.3 and 6.3. In this section, we conducted a combined experimental and numerical investigation to evaluate the role of g-C_3N_4 (GCN) as a functional interfacial layer in $Sb_2(S,Se)_3$ solar cells. Initially, GCN was synthesized using a modified thermal polymerization of urea, and its structural, morphological, and optical features were characterized employing techniques such as XRD, XPS, FESEM, EDS, and UV–Vis spectroscopy. The experimentally obtained parameters, including bandgap, electron affinity, and crystallinity, were integrated into SCAPS-1D simulations to accurately reflect realistic material behavior in the modeled devices. Starting from a validated experimental baseline configuration, the device was systematically optimized to assess the influence of interfacial and layer-level engineering on charge transport and PV response. The incorporation of the GCN interlayer between the $Sb_2(S,Se)_3$ absorber and the CdS ETL significantly enhanced charge extraction and suppressed interfacial

recombination, achieving an impressive PCE of approximately 18%. We performed full device optimization by systematically varying the thickness and doping concentrations of the ETL, absorber, GCN interlayer, and HTL to determine their combined effect on device performance. Following the establishment of the optimized configuration, a detailed analysis was conducted to investigate how interface defect density and defect energy levels impacted PV performance. The relationship between interface defects and key parameters such as PCE, carrier density, and recombination rate was thoroughly examined to understand their effects on charge dynamics and stability. Upon complete optimization, the device achieved a PCE of 27.42% and a QE exceeding 90% across the visible spectrum. Furthermore, we analyzed the variation in PCE concerning interfacial defect energy levels, the spatial distribution of electron and hole concentrations, generation–recombination profiles, and energy band alignment of the optimized device. This allowed us to elucidate how GCN modifies interfacial properties and carrier transport pathways. The combined synthesis–simulation approach establishes a robust framework that bridges experimental and theoretical perspectives, positioning GCN as a promising sustainable interfacial material for next-generation chalcogenide thin-film PVs. This work has been submitted for publication in the **Journal of Alloys and Compounds, Elsevier, 2025**.

5. Methodology

5.1. Simulation Procedure for $Sb_2(S,Se)_3$ Solar Cells using Triazatruxene Hole Transport Layers

In this study, the performance of $Sb_2(S,Se)_3$ solar cells was analyzed using SCAPS-1D, incorporating five triazatruxene-based HTLs such as CI-B2, CI-B3, TAT-H, TAT-TY1, and TAT-TY2 along with the conventional Spiro-OMeTAD. The device structure consists of FTO/CdS/$Sb_2(S,Se)_3$/HTL/Au, a commonly adopted configuration in high-performance $Sb_2(S,Se)_3$-based solar cells. **Fig. 5(a)** illustrates the proposed structure and the alternative HTLs. The simulation parameters used in this study are taken from experimental and theoretical reports and from the calculations as detailed in **Tables 1, 2, and 3**. Parameters such as bandgap (E_g), affinity (χ), dielectric permittivity (ε_r), electron and hole mobilities (μ_n, μ_p) were directly taken from the experimental reports. The defect densities (N_t) were obtained from SCAPS 1D based on the lifetime values experimentally reported in the literature for those materials. Whereas effective density of states in the conduction (N_c) and valence bands (N_v), donor and acceptor densities (N_D, N_A) were obtained using calculations where the values required for the

calculations were directly taken from the experimental reports. The formulae utilized for the calculation are as follows [64],

$$N_c = 2\left[\frac{2\pi m_e k_B T}{h^2}\right]^{3/2} \text{ and } N_v = 2\left[\frac{2\pi m_h k_B T}{h^2}\right]^{3/2} \quad (9)$$

$$m_e = \frac{e\tau}{\mu_e} \text{ and } m_h = \frac{e\tau}{\mu_h} \quad (10)$$

$$p = \frac{\sigma}{q\mu_h} \text{ (for p-type material)} \quad (11)$$

$$n = \frac{\sigma}{q\mu_e} \text{ (for n-type material)} \quad (12)$$

Where m_e and μ_e are the effective mass and mobility of electrons, m_h and μ_h are the effective mass and mobility of holes, T is temperature, h is planks constant, K_B is Boltzmann constant, e is the elementary charge, τ is the relaxation time, and are the electron and hole mobilities, σ is the conductivity, q is electric charge, p is the acceptor (N_A) density and n is the donor (N_D) density.

Table 1. Input parameters of all layers required for base device simulation.

Parameters	**FTO**	**CdS**	**$Sb_2(S,Se)_3$**	**Triazatruxenes**					
				Spiro	**CI-B2**	**CI-B3**	**TAT-H**	**TAT-TY1**	**TAT-TY-2**
Thickness (µm)	0.350	0.060	0.207	0.100	0.100	0.100	0.100	0.100	0.100
E_G (eV)	3.6	2.44	1.43	3.1	2.06	1.98	3.4	3.14	3.26
χ (eV)	4.5	4.1	3.81	2.1	3.22	3.33	1.45	2.03	1.84
ε_r	8.9	10	15.00	3	3.2	3.6	2.8	2.7	2.1
N_C (cm^{-3})	2.2E+18	2.2E+18	2.2E+18	2.2E+18	1.66E+19 [C]	8.85E+17 [C]	4.59E+20 [C]	4.53E+15 [C]	2.88E+16
N_V (cm^{-3})	1.8E+19	1.8E+19	1.8E+19	1.8E+19	4.70E+19 [C]	2.50E+17 [C]	1.30E+21 [C]	1.28E+16 [C]	8.15E+16
μ_n (cm^2/Vs)	100	100	9.8	2E-4	8.00E-05	1.3E-4	4E-6	2.9E-3	1E-3
μ_h (cm^2/Vs)	25	25	10	2E-4	1.60E-04 [C]	2.60E-04 [C]	8.00E-06 [C]	5.80E-03[C]	2.00E-03[C]
N_A (cm^{-3})	0	0	1.66E+16	4E+18	4.16E+16 [C]	4.62E+17 [C]	5.31E+18 [C]	3.02E+16[C]	9.38E+16[C]
N_D (cm^{-3})	1E+20	1.1E+18	0	0	0	0	0	0	0
N_t (cm^{-3})	1E+16	1.00E+14		1E+15	3.2E+15 [C]	3E+15 [C]	7.00E+15 [C]	4.33E+16	5.01E+16
References	[47][42]	[47][42]	[47][42]	[47][42]	[121]	[121]	[108]	[108]	[108]
[C] indicate that the parameters are calculated using experimentally reported values from [108,121].									

Table 2. Details of defect types and defect densities of $Sb_2(S,Se)_3$ absorber

Parameters	**Defect 1** [42]	**Defect 2** [42]
Electron capture cross section σ_n (cm^2)	1.99E-17	5.91E-17
Hole capture cross section σ_p (cm^2)	1.99E-17	5.91E-17
Reference for defect energy level E_t	Above the highest Ev	Above the highest Ev
Energy with respect to reference (eV)	0.5	0.671
Defect density N_t (cm^{-3})	6.28E+12	1.88E+13

Table 3. Table 3. Details of defect types and defect densities at the ETL/ $Sb_2(S,Se)_3$ and HTL/ $Sb_2(S,Se)_3$ interfaces.

Parameters	**CdS/$Sb_2(S,Se)_3$ interface**	**$Sb_2(S,Se)_3$/spiro OMeTAD interface**	**$Sb_2(S,Se)_3$/Triazatruxenes interface**
Defect type	Neutral	Neutral	Neutral
Electron capture cross section σ_n (cm^2)	1E-15	1E-19	1E-19
Hole capture cross section σ_p (cm^2)	1E-15	1E-19	1E-19
Reference for defect energy level E_t	Above the highest Ev	Above the highest Ev	Above the highest Ev
Energy with respect to reference (eV)	0.6	0.6	0.6
Defect density N_t (cm^{-2})	2.5E+14	1.4E+14	1E+12

Initially, we have replicated the experimental base device through SCAPS-1D simulation with the configuration of an experimentally reported high PCE device utilizing the parameters mentioned in **Tables 1, 2, and 3**. We performed the simulations at 300 K under the AM 1.5G solar spectrum irradiance. The work function of gold (Au) was set to -5.1 eV. Surface recombination velocities for both electrons and holes of each layer were configured as 1×10^7 cm/s, as outlined in **Table 1**. Further, neutral defects were introduced at the Absorber/HTL and ETL/Absorber interfaces to ensure realistic operating conditions for simulation, as detailed in **Table 3**. The series resistance (R_S) of 3.7 $\Omega\cdot cm^2$ and shunt resistance (R_{SH}) of 752.1 $\Omega\cdot cm^2$ for the device, along with the absorption coefficient of 2.28×10^5 cm^{-1} for the absorber layer, were chosen to align with experimental data [42]. The JV curve of the experimental and simulated base device shown in **Fig. 5(b)**. The PV parameters presented in the inset table validate the reliability of the simulation method, with negligible deviations of 0.02 V for V_{OC}, 0.17 mA/cm^2 for J_{SC}, 1.82% for FF, and no variation in PCE. After reproducing these values, various triazatruxene-based HTLs were explored as replacements for Spiro-OMeTAD. Details of the HTL input and interface parameters are provided in **Tables 1 and 3**.

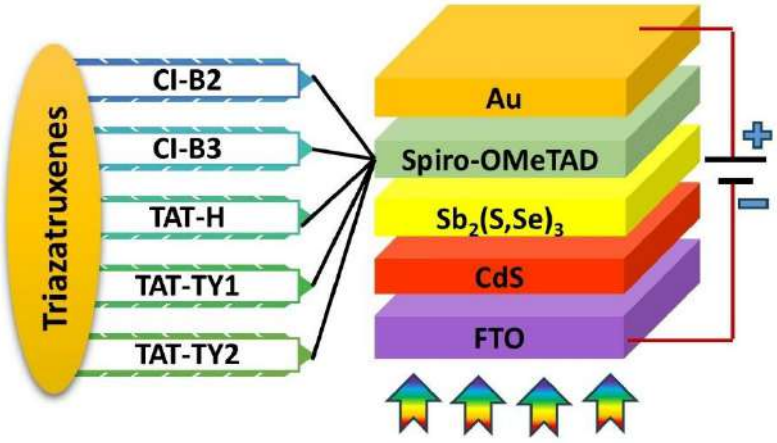

Fig. 5. (a) Base device configuration and the proposed triazatruxene HTLs

The study then investigated the effects of varying the thickness from 0.05 to 0.2 μm for HTL, from 0.05 to 0.15μm for ETL, and from 0.1 to 1.0 μm for the absorber, respectively. And the N_A of HTL and absorber and N_D of ETL was varied from 10^{12} to 10^{20} cm^{-3}. Additionally, changes with respect to the defects at the ETL/absorber and absorber/HTL interfaces in the range of 10^{10} to 10^{18} cm^{-2} were examined. The results were confirmed through various analytical outcomes of SCAPS 1D simulation, such as electric field distribution, recombination analysis, energy band structure assessments, J-V, C-F, and QE measurements. The study also explores the effects of operating temperature and light intensity on device performance, offering guidance for designing more stable and efficient solar cells under practical conditions.

5.2. Simulation Strategies for Cd-free Strontium Titanate Electron Transport Layer in $Sb_2(S,Se)_3$ Solar Cell

In this research, we utilized the SCAPS-1D simulation software to investigate the performance of a heterojunction solar cell configured as FTO/STO/$Sb_2(S,Se)_3$/Spiro-OMeTAD/Au as shown in **Fig.6**. A key aspect of this study was the introduction of STO as a novel ETL**.** To assess its impact on device behavior, simulations were performed by systematically varying both the thickness and donor density of STO. All simulations were conducted at 300 K and under the AM1.5G solar spectrum**,** with a standard irradiance of 100 mW/cm^2**.** The back contact (Au) was modelled with a work function of −5.1 eV. A surface recombination velocity of 1×10^7 cm/s was applied at the interfaces, and neutral interface defects were introduced at the ETL/absorber and absorber/HTL junctions to replicate realistic interfacial effects. Specific parameters for each layer and their interfaces are provided in **Table 4, 5 and 6**.

Table 4. Base device layer parameters for device with STO ETL.

Parameters	**FTO**	**$SrTiO_3$**	**$Sb_2(S,Se)_3$**	**Spiro-OMeTAD**
Thickness (µm)	0.350	0.100	0.207	0.100
E_G (eV)	3.6	3.2	1.43	3.1
χ (eV)	4.5	4.0	3.81	2.1
ε_r	8.9	8.7	15.00	3
N_C (cm^{-3})	2.2E+18	1.7E+19	2.2E+18	2.2E+18
N_V (cm^{-3})	1.8E+19	2E+20	1.8E+19	1.8E+19
μ_n (cm^2/Vs)	100	5E+3	9.8	2E-4
μ_h (cm^2/Vs)	25	6.6E+2	10	2E-4
N_A (cm^{-3})	0	0	1.66E+16	4E+18
N_D (cm^{-3})	1E+20	2E+16	0	0
N_t (cm^{-3})	1E+16	1E+15		1E+15
References	[44]	[138]	[44]	[44]

Table 5. Absorber defect parameters for device with STO ETL [44]

Parameters	**Defect 1**	**Defect 2**
Electron capture cross section σ_n (cm^2)	1.99E-17	5.91E-17
Hole capture cross section σ_p (cm^2)	1.99E-17	5.91E-17
Reference for defect energy level E_t	Above the highest Ev	Above the highest Ev
Energy with respect to reference (eV)	0.5	0.671
Defect density N_t (cm^{-3})	6.28E+12	1.88E+13

Table 6. Interface defect parameters for device with STO ETL. [44,138]

Parameters	**STO/ $Sb_2(S,Se)_3$**	**$Sb_2(S,Se)_3$ /spiro OMeTAD**
Defect type	Neutral	Neutral
Electron capture cross section σ_n (cm^2)	1E-15	1E-19
Hole capture cross section σ_p (cm^2)	1E-15	1E-19
Reference for defect energy level E_t	Above the highest Ev	Above the highest Ev
Energy with respect to reference (eV)	0.6	0.6
Defect density N_t (cm^{-2})	1E+14	1.4E+14

The simulation also incorporated a series resistance (R_s) of 3.7 Ω.cm^2 and a shunt resistance (R_{sh}) of 752.1 Ω.cm^2, reflecting practical device characteristics. The absorption coefficient of the $Sb_2(S,Se)_3$ absorber was set to 2.28×10^5 cm^{-1}, based on previously reported experimental data [139].

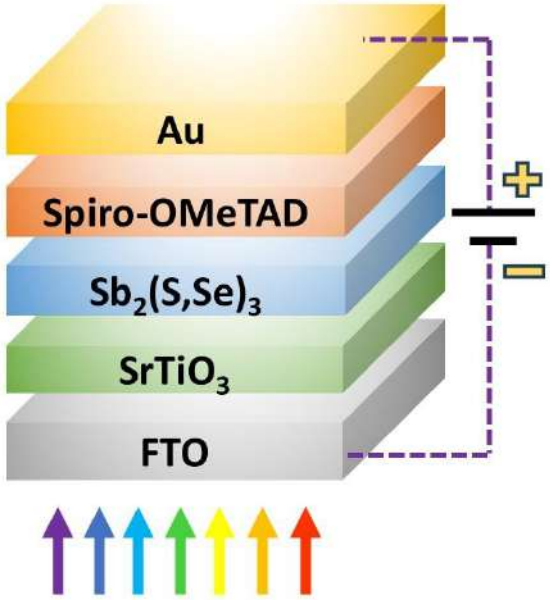

Fig. 6. Base device structure with STO as ETL.

5.3. Experimental and Simulation Procedure for Graphitic Carbon Nitride Interfacial Layer in $Sb_2(S, Se)_3$ Solar Cells

5.3.1. Experimental Procedure

GCN was prepared through a modified thermal polymerization approach based on an earlier protocol [140]. In this process, 10 g of urea (ACS reagent grade, ≤0.001% (Heavy Metals by ICP-OES, metals basis), 99.0-100.5%, solid) was placed into a lidded ceramic crucible and subjected to heat treatment under atmospheric conditions. The crucible was then introduced into a programmable muffle furnace (Isotemp 650-750 Series, Fisher Scientific), where the temperature was ramped up to 550°C and maintained for 3 hours to promote complete thermal decomposition and polymerization of the precursor. After the heating cycle, the furnace was allowed to cool naturally to room temperature. The obtained yellow powder was subsequently washed with 0.1 mol L^{-1} nitric acid (Bakers ACS reagent, 66.5%), followed by repeated rinsing with distilled water to remove any remaining alkaline residues such as surface-bound ammonia. The product was then dried at 80 °C for 12 hours and finally ground into a fine powder using a mortar and pestle for use in further characterization studies.

5.3.2. Characterization Techniques

The investigation of the crystal structure and orientation of the samples was employed by XRD with Cu-Kα radiation (λ = 1.5406 Å) using Smart Lab, RIGAKU instrument. The XRD scans were conducted with a step size of 0.04° at 20 mA and 45 kV. The optical properties of the samples were determined using a Shimadzu UV2450 UV-Vis spectrophotometer at room temperature. FESEM images were subsequently recorded using a JSM-7401F (JEOL) instrument at an operating voltage of 5 kV. The chemical composition analysis was then carried out through EDS at 6 kV using an XFlash 5010 detector (BRUKER) coupled with FESEM. The surface chemistry was further analyzed by XPS using a Thermo Scientific K-Alpha spectrometer supplied with a monochromatic Al Kα X-ray source (1486.6 eV). Survey spectra were recorded over a range of -10 to 1350 eV with a pass energy and step size of 200 eV and 1 eV, respectively. High-resolution spectra and valence band position were then recorded with a pass energy and step size of 50 eV and 0.1 eV, respectively.

5.3.3. Simulation Details and Experimental Base Device Validation

In this study, the solar cell device structure considered is FTO/Spiro-OMeTAD/$Sb_2(S, Se)_3$/GCN/CdS/Au, where GCN is introduced as a novel interfacial layer between the $Sb_2(S, Se)_3$ absorber and the CdS ETL layer. The electrical and optical parameters for all layers including bandgap (E_g), electron affinity (χ), dielectric permittivity (ε_r), electron and hole mobilities (μ_n, μ_p), effective density of states in the conduction (N_c) and valence bands (N_v), defect densities (N_t), donor and acceptor densities (N_D, N_A) are listed in **Table 7, 8**. Parameters for each layer in the baseline device were adopted from previous experimental reports, while those for the GCN, the key parameters such as E_g, χ, ε_r were extracted from our experimental data (from UV-Vis absorbance, transmittance, XPS) and other dependent parameters from standard literature. To realistically model the interfaces and their impact on device performance, interface defect layers were introduced at the HTL/absorber, absorber/GCN, GCN/ETL, and absorber/ETL junctions for both the baseline device and the GCN-modified device, as detailed in **Table 9**. The simulations were performed under standard operating conditions of AM1.5G illumination (1000 W/m^2) at a temperature of 300 K. The series resistance (R_S) and shunt resistance (R_{SH}) were fixed at 3.7 Ω.cm^2 and 752.1 Ω.cm^2, respectively. The back contact (Au) work function was set to -5.1 eV [42]. The energy distribution of these interface defects was assumed to be Gaussian, and the parameters were adjusted to represent mid-gap recombination centers.

Table 7. Input parameters of all layers required for base device simulation

Parameters	**FTO**	**CdS**	**GCN**	**$Sb_2(S,Se)_3$**	**Spiro-OMeTAD**
Thickness (µm)	0.350	0.060	0.050	0.207	0.100
E_G (eV)	3.6	2.44	2.8 [Exp]	1.43	3.1
χ (eV)	4.5	4.1	3.6 [Exp]	3.81	2.1
ε_r	8.9	10	7 [Exp]	15.00	3
N_C (cm^{-3})	2.2E+18	2.2E+18	2.2E+18	2.2E+18	2.2E+18
N_V (cm^{-3})	1.8E+19	1.8E+19	1.8E+19	1.8E+19	1.8E+19
μ_n (cm^2/Vs)	100	100	100	9.8	2E-4
μ_h (cm^2/Vs)	25	25	100	10	2E-4
N_A (cm^{-3})	0	0	0	1.66E+16	4E+18
N_D (cm^{-3})	1E+20	1.1E+18	1E+18	0	0
N_t (cm^{-3})	1E+16	1.00E+14	2.5E+14		1E+15
References	[47][42]	[47][42]	[141–143]	[47][42]	[47][42]
[Exp] indicates that the parameters are extracted from our experimental results.					

Table 8. Details of defect types and defect densities of $Sb_2(S, Se)_3$ absorber

Parameters	**Defect 1** [42]	**Defect 2** [42]
Electron capture cross section σ_n (cm^2)	1.99E-17	5.91E-17
Hole capture cross section σ_p (cm^2)	1.99E-17	5.91E-17
Reference for defect energy level E_t	Above the highest Ev	Above the highest Ev
Energy with respect to reference (eV)	0.5	0.671
Defect density N_t (cm^{-3})	6.28E+12	1.88E+13

Table 9. Details of defect types and defect densities at the interfaces

Parameters	**$Sb_2(S,Se)_3$/ spiro OMeTAD**	**$Sb_2(S,Se)_3$/ CdS**	**GCN/ $Sb_2(S,Se)_3$**	**GCN/CdS**
Defect type	Neutral	Neutral	Neutral	Neutral
Electron capture cross section σ_n (cm^2)	1E-19	1E-15	1E-15	1E-19
Hole capture cross section σ_p (cm^2)	1E-19	1E-15	1E-15	1E-19

Reference for defect energy level E_t	Above the highest Ev	Above the highest Ev	Above the highest Ev	Above the highest Ev
Energy with respect to reference (eV)	0.6	0.6	0.6	0.6
Defect density N_t (cm^{-2})	1.4E+14	2.5E+14	1E+14	2.5E+14

The baseline FTO/CdS/$Sb_2(S, Se)_3$/Spiro-OMeTAD/Au solar cell was initially simulated to reproduce the experimentally reported device behavior. Then GCN interfacial layer was incorporated between CdS and $Sb_2(S,Se)_3$ (schematically shown in **Fig. 7**, whose J–V, QE, electric field distribution Nyquist Plot, Generation and recombination rate and energy band diagram are extracted for baseline devices without and with GCN and analysed in detail.

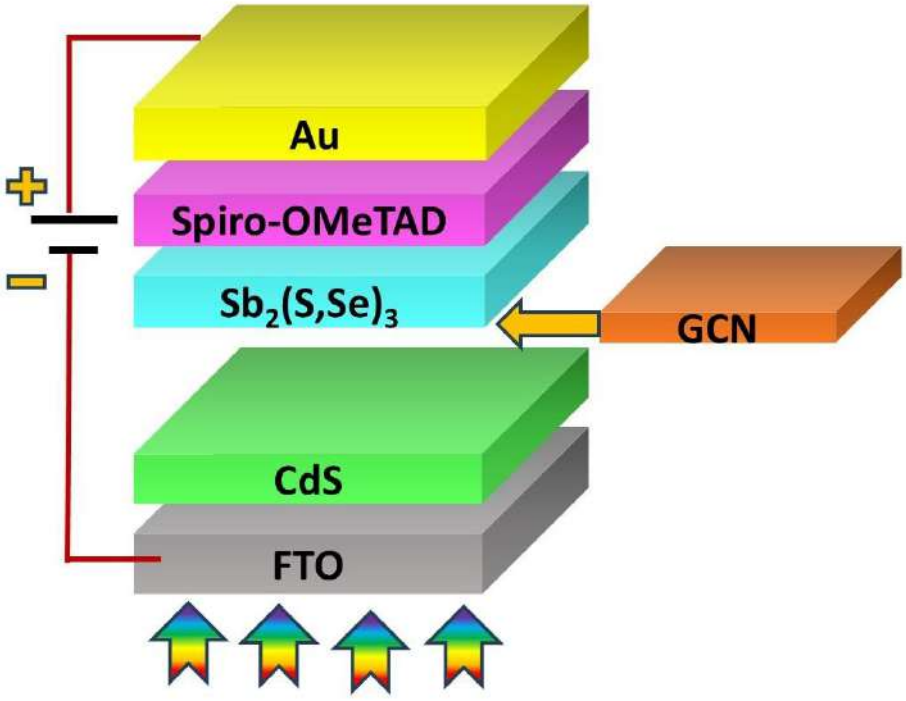

Fig. 7. Base device structure and GCN introduction.

Following baseline and GCN incorporation validation, a comprehensive optimization of thickness and carrier densities of each layer was carried out to maximize device performance. For instance, he effects of varying the thickness from 0.05 to 0.15 µm for the HTL, from 0.1 to 1 µm for the $Sb_2(S, Se)_3$ absorber, from 0.01 to 0.1 µm for the GCN interfacial layer, and from 0.05 to 0.1 µm for the ETL, respectively. The acceptor density (N_A) of the HTL (10^{12} to 10^{20} cm^{-3}) and the $Sb_2(S, Se)_3$ absorber (10^{12} to 10^{18} cm^{-3}), and the donor density (N_D) of the GCN (10^{12} to 10^{20} cm^{-3}) and the ETL (10^{12} to 10^{20} cm^{-3}) were varied. Additionally, the effect of interface defect densities at the HTL/$Sb_2(S, Se)_3$, ETL/$Sb_2(S, Se)_3$, $Sb_2(S, Se)_3$/GCN, and

GCN/ETL interfaces was examined in the range of 10^{12} to 10^{20} cm^{-2}. The variation in PV parameters on optimization of devices with and without GCN incorporation is compared and analyzed through various SCAPS-1D analytical outputs, including generation–recombination analysis, electric field distribution, energy band structure assessment, J–V curves, QE responses, C–V, Mott-Schottky, and C–F measurements. The study also explored the effects of operating temperature and light intensity on device performance, providing insights for designing more efficient and stable $Sb_2(S, Se)_3$-based solar cells with GCN interfacial engineering. These analyses helped in understanding the role of GCN in suppressing interface recombination and improving carrier extraction efficiency.

6. Results and Discussion

6.1. Modelling Insights of $Sb_2(S,Se)_3$ Solar Cells using Triazatruxene Hole Transport Layers

6.1.1. Initial Device Performance

The JV curve of the experimental and simulated base device shown in **Fig. 8**. The PV parameters presented in the inset table validate the reliability of the simulation method, with negligible deviations of 0.02 V for V_{OC}, 0.17 mA/cm^2 for J_{SC}, 1.82% for FF, and no variation in PCE. After reproducing these values, various triazatruxene-based HTLs were explored as replacements for Spiro-OMeTAD. Details the PV parameters of base devices employing Spiro-OMeTAD and the alternative HTLs is presented in **Table 10**.

Table 10. Device performance for the initial devices.

Device structure	V_{OC} (V)	J_{SC} (mA/cm^2)	FF (%)	PCE (%)
FTO/CdS/$Sb_2(S,Se)_3$/Spiro-OMeTAD/Au	0.65	25.10	65.53	10.75
FTO/CdS/$Sb_2(S,Se)_3$/CI-B2/Au	0.64	24.53	39.42	6.24
FTO/CdS/$Sb_2(S,Se)_3$/CI-B3/Au	0.63	24.45	33.19	5.12
FTO/CdS/$Sb_2(S,Se)_3$/TAT-H/Au	0.67	24.35	52.51	8.58
FTO/CdS/$Sb_2(S,Se)_3$/TAT-TY1/Au	0.65	24.81	59.14	9.57
FTO/CdS/$Sb_2(S,Se)_3$/TAT-TY2/Au	0.65	24.94	64.95	10.60

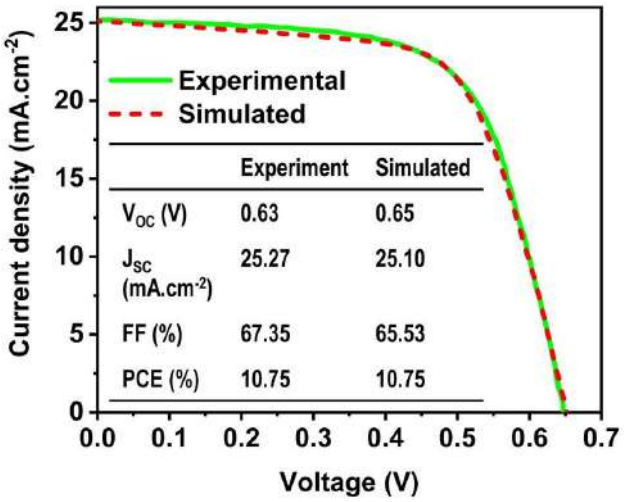

Fig. 8. Comparison of experimental and simulated JV curve.

6.1.2. Optimization of HTL, ETL and Absorber Properties

6.1.2.1. Effect of HTL Thickness and N_A

The impact of HTL thickness is pivotal in controlling the hole transport from the absorber to the back contact, while also minimizing the direct interaction between the absorber and the back contact.[144] Therefore, optimizing HTL thickness is essential for enhancing solar cell efficiency. To explore this, we varied the thickness of Spiro-OMeTAD, CI-B2, CI-B3, TAT-H, TAT-TY1, and TAT-TY2 HTLs between 0.05 and 0.2 μm. The resulting variations in V_{OC}, J_{SC}, FF, and PCE are outlined in **Fig. 9(a-d)**. As the HTL thickness increases, there are no substantial variations in V_{OC}, J_{SC}, FF, and PCE for Spiro-OMeTAD, CI-B3, TAT-H, TAT-TY1and TAT-TY2 HTLs-based solar cells, indicating HTL thickness has minimal effect in the performance of these solar cells. However, a slight decrement is observed in all PV parameters for CI-B2-based solar cells as thickness increased from 0.05 to 0.2 μm. This is because an increase in HTL thickness leads to a rise in series resistance, which refers to the opposition encountered by charge carriers as they move through the HTL.[57,145,146] A thicker HTL extends the transport path for holes, increasing resistive losses and enhancing scattering events, where carriers undergo more collisions with atoms or other carriers, thus reducing their mobility.[147,148] This reduced mobility and increased resistance hinder efficient hole extraction, leading to voltage drops across the device and subsequently lowering V_{OC} and FF. Additionally, the longer transport path in a thicker HTL raises the probability of charge carrier recombination before reaching the electrode, further diminishing the J_{SC} and device efficiency.[146,149–151] Therefore, the combined effects of higher series resistance, enhanced scattering, and increased recombination with thicker HTLs directly contribute to the observed decline in overall solar cell performance. Hence, a thickness of 0.08 μm for TAT-TY1 and 0.06

μm for the remaining HTLs was selected considering maximum PCE and material cost. This is consistent with experimentally reported HTL thickness of $Sb_2(S,Se)_3$-based solar cell.[152] To validate this behavior, we have compared the Nyquist plot extracted for devices with initial and optimized HTL thickness.

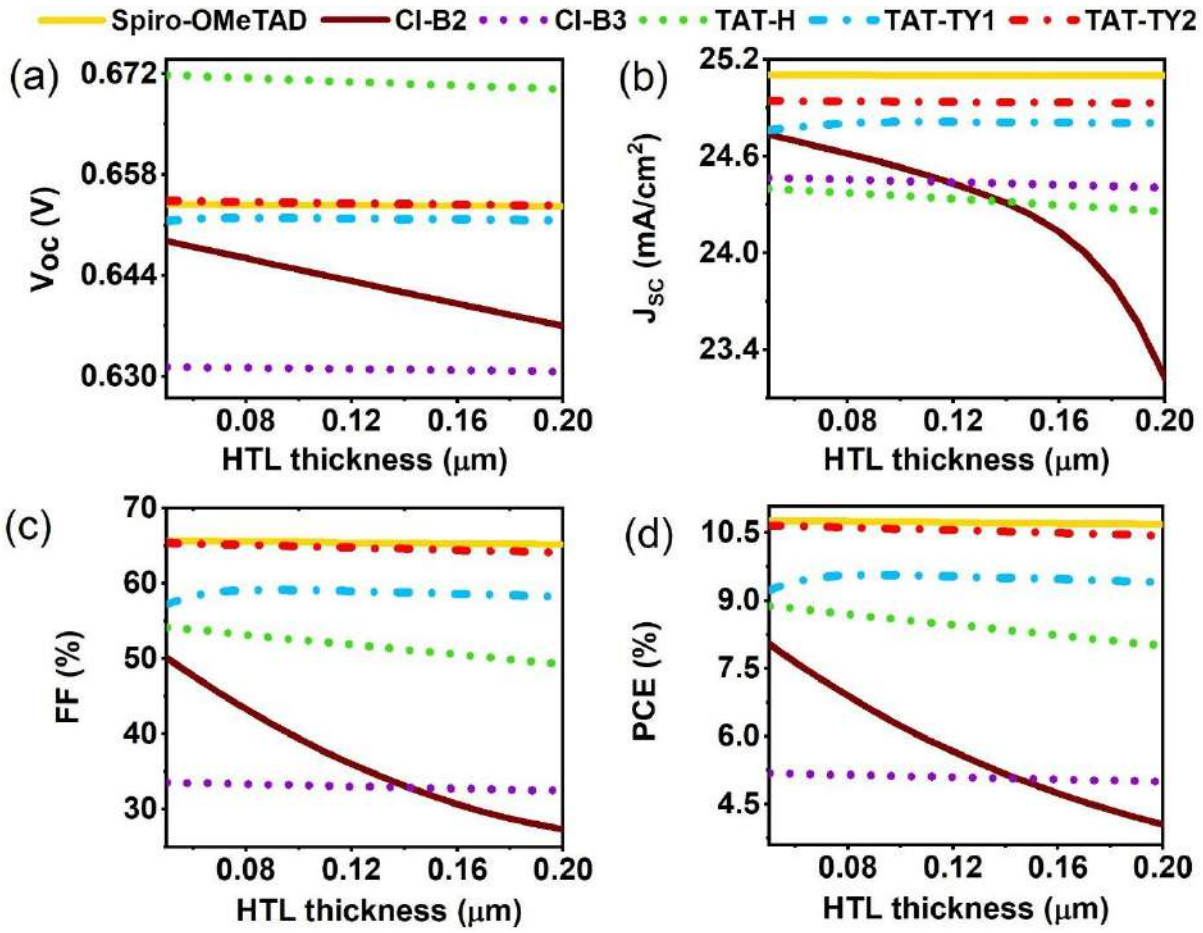

Fig. 9. Impact of HTL thickness on a) V_{OC}, b) J_{SC}, c) FF, d) PCE.

Fig. 10 (a-f) shows the Nyquist plots generated from C–f measurements extracted from SCAPS 1D. These plots exhibit a semicircular pattern across all cases whose diameter increased for the optimized HTL thickness compared to the final thickness, indicating that the optimized thickness possesses higher resistance to charge carrier recombination. This facilitates more effective charge separation and transport through HTL, allowing carriers to reach the contact before recombining.[153] Consequently, this observation supports the changes discussed previously. These findings highlight the significant impact of HTL thickness on the efficient operation of solar cells.

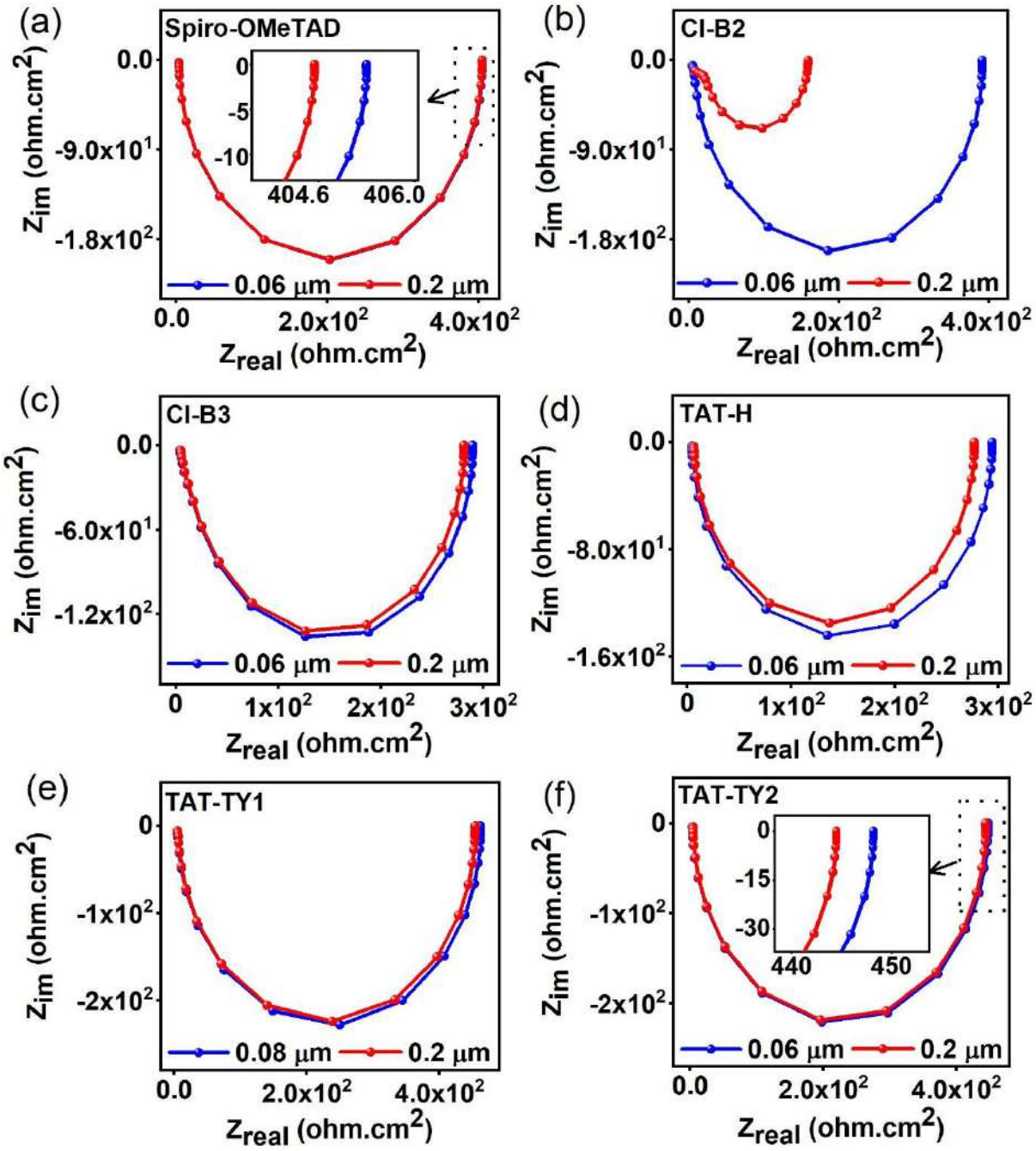

Fig. 10. (a-f) Nyquist plot for the effect of HTL thickness for all solar cells.

We varied the N_A of all HTLs from 10^{12} to 10^{20} cm^{-3}. The changes in the PV parameters concerning the variation in N_A are shown in **Fig. 11(a-d)**. When the N_A is increased from 10^{12} to 10^{15} cm^{-3}, no significant changes are observed in V_{OC}, J_{SC}, FF, and PCE for all HTLs. The enhancement in all PV parameters becomes evident as the N_A surpasses 10^{15} cm^{-3}, leading to a notable improvement in PCE. This behavior is closely linked to the N_A balance between the absorber and HTL. When the HTL has a lower N_A than the absorber, energy band alignment remains stable, and solar cell performance remains unaltered till 10^{15} cm^{-3}. Moreover, barriers

at the HTL/Absorber interface and the back contact lead to the formation of recombination centers, hindering efficient charge transport and negatively affecting the device performance. As the N_A of the HTL surpasses that of the absorber, significant energy band realignment occurs, which reduces the interfacial barriers and promotes more efficient charge carrier separation. This improvement enhances the transport efficiency thereby minimizing recombination losses at the HTL/Absorber interface.[154,155] This trend is further evidenced by the QE measurements depicted in **Fig. 12(a-f)**, where an evident increase in QE is observed with optimized N_A. For the lower N_A of 10^{12} cm^{-3}, the QE was lower with 27.50%, 11.07%, 0.07%, 0.48%, 20.40%, 67.15% for Spiro-OMeTAD, CI-B2, CI-B3, TAT-H, TAT-TY1, and TAT-TY2-based solar cells respectively. The drastic rise in QE >70% was attained for all the solar cells at the optimal N_A, attributed to enhanced absorption and charge collection at the respective contacts, enabled by favorable energy level alignment and the formation of suitable barriers for efficient hole transfer.[156] These adjustments ensure more effective charge extraction and contribute to the improved performance of the solar cell.

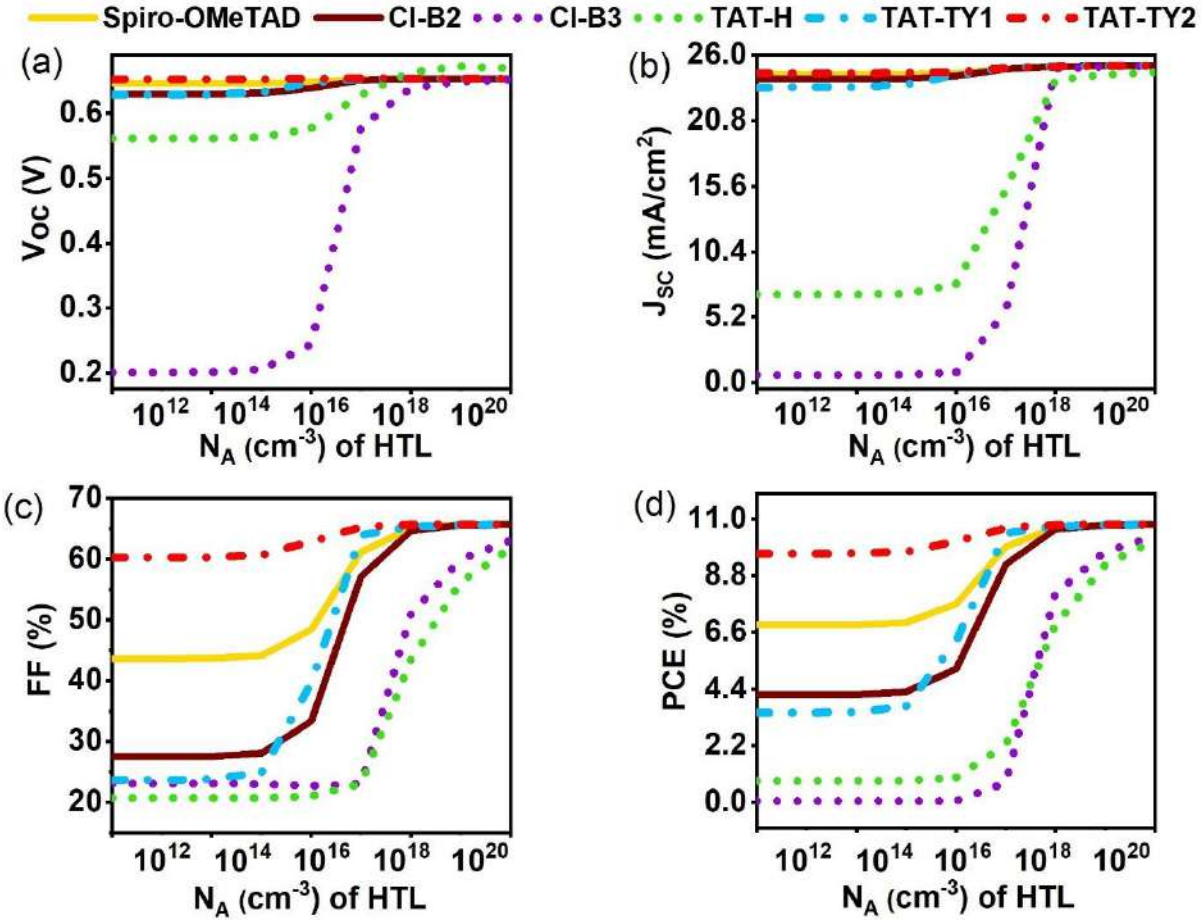

Fig. 11. Impact of N_A of HTLs on a) V_{OC}, b) J_{SC}, c) FF, d) PCE.

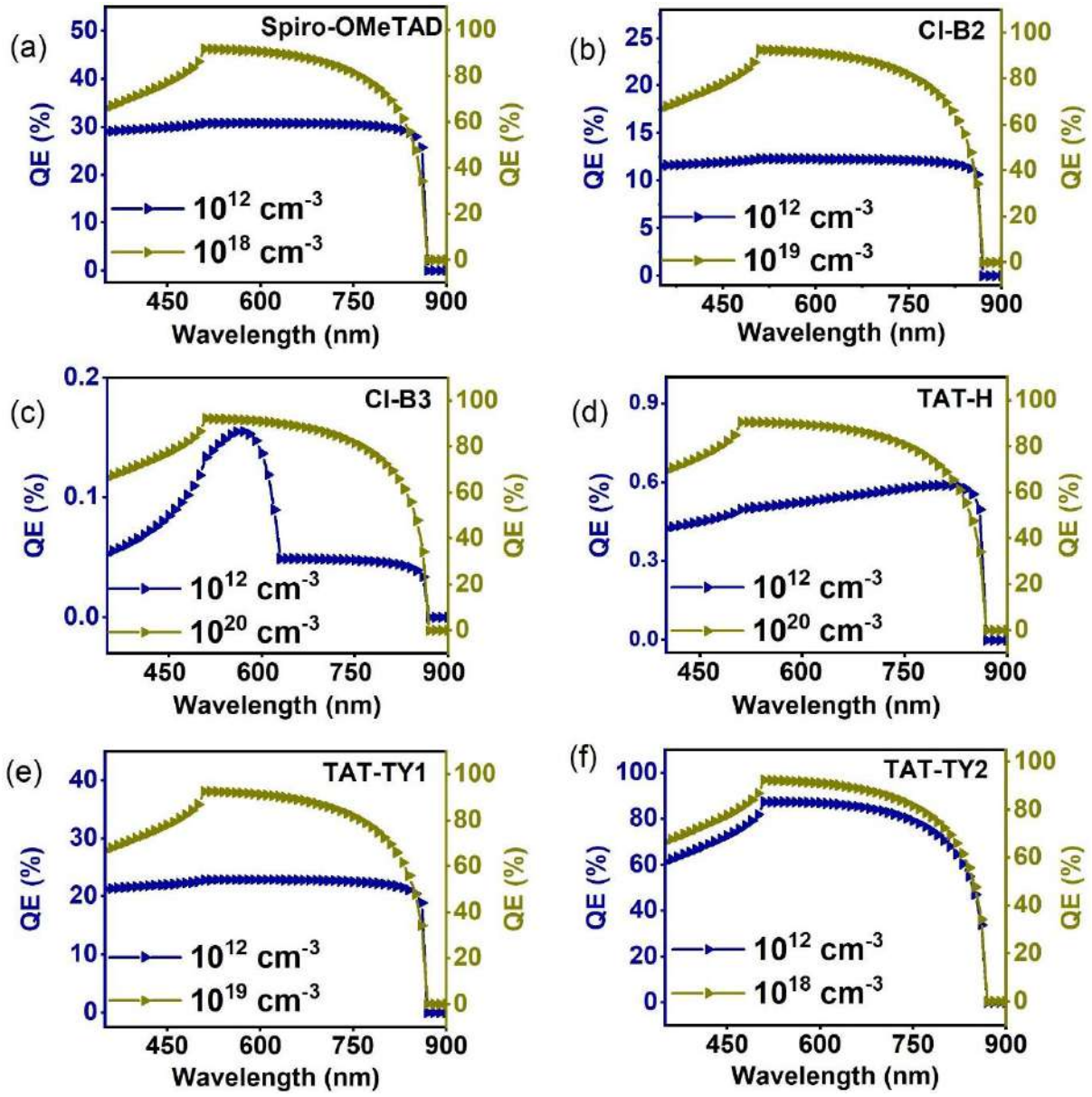

Fig. 12. (a-f) QE plots for the effect of HTL N_A for all solar cells.

6.1.2.2. Effect of ETL Thickness and N_D

The ETL has a significant impact on improving the transmission of light and reducing the recombination of charge carriers within solar cells. As such, optimizing the characteristics of the charge transport layer is critical in achieving better performance.[157] In this investigation, the thickness of CdS was varied between 0.05 μm and 0.15 μm. The relationship between the ETL thickness and PV parameters is demonstrated in **Fig. 13(a-d)**. With increasing ETL thickness from 0.05 to 0.15 μm, a decrease in V_{OC}, J_{SC}, and PCE was observed. This is due to the elevated charge carrier recombination as the ETL becomes thicker. A thicker ETL extends the transport path for electrons, raising the possibility of electrons recombining with holes before being collected at FTO. Additionally, a thicker ETL reduces optical transparency,

limiting photon penetration into the absorber layer, thereby decreasing charge carrier generation.[158] In contrast, the FF demonstrated a slight improvement with increasing ETL thickness. This improvement can be ascribed to lower R_S, which enhances charge transport efficiency.[159] However, the improvement in FF was not sufficient to compensate for the reduction in V_{OC} , J_{SC}, and PCE caused by heightened charge carrier recombination and optical losses.

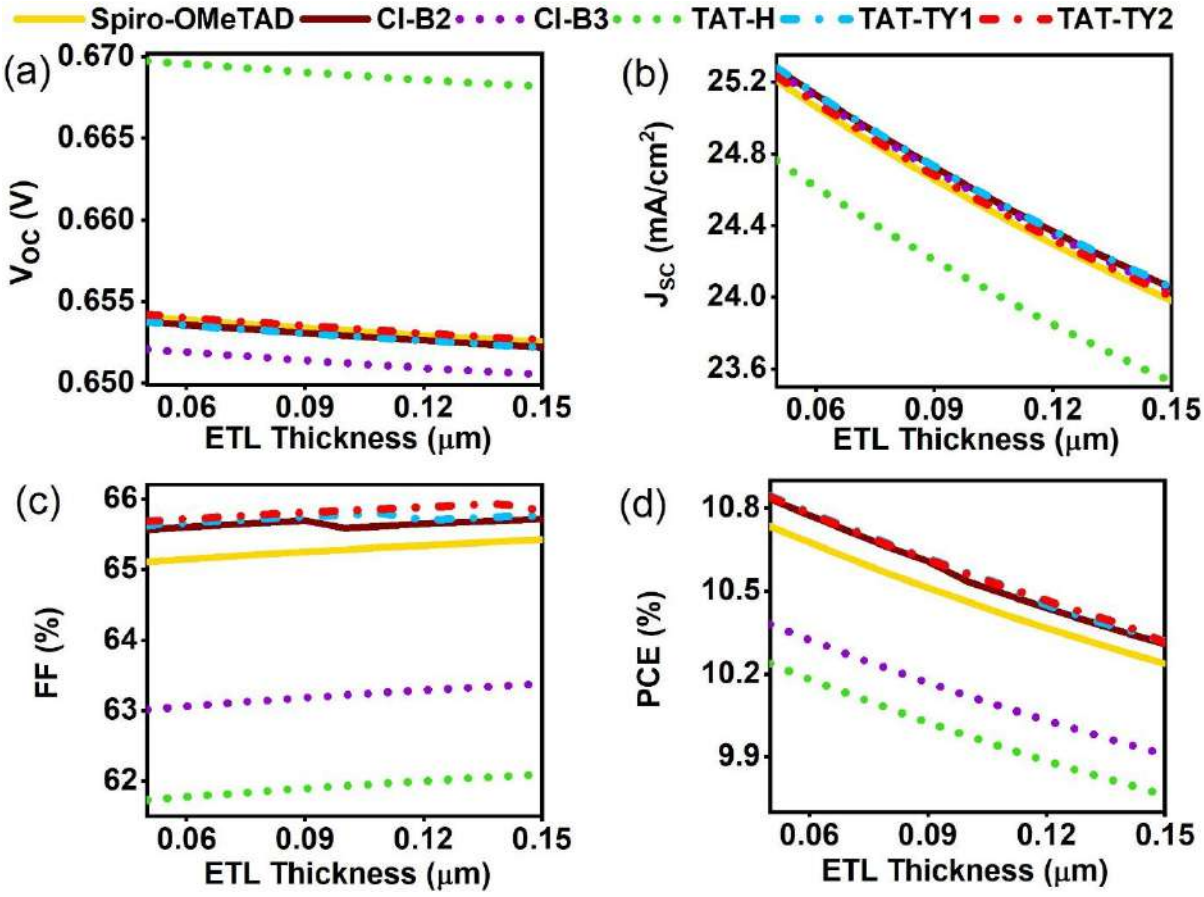

Fig. 13. Impact of ETL thickness on a) V_{OC}, b) J_{SC}, c) FF, d) PCE.

These changes are validated through **(Fig. 14(a-f)** that highlights the comparison of charge carrier recombination rates for the optimized (0.05 μm) and maximum (0.15μm) ETL thicknesses. A higher recombination rate, nearly $6x10^{18}$ to $1x10^{19}$ $cm^{-3}s^{-1}$, is observed for higher thickness, while it was substantially minimized by a factor of ~ $3x10^{18}$ $cm^{-3}s^{-1}$ at the optimized thickness for all solar cells. In practice, selecting the appropriate ETL thickness during fabrication is essential for ensuring adequate substrate coverage, effective charge separation, and the reduction of recombination at the ETL/absorber interface. Experimental findings reveal that increasing the ETL thickness beyond 0.1 μm leads to higher recombination rates, primarily due to the longer electron transport path and parasitic absorption within the ETL.[160,161]

Conversely, an excessively thin ETL (<0.05 μm) compromises substrate coverage, poor junction formation, and leakage currents, all of which further elevate charge carrier recombination.[162–164] These experimental results emphasize the critical role of optimizing the ETL thickness to maximize efficiency and minimize recombination. Consistent with these experimental findings, our observations confirm that an ETL thickness of 0.05 μm strikes the ideal balance between minimizing recombination, maintaining sufficient optical transparency, and ensuring effective charge transport.

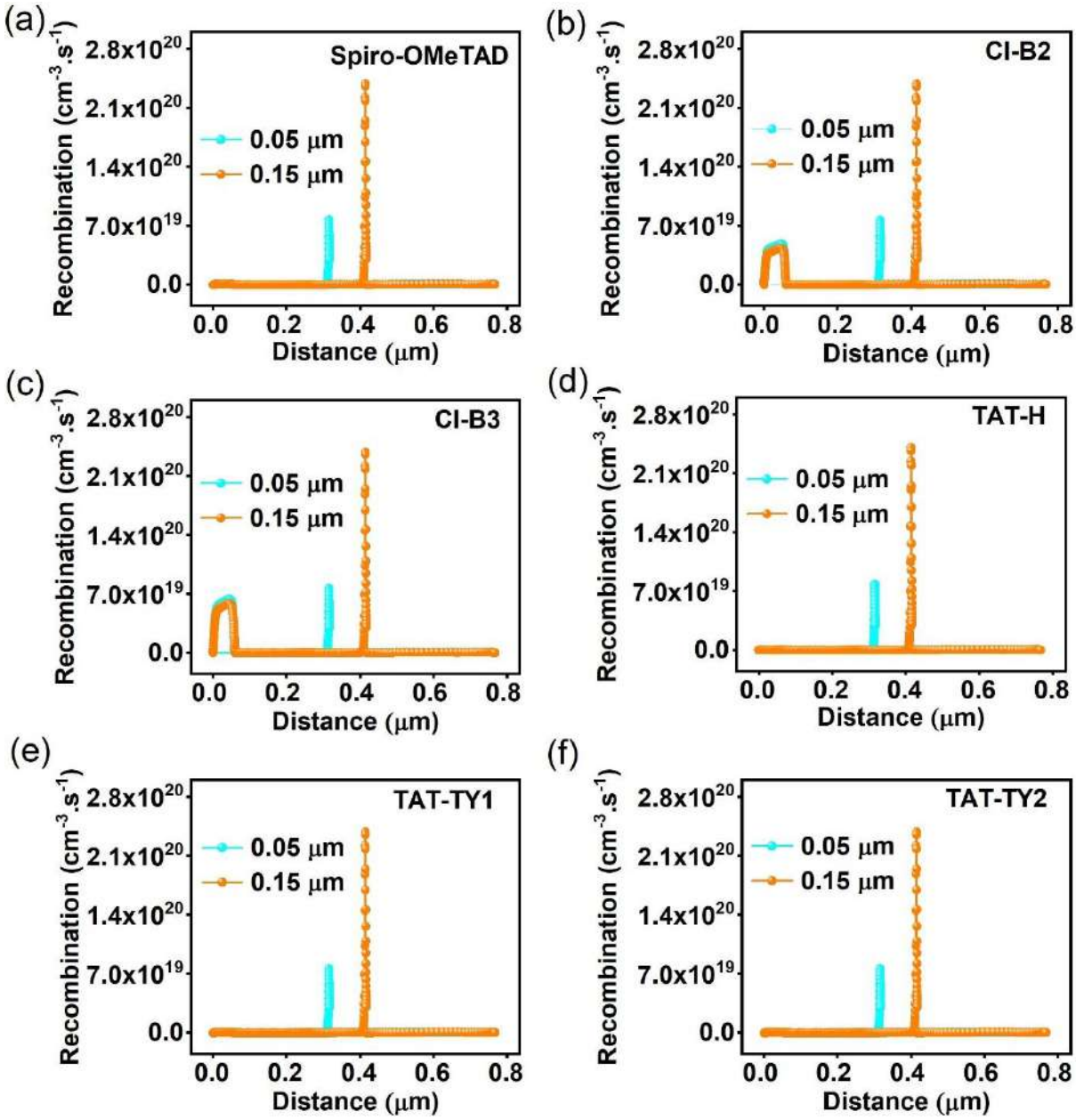

Fig. 14. (a-f) Recombination rate for the effect of ETL thickness for all solar cells.

The N_D of the ETL is a key parameter that influences the effective formation of the p-n junction and the alignment of energy bands.[165] The variation of N_D significantly impacts the PV parameters, as shown in **Fig. 15(a-d)**. Up to an N_D of ~10^{16} cm^{-3}, the parameters V_{OC}, FF, J_{SC}, and PCE remain relatively constant, and changes are insignificant, indicating that the device performance is unaffected within this range. Beyond 10^{16} cm^{-3}, all parameters show a consistent improvement, leading to higher PCE values. These enhancements are attributed to the improved built-in potential and enhanced conductivity, which facilitate better charge transport and reduce recombination losses.[166] The optimum N_D is determined to be 10^{20} cm^{-3}, where maximum performance in relation to V_{OC}, J_{SC}, FF, and PCE is achieved, indicating efficient energy band alignment and charge separation.

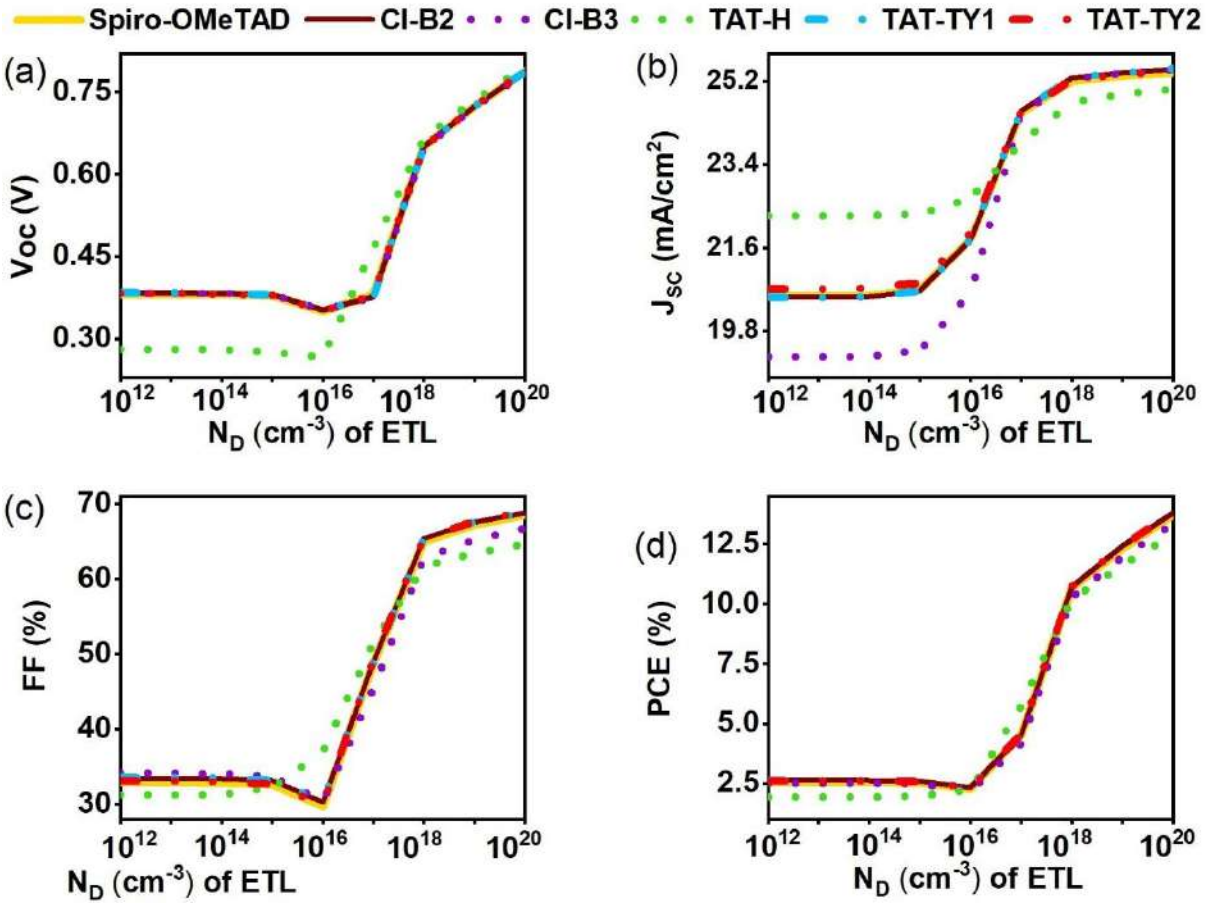

Fig. 15. Impact of N_D of ETL on (a) V_{OC}, (b) J_{SC}, (c) FF, (d) PCE.

The electric field distribution, illustrated in **Fig. 16(a-f)**, provides strong support for the trends observed. At the initial N_D of 10^{12} cm^{-3}, a minimal electric field is observed, resulting in limited charge separation and increased recombination losses. This in turn corresponds to the lower PCE. At the optimized N_D of 10^{20} cm^{-3}, the electric field is significantly stronger throughout the device layers. This stronger field ensures more efficient separation of electron-hole pairs,

reducing recombination losses and enabling better charge collection. The enhanced electric field also increases the built-in potential and improves charge carrier mobility, contributing to improved V_{OC} and FF values.[167] Overall, the stronger electric field at the optimized N_D aligns with the observed improvements in V_{OC}, J_{SC}, FF, and PCE. This highlights the critical role of achieving the optimum N_D to enhance both electric field strength and solar cell performance.

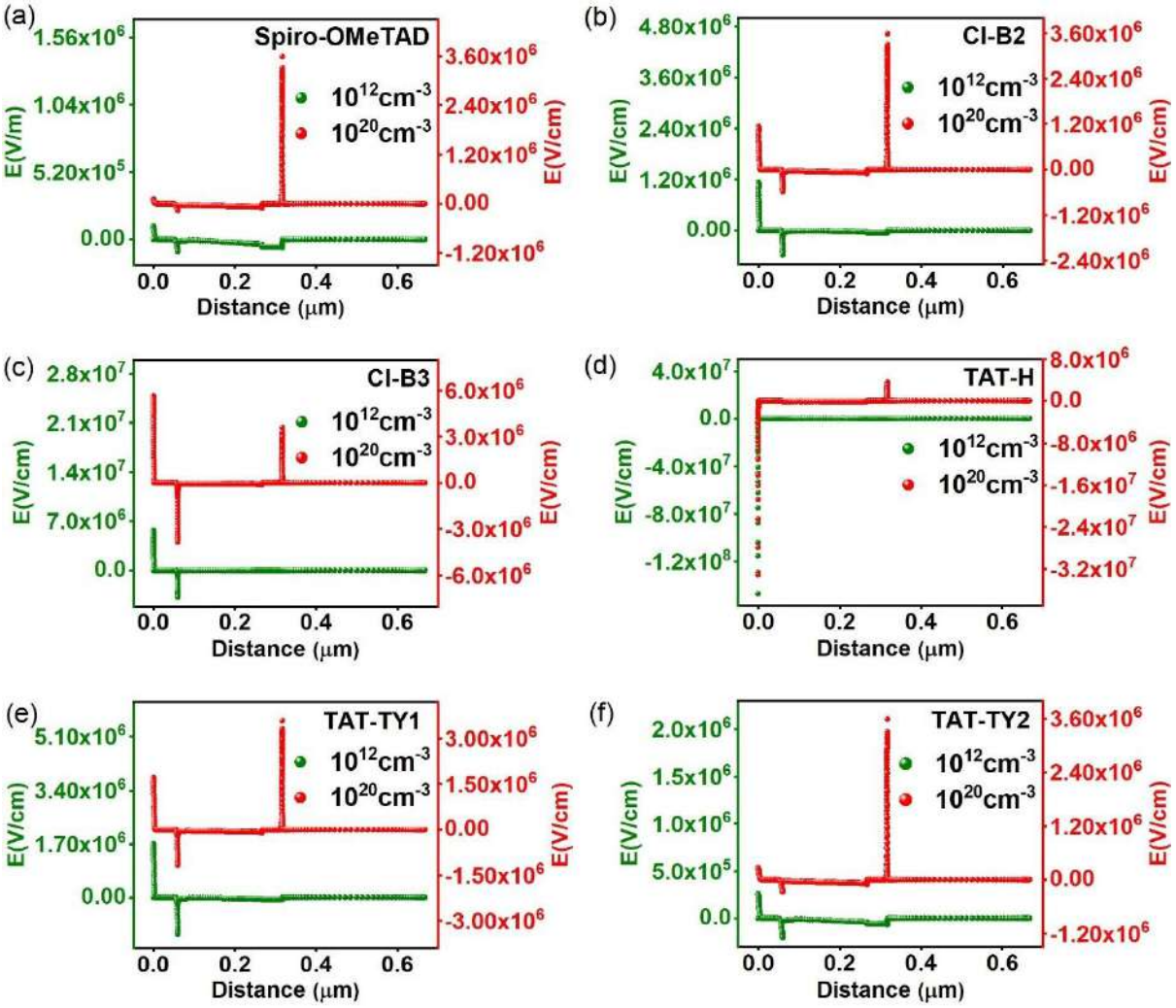

Fig. 16. (a-f) Electric field for effect of ETL N_D for all solar cells.

6.1.2.3. Effect of absorber thickness and N_A

The absorber layer thickness significantly impacts solar cell performance by influencing photon absorption and efficiency. While a thinner layer reduces charge carrier generation, an excessively thick layer limits carrier diffusion.[168–170] Achieving an optimal absorber thickness is, therefore, essential for enhancing PCE. In this study, the $Sb_2(S,Se)_3$ absorber thickness was varied between 0.1 to 1 μm to identify the optimal value.

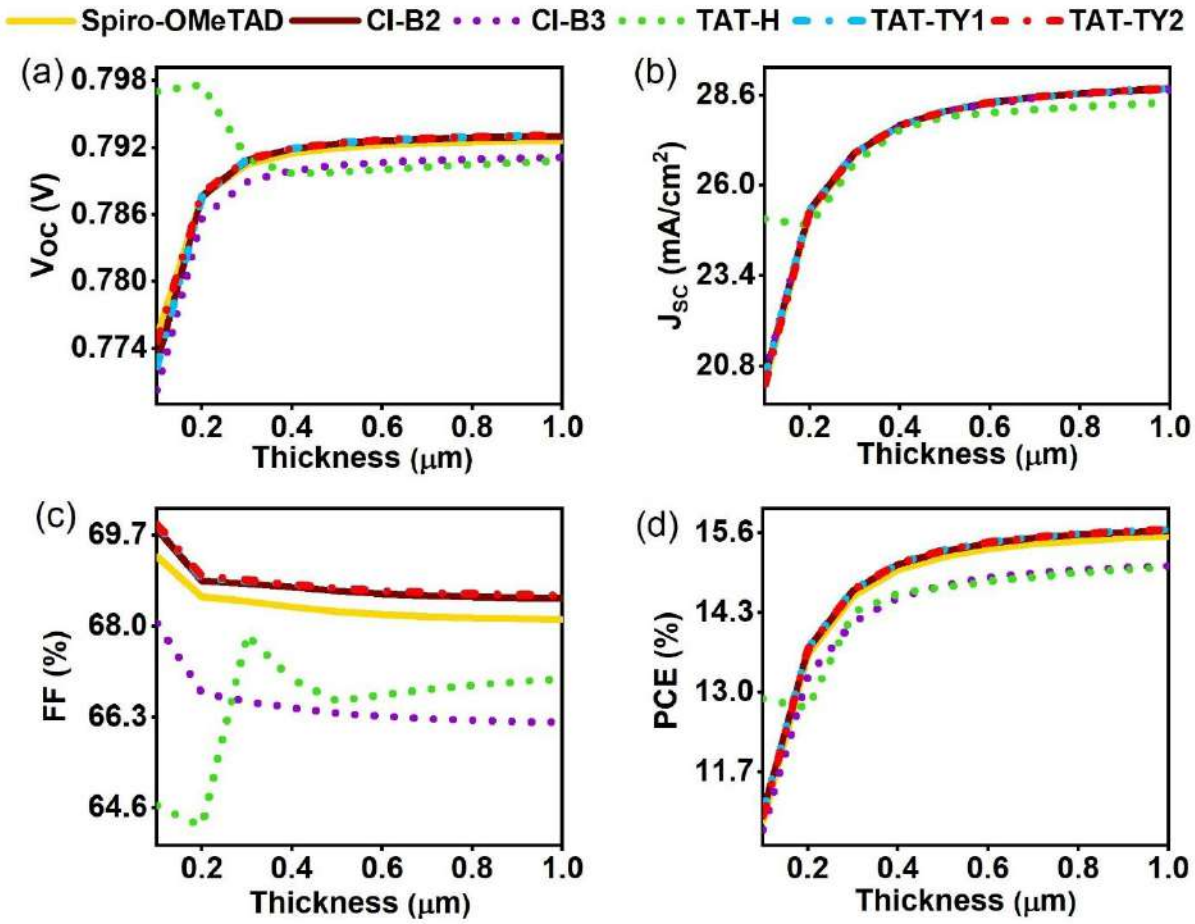

Fig. 17. Impact of absorber thickness on a) V_{OC}, b) J_{SC}, c) FF, d) PCE.

In this study, varying the absorber thickness from 0.1 to 1 μm showed distinct trends in the performance of solar cells, as shown in **Fig. 17(a-d)**. It can be observed that V_{OC} slightly decreases for the TAT-H-based cell up to a certain thickness and reaches saturation, while for the other solar cells, it initially improves and then stabilizes. The initial enhancement in V_{OC} for Spiro-OMeTAD, CI-B2, CI-B3, TAT-TY1, and TAT-TY2 is due to enhancement in the splitting of quasi-Fermi levels, whereas the decrement in V_{OC} for TAT-H and the saturation observed beyond a certain thickness for all solar cells result from an increase in dark saturation current associated with larger absorber thicknesses.[171] On the other hand, FF was decreased for Spiro-OMeTAD, CI-B2, CI-B3, TAT-TY1, and TAT-TY2-based solar cells. Lower FF is typically associated with an increase in series resistance at higher absorber thicknesses, which can hinder effective charge carrier transport.[171] However, TAT-H-based solar cells showed an increase in FF when the thickness was increased from 0.1 μm to 1 μm but exhibited fluctuations. This unusual behavior could be attributed to the specific characteristics of TAT-H, which requires further experimental investigation to understand the underlying reasons better.

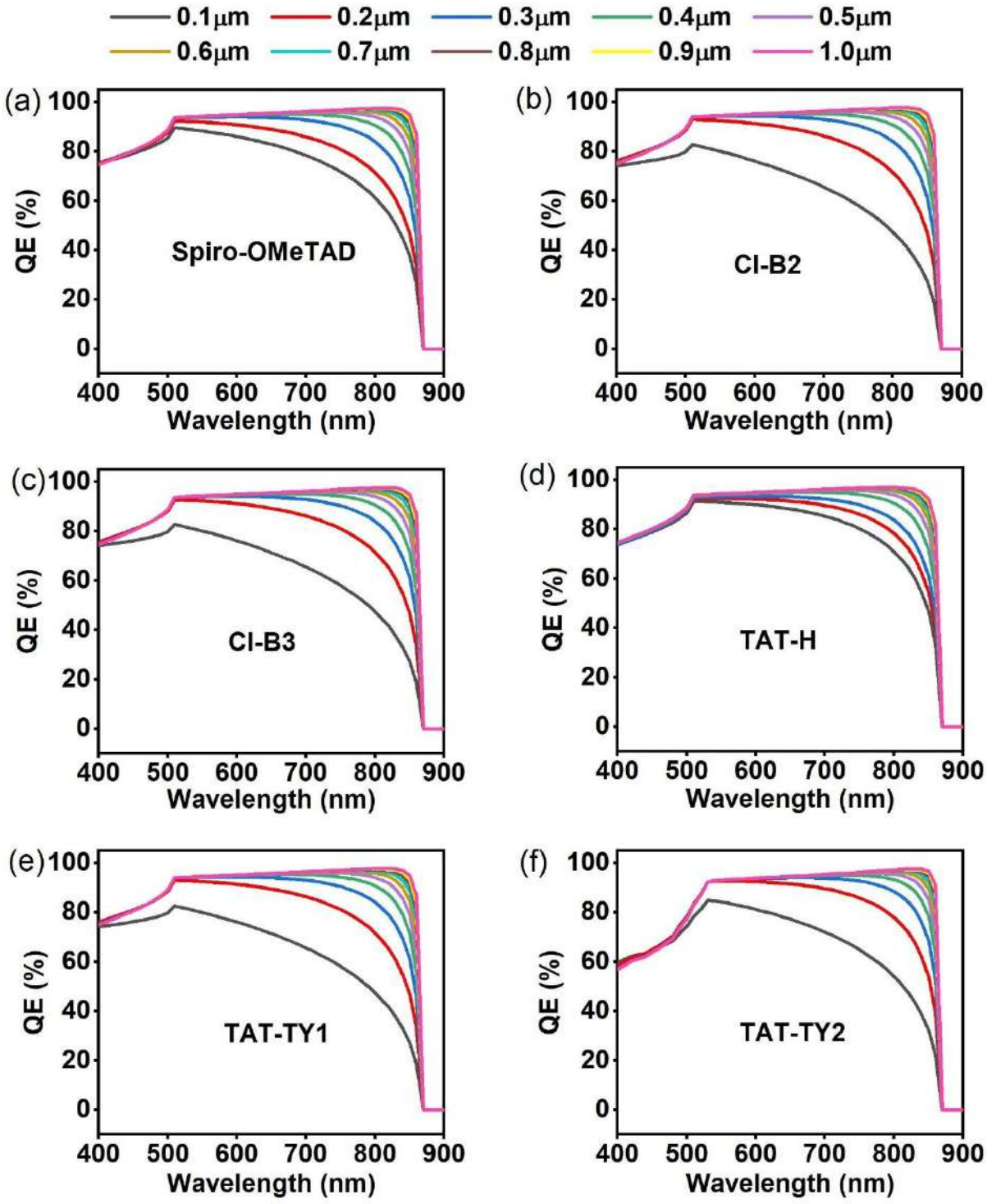

Fig. 18. (a-f) QE plots for the effect of absorber thickness for all solar cells.

In addition, J_{SC} consistently increased with absorber thickness in all solar cells, with a difference of ~3 mA/cm^2 for TAT-H-based cells and ~8 mA/cm^2 for the others as thickness increased from 0.1 to 1 μm. The increase in J_{SC} was significant up to optimal thicknesses of 0.7 μm for Spiro-OMeTED, CI-B2, and TAT-TY2, 0.8 μm for CI-B3, 0.6 μm for TAT-H, and 0.9 μm for TAT-TY1-based solar cells. A similar trend was observed for PCE, which increased by

over 2% as thickness reached the optimal values. Beyond these optimal thicknesses, only marginal improvements of ~0.2 mA/cm^2 and ~0.1% in the J_{SC} and PCE were observed, indicating saturation of photon absorption. Thicker absorber layers require longer charge carrier travel distances, leading to increased recombination as a result of shorter diffusion lengths, thereby saturating the solar cell performance.[172] The QE data in **Fig. 18(a-f)** further supports this, showing continuous improvement with thicker absorbers, plateauing beyond a certain thickness. For example, absorption increased from 67.10%-79.07%, 60.09%-79.28%, 60.05%-79.31%, 74.04%-84.57%, 60.11%-79.70%, and 62.42%-80.46% for Spiro-OMeTAD, CI-B2, CI-B3, TAT-H, TAT-TY1, and TAT-TY2-based solar cells, respectively, when thickness increased from 0.1 μm to the optimal thicknesses. Further increase in thickness resulted in only a negligible absorption improvement of 0.1%-0.4%. These findings confirm that thicker absorbers improve photon absorption but with diminishing returns at larger thicknesses. The optimal absorber thicknesses for each HTL-based solar cell were identified as 0.7 μm for Spiro, CI-B2, and TAT-TY2, 0.8 μm for CI-B3, 0.6 μm for TAT-H, and 0.9 μm for TAT-TY1-based solar cells respectively, offering the best balance of performance and manufacturability.

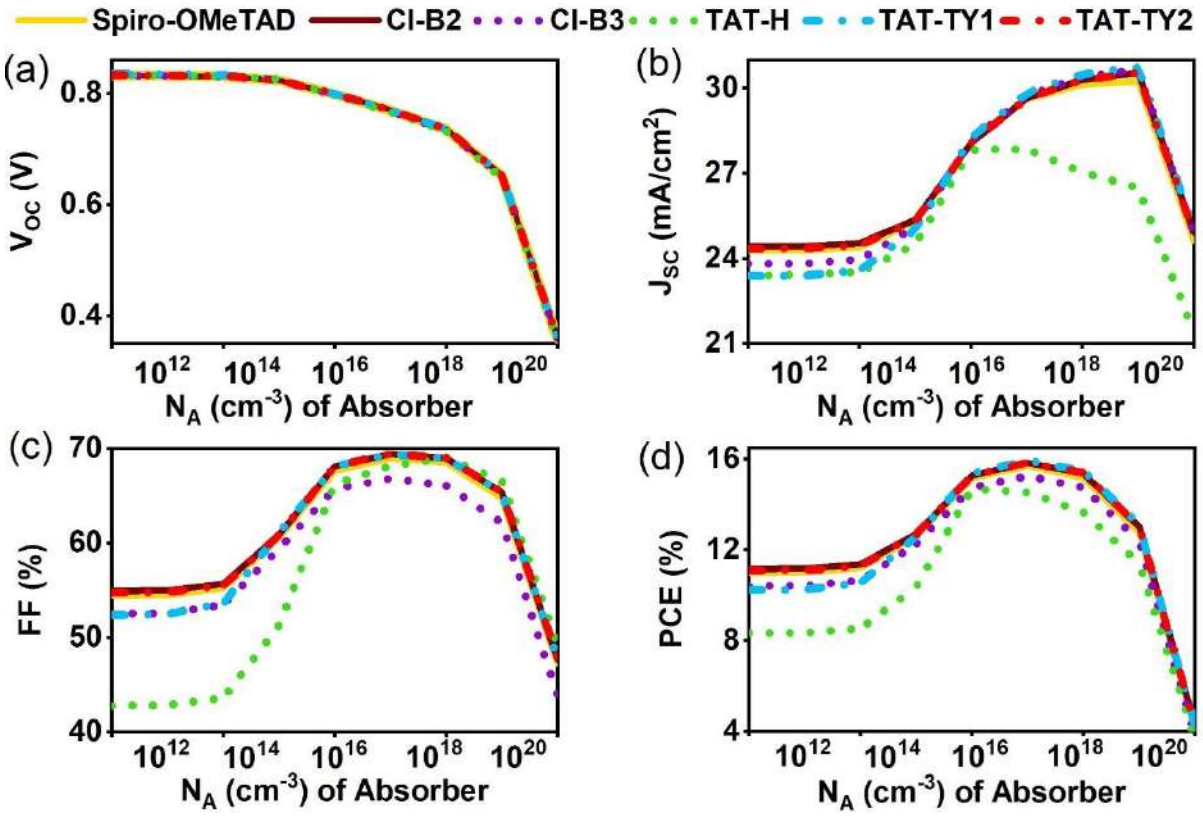

Fig. 19. Impact of N_A of absorber on a) V_{OC}, b) J_{SC}, c) FF, d) PCE.

The acceptor density of the absorber layer plays a pivotal role in enhancing carrier transport and overall stability in solar cells. We varied the N_A from 10^{12} cm^{-3} to 10^{20} cm^{-3} to find the optimal value for improving solar cell performance. The changes in the PV parameters are depicted in **Fig. 19(a-d)**.

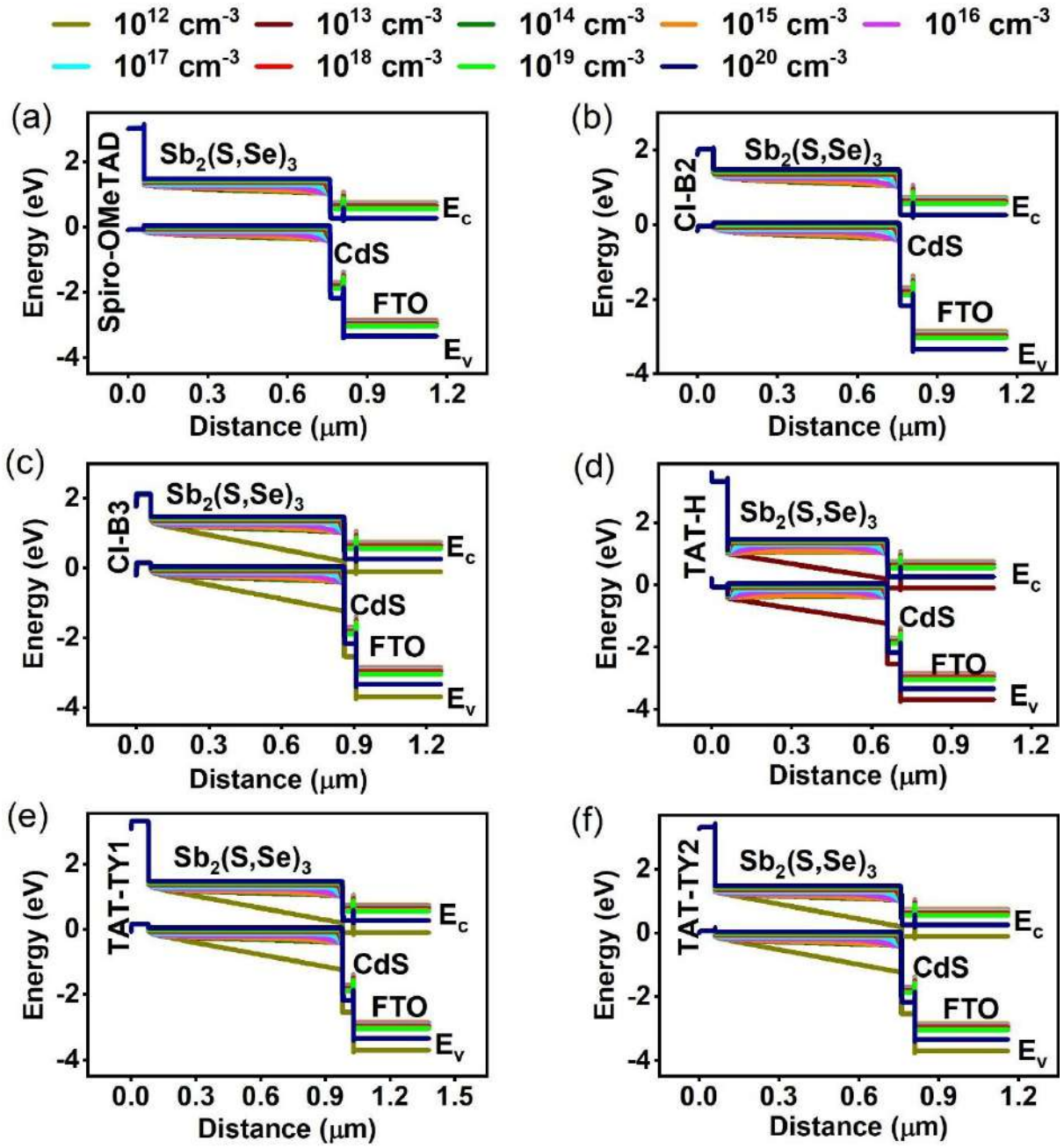

Fig. 20. (a-f) Energy band diagram for effect of absorber N_A for all solar cells.

Initially, V_{OC} stayed almost constant with minimal variation up to 10^{16} cm^{-3}. However, beyond this point, V_{OC} dropped sharply for all solar cells, primarily due to increased non-radiative recombination that hindered hole mobility.[173,174] The J_{SC} increased abruptly with rising N_A,

reaching a peak at 10^{16} cm^{-3} for TAT-H-based cells and at 10^{19} cm^{-3} for the other solar cells, after which it started to decrease. This drop in J_{SC} can be attributed to a reduction in the depletion width along the absorber layer, which negatively affects light absorption and charge carrier generation.[175] Both FF and PCE followed an increasing trend as the N_A rose from 10^{12} cm^{-3} to 10^{16} cm^{-3} for TAT-H-based solar cells and from 10^{12} cm^{-3} to 10^{17} cm^{-3} for the remaining solar cells. Beyond this optimal range, both parameters experienced a significant decrease. These changes were linked to shifts in the energy level alignments, as demonstrated by the energy band diagrams for N_A varied in the range of 10^{12} cm^{-3} to 10^{20} cm^{-3} (**Fig. 20(a-f)**).

The upward shift of the conduction band (E_C) and valence band (E_V) in the absorber layer altered the band offsets at the interfaces, modifying the barriers for photogenerated holes and electrons. This shift created suitable barriers for charge carriers at the optimal N_A, while values either lower or higher than the optimal resulted in performance degradation.[176] Supporting these observations, Nyquist plots (**Fig. 21(a-f)**) from C-f measurements were extracted for the initial (10^{12} cm^{-3}), optimized (10^{16} cm^{-3} for TAT-H-based solar cells and 10^{17} cm^{-3} for the remaining solar cells) and final (10^{20} cm^{-3}) N_A. For the initial N_A, the diameter of the semicircle was smaller, whereas an increase in the semicircle diameter at the optimized N_A was observed, indicating improved carrier transport. However, beyond this point, the diameter decreased as N_A rose to 10^{20} cm^{-3}, further supporting the optimal range. In addition, QE plots (**Fig. 21(g-l)**) showed an increase in QE from 10^{12} cm^{-3} to the optimal N_A, followed by a decline as N_A reached 10^{20} cm^{-3}. This confirms that the optimized N_A creates a suitable barrier for efficient carrier transport, while deviations from this range lead to recombination and inefficient transport to the contacts.[177,178] Based on these results, we determined that the optimal N_A is 10^{16} cm^{-3} for TAT-H-based cells and 10^{17} cm^{-3} for remaining solar cells.

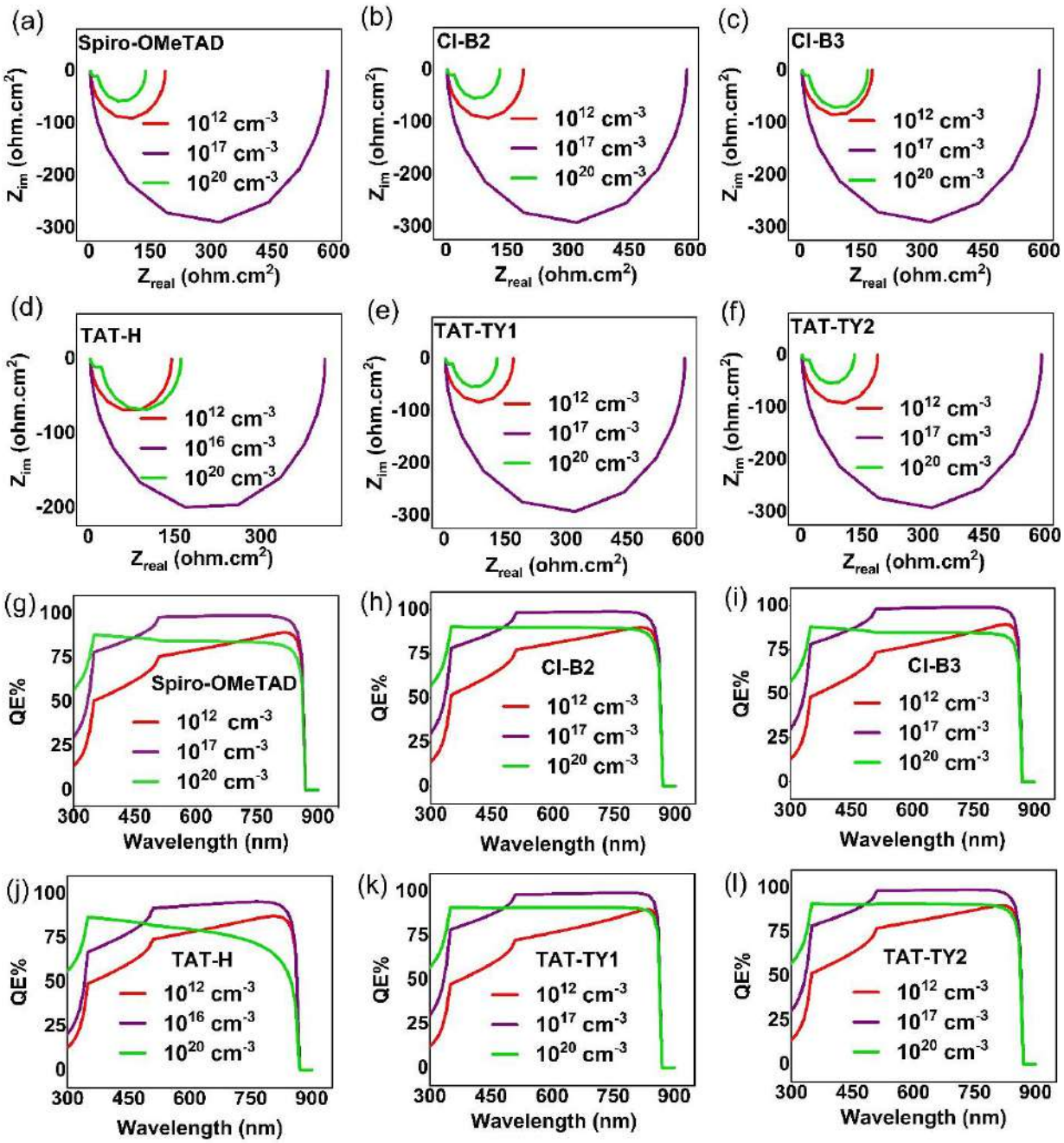

Fig. 21. (a-f) Nyquist plots and (g-l) QE plots for the initial, optimized and final N_A.

6.1.3. Optimization of Interface Properties

Interface defects are inevitable in solar cells due to structural imperfections during fabrication. Even with optimal band alignment, non-radiative recombination at interfaces must be considered. For instance, $Sb_2(S,Se)_3$ has an orthorhombic structure, while CdS and spiro-OMeTAD adopt hexagonal and triclinic structures, respectively. These structural incompatibilities at the Absorber/HTL and ETL/Absorber interfaces lead to non-radiative recombination that hinders solar cell performance.[179] Thus, optimizing these defects is

crucial for reducing interface recombination. We varied defect densities from 10^{10} to 10^{18} cm^{-2} at the HTL/Absorber interface, with the results shown in **Fig. 22(a-d)**. PV parameters remained unaltered up to a certain defect density, after which a decline in performance occurred due to trap-assisted recombination.[180] The optimal defect densities were found to be 10^{13} cm^{-2} for spiro-OMeTAD and TAT-TY2, 10^{14} cm^{-2} for CI-B2, 10^{16} cm^{-2} for CI-B3, 10^{12} cm^{-2} for TAT-H, and 10^{15} cm^{-2} for TAT-TY1 respectively.

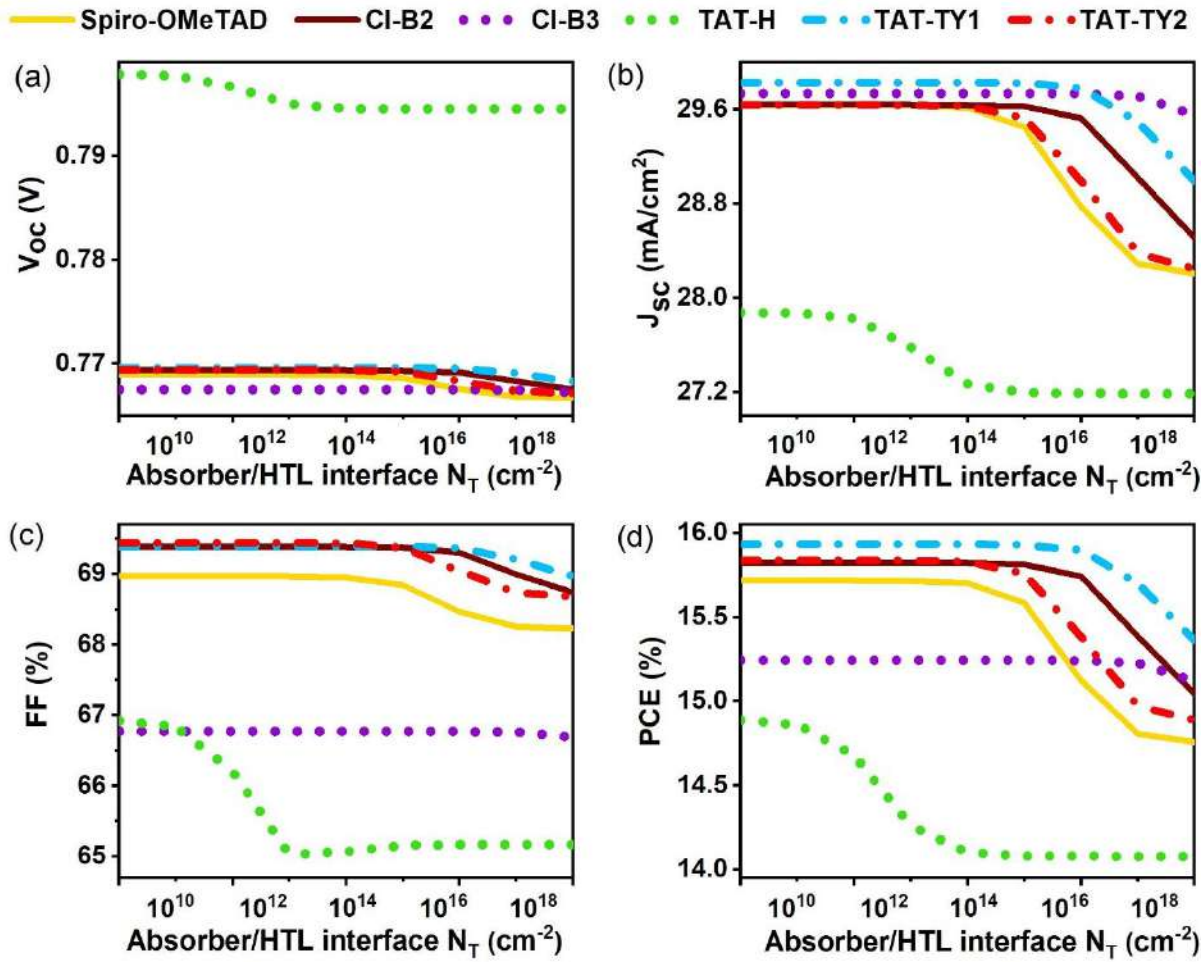

Fig. 22. Impact of defect density at the absorber/HTL interface on a) V_{OC}, b) J_{SC}, c) FF, and d) PCE.

Similarly, varying the defect density at the ETL/Absorber interface, as shown in **Fig. 23(a-d)**, caused all PV parameters to decrease rapidly from 10^{10} to 10^{15} cm^{-2}, with values stabilizing beyond 10^{15} cm^{-2}. Therefore, a defect density of 10^{10} cm^{-2} was selected for all solar cells, consistent with experimental reports for similar structures.[181] The performance degradation with higher interface defects is due to increased trapping of photo-generated electrons at the ETL/Absorber interface and holes at the HTL/Absorber interface, which accelerates

recombination.[180] After optimizing the defect densities, the maximum PCEs achieved were 22.97%, 23.09%, 22.47%, 21.08%, 23.24%, and 23.11% for Spiro-OMeTAD, CI-B2, CI-B3, TAT-H, TAT-TY1, and TAT-TY2 solar cells, respectively. Notably, the HTL/Absorber interface showed less PCE degradation compared to the ETL/Absorber interface, indicating that these solar cells are more sensitive to later defects.

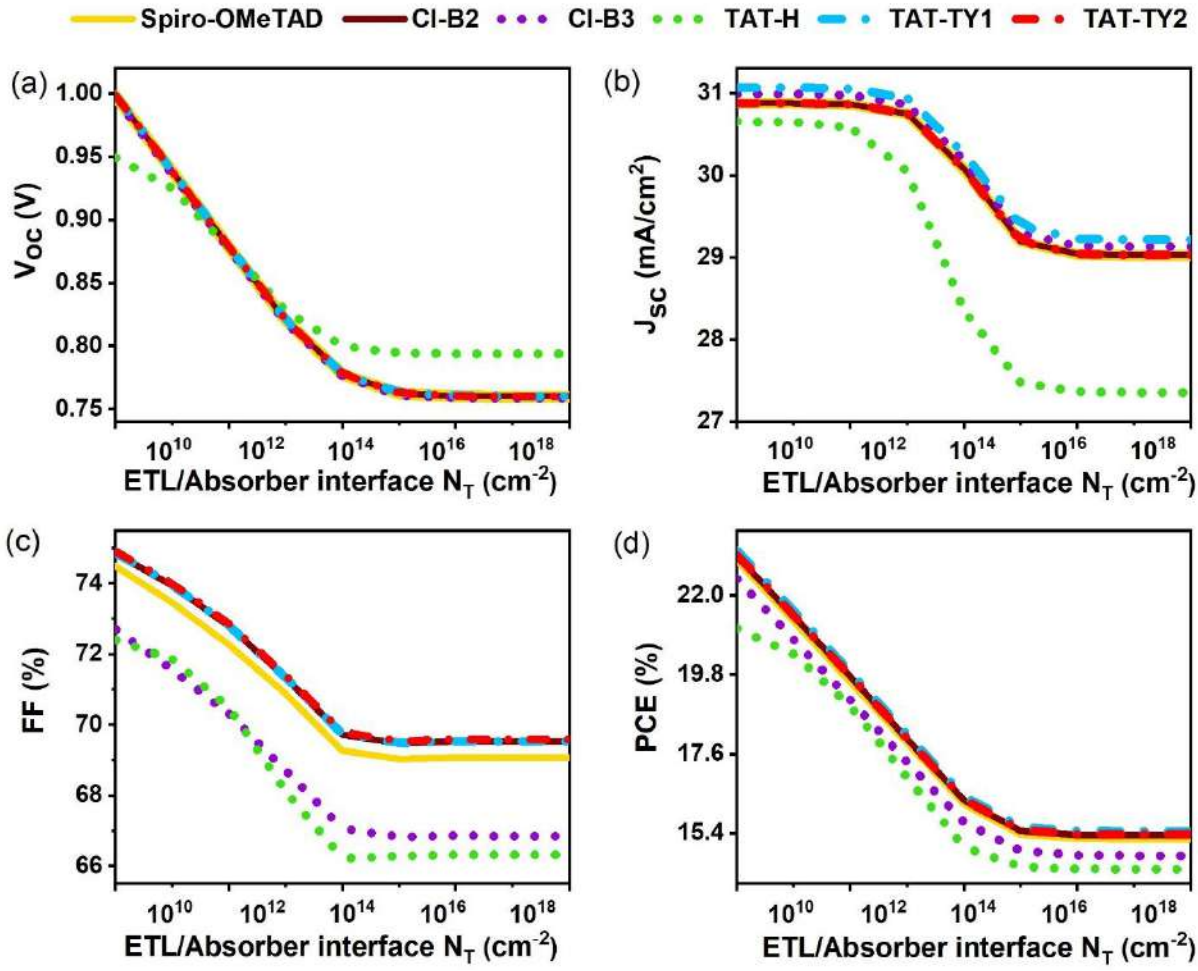

Fig. 23. Impact of defect density at the ETL/absorber interface on a) V_{OC}, b) J_{SC}, c) FF, and d) PCE.

6.1.4. Summary and Optimal Solar Cell Design

6.1.4.1. Optimized Device Performance

In conclusion, this study systematically optimized the layer parameters of $Sb_2(S,Se)_3$ solar cells with an FTO/CdS/$Sb_2(S,Se)_3$/Spiro-OMeTAD/Au device structure. Diverse triazatruxene-based HTLs, including CI-B2, CI-B3, TAT-H, TAT-TY1, and TAT-TY2, were tested and found to be promising alternatives to spiro-OMeTAD.

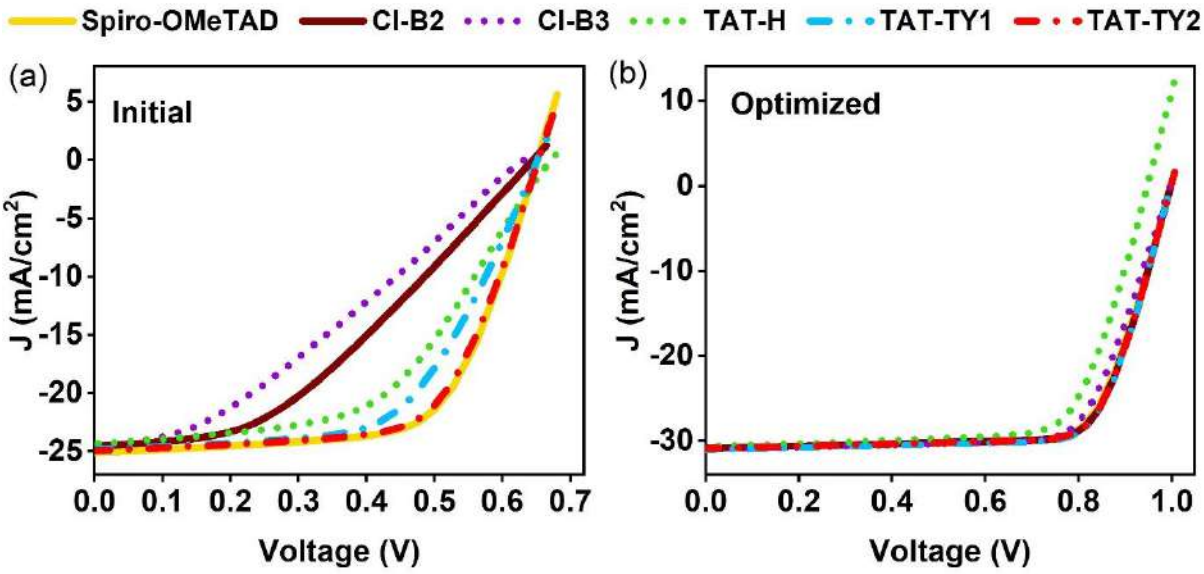

Fig. 24. J-V measurement for a) initial and b) optimized devices.

Table 11. Device performance for the optimized devices.

Device structure	**V_{OC} (V)**	**J_{SC} (mA/cm^2)**	**FF (%)**	**PCE (%)**
FTO/CdS/$Sb_2(S,Se)_3$/ Spiro-OMeTAD /Au	1.00	30.88	74.49	22.97
FTO/CdS/$Sb_2(S,Se)_3$/CI-B2 /Au	1.00	30.88	74.94	23.09
FTO/CdS/$Sb_2(S,Se)_3$/ CI-B3/Au	1.00	30.99	72.71	22.47
FTO/CdS/$Sb_2(S,Se)_3$/ TAT-H/Au	0.95	30.66	72.41	21.08
FTO/CdS/$Sb_2(S,Se)_3$/ TAT-TY1 /Au	1.00	30.88	74.87	23.24
FTO/CdS/$Sb_2(S,Se)_3$/ TAT-TY2 /Au	1.00	30.88	74.91	23.11

The high-performance device structures for the various HTL-based solar cells, along with their corresponding solar cell parameters, are presented in **Table 11**. The initial and final device J-V characteristics are illustrated in **Fig. 24 (a,b)**. As shown in Table 5, all HTL-based solar cells achieved PCE greater than 21%. In addition, the initial V_{OC} of ~0.63-0.65 V was increased to ~1V for all the solar cells. These results indicate that the energy losses were minimized, resulting in a reduced V_{OC} deficit of approximately 0.4V in the optimized solar cells. Furthermore, all HTL-based solar cells demonstrated J_{SC} values exceeding 30 mA/cm^2 and FF around 72 to 74%, highlighting the effectiveness of these materials in optimizing solar cell performance. Overall, the maximum PCEs attained were 22.97%, 23.09%, 22.47%, 21.08%, 23.24%, and 23.11% for Spiro-OMeTAD, CI-B2, CI-B3, TAT-H, TAT-TY1, and TAT-TY2-based solar cells, respectively. The efficiencies of diverse triazatruxene HTLs are comparable

to Spiro-OMeTAD, unveiling their immense potential and applicability in $Sb_2(S,Se)_3$ solar cells.

6.1.4.2. Energy Band Diagram of Optimized Devices

The transport of photogenerated charge carriers in solar cells is critically governed by the band alignment at the heterojunction interfaces, which plays a pivotal role in determining the overall device performance.[182] In this study, CBO and VBO at the HTL/absorber interfaces were analyzed to understand their impact on the PV parameters. For the HTL/absorber interface, CBO is calculated as the difference between the conduction band minimum (E_C) of the absorber and the conduction band minimum of the HTL, while the VBO is derived from the difference between the valence band maximum (E_V) of the HTL and that of the absorber. Herein, the negative (–) sign indicates the cliff-like barrier, and the positive (+) sign represents the spike-like barrier for the respective charge carriers at the interfaces.[183,184] **Fig. 25(a-f)** shows the energy band diagram of all the devices. The CBO and VBO values at the HTL/absorber interfaces estimated from Figure 12 are listed in **Table 12**. These values that are extracted from the energy band diagram are also consistent with the CBO and VBO calculated using the following relation:[185]

$$CBO = \chi_{Absorber} - \chi_{HTL} \tag{13}$$

$$VBO = \left[E_{g\,HTL} + \chi_{HTL}\right] - \left[E_{g\,Absorber} + \chi_{Absorber}\right] \tag{14}$$

The values of CBO and VBO obtained both theoretically and from the energy band diagram are consistent with each other, validating the bandgap matching advantage of the HTL and the absorber.

Further all the investigated HTLs—CI-B2, CI-B3, TAT-H, TAT-TY1, and TAT-TY2—along with the benchmark Spiro-OMeTAD, demonstrated energy band alignments suitable for efficient hole extraction from the absorber while effectively suppressing the backflow of electrons through high CBOs. Notably, the CBO values at the HTL/absorber interfaces of all devices are significantly positive, indicating substantial spike-like barriers that effectively block electrons from recombining at the HTL side. Meanwhile, the VBO values remain relatively small in magnitude, ranging from –0.037 eV to –0.358 eV, with cliff-like barriers for the transport of photogenerated holes to the HTL. These band alignment characteristics validate that all HTLs exhibit potential as viable alternatives to Spiro-OMeTAD for efficient hole extraction. However, among them, TAT-H showed the lowest efficiency of 21.08%, which can

be primarily attributed to its large VBO of –0.358 eV at the HTL/absorber interface. This substantial cliff-like barrier poses a hindrance to the transport of holes, thereby increasing recombination losses and adversely affecting performance [].[183,184] In contrast, HTLs like TAT-TY1 and TAT-TY2, with VBOs of only –0.06 eV and –0.146 eV respectively, facilitate smoother hole transport, resulting in improved PCEs of 23.24% and 23.11%, both of which slightly surpass the 22.97% efficiency of the standard Spiro-OMeTAD device. Regarding the ETL/absorber and ETL/FTO interfaces, all solar cell configurations exhibit consistent and favorable band alignments across the devices. The ETLs form small CBOs with the absorber, enabling efficient electron transport while presenting significant VBOs that act as spike-like barriers for holes. This alignment effectively suppresses hole back-injection towards the front contact, enhancing carrier selectivity and reducing recombination losses.[186–188] The similarity in these offsets across all devices confirms that the differences in performance arise predominantly from the HTL/absorber interface properties.

In summary, all the investigated HTLs exhibit favorable band alignment with the absorber, supporting efficient charge extraction and minimal recombination losses. The close range of PCEs achieved across the devices indicates that their overall performance is on par with that of the benchmark spiro-OMeTAD. This comparable efficiency, coupled with suitable energetic alignment, highlights their potential as viable alternatives to conventional HTLs in next-generation PV devices.

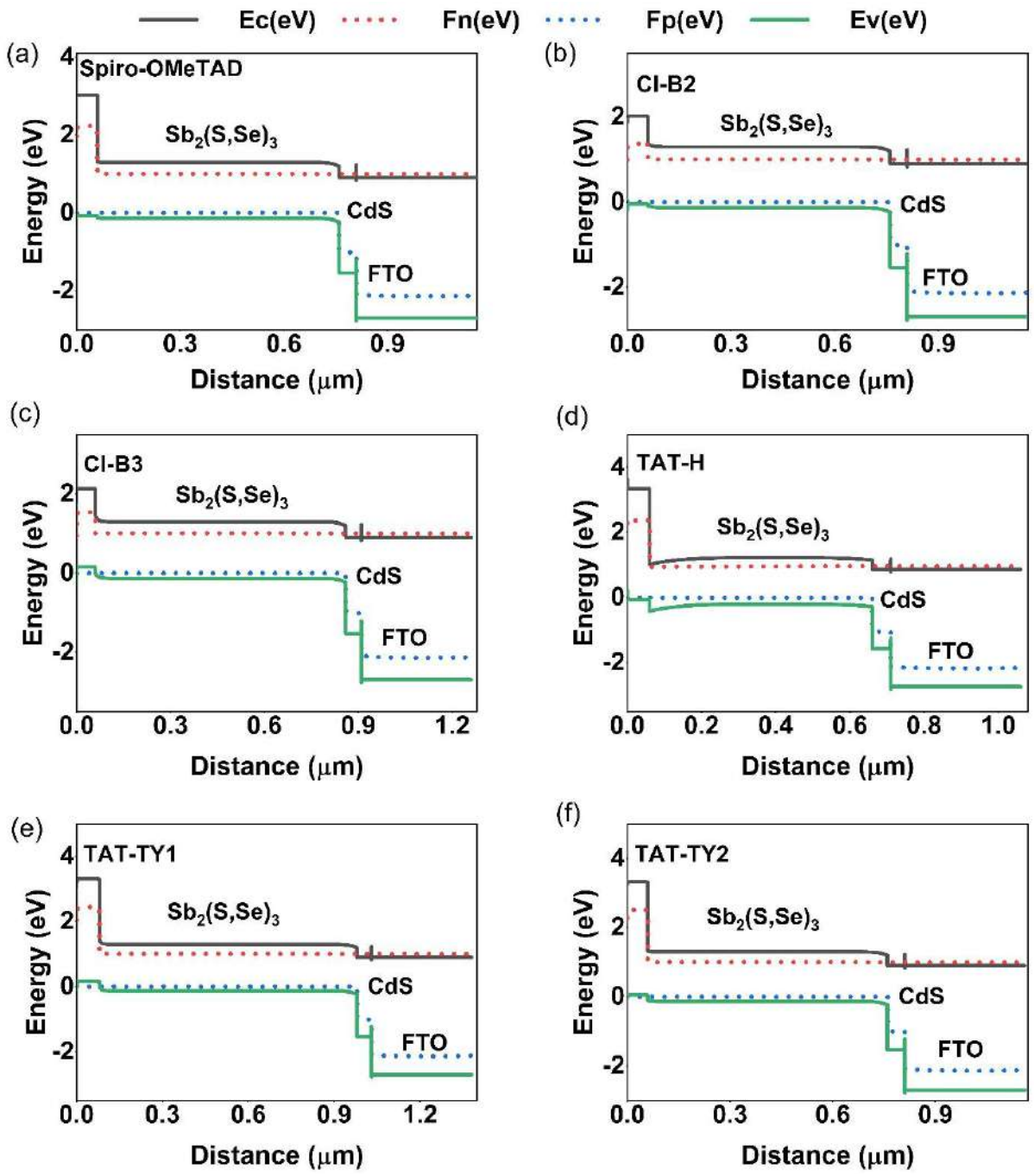

Fig. 25. (a-f) Energy band diagrams of optimized devices with diverse triazatruxene HTLs.

Table 12. Energy band offset values at the HTL/absorber interfaces are estimated from Fig. 25

HTL/absorber interfaces	**CBO**	**VBO**
Spiro-OMeTAD/$Sb_2(S,Se)_3$	+1.717	-0.04
CI-B2/$Sb_2(S,Se)_3$	+0.64	-0.037
CI-B3/$Sb_2(S,Se)_3$	+0.52	-0.078
TAT-H/$Sb_2(S,Se)_3$	+2.33	-0.358

TAT-TY1/$Sb_2(S,Se)_3$	+1.8	-0.06
TAT-TY2/$Sb_2(S,Se)_3$	+1.972	-0.146

6.1.4.3. Comparison of Present Outcomes with Other SCAPS-1D Studies in the Literature

A comparative analysis of these findings with existing literature is provided in **Table 13**, demonstrating the competitiveness of the reported results. The efficiency achieved in this study is comparable to those reported in the literature for devices with Spiro-OMeTAD. Furthermore, our results exceed the performance of devices incorporating other previously reported HTLs, namely, MoS_2, Cu_2O, $MoSe_2$, MnS, NiO and $CuSbS_2$ respectively. Therefore, this study could unlock new possibilities for high-efficiency thin-film solar cells by employing $Sb_2(S,Se)_3$ as the absorber and triazatruxene-based HTLs as innovative, cost-effective alternatives for Spiro-OMeTAD.

Table 13. Comparison of the device performance from existing reports and the present study.

Device structures	**V_{OC} (V)**	**J_{SC} (mA·cm^{-2})**	**FF (%)**	**PCE (%)**	**Ref.**
FTO/CdS/$Sb_2(S,Se)_3$/Spiro-OMeTAD/Au	1.31	24.05	58.56	18.43	[179]
ITO/CdS/$Sb_2(S,Se)_3$/MoS_2/Mo	0.95	35.32	75.96	25.67	[189]
FTO/$Cd_{0.6}Zn_{0.4}S$/$Sb_2(S,Se)_3$/Spiro-OMeTAD/Au	0.88	26.67	74.22	17.43	[190]
FTO/ZnO/$Sb_2(S,Se)_3$/Cu_2O/Au	0.95	27.70	68.00	18.00	[191]
FTO/ZnO/$Sb_2(S,Se)_3$/NiO/Au	0.94	27.6	67.00	17.3	[191]
FTO/$Cd_{0.6}Zn_{0.4}S$/$Sb_2(S,Se)_3$/Cu_2O/Au	0.89	27.4	71.00	17.3	[191]
ITO/CdS/$Sb_2(S,Se)_3$/MnS/Au	0.72	25.29	69.54	12.70	[192]
Al/ZnO/$Cd_{0.6}Zn_{0.4}S$/TiO_2/$Sb_2(S,Se)_3$/$MoSe_2$/Mo	0.64	32.34	75.75	15.65	[193]
FTO/ZnSe/$Sb_2(S,Se)_3$/$CuSbS_2$/Au	0.93	28.64	74.54	20.01	[194]
FTO/CdS/$Sb_2(S,Se)_3$/Spiro-OMeTAD/Au	0.99	30.93	87.09	26.77	[47]
FTO/CdS/$Sb_2(S,Se)_3$/Spiro-OMeTAD/Au	1.00	30.88	74.49	22.97	This work
FTO/CdS/$Sb_2(S,Se)_3$/CI-B2/Au	1.00	30.88	74.94	23.09	This work
FTO/CdS/$Sb_2(S,Se)_3$/CI-B3/Au	1.00	30.99	72.71	22.47	This work
FTO/CdS/$Sb_2(S,Se)_3$/TAT-H/Au	0.95	30.66	72.41	21.08	This work
FTO/CdS/$Sb_2(S,Se)_3$/TAT-TY1/Au	1.00	30.88	74.87	23.24	This work
FTO/CdS/$Sb_2(S,Se)_3$/TAT-TY2/Au	1.00	30.88	74.91	23.11	This work

6.1.5. Impact of Operating Temperature and Light Intensity

Temperature plays a crucial role in determining the operational stability and efficiency of solar cells by influencing carrier generation, recombination, and transport dynamics. To assess this effect, we varied the temperature from 280 K to 400 K, and the corresponding PV parameters are extracted and are depicted in **Fig. 26(a-d)**.

As shown in the figure, V_{OC} decreases with the rising temperature of all the devices. This decline is primarily due to the increase in recombination processes, particularly Shockley-Read-Hall (SRH) recombination, which becomes more pronounced at higher temperatures. The relationship between V_{OC} and temperature can be understood from the equation (15):

$$\frac{d}{dT}(V_{OC}) = \frac{(V_o - E_g)/q}{T} \tag{15}$$

where V_O is V_{OC} at absolute temperature (0K), E_g is the bandgap energy, q is the charge of the electron, and T is the temperature. Equation (4) signifies that as temperature increases, the saturation current increases, which in turn enhances recombination rates, resulting in a decrease in V_{OC}.[195,196] This is consistent with findings in the literature, where higher temperatures have been shown to reduce V_{OC} due to increased recombination and a slight reduction in the material's bandgap.[197] Along with V_{OC}, the FF and PCE of all the devices also decrease as the temperature rises. This behavior can be attributed to an increase in the series resistance and a reduction in the carrier diffusion length at higher temperatures. The higher series resistance at elevated temperatures causes a drop in FF, while the increased recombination reduces the efficiency of charge carrier collection, leading to a decrease in PCE. These trends are in agreement with studies by Ouédraogo et al. (2021), who observed similar decreases in both FF and PCE due to enhanced recombination and increased series resistance at higher temperatures.[198]

To understand the underlying reason for such degradation in transport characteristics, one should also consider the temperature dependence of carrier mobility, which generally follows the relation:

$$\mu(T) \propto T^{-m} \tag{16}$$

where m>0 for phonon-limited scattering.[199] This implies that as temperature increases, mobility decreases due to increased phonon (lattice vibration) scattering, which adversely affects charge transport and extraction, contributing further to losses in FF and efficiency.[200]

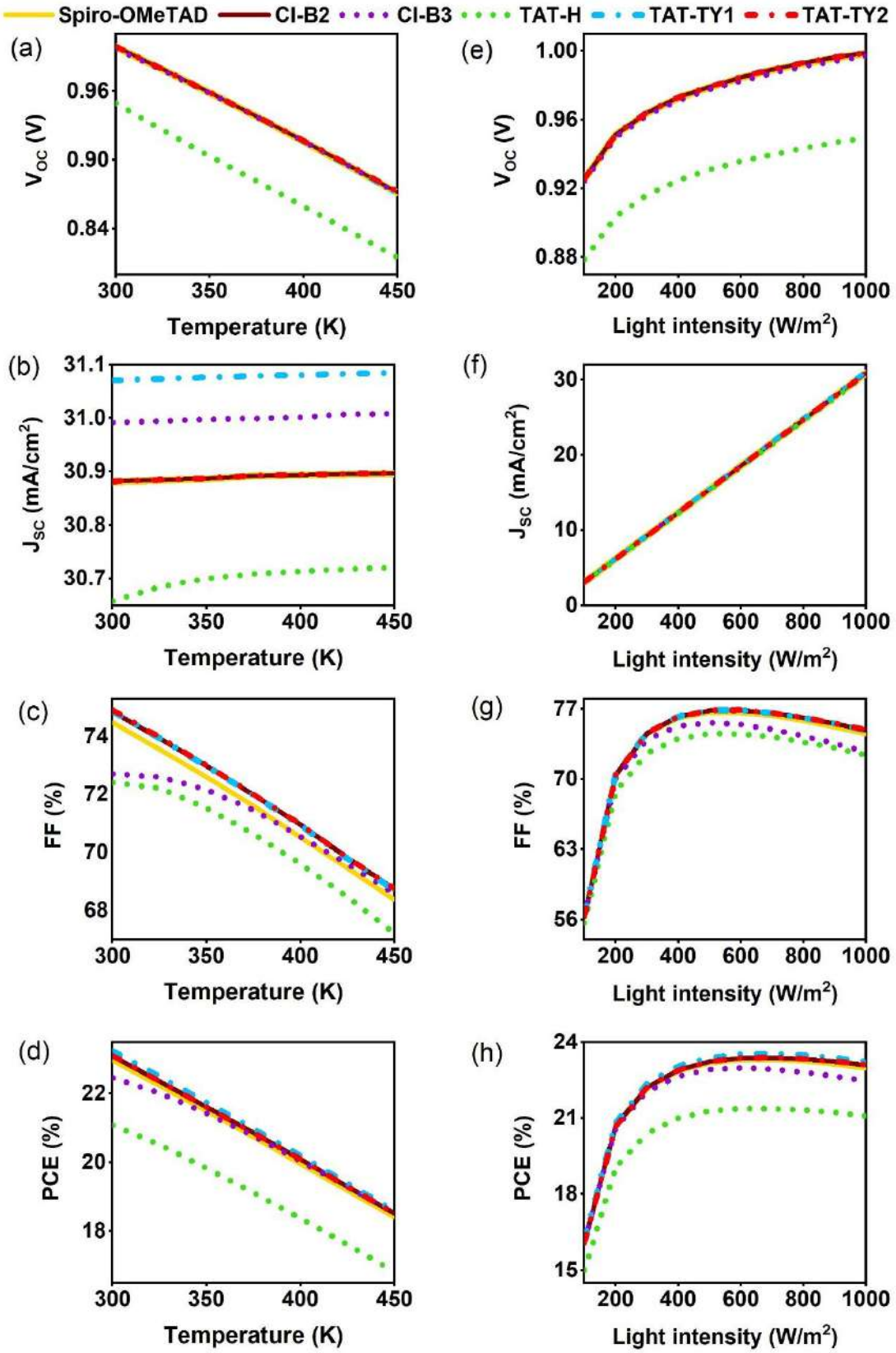

Fig. 26. PV parameters under varying conditions: (a–d) V_{OC}, J_{SC}, FF, and PCE vs. temperature; (e–h) V_{OC}, J_{SC}, FF, and PCE vs. light intensity.

Furthermore, J_{SC} exhibited a slight increase with temperature. This is primarily due to the reduction in bandgap of the absorber at higher temperatures, leading to the absorption of longer-wavelength photons and generation of more charge carriers. Although the increased generation may contribute positively to J_{SC}, the accompanying dark current and recombination mechanisms often negate these benefits. Therefore, the observed increase in J_{SC} remains minimal or stagnates at higher temperatures.[201,202] Overall, the results from the SCAPS-1D simulation show that temperature has an apparent effect on the performance of the solar cells. While J_{SC} remains stable primarily, the decrease in V_{OC}, FF, and PCE can be attributed to increased recombination, higher series resistance, and reduced carrier diffusion length at higher temperatures.

Progressively to investigate the illumination-dependent performance, we performed simulations under different light intensities ranging from 100 W/m^2 to 1000 W/m^2, adjusted through the variation of Neutral Density (ND) filter values from 1 to 0 in steps of 0.1. The transmission (T) as a function of ND is given by [203]

$$T = 100\% \times 10^{-ND} \tag{17}$$

At ND=0 the light intensity is 1000 W/m^2 which is equivalent to 1 sun. Then to calculate ND, different intensities are applied in following relation,

$$ND = -\log\left(\frac{I}{I_o}\right) \tag{18}$$

Where I_o = 1000 W/m^2 and I is varying intensities.

For each light intensity, the PV parameters were extracted, and the results are shown in **Fig. 26 (e-h)**. The J_{SC} showed a linear increase with increasing light intensity, which is consistent with the increase in incident photon flux. This behavior validates the expected direct proportionality between the short-circuit current and light intensity, as the generation of photocarriers scales with the number of absorbed photons.[204] Similarly, the V_{OC} increased logarithmically with light intensity, following the well-known relation

$$V_{OC} = \frac{2KT}{q}\ln\left(\frac{G_L\tau_o}{n_i}\right) \tag{19}$$

where G_L is the generation rate of carriers, τ_o is the effective carrier lifetime, and n_i is the intrinsic carrier concentration. The increase in V_{OC} is attributed to the enhanced splitting of the quasi-Fermi levels due to the higher carrier density under stronger illumination.[203,205]

Interestingly, the FF initially increases with light intensity, reflecting reduced series resistance effects and improved carrier transport.[206] However, beyond a certain threshold (~800 W/m^2), FF exhibits a saturation behavior with no significant further enhancement. This suggests that beyond a certain illumination level, the FF reaches a saturation point, where further increases in light intensity do not significantly improve carrier extraction efficiency. At this stage, intrinsic recombination processes and fixed resistive losses in the device become dominant factors, limiting further enhancement in FF. A similar trend is observed for the PCE, indicating it is highly influenced by changes in FF with varying light intensities.[204,207,208]

To further validate these observations and understand the carrier dynamics, we analyzed the total generation and recombination rates extracted from SCAPS-1D simulations under various light intensities as depicted in **Fig. 27**. The results show that both the generation and recombination rates increase with increasing light intensity. However, a notable trend is that the rate of increase in generation and recombination is much steeper from 100 W/m^2 up to mid-range intensities (~700–800 W/m^2), whereas beyond this point, the increment becomes relatively minimal which supports the changes observed in FF and PCE. This suggests that the device enters a quasi-saturation regime where additional photons do not lead to proportionally higher carrier generation or recombination.[208] Importantly, at all light intensities, the generation rate remained significantly higher than the recombination rate, ensuring a net increase in collected carriers. This supports the high PCE observed even at maximum light intensity. For example, the maximum generation rate of ~2 x10^{22} cm^{-3}. s^{-1} is observed at high intensity (1000 W/m^2) while the maximum recombination rate was ~8 x 10^{20} cm^{-3}. s^{-1} which is lower than the generation rate for all the devices.

These findings indicate that the simulated solar cell maintains efficient photocarrier generation and transport across a broad illumination range, with minimal losses due to recombination. The saturation trends observed in FF and PCE at higher intensities further suggest that the device performance is predominantly limited by intrinsic material properties rather than external optical constraints. The analysis confirms that the device configuration is robust and stable under varying real-world sunlight intensities.

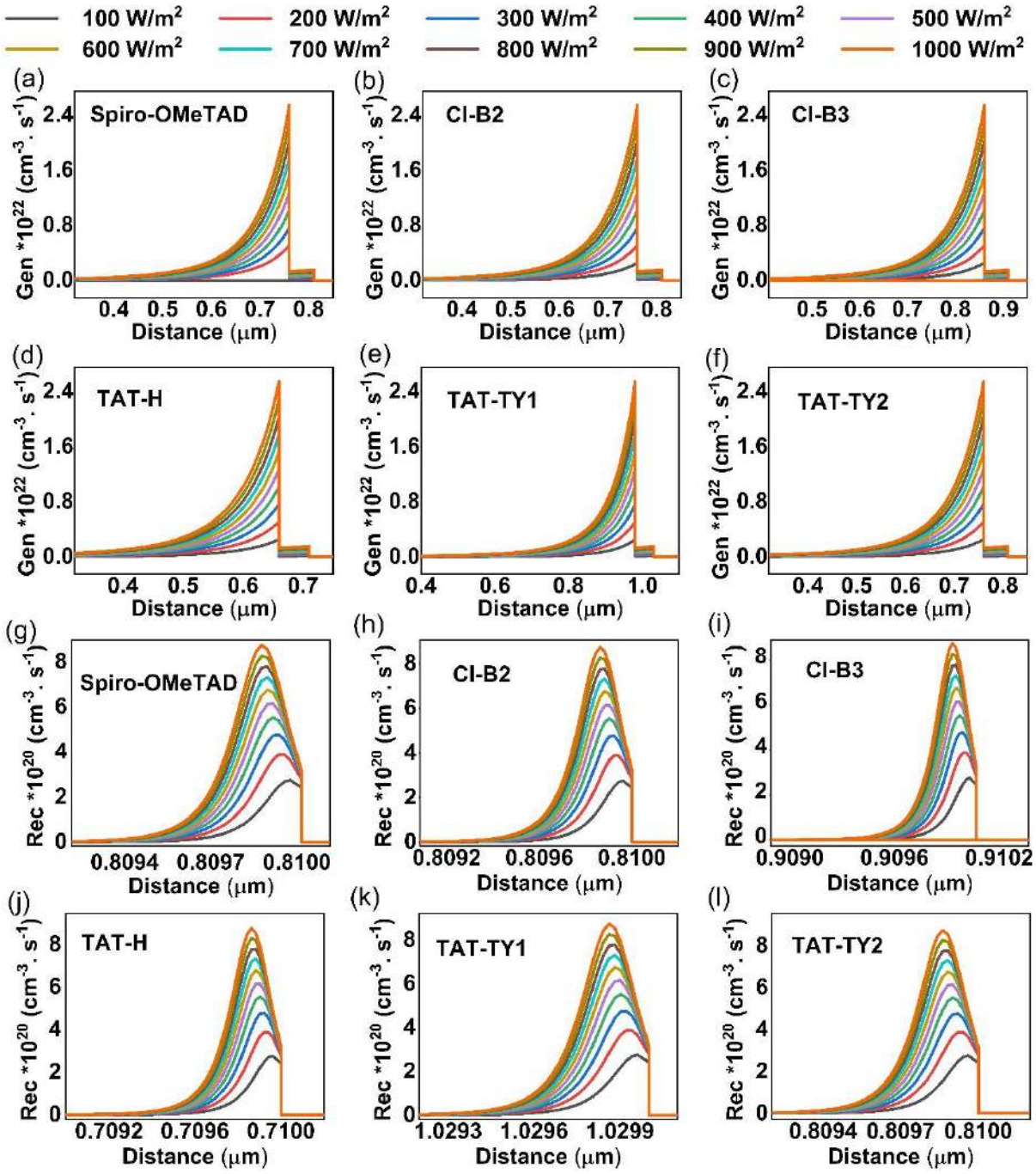

Fig. 27. (a-f) Generation rate and (g-l) recombination rate with respect to various light intensities.

6.2. Numerical Simulation of Cd-free Strontium Titanate Electron Transport Layer in $Sb_2(S,Se)_3$ Solar Cell

6.2.1. Base Device Performance with STO

Fig. 28 (a) shows the QE plot of the base device structure. Similarly, the JV characteristics is illustrated in **Fig. 28(b)** with the respective PV parameters in the inset. At the first introduction, the device achieved an impressive efficiency of ~14%, surpassing the reported experimental benchmark of 10.75%, owing to an improved QE of 81.8%. The QE spectrum exhibits slightly reduced response in the UV region (<400 nm) due to front-surface recombination, near-unity QE in the 400–600 nm range indicating minimal surface recombination, and a gradual decline at longer wavelengths reflecting bulk recombination within the absorber. The sharp drop near 850–900 nm corresponds to the band edge of $Sb_2(S,Se)_3$ [67]. These observations demonstrate that the $SrTiO_3$ ETL effectively reduces both surface and bulk recombination, enhancing carrier collection and overall device performance.

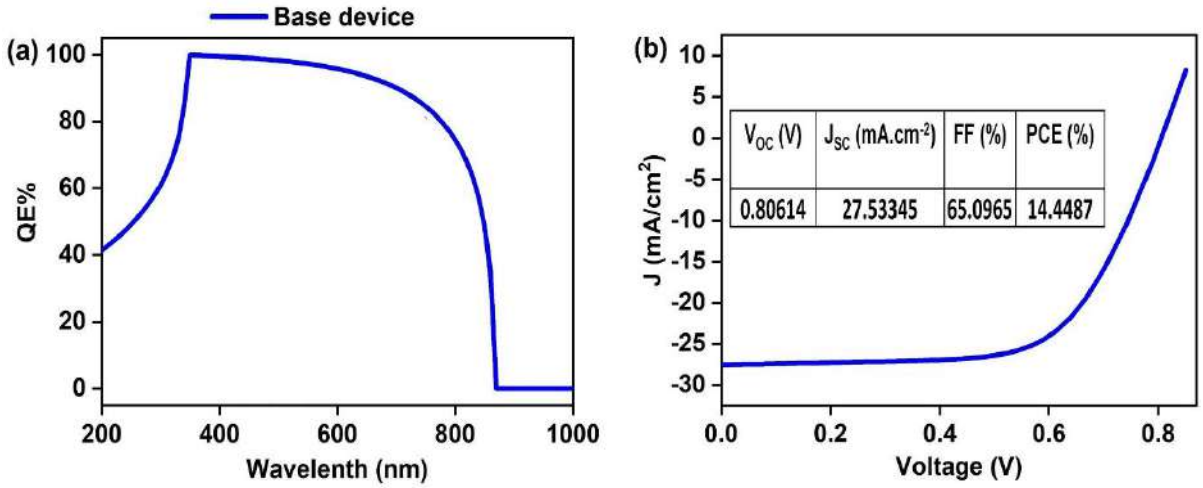

Fig. 28. (a) QE plot (b) JV curve of base device

6.2.2. Optimization of ETL Thickness

The thickness of the ETL plays a vital role in the performance of the solar cell by influencing the extraction and transport of photogenerated electrons from the absorber to the front contact. Hence the ETL thickness was varied from 0.01 µm to 0.1 µm to investigate the effect on key PV parameters. The variations in V_{OC} and J_{SC} are illustrated in **Fig. 29(a)**, while **Fig. 29(c)** displays the trends in FF and PCE. It was observed that as the thickness of STO increased, V_{OC}, FF, and PCE exhibited a decreasing trend, while J_{SC} showed a slight increase. The highest PCE was obtained for the thinnest ETL layer (0.01 µm), likely due to reduced series resistance and minimal charge recombination losses at this thickness [159]. However, in practical device

fabrication, using an ETL as thin as 0.01 µm can lead to incomplete coverage over the substrate and poor interface formation with the absorber, which may result in increased leakage currents and degraded device stability [160].

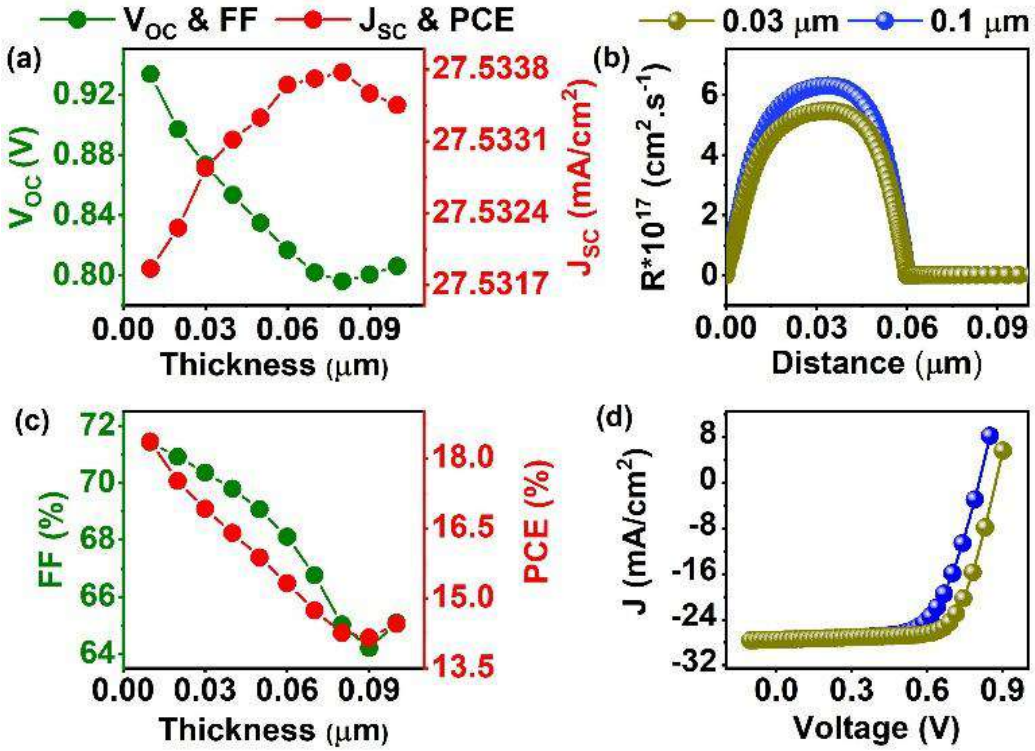

Fig. 29. (a) V_{OC} and J_{SC}, (b) FF and PCE (c) Recombination rate and (d) JV curve for varying ETL thickness

Interestingly, the increase in J_{SC} with thicker ETL may appear counterintuitive, as ETLs like STO do not contribute significantly to light absorption. This slight increase may be attributed to better charge collection efficiency due to improved physical coverage. However, this benefit is outweighed by the higher recombination and resistance at greater thicknesses. The recombination rate plot (**Fig. 29(b)**) shows noticeably higher recombination at 0.1 µm compared to 0.03 µm, confirming that thicker ETLs induce greater losses with difference of ~0.12 × 10^{17} $cm^2.s^{-1}$. Likewise, the J–V curve at 0.03 µm (**Fig. 29(d)**) exhibits superior performance over the 0.1 µm counterpart. Moreover, from a device design standpoint, a thinner ETL compared to the HTL is generally preferred, since electrons typically exhibit higher mobility than holes. A relatively thicker HTL ensures balanced charge extraction and suppresses interfacial recombination [162]. Therefore, selecting an ETL thickness lower than that of the HTL not only follows simulation outcomes but also aligns with well-established architectural guidelines. Excessively thick ETLs (>0.05 µm) are known to introduce resistive

losses and weaken the built-in electric field at the ETL/absorber interface, while ultra-thin ETLs (<0.02 μm) may suffer from non-uniform coverage, causing shunt paths and performance degradation [162,209].. Taking into account the recombination behavior, J–V characteristics, and practical considerations, an optimal STO thickness of 0.03 μm was selected. This value is consistent with the literature, achieves a good balance between minimal recombination, proper coverage, and compatibility with standard device design, ensuring stable and efficient solar cell operation [61].

6.2.3. Optimization of Donor density (N_D) of ETL

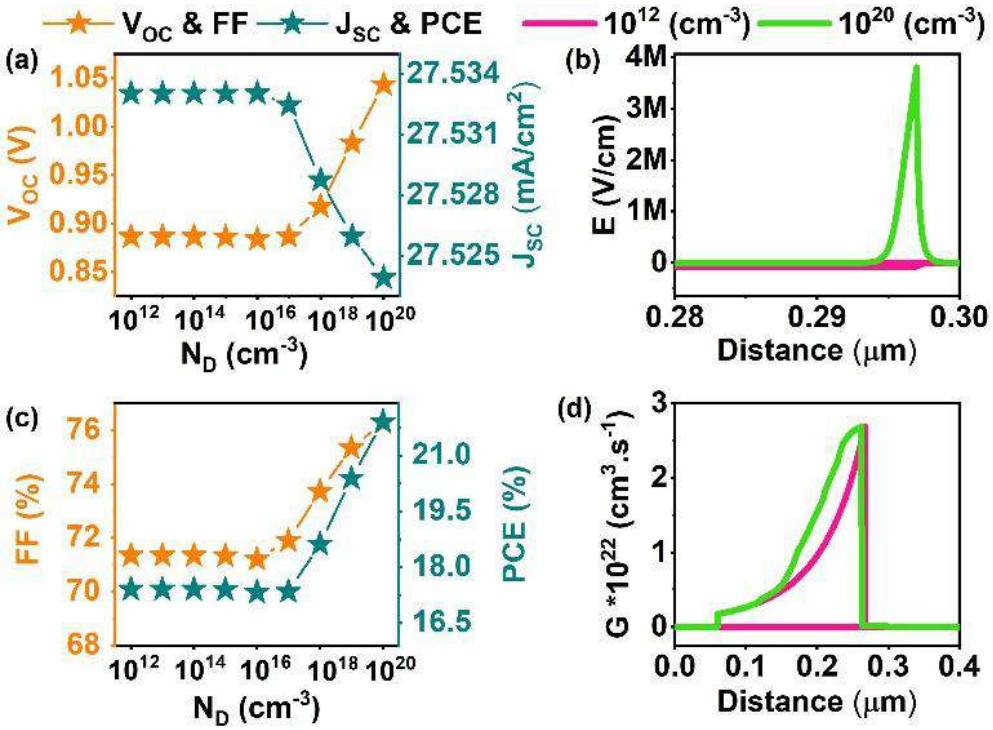

Fig. 30. (a) V_{OC} and J_{SC}, (b) FF and PCE (c) Recombination rate and (d) JV curve for varying ETL N_D.

The N_D in the ETL influences both electrical and optical behavior of the device by modifying the internal electric field and junction properties [210]. In this study, the N_D of STO was varied from 10^{12} to 10^{20} cm^{-3}, and its impact on device parameters was analyzed. Respective changes in V_{OC} and J_{SC} are shown in **Fig. 30(a)**, while FF and PCE are plotted in **Fig. 30(c)**.

As N_D increased, all PV parameters remained constant up to 10^{17} cm^{-3} and beyond, which a consistent rise in V_{OC}, FF, and PCE was observed. However, J_{SC} decreased slightly with higher doping levels. This does not suggest optical losses in the ETL. On the contrary, STO, being a

wide bandgap material, does not absorb light in the visible range. The observed drop in J_{SC} is likely due to electric field redistribution at high doping levels, which could slightly affect charge collection. To clarify the optical behavior, generation rate distribution (**Fig. 30(d)**) was analyzed. As seen in the simulation results, the generation rate is significantly higher on average 3.21×10^{21} $cm^2.s^{-1}$ at 10^{20} cm^{-3} than at lower doping of 10^{12} cm^{-3} with 2.67×10^{21} $cm^2.s^{-1}$ in the absorber region. This confirms that the ETL continues to efficiently transmit incident light to the absorber without absorption, allowing better light penetration and generation in the active region. In other words, although J_{SC} drops slightly, the absorber receives more light and supports improved carrier generation, as confirmed by the generation rate profile. In addition, the electric field distribution (**Fig. 30(b)**) supports this observation. At low N_D, the internal field is weak, which limits carrier separation and contributes to recombination. At the optimized level of 10^{20} cm^{-3}, the field strength across the junction is significantly higher, promoting efficient charge separation and enhancing both V_{OC} and FF [167,211].. Considering all these effects, including field strength and optical transparency, 10^{20} cm^{-3} was chosen as the optimal ETL doping concentration. It ensures minimal optical loss, stronger internal field, improved charge separation, and higher overall efficiency as consistent with trends reported in earlier studies [167,210,211].

6.2.4. Final Device Performance

To better understand the origin of performance enhancement upon optimizing the ETL properties, the JV characteristics, generation rate, and energy band diagrams of the initial and final devices were analyzed, as shown in **Fig. 31(a–d)**. A clear improvement in device performance is evident from the JV plot (**Fig. 31(a)**), where the optimized structure demonstrates higher current density and V_{OC} compared to the initial configuration.

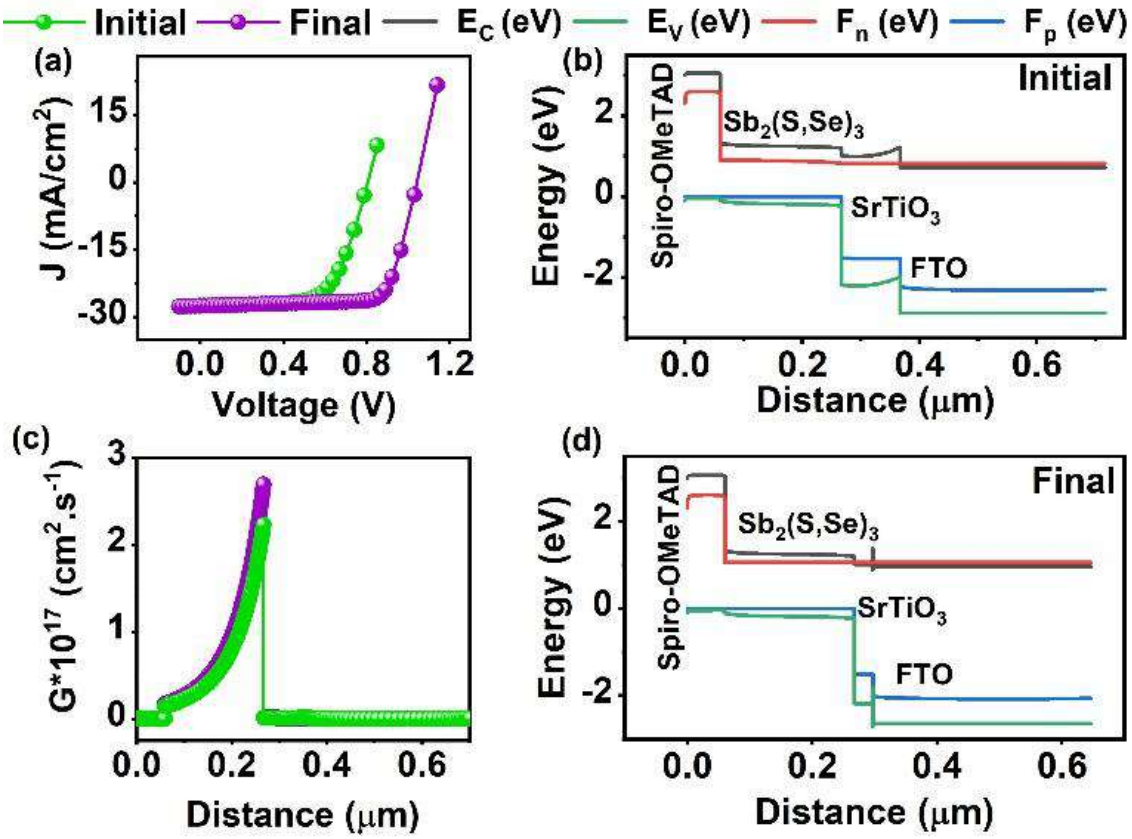

Fig. 31. Comparison of (a) JV curve, (c) Generation rate, (b,d) Energy band alignment for initial and final device

This enhancement signifies more efficient charge separation, reduced recombination, and better carrier extraction in the optimized device. The generation rate distribution (**Fig. 31(c)**) further supports this observation. A sharper and more intense peak is observed in the final device with maximum carrier generation of 2.69×10^{22} cm^2.s^{-1} particularly in the absorber region, indicating more effective photogeneration. Despite a slight drop in J_{SC} with increasing ETL doping, STO remains optically transparent due to its wide bandgap and does not interfere with light absorption. Instead, it enables efficient light transmission to the absorber, which is confirmed by the increased generation rate [209]. This clearly demonstrates that the optimization promotes not only charge transport but also enhances photon harvesting in the active layer, contributing to the improved efficiency. The energy band diagrams of the initial and optimized devices (**Fig. 31(b) and (d)**) provide further insights into the underlying mechanism. In the initial device, the band alignment appears relatively flat, with minimal electric field across the layers. Such weak field conditions limit carrier separation and can increase recombination losses at interfaces. After optimization, the bands exhibit stronger bending across the STO and $Sb_2(S,Se)_3$ junction, indicating the presence of a steeper internal electric field that facilitates

rapid carrier drift and reduces recombination. This improved alignment results in a more favorable conduction band offset (CBO) at the ETL/absorber interface. The formation of a small cliff-type CBO is considered beneficial, as it avoids creating energy barriers for electron transport, enabling smooth extraction toward the front contact [212]. Simultaneously, the valence band offset (VBO) presents a substantial spike, effectively blocking holes from diffusing into the ETL. This configuration helps suppress interfacial recombination, which can otherwise compromise device performance. The distinct positioning of the quasi-Fermi levels in the final band diagram (**Fig. 31(d)**) further confirms enhanced charge separation and collection. These improvements in field strength, band energetics, and optical behavior all contribute synergistically to the enhanced PV performance after optimization with reduced V_{OC} loss of ~0.39V. Overall, V_{OC} of 1.04 eV, J_{SC} of 27.52 mA.cm2, FF of 76.29% and PCE of 21.91% were achieved for the final device and are compared with other reported emerging solar cells (**Table 14**). The simulation outcomes are consistent with previous findings on interface energetics, where appropriate band offsets especially small electron cliffs and significant hole barriers are essential for minimizing recombination while supporting efficient carrier flow [209].

Table 14. Comparison of our results with scaps 1d reports of Cd- free $Sb_2(S,Se)_3$ solar cells and other emerging lead free PSCs.

Structure	**V_{OC}**	**J_{SC}**	**FF**	**PCE**	**Ref**
ITO/ZnO/$MAGeI_3$/Spiro-OmeTAD/Au	1.74	64.52	16.27	18.3	[43]
FTO/TiO2/$CH_3NH_3SnBr_3$/NiO	0.80	84.89	31.88	21.66	[44]
ZnO/$MASnI_3$/Spiro-OmeTAD/Au	0.876	76.19	33.19	22.16	[45]
glass + SnO_2/ $FASnI_3$ /rGO /Au	1.12	85.91	26.58	25.65	[46]
FTO/WS_2/$CsSnI_3$/rGO/Pt	1.15	88.48	30.47	31.00	[47]
FTO/WS_2/$CsBaCl_3$/rGO/Pt	1.47	91.10	24.49	32.83	[48]
FTO/WS_2/$RbTiBr_3$/rGO/Pt	1.48	91.19	24.27	32.77	[48]
FTO/SnO_2/$SrZrS_3$/Cu- MOF/Ni	1.17	29.54	88.40	30.60	[49]
FTO/TiO_2/$BaZrS_3$/ $CuFeO_2$/Au	1.51	21.94	85.54	28.35	[50]

Structure	V_{OC}	J_{SC}	FF	PCE	Ref
Glass/ITO/ZnO/Cs_2BiAgI_6/CBTS/Au	1.08	32.06	84.5	29.06	[51]
FTO/ZnO/$Cs_2AgBi_{0.75}Sb_{0.25}Br_6$/Spiro-OMeTAD/Au	1.6	16.04	78.34	18.18	[52]
FTO/ZnO/$Sb_2(S,Se)_3$/Cu_2O/Au	0.95	27.70	68.00	18.00	[53]
FTO/ZnSe/$Sb_2(S,Se)_3$/$CuSbS_2$/Au	0.93	28.64	74.54	20.01	[54]
FTO/STO/$Sb_2(S,Se)_3$/Spiro-OMeTAD/Au	**1.04**	**27.52**	**76.29**	**21.91**	**This work**

Practically, in STO, recombination arises from oxygen (V_O) and titanium (V_{Ti}) vacancies forming deep in-gap states, oxygen (O_i) and titanium (Ti_i) interstitials introducing recombination centers, and antisite defects (Ti_{Sr}, Sr_{Ti}) distorting the lattice, while dislocations and grain boundaries act as nonradiative pathways. These defects limit carrier lifetime and ETL performance but can be mitigated by oxygen-rich annealing, precise stoichiometry, high-quality thin-film growth, and interface passivation [213,214].. At the STO/$Sb_2(S,Se)_3$ junction, further issues include unfavorable band offsets, interface defect densities, and damage during high-energy/high-temperature processing, and lattice-orientation effects [70]. As demonstrated for Cd-free ETLs (TiO_2, Zn(O,S), etc.), band-offset engineering, ultrathin passivation layers (ZnS, $TiCl_4$, halides), low-temperature ALD buffers, and optimized annealing are effective strategies for STO-based devices[47,215].. In terms of commercialization, STO offers advantages over CdS ETL. While CdS is simple and low-cost to synthesize, its reliance on toxic chemicals requires strict waste management, raising operational expenses. STO, on the other hand, can be deposited by eco-friendly solution methods such as polymer-assisted deposition, potentially lowering processing costs. Its high thermal stability and favorable electronic properties further enhance performance and durability, reducing degradation and long-term maintenance costs [216].

6.2.5. Effect of Varying Operating Conditions

The performance stability of a solar cell under varying environmental conditions is crucial for its practical application. Therefore, the temperature and illumination dependencies of the optimized device were investigated. The effect of temperature on the key parameters such as V_{OC}, J_{SC}, FF, and PCE is illustrated in **Fig. 32(a) and (b)**. A clear decline in V_{OC} is observed as the temperature increases from 300 to 450 K. This behavior aligns with the known trend that

elevated temperatures enhance intrinsic carrier concentration and increase Shockley-Read-Hall recombination, which in turn reduces the quasi-Fermi level splitting and hence the V_{OC} [195]. The decrease in FF and PCE with rising temperature is also evident, likely due to increased series resistance and reduced carrier mobility. Additionally, thermal energy can lead to increased phonon scattering, reducing diffusion lengths and making carrier collection less efficient at elevated temperatures. Interestingly, J_{SC} shows a very slight increasing trend with temperature. This minor rise can be attributed to the marginal narrowing of the absorber's bandgap at higher temperatures, which enables absorption of longer-wavelength photons and slightly enhances the photogeneration of carriers [195]. However, this increase is not sufficient to offset the performance losses induced by recombination and resistive effects. To assess the device response under different illumination conditions, simulations were carried out from 100 to 1000 W/m², and the results are displayed in **Fig. 32(c) and (d)**. The J_{SC} increases linearly with light intensity, indicating effective utilization of incoming photons and proportional generation of photocarriers. This linearity supports the expected correlation between incident photon flux and charge carrier generation [204].

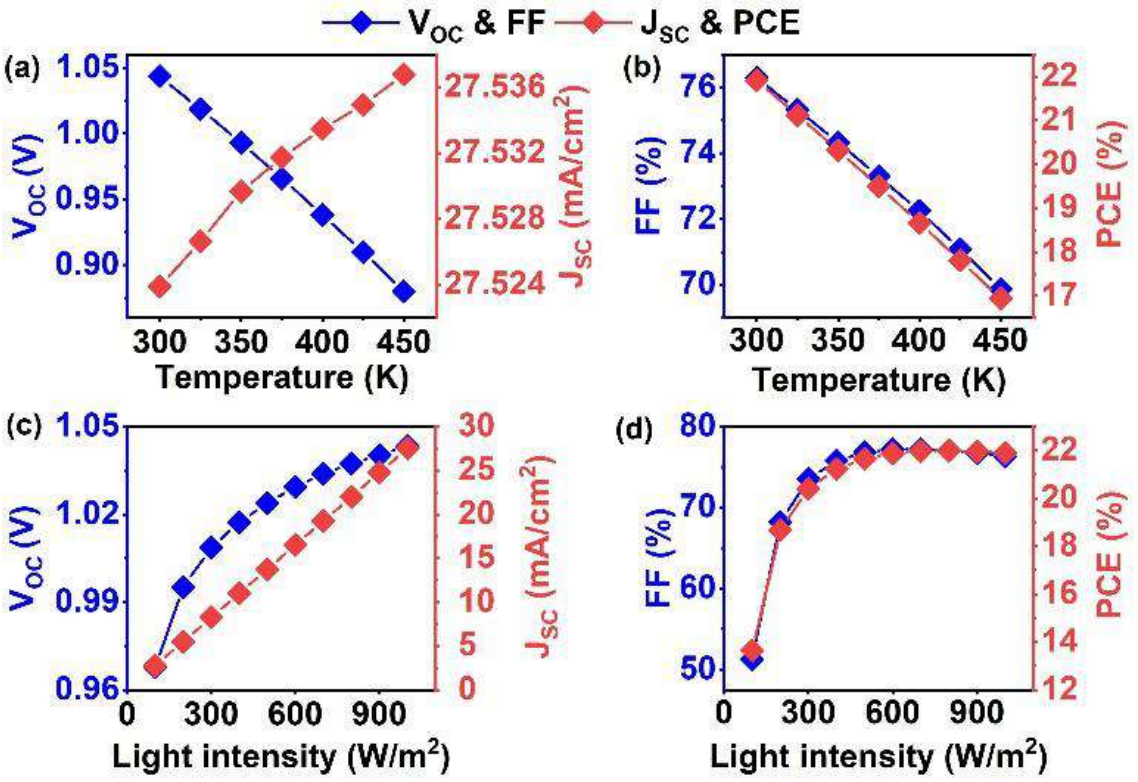

Fig. 32. Change in (a,c) V_{OC} and J_{SC}, (b,d) FF and PCE with temperature and light intensities.

Simultaneously, V_{OC} increases logarithmically with illumination, which is a well-established response governed by the increased splitting of quasi-Fermi levels under higher carrier

densities. In the case of FF, a sharp rise is noticed initially with light intensity, followed by a tendency to saturate beyond 800 W/m^2, as seen in **Fig. 32(d)**. This plateau suggests that at high illumination, the benefits from enhanced carrier injection are offset by saturation of carrier mobility or increased recombination implying that fixed resistive losses begin to dominate. A similar trend is reflected in the PCE, which follows FF closely, highlighting that its dependence lies not only on light-induced generation but also on the ability of the device to transport and extract the generated carriers effectively [44,204]. Overall, while the cell maintains reasonable operational integrity, elevated temperature and high illumination reduce efficiency. To enhance thermal and operational stability, interface passivation with TiO_2 or Al_2O_3 can suppress interfacial recombination, Cl or Na doping in the absorber or Zn-doping in STO can improve carrier mobility and reduce resistive losses, and thermally conductive substrates such as AlN or graphene-based layers can limit temperature rise and maintain PCE under harsh conditions [217,218].

6.3. Exploring Interfacial Charge Dynamics in $Sb_2(S, Se)_3$ Solar Cells with Graphitic Carbon Nitride: Experimental Parameters Applied in SCAPS-1D Modeling

6.3.1. Experimental result

The XRD profile of the synthesized GCN (**Fig. 33(a)**) showed a distinct diffraction peak near $2\theta = 27.4^{o}$, which corresponds to the (002) crystallographic plane. This peak is characteristic of the interlayer stacking of aromatic systems in the GCN structure, indicating a layered arrangement similar to that found in graphite. The appearance and intensity of the (002) peak confirm the successful thermal polymerization and formation of a two-dimensional layered GCN framework. Such structural features are crucial for charge transport performance, as they facilitate π–π interactions between adjacent layers. This observation is consistent with previous reports in which the (002) reflection is regarded as a signature of GCN's crystalline stacking, especially in materials synthesized via urea or melamine pyrolysis methods under ambient conditions [219,220].. The optical response of the synthesized GCN was investigated using UV–Vis spectrum data. As shown in **Fig. 33(b)**, the material exhibits strong absorption in the UV–visible region with an absorption edge observed around 450 nm, which is typical for GCN synthesized via thermal condensation of urea. To estimate the bandgap energy, a Tauc plot was constructed. The Tauc plot (**Fig. 33(c)**) revealed an indirect bandgap of approximately 2.8 eV, consistent with previously reported values for pristine GCN [221]. To further understand the optical behavior, the complex dielectric function was derived from the UV–Vis data. The real part indicates the material's polarizability and energy storage capability, while the imaginary

part relates to energy dissipation during photon–electron interactions. These are calculated using the following standard equations [222]:

$$\varepsilon_r' = n^2 - k^2 \quad (20)$$

$$\varepsilon_r'' = 2nk \quad (21)$$

Where n is the refractive index and k is the extinction coefficient estimated [223],

$$n = \frac{1}{T} + \sqrt{\frac{1}{T^2}} - 1 \quad (22)$$

$$k = \frac{\alpha\lambda}{4\pi} \quad (23)$$

Where α is the absorption coefficient obtained from the absorbance spectrum

λ is wavelength and T is transmittance calculated using Absorbance (A) as follows [224],

$$T = [10^{-A}] \quad (24)$$

These values are obtained using UV-Vis data from **Fig. 33(b)**

As depicted in **Fig. 33(d)**, the imaginary part of the dielectric permittivity showed a prominent peak around the bandgap region (~2.8 eV), with a value of approximately 7.01. This peak indicates strong interband transitions and significant optical loss due to absorption processes. The real part, plotted alongside, reflects the material's polarizable nature across the examined spectral range. The obtained value of ε_r'' = 7.01 at the absorption edge is consistent with literature reports, where similar magnitudes have been observed for polymeric GCN [225]. The EDS spectrum in **Fig.27(e)** confirms the elemental composition of the synthesized GCN. The prominent peaks observed for carbon (C) and nitrogen (N) correspond to the primary constituents of graphitic carbon nitride, affirming the successful formation of the material. The typical atomic percentages show a C:N ratio close to the theoretical value (~0.75) expected for polymeric GCN structures based on heptazine or tri-s-triazine units. The absence of other significant impurity peaks (except for a minor oxygen signal, possibly due to surface adsorption or air exposure) further indicates the purity of the synthesized sample. This result supports the formation of a stoichiometrically stable C–N framework, consistent with literature reports on urea-derived GCN materials [219,226].

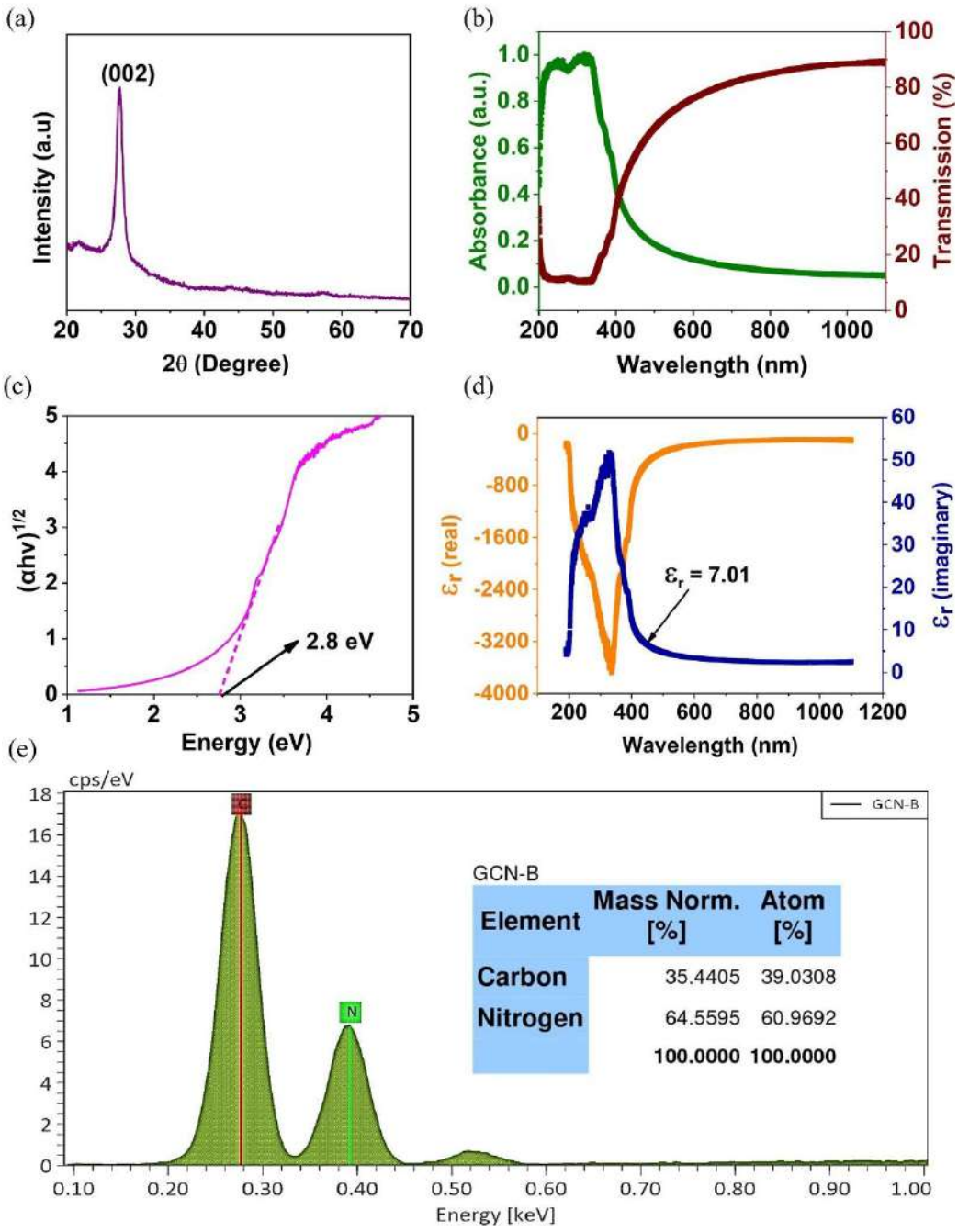

Fig. 33. (a) XRD, (b) UV-Vis absorbance and Transmission (T%) spectrum, (c) Tauc plot, (d) Real and imaginary part of dielectric permittivity, and **e** EDS spectrum with elemental composition in the inset

Further, the surface chemistry was analyzed using XPS analysis. The high-resolution XPS analysis of the synthesized sample provides valuable insight into its chemical structure. In the C 1s spectrum (**Fig. 34(a)**), two prominent peaks are observed at binding energies of approximately 282.6 eV and 286 eV. The lower energy peak is associated with C=C bonds, indicating the presence of graphitic or sp^2-hybridized carbon. The peak at 286 eV corresponds

to N–C=N bonds, which are characteristic of the heptazine or triazine units in graphitic carbon nitride. Similarly, the N 1s spectrum (**Fig. 34(b)**) reveals three distinct peaks centered at 396.2 eV, 397.2 eV, and 398.3 eV. The first peak is attributed to the C=N–C configuration, suggesting nitrogen is bonded in a sp^2-hybridized planar structure. The second peak at 397.2 eV corresponds to nitrogen coordinated with three carbon atoms ($N–[C]_3$), which is typical of aromatic nitrogen in the heptazine ring system. The third peak at 398.3 eV indicates the presence of terminal or edge nitrogen groups such as –NH or $–NH_2$. Together, these results confirm the formation of a polymeric carbon nitride structure with both graphitic carbon and nitrogen-rich bonding environments, consistent with the expected features of GCN synthesized through thermal polymerization [226]. **Fig. 34(c)** illustrates the Valence band spectrum of the synthesized GCN. The valence band edge appears at approximately 1.6 eV, indicating the energy difference between the Fermi level and the valence band maximum. This value complements the bandgap (~2.8 eV from UV-Vis), suggesting that the conduction band minimum is near 1.2 eV, supporting efficient electron transport [227]. The wide-scan (survey) spectrum in **Fig. 34(d)** shows clear peaks for C 1s and N 1s, confirming the purity of GCN without any significant impurities. No signals for oxygen, metals, or other elements are detected, supporting high sample quality. To estimate the electron affinity (EA) of the synthesized GCN, the following equation was used [64,228]:

$$\chi = \Phi - (E_g - VBM) \tag{25}$$

Where Φ is the work function (taken as 4.8 eV from literature [229]), E_g is bandgap energy (2.8 eV from UV–Vis Tauc plot) and VBM is the valence band maximum (1.6 eV from XPS). The resulting EA of 3.6 eV aligns well with values reported in previous studies for urea-derived GCN [230]. The relatively high EA indicates a deep conduction band minimum, which is beneficial for electron transport and charge separation in PV applications. Finally, the surface morphology of GCN was analyzed using FESEM. The FESEM images presented in **Fig. 34(e) and (f)** provide a comprehensive view of the surface morphology of the synthesized GCN. At low magnification (**Fig. 34(e)**), the material exhibits a rough, sponge-like texture with large, interconnected clusters composed of crumpled sheet-like structures. These features suggest a layered framework with significant surface roughness and porosity across the micrometer scale. This is further clarified in the high-magnification image (**Fig. 34(f)**), where the individual nanosheets become more distinguishable. The surface reveals tightly packed, wrinkled layers and folds that are characteristic of the graphitic structure of GCN formed through thermal polycondensation of nitrogen-rich precursors like urea. This structure results from the release

of gases like ammonia and cyanuric acid during pyrolysis, creating voids and wrinkles. These nanoscale wrinkles and curvatures not only support the layered stacking observed at lower magnification but also point to a high density of edge sites and voids. Such a hierarchical structure, porous and loosely packed at the microscale, yet compact and wrinkled at the nanoscale, is advantageous for optoelectronic applications, as it enhances surface area, facilitates charge transfer, and improves light scattering [231].

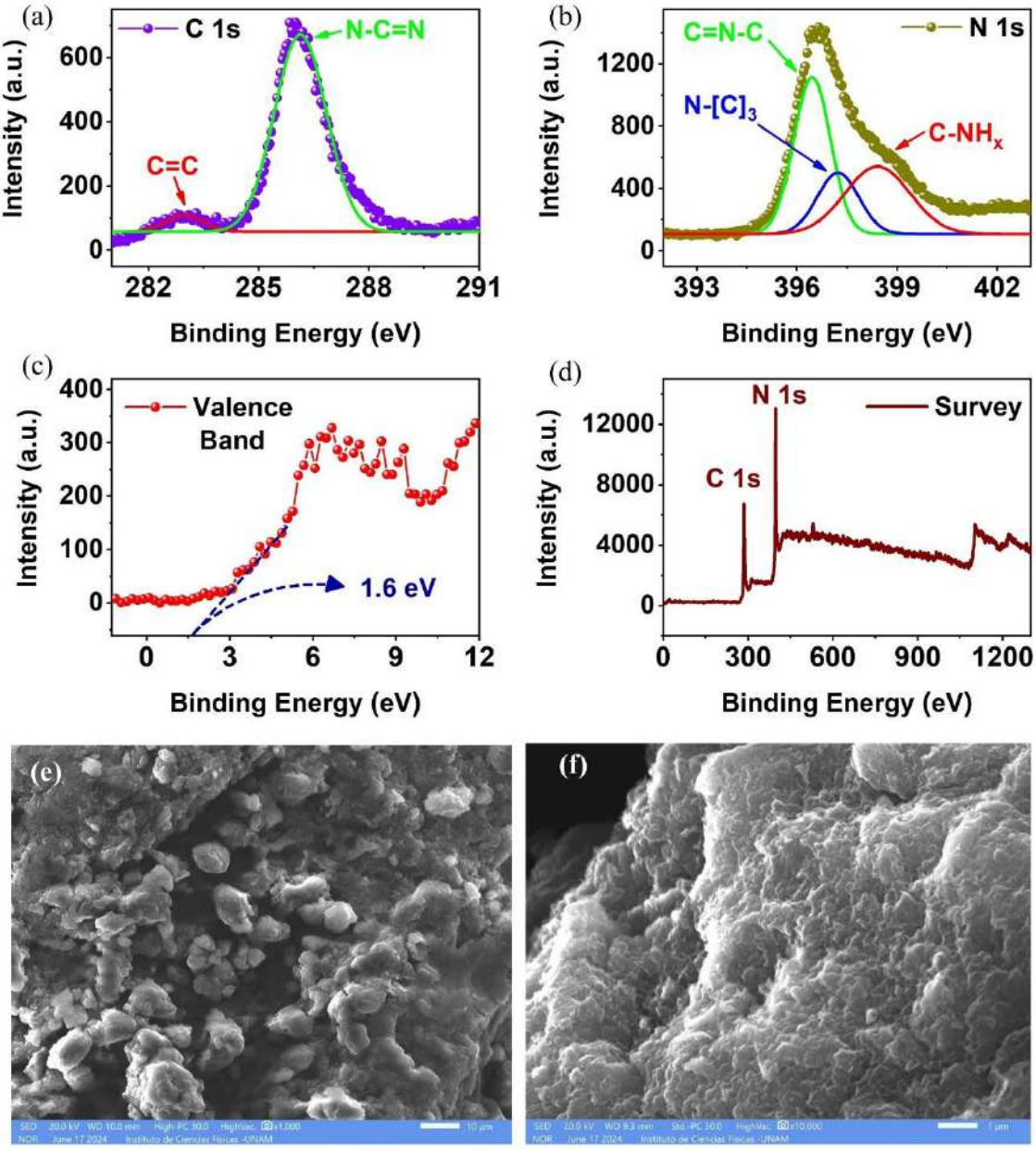

Fig. 34. High resolution XPS spectrum of (a) C1s, (b) N1s, (c) Valence band, (d) wide scan-survey, (e,f) low and high magnification FESEM images of GCN

6.3.2. Baseline Device Validation and Performance

The baseline FTO/CdS/$Sb_2(S, Se)_3$/Spiro-OMeTAD/Au solar cell was initially simulated to reproduce the experimentally reported device behavior, as presented in **Fig. 35(a)**. The simulated J–V curve shows a close agreement with the experimental counterpart, confirming that the selected material and interface parameters accurately describe the physical device. The resulting PV parameters, such as V_{OC}, J_{SC}, FF, and PCE of the experimental and simulated devices are summarized in **Table 15**, demonstrating that the baseline model successfully reproduces the experimental device efficiency, confirming the reliability of the model. The QE spectra (**Fig. 35(b)**) further substantiate this model fidelity. The baseline device exhibits a strong spectral response, consistent with the optical absorption range of $Sb_2(S, Se)_3$. However, a slight dip observed in the mid-visible region indicates localized recombination losses, likely arising from interfacial trap states near the CdS/$Sb_2(S, Se)_3$ junction [232,233]. For this reason GCN is introduced between CdS and $Sb_2(S,Se)_3$. Upon the incorporation of the GCN both the J–V and QE responses (**Fig 35 (a) and (b)**) exhibit pronounced enhancement. The modified device demonstrates an improvement in PCE from 10.75% to 18.3%, accompanied by an increase in PV parameters, as summarized in **Table 15**. The enhanced performance stems primarily from the improved charge extraction and reduced recombination at the CdS/$Sb_2(S,Se)_3$ interface facilitated by the GCN interlayer. The QE spectrum of the GCN-modified device displays a more uniform and broadened response across the entire visible range, with an extended tail toward longer wavelengths, suggesting enhanced minority-carrier collection from deeper regions of the absorber. The smoother QE profile also indicates the suppression of abrupt recombination losses and a shift toward a more ideal QE distribution. This improvement is attributed to intermediate energy levels and passivation effect of GCN, which mitigate interface trap density and enable efficient photogenerated carrier transport[234,235].. In particular, the reduction in mid-visible suppression confirms the decreased SRH recombination at the CdS/$Sb_2(S,Se)_3$ interface, while the higher long-wavelength response signifies improved carrier lifetime and diffusion length within the absorber. Overall, the incorporation of GCN as an interfacial modifier effectively tunes the charge dynamics by improving band alignment and reducing recombination pathways, resulting in a more efficient charge extraction and a notable improvement in overall device performance [236,237].

Table 15. Device performance for the initial devices

Device structure	V_{OC} (V)	J_{SC} (mA/cm^2)	FF (%)	PCE (%)
FTO/CdS/$Sb_2(S,Se)_3$/Spiro-OMeTAD/Au (**Experimental**)	0.63	25.27	67.35	10.75
FTO/CdS/$Sb_2(S,Se)_3$/Spiro-OMeTAD/Au (**Simulated**)	0.65	25.10	65.53	10.75
FTO/CdS/GCN/$Sb_2(S,Se)_3$/Spiro-OMeTAD/Au (**With GCN**)	0.97	25.4	73.9	18.29

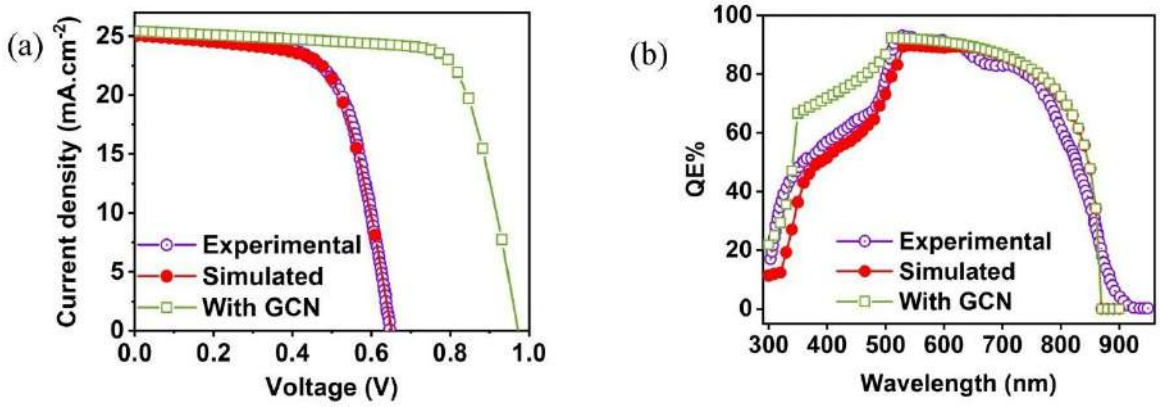

Fig. 35. (a) JV, (b) QE plot for the experimental and simulated and GCN incorporated baseline devices.

6.3.3. Electric Field Distribution and Nyquist Plot Analysis

The internal electric field distribution obtained from SCAPS-1D, illustrated in **Fig. 36(a)**, provides key insight into the role of GCN in modulating interfacial electrostatics. In the baseline device, the electric field is highly localized near the CdS/$Sb_2(S, Se)_3$ junction, showing an abrupt potential drop that signifies strong band bending and carrier accumulation. Such field non-uniformity is often associated with barrier formation, trigger interface recombination. In contrast, the GCN-modified structure exhibits a more homogeneous and slightly intensified electric field across the depletion region, promoting efficient charge separation. The smoother potential gradient across the GCN layer originates from its moderate dielectric constant and interfacial dipole, which reduces the abrupt discontinuity between CdS and $Sb_2(S, Se)_3$ [238,239].. The improved field assists electrons in drifting swiftly toward the ETL while simultaneously enhancing the driving force for hole extraction toward the HTL, thereby improving carrier mobility balance and fill factor[232,240].. Complementary evidence is provided by the Nyquist plots (**Fig. 36(b)**), which reveal a significant decrease in charge transfer resistance (R_{CT}) upon GCN incorporation. The semicircular arc diameter, associated

with the interfacial recombination and charge transport resistance, is markedly smaller for the GCN device, confirming its superior charge extraction capability. The extracted R_{CT} decreases from 625.4 Ω.cm^2 to 401.3 Ω.cm^2, while the R_S also reduces from 3.7 Ω.cm^2 to 3.5 Ω.cm^2. This lowered impedance indicates that GCN not only improves electronic coupling at the $Sb_2(S, Se)_3$/CdS interface but also mitigates trap-assisted recombination losses, consistent with its role as an efficient charge transfer mediator [196,241,242].

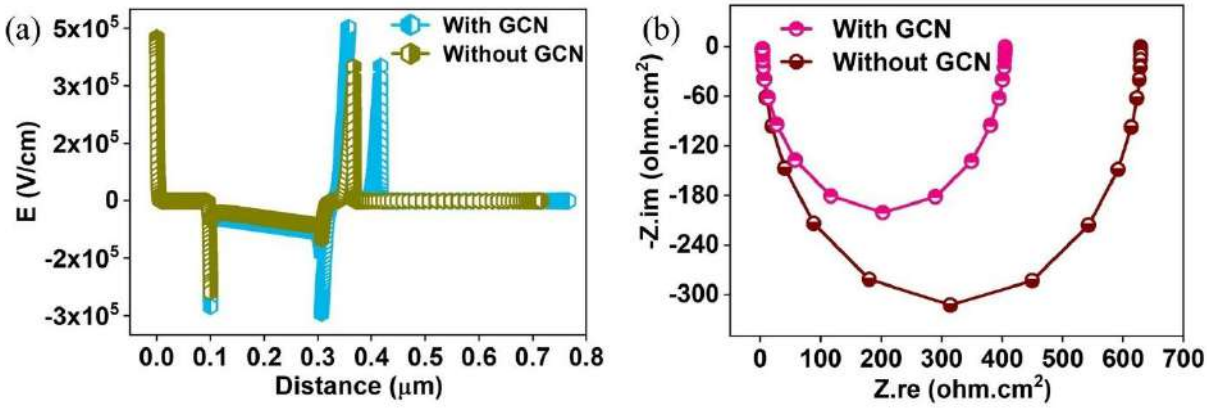

Fig. 36. (a) Electric field distribution (b) Nyquist plot of initial devices with and without GCN.

6.3.4. Generation and Recombination Mechanism

The simulated recombination and generation rate profiles for both devices are plotted in **Fig. 37(a) and (b)**. In the baseline device, the maximum recombination occurs near the CdS/$Sb_2(S, Se)_3$interface, indicating the presence of a high density of defect states that trap photogenerated carriers[243]. The average recombination rate reaches approximately 1.5x10^{19} cm^{-3}. s^{-1}, confirming severe non-radiative losses at this interface. Upon introducing GCN, this recombination rate is significantly suppressed, reducing to 3.4x10^{18} cm^{-3}. s^{-1}. The overall photogeneration rate concurrently increases by the factor of 5x10^{20} cm^{-3}. s^{-1}, highlighting that GCN not only passivates interfacial defects but also enhances optical absorption by improving internal light scattering and photon recycling at the interface. GCN introduces a passivating layer rich in lone-pair nitrogen sites that can interact with undercoordinated metal atoms on the $Sb_2(S, Se)_3$ surface, thereby neutralizing defect states responsible for SRH recombination. The suppression of SRH processes leads to a longer carrier lifetime and a larger diffusion length within the absorber, demonstrating the overall improvement in carrier dynamics induced by GCN [244,245].

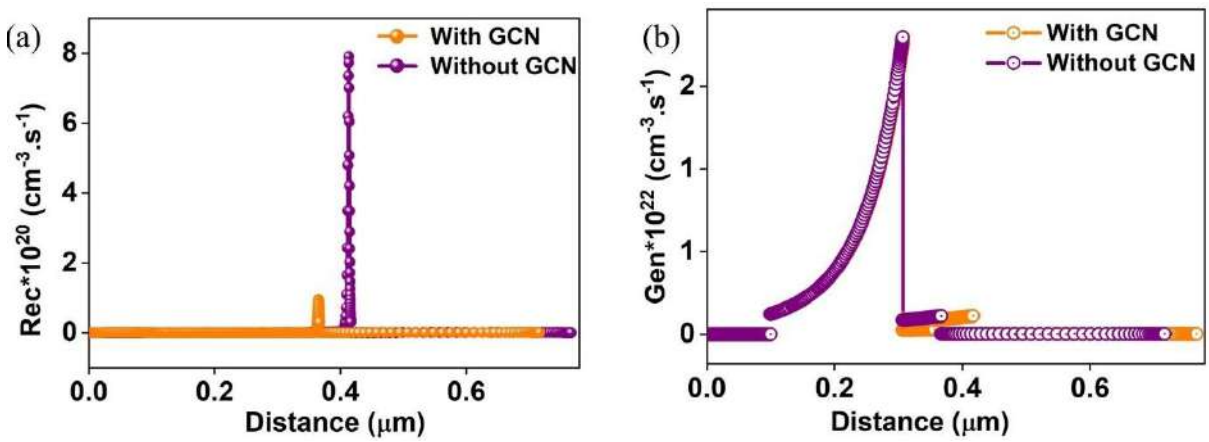

Fig. 37. (a) Recombination and (b) Generation rate of initial devices with and without GCN.

6.3.5. Energy Band Alignment

The energy band diagrams illustrated in **Fig. 38(a)** and **(b)** elucidate the crucial role of GCN in governing interfacial charge dynamics and carrier selectivity. In the baseline configuration (**Fig. 38(a)**), the CdS/$Sb_2(S, Se)_3$ interface exhibits a misaligned energy junction, where the conduction band edge of CdS is positioned slightly higher relative to the absorber, forming a weak barrier that obstructs electron extraction. This discontinuity creates an unfavorable potential landscape that causes electron accumulation at the interface and increases the probability of interfacial recombination [233]. Simultaneously, the valence band alignment at the $Sb_2(S, Se)_3$/Spiro-OMeTAD interface facilitates partial backflow of holes into the absorber, further aggravating recombination losses and limiting both V_{OC} and FF [36]. The resulting band architecture in the baseline device thus lacks sufficient selectivity, allowing carriers to leak across interfaces and undergo recombination before extraction. Upon the introduction of the GCN interlayer (**Fig. 38(b)**), the interfacial energies are profoundly altered, producing a cascade-like band configuration between $Sb_2(S, Se)_3$ and CdS. The GCN layer provides an intermediate conduction band position that smoothens the transition for electrons moving from the absorber to the ETL, thereby eliminating potential energy spikes that hinder carrier transport [246,247].. This stepwise alignment enables electrons to transfer seamlessly through the GCN bridge while simultaneously preventing their reflection back into the absorber. In contrast, the valence band of GCN lies sufficiently below that of $Sb_2(S, Se)_3$, establishing an energetic barrier that effectively blocks holes from diffusing toward the ETL. This selective transport mechanism ensures that electrons are efficiently extracted toward the CdS layer, whereas holes are confined within the absorber and directed toward the HTL, thereby minimizing charge accumulation at both interfaces [248]. Additionally, the presence of GCN modulates the interfacial dipole moment and surface potential, resulting in improved band

bending within the absorber near the junction region. The enhanced downward bending of the conduction band strengthens the internal electric field, facilitating faster electron drift and promoting efficient charge separation under illumination. This improved energetic landscape reduces interfacial trap-assisted recombination and maintains a wider quasi-Fermi level separation, which translates directly to the observed increase in V_{OC} and FF [248,249].. Overall, the GCN interlayer transforms the non-selective and discontinuous band structure of the baseline device into a well-aligned graded configuration that promotes unidirectional carrier flow, suppresses recombination losses, and thereby enables superior PV performance.

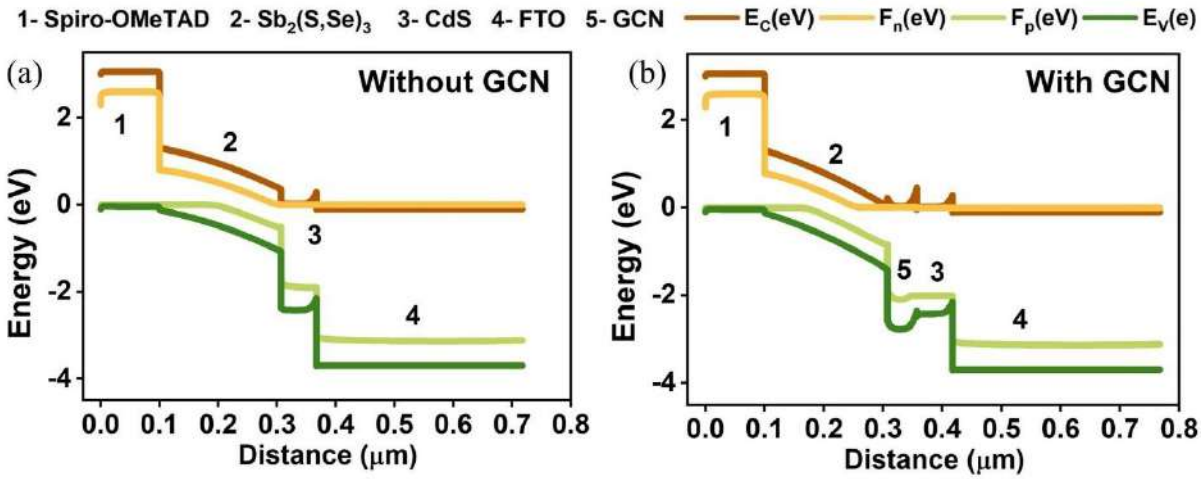

Fig. 38. Energy band alignment for Base devices (a) with and (b) without GCN

Following baseline and GCN incorporation validation, a comprehensive optimization of thickness and carrier densities of each layer was carried out to maximize device performance. For instance, he effects of varying the thickness from 0.05 to 0.15 μm for the HTL, from 0.1 to 1 μm for the $Sb_2(S, Se)_3$ absorber, from 0.01 to 0.1 μm for the GCN interfacial layer, and from 0.05 to 0.1 μm for the ETL, respectively. The acceptor density (N_A) of the HTL (10^{12} to 10^{20} cm^{-3}) and the $Sb_2(S, Se)_3$ absorber (10^{12} to 10^{18} cm^{-3}), and the donor density (N_D) of the GCN (10^{12} to 10^{20} cm^{-3}) and the ETL (10^{12} to 10^{20} cm^{-3}) were varied. Additionally, the effect of interface defect densities at the HTL/$Sb_2(S, Se)_3$, ETL/$Sb_2(S, Se)_3$, $Sb_2(S, Se)_3$/GCN, and GCN/ETL interfaces was examined in the range of 10^{12} to 10^{20} cm^{-2}. The variation in PV parameters on optimization of devices with and without GCN incorporation is compared and analyzed through various SCAPS-1D analytical outputs, including generation–recombination analysis, electric field distribution, energy band structure assessment, J–V curves, QE responses, C–V, Mott-Schottky, and C–F measurements. The study also explored the effects of operating temperature and light intensity on device performance, providing insights for

designing more efficient and stable $Sb_2(S, Se)_3$-based solar cells with GCN interfacial engineering. These analyses helped in understanding the role of GCN in suppressing interface recombination and improving carrier extraction efficiency.

6.3.6. Optimization of Each Layer Parameters with and without GCN

6.3.6.1. Optimization of HTL Thickness and N_A

The HTL functions as a crucial layer between the absorber and back contact, facilitating efficient hole extraction while blocking electron backflow [144]. To assess the influence of HTL thickness on device performance, simulations were conducted by varying the thickness from 0.05 to 0.15 μm while keeping all other parameters constant. The variations in the PV parameters are presented in **Fig. 39(a-d)** for devices with and without a GCN interfacial layer. For the device without GCN, it was observed that variations in HTL thickness resulted in negligible changes across all PV parameters. Specifically, V_{OC} and J_{SC} remained stable at ~0.65 V and 25.10 mA/cm^2, respectively, while FF gradually decreased fro[61]m 65.63% to 65.30%, leading to a minor decline in PCE from 10.77% to 10.71%. This trend indicates that beyond a certain thickness, the additional transport path may introduce slight series resistance, marginally affecting charge transport and collection efficiency [57,145,146]. A similar trend was observed for the device incorporating GCN, where the PV parameters remained unchanged with increasing HTL thickness. V_{OC} and J_{SC} consistently retained values around 0.97 V and 25.43 mA/cm^2, respectively, while FF decreased slightly from 73.98% to 73.82%, resulting in a minimal reduction in PCE from 18.32% to 18.28%. These results imply that HTL thickness has a limited impact on device performance, as long as it maintains sufficient coverage to support hole transport and prevent recombination at the back contact. Considering both the performance output and material cost, a thickness of 0.06 μm was selected as optimal for the HTL. This choice ensures minimized resistive losses while avoiding unnecessary material usage [147,148].

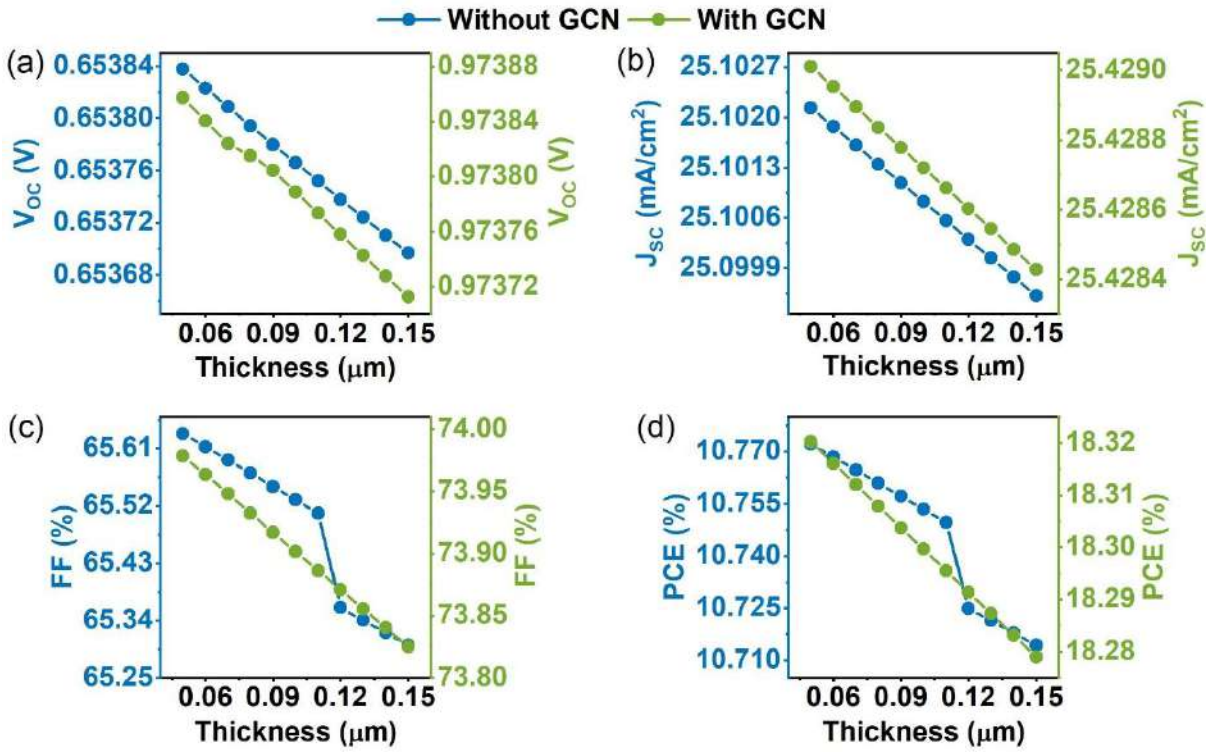

Fig. 39. Variation in (a) V_{OC}, (b) J_{SC}, (c) FF, (d) PCE for different HTL thicknesses for the devices with and without GCN.

The influence of the HTL N_A on the PV performance of $Sb_2(S, Se)_3$ solar cells was systematically examined over the range of 10^{12} to 10^{20} cm^{-3} for both device configurations (with and without the GCN interfacial layer) as shown in **Fig. 40 (a–d)**. In the reference device without GCN, all the PV parameters remained almost constant as N_A increased from 10^{12} to 10^{15} cm^{-3}. At higher concentrations (10^{16} cm^{-3}), a significant enhancement in the PV parameters, leading to a PCE improvement from 6.99% to a maximum PCE of 10.79% at $N_A=10^{20}$ $cm^{-3,}$ was observed due to improved hole transport and reduced interfacial recombination. In the GCN-based device, a similar increasing trend was observed with increasing N_A, but with significantly higher performance at every doping level compared to the non-GCN structure. Even at a low doping of 10^{12} to 10^{15} cm^{-3}, the device with GCN exhibited a remarkable PCE of 13.81%, indicating the strong impact of GCN on enhancing charge extraction and interface quality. With increasing N_A, performance continued to improve, reaching a maximum PCE of 18.35% at 10^{20} cm^{-3}, with V_{OC}=0.97 V, J_{SC}=25.44 mA/cm^2, and FF = 74.04%. The inferior performance at lower N_A for both configurations is primarily attributed to weak electric fields within the absorber, which hinder the effective separation and collection of photogenerated carriers. Low N_A in the HTL leads to insufficient band bending at the absorber/HTL interface, creating potential barriers that inhibit hole extraction and increase

recombination losses [154,155]. As N_A increases, the built-in potential strengthens, resulting in enhanced electric field strength across the junction. This leads to improved carrier drift, more efficient separation of electron–hole pairs, and reduced interfacial recombination, ultimately boosting device performance [166][167].[167]. Hence, 10^{20} cm^{-3} was selected as the optimal N_A value for both devices.

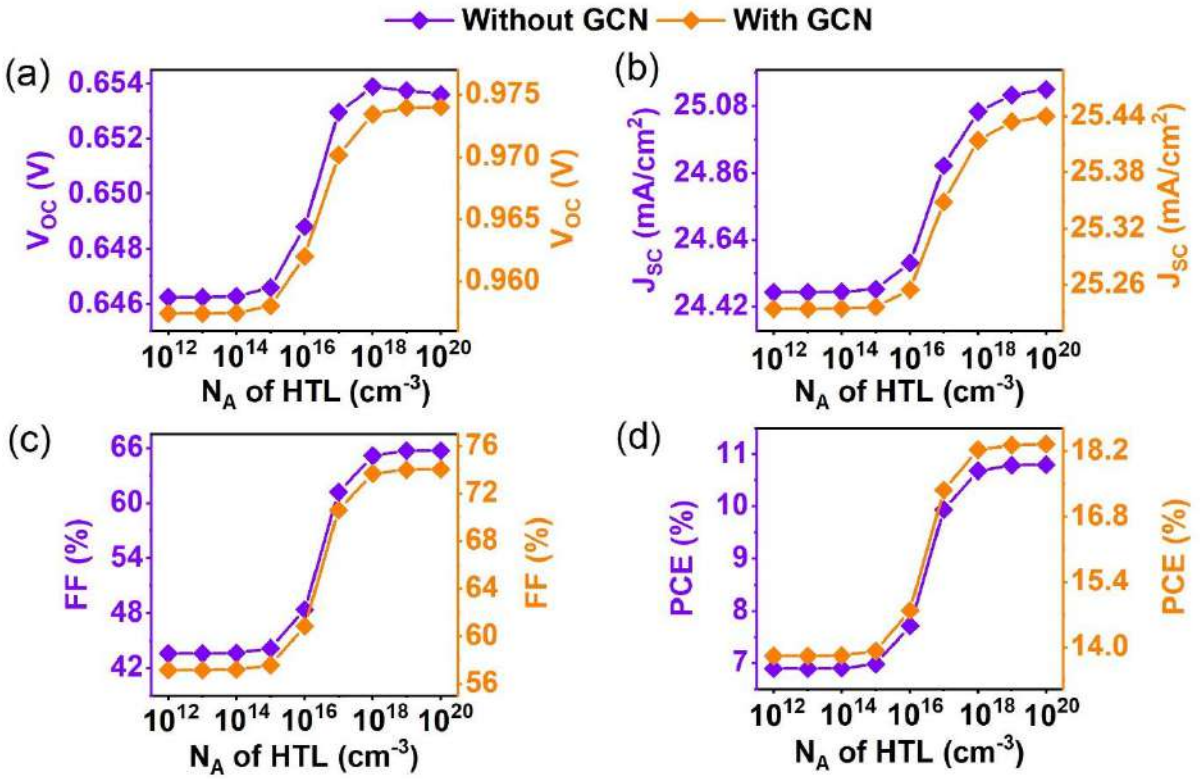

Fig. 40. Variation in (a) V_{OC}, (b) J_{SC}, (c) FF, (d) PCE for different HTL N_A.

To support this explanation, **Fig. 41 (a) and (b)** presents the electric field distribution for both device configurations at low and optimal N_A values. In the absence of GCN, the electric field within the absorber region is relatively weak and the depletion region is narrower, indicating limited junction strength and reduced charge separation efficiency, particularly at lower N_A, which limits carrier extraction. In contrast, the GCN-based structure exhibits a stronger and more uniform electric field broader depletion width across the absorber even at lower doping levels. This enhancement in the internal field contributes directly to the improved PV metrics observed in the GCN-containing devices, confirming the role of GCN in facilitating better charge transport and suppressing recombination via interface passivation and band alignment optimization [167].

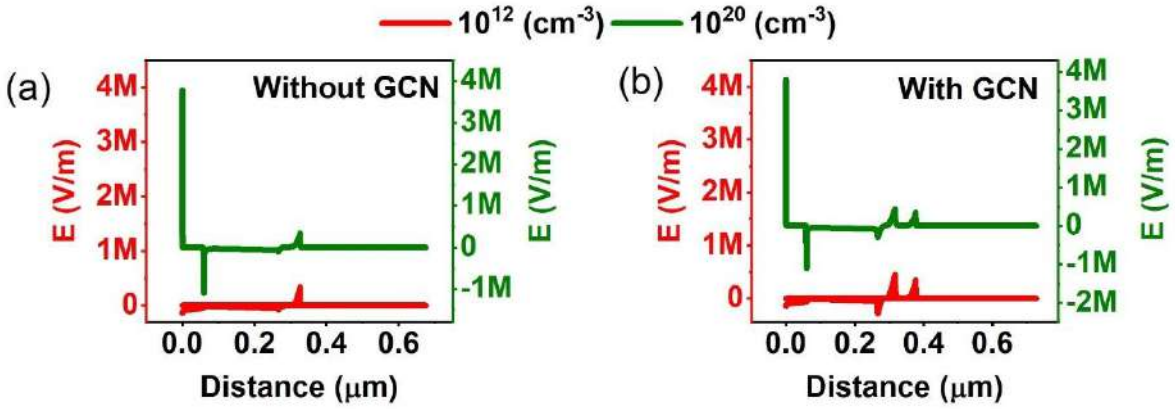

Fig. 41. Electric field distribution for initial and optimized N_A of HTL for the devices (a) without and (b) with GCN

6.3.6.2.Optimization of Absorber Thickness and N_A

The thickness of the $Sb_2(S,Se)_3$ absorber layer strongly impacts the solar performance by controlling photon absorption and charge carrier dynamics. A thinner absorber limits photon absorption, reducing charge carrier generation and thus J_{SC}, while an excessively thick absorber increases the distance charge carriers must travel, which can lead to higher recombination losses due to limited diffusion lengths [168–170]. Therefore, optimizing the absorber thickness is critical to balance enhanced light harvesting with minimized recombination, maximizing the PCE. In this regard, the absorber thickness was varied from 0.1 μm to 1.0 μm for both the baseline device and the device modified with the GCN interfacial layer, and the trends in V_{OC}, J_{SC}, FF, and PCE are presented in **Fig. 42(a–d)**. For the baseline device, V_{OC} increased from 0.63 V at 0.1 μm to 0.66 V at around 0.7 μm, beyond which it stabilized, reflecting enhanced splitting of the quasi-Fermi levels with increasing thickness. However, the saturation beyond 0.7 μm is likely due to an increase in the dark saturation current associated with thicker absorbers, which leads to enhanced recombination [171]. J_{SC} consistently increased from 20.19 mA/cm^2 at 0.1 μm to 28.23 mA/cm^2 at 0.7 μm and showed marginal improvement beyond this thickness, indicating saturation of photon absorption. This increase in J_{SC} is the primary driver for the overall enhancement in PCE with increasing thickness. The FF exhibited a very slight decrease from 66.38% at 0.1 μm to 65.23% at 0.7 μm. But this decrement was negligible and did not significantly affect the device performance. Such a small FF drop is commonly attributed to increased series resistance and reduced charge carrier transport efficiency at higher thicknesses.[171] Consequently, the PCE improved from 8.42% to 12.13% at 0.7 μm, with only marginal increases beyond this thickness, indicating the optimal absorber thickness lies near 0.7 μm for the baseline device. This thickness provides the best compromise between

maximizing photon absorption and minimizing recombination losses. In the GCN-modified device, similar trends were observed but with notably enhanced PV parameters at all thicknesses. V_{OC} rose from 0.96 V at 0.1 μm to 0.98 V at 0.7 μm and then saturated, indicating that the GCN layer effectively suppresses interface recombination. J_{SC} increased significantly from 20.10 mA/cm^2 to 28.67 mA/cm^2 at 0.7 μm, saturating thereafter. The FF slightly decreased from 74.47% to 73.64%, but this minor reduction again had a negligible impact on the overall device efficiency. The PCE improved dramatically from 14.44% at 0.1 μm to 20.64% at 0.7 μm and remained stable beyond, confirming the critical role of GCN in enhancing carrier extraction and reducing recombination losses [172]. The QE plots (**Fig. 42(e) and (f)**) further validate these results by showing increased photoresponse with thicker absorbers, especially at longer wavelengths where photon absorption is crucial. QE increased steadily from 0.1μm up to 0.7 μm, with improvement of 19.25% and 21.09% for the devices without and with GCN, after which the response plateaued with only ~0.5% improvement beyond this optimal thickness. This indicates that photon absorption saturates beyond this thickness due to the balance between absorption and recombination effects. The GCN device consistently demonstrated higher QE across all thicknesses, confirming its role in improving carrier collection efficiency and lowering recombination losses [172]. In summary, the optimal absorber thickness for $Sb_2(S, Se)_3$ solar cells is approximately 0.7 μm, offering the best balance between photon absorption and recombination. Incorporating the GCN interfacial layer further enhances the PCE by a difference of 8.51% compared to the device without GCN, by effectively reducing interface recombination and improving charge transport.

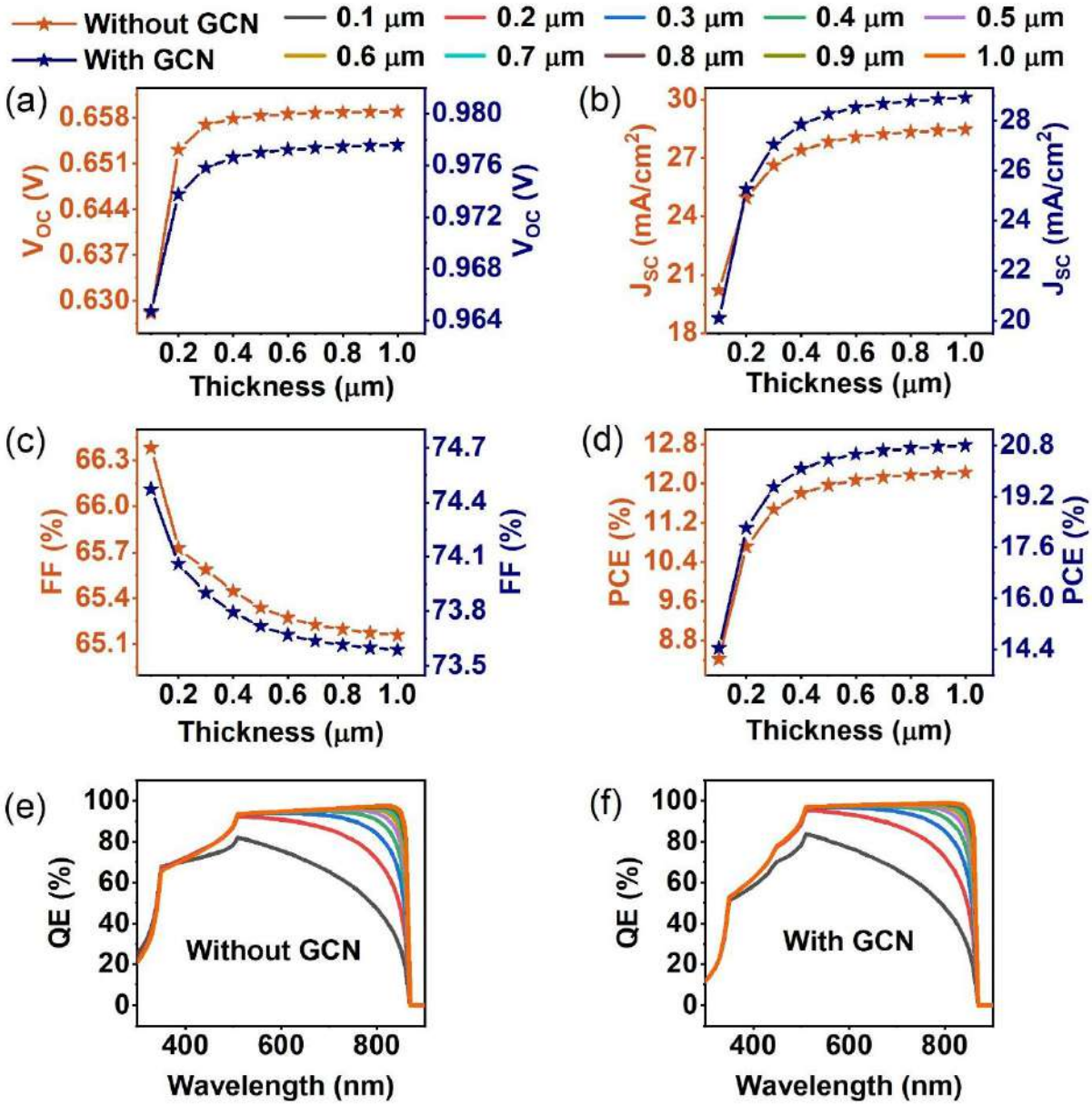

Fig. 42. Variation in (a) V_{OC}, (b) J_{SC}, (c) FF, (d) PCE for different absorber thicknesses, and (e,f) QE plots at different absorber thicknesses for the devices without and with GCN

The N_A in the absorber has a direct impact on carrier dynamics and is crucial for tuning the performance and internal physics of the solar cell. To investigate this effect, NA was varied from 10^{12} to 10^{18} cm^{-3}, and the evolution of V_{OC}, J_{SC}, FF, and PCE was examined for devices with and without GCN, as shown in **Fig. 43(a-d)**. Without GCN, V_{OC} remained around 0.72 V from 10^{12} to 10^{16} cm^{-3} and began to decline at higher doping, dropping sharply to 0.29 V at 10^{18} cm^{-3}. With GCN, V_{OC} was consistently higher, holding steady at 0.98 V up to 10^{16} cm^{-3}, decreasing slightly to 0.96 V at 10^{17} cm^{-3}, and then falling to 0.35 V at 10^{18} cm^{-3}. J_{SC} increased steadily in both cases, peaking at 10^{16} cm^{-3}, with GCN devices achieving higher absolute values

(29.07 mA/cm^2). FF in the GCN device stayed around 73%, while in the device without GCN, it peaked at 10^{16} cm^{-3} before declining. PCE followed the same trend, reaching 12.07% at 10^{16} cm^{-3} without GCN and maintaining approximately 20.5% up to 10^{16} cm^{-3} with GCN, before a sharp drop at 10^{18} cm^{-3}.

The increase in PV parameters up to the optimal N_A is mainly due to enhanced built-in potential and stronger electric fields in the absorber, which promote effective charge separation and transport, thereby reducing recombination losses [173,174]. Beyond the optimal doping, the performance deteriorates because of increased non-radiative recombination caused by defect states and impurity-assisted pathways at higher N_A levels. Additionally, the depletion width narrows, limiting the volume available for photogeneration and thus reducing J_{SC} [175]. Band alignment changes also contribute significantly as N_A increases; the upward shifts in E_C and E_V alter interface band offsets, initially facilitating carrier separation, but at excessive doping, creating energy barriers that hinder hole extraction and increase recombination at the interface [176].

Nyquist plots further support these observations. These plots exhibit a semicircular pattern across all cases, with the diameter increasing at the optimized N_A, indicating that the optimized N_A offers higher resistance to charge carrier recombination. This promotes more effective charge separation and transport through the absorber layer, allowing carriers to reach the contacts before recombining [250]. **Fig. 43(e,f)** shows Nyquist plots obtained at Nyquist plots at N_A = 10^{12} (low), 10^{16} (optimal), 10^{18} (high)cm^{-3}. For both devices, the semicircle diameter was small at 10^{12} cm^{-3}, indicating high recombination, expanded at 10^{16} cm$^{-3,}$ signifying improved carrier transport, and shrank again at 10^{18} cm$^{-3,}$ reflecting increased resistive and recombination losses [177,178]. These observations strongly support the changes noticed in the PV parameters. Despite improvements from GCN, both device types showed performance degradation at very high N_A, but the GCN device maintained better tolerance and stability.

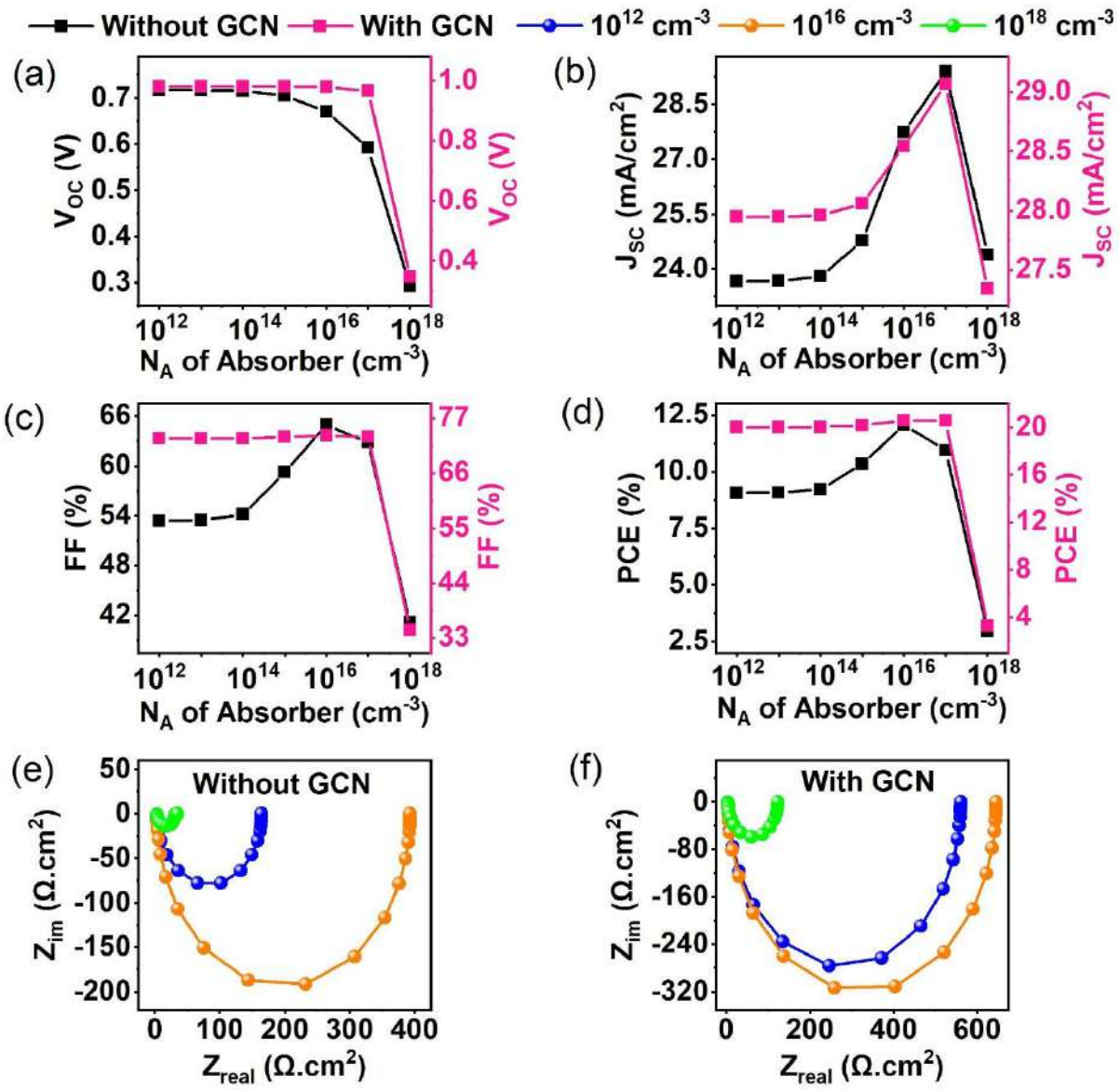

Fig. 43. Variation in (a) V_{OC}, (b) J_{SC}, (c) FF, (d) PCE for different N_A of absorber and (e,f) Nyquist plots at $N_A = 10^{12}$ (low), 10^{16} (optimal), 10^{18} (high)cm^{-3} of absorber for the devices without and with GCN

6.3.6.3.Optimization of GCN Thickness and N_D

The interfacial layer plays a crucial role in suppressing ion migration and optimizing energy level alignment at the Absorber/HTL interface, which enhances charge transfer and reduces recombination losses. In this study, we systematically vary the interfacial layer thickness from 0.01 to 0.1 μm to identify the optimal thickness for improved device performance [251]. **Fig. 44 (a) and (b)** illustrate the effect of varying the thickness of the GCN interfacial layer on the PV parameters. It is observed that increasing the GCN thickness from 0.01 μm to 0.04 μm significantly improves V_{OC} (from 0.81 V to 0.98 V), J_{SC} (from 28.37 to 28.60 mA/cm^2), FF

(from 67.38% to 73.51%), and PCE (from 15.41% to 20.53%). Beyond 0.04 μm, the PV parameters saturate, indicating an optimal thickness around 0.04 μm. This saturation suggests that at thicknesses greater than 0.04 μm, further increases do not substantially affect charge carrier collection or recombination dynamics, consistent with prior reports showing that an optimized interfacial layer thickness balances effective charge transport and minimal series resistance [251]. To understand the origin of this improvement, we consider the frequency-dependent capacitance behavior, where capacitance is decomposed into high (CHF), intermediate (CIF), and low-frequency (CLF) components. The intermediate-frequency capacitance (CIF), often associated with interface processes such as trap-assisted charge accumulation and energy alignment, is especially sensitive to the quality and coverage of the interfacial layer. At lower thickness (0.01 μm), incomplete coverage or defects likely hinder CIF, limiting charge accumulation and contributing to non-radiative recombination. In contrast, the 0.04 μm layer ensures better surface passivation and enhanced charge accumulation at the interface, improving carrier dynamics and reducing interfacial recombination losses [252]. To validate these observations, C–V and Mott-Schottky analyses were conducted, as shown in **Fig. 44(c) and (d)**. The optimized thickness shows a marked increase in capacitance and a positive shift in V_{bi} from 0.42 V to 0.8 V. This shift indicates enhanced charge accumulation and a stronger electric field at the junction, which facilitates efficient charge separation and collection. These improvements in built-in potential are critical for reducing recombination losses and improving overall device performance [162,249].

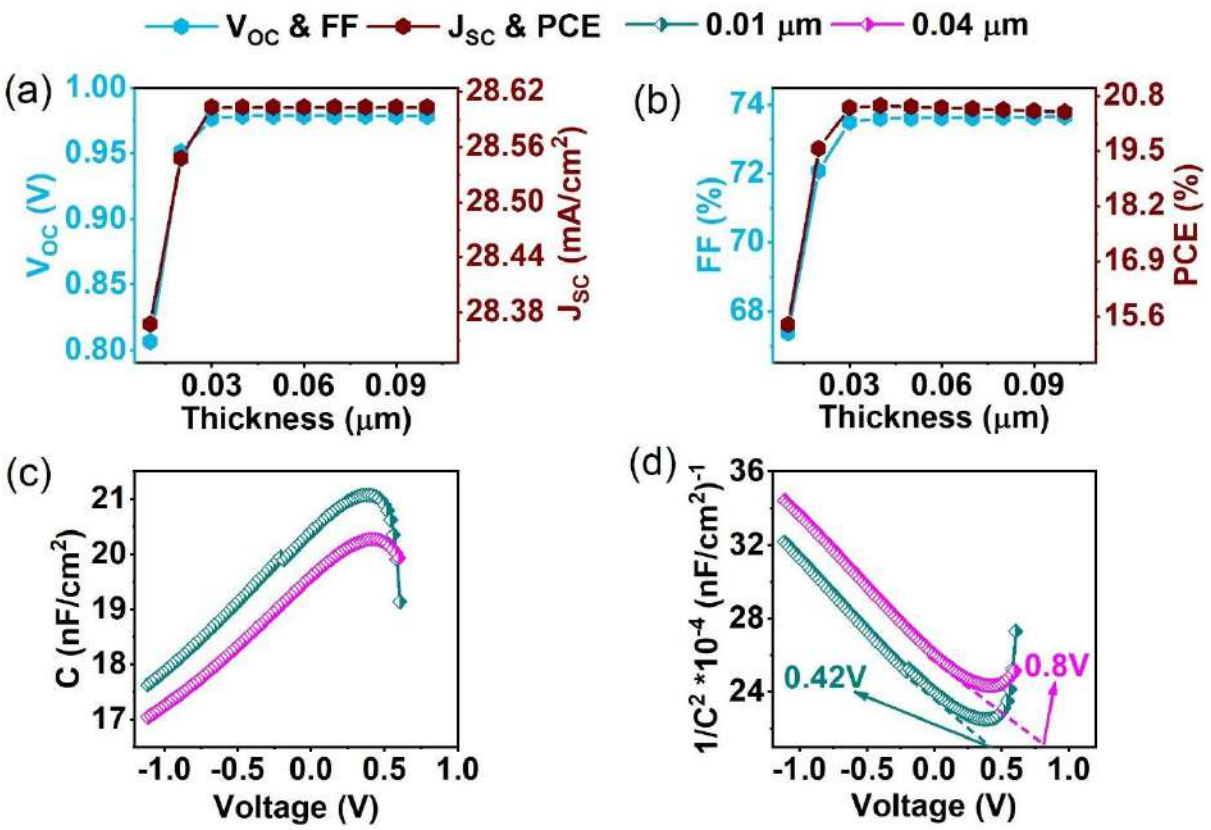

Fig. 44. (a,b) Variation in PV parameters for different GCN thickness, (c) CV measurement and (d) Mott- Schottky plots for the initial and optimized GCN thicknesses

To further enhance device performance, N_D in the GCN interfacial layer was systematically varied, and its effect on PV parameters was studied. **Fig. 45 (a) and (b)** demonstrate that at low N_D (10^{12} to 10^{16} cm^{-3}), the device shows limited performance with V_{OC} around 0.90 V, FF below 32%, and PCE under 8%, primarily due to insufficient free carrier concentration, causing higher series resistance and poor charge extraction [249]. Increasing N_D beyond 10^{17} cm^{-3} significantly improves electrical conductivity and carrier density in the GCN layer, resulting in a steep rise in PV parameters, with peak efficiency 24.23% at $N_D = 10^{20}$ cm^{-3}. The Nyquist plots in **Fig. 45(c)** exhibit an increased semicircle diameter at the optimized N_D compared to the low N_D case, signifying enhanced charge recombination resistance. This improved resistance supports more effective charge separation and transport through the absorber layer, reducing recombination losses. Additionally, **Fig. 45(d)** shows a stronger and more uniform electric field distribution near the interface at the optimized N_D, further facilitating carrier separation and collection. These observations confirm that precise tuning of donor density in the GCN interfacial layer critically modulates the device electrostatics and charge transport

characteristics, thereby directly contributing to the enhanced PV performance observed [249,251].

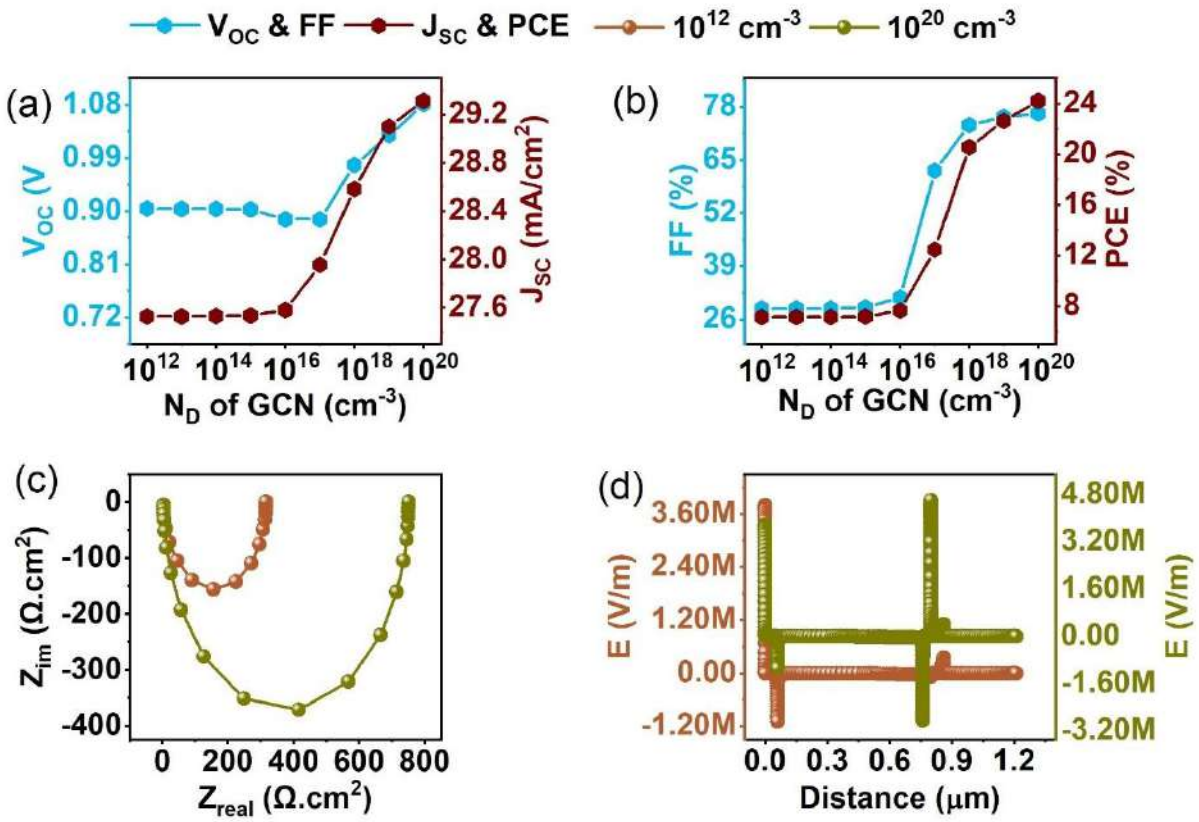

Fig. 45. (a,b) Variation in PV parameters for different N_D of GCN, (c) Nyquist plots and (d) electric field distribution for the initial and optimized N_D

6.3.6.4.Optimization of ETL Thickness and N_D

The effect of ETL thickness on device performance was investigated by varying it from 0.05 to 0.15 μm for devices with and without the GCN interfacial layer. As shown in **Fig. 46 (a–d)**, V_{OC} remained nearly constant at 0.67 V for the device without GCN and 1.08 V with GCN, indicating that variations in ETL thickness do not significantly affect the built-in potential or band alignment [209,253].. In contrast, JSC exhibited a steady decline with increasing thickness, i.e, without GCN, J_{SC} drops from 27.88 to 26.63 mA/cm^2, and with GCN, it decreases from 29.50 to 27.95 mA/cm^2 as the thickness increases from 0.05 to 0.15 μm, primarily due to reduced light transmission through the thicker ETL [158]. Although FF showed a slight improvement with thickness owing to enhanced uniformity and reduced interfacial recombination, the corresponding reduction in JSC led to a gradual decrease in PCE. The PCE dropped from 12.13% to 11.63% for the device without GCN and from 24.37% to 23.15% with GCN. Across all thicknesses, the GCN-modified device exhibited superior

performance, confirming GCN's role in facilitating efficient charge extraction and suppressing recombination. Based on these findings, an ETL thickness of 0.05 µm was identified as optimal, offering the best compromise between optical transparency and charge transport. Thinner ETLs risk incomplete coverage and leakage losses, whereas thicker layers increase series resistance and limit light absorption within the absorber [161,254–256].. This observation is supported by the carrier generation rate profiles in **Fig. 46(e,f)**, where thinner ETLs allowed greater photon penetration and higher carrier generation. The observed ~0.20 × 10^{21} $cm^{-3}.s^{-1}$ decrease in average generation rate with increasing ETL thickness aligns with prior simulation studies reporting similar behavior due to elevated recombination and reduced photon flux [257].

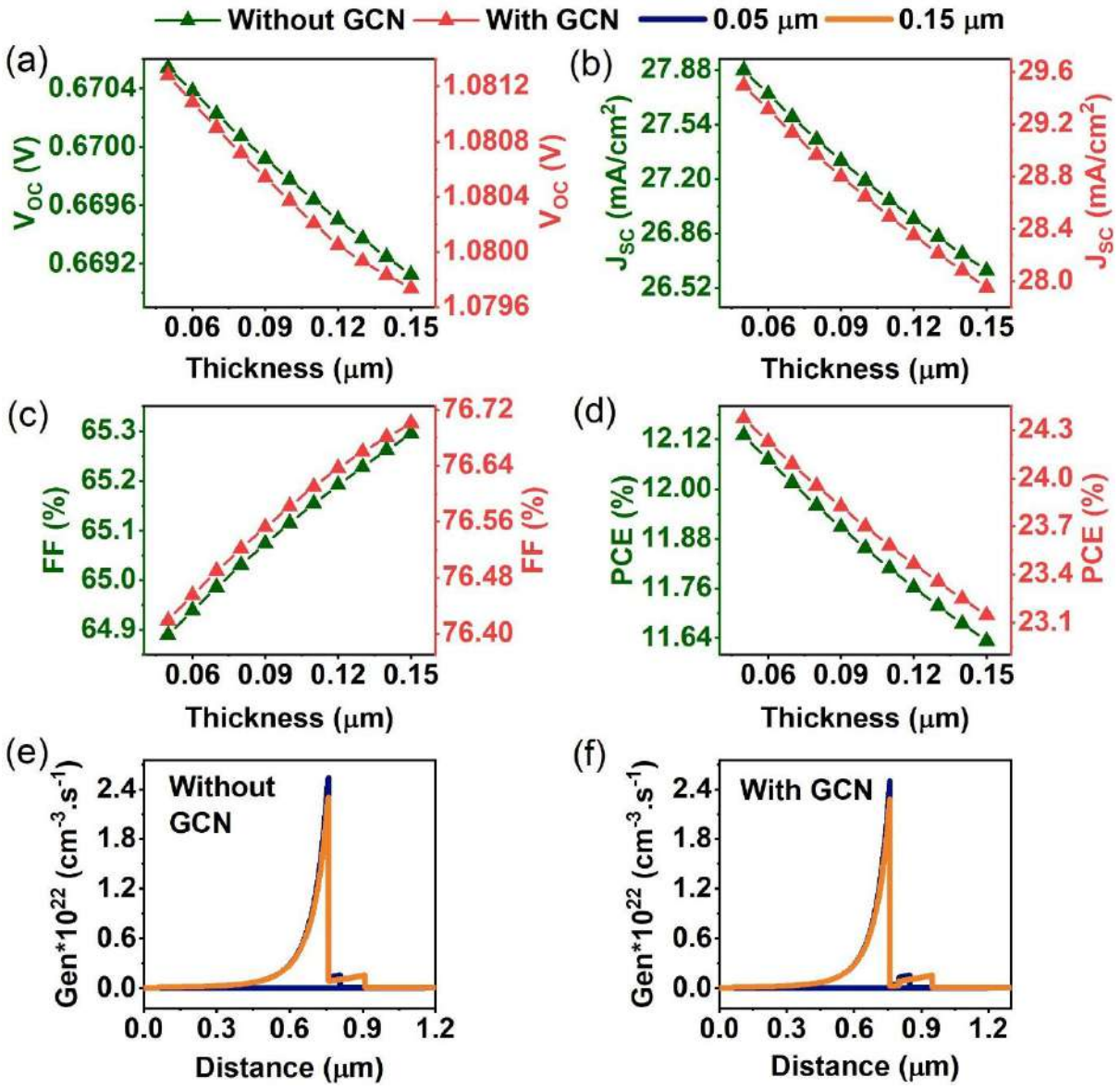

Fig. 46. Variation in (a) V_{OC}, (b) J_{SC}, (c) FF, (d) PCE for different ETL thickness, and (e,f) generation rate for optimized and final thickness of ETL for the devices without and with GCN

The doping concentration of the ETL is a critical factor influencing the charge extraction and built-in potential at the ETL/absorber interface. Herein, the N_D of the ETL was varied systematically from 10^{12} to 10^{20} cm^{-3}, and its effect on PV parameters was analyzed for devices with and without the GCN interlayer, as shown in **Fig. 47 (a-d)**. For both device configurations, no appreciable changes were observed in the V_{OC}, J_{SC}, FF, and PCE when N_D was below 10^{15} cm^{-3}, suggesting that such low doping levels do not significantly influence the electric field strength or interface energy. As N_D increased beyond 10^{15} cm^{-3}, a substantial enhancement in device performance was observed. Notably, the device without GCN exhibited a rise in V_{OC} from 0.31 V at 10^{15} cm^{-3} to 0.80 V at 10^{20} cm^{-3}, while J_{SC} increased from 26.00 to 28.07 mA/cm^2. FF improved drastically from 28.3% to 68.19%, resulting in an overall PCE enhancement from 2.25% to 15.29%. A similar trend was observed in the GCN-modified device, though the V_{OC} and J_{SC} remained almost constant, with a marginal increase at higher doping levels. The FF and PCE exhibited slight improvements, particularly at $N_D \geq 10^{17}$ cm^{-3}, indicating the role of enhanced doping in facilitating efficient electron transport and suppressing recombination. The maximum PCE of 24.374% achieved at an optimal 10^{20} cm^{-3} N_D. This suggests that while the GCN interlayer already aids charge extraction by passivating traps and improving interfacial contact, additional doping further optimizes energy level alignment and enhances the built-in field. The overall improvement in device performance highlights the importance of optimizing N_D to balance the field strength and interface quality for efficient charge extraction. Hence, for both device structures, an N_D of 10^{20} cm^{-3} was found to be optimal for both devices, delivering the highest efficiency due to enhanced charge carrier dynamics [161].

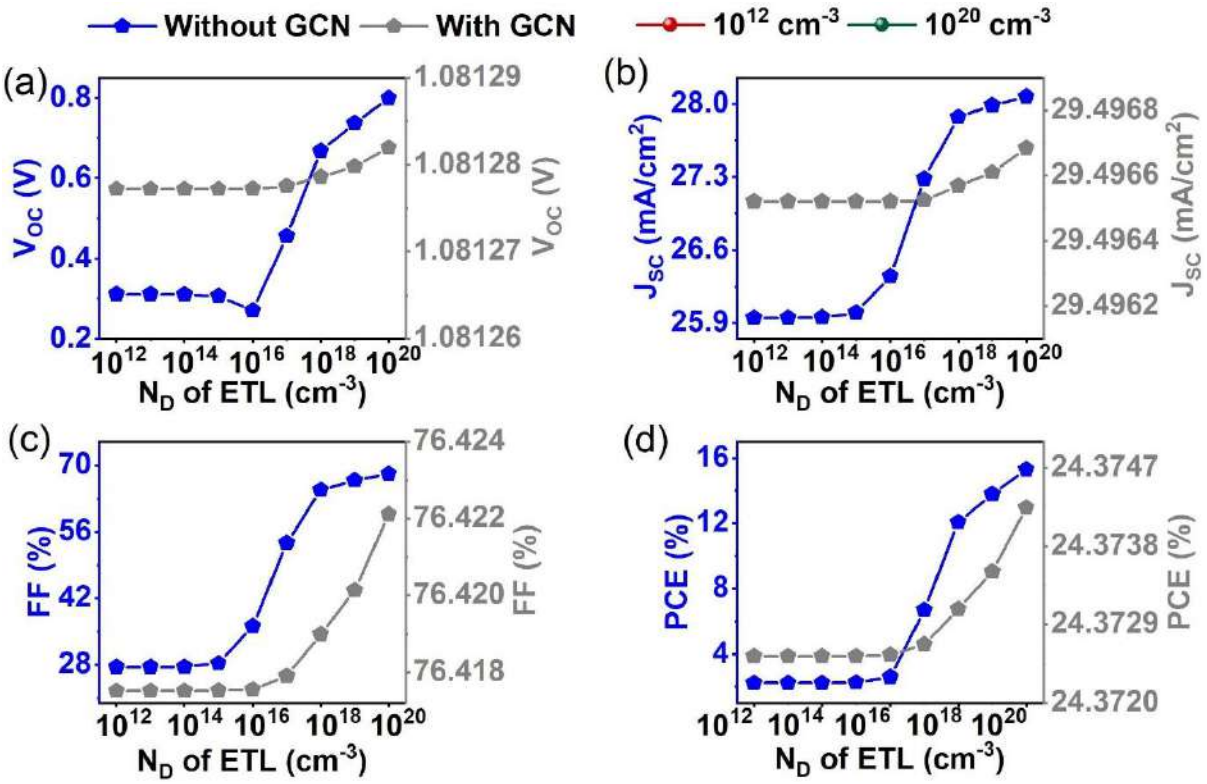

Fig. 47. Variation in (a) V_{OC}, (b) J_{SC}, (c) FF, (d) concerning different N_A of ETL.

6.3.7. Optimization of Interface Properties.

Interface defects at the absorber/contact layer interfaces are unavoidable due to structural imperfections during fabrication and intrinsic mismatches in crystal structures, which lead to non-radiative recombination and reduced solar cell performance [179]. In this work, N_t ranging from 10^{10} to 10^{18} cm^{-2} were systematically varied at the interfaces of HTL, ETL, and GCN with the absorber, and their impact on PV parameters was analyzed. For the HTL/absorber interface without GCN (**Fig. 48 (a,b)**), all PV parameters remain almost unchanged, with only a slight decrease beyond 10^{15} cm^{-2}. This indicates a relative insensitivity of this interface to defect-induced recombination in the absence of GCN, and thus a defect density of 10^{14} cm^{-2} was selected as optimal for device modelling in accordance with experimentally achievable limits. With GCN incorporated, the HTL/absorber interface demonstrates enhanced PV performance (**Fig. 48 (e,f)**), achieving V_{OC} values of approximately 1.08 V and PCEs near 24.4% at low defect densities (10^{10} to 10^{14} cm^{-2}), while maintaining relative stability up to 10^{14} cm^{-2}. This improvement suggests that GCN effectively passivates interface traps and increases defect tolerance. In contrast, the ETL/absorber interface without GCN (**Fig. 48 (c,d)**) shows a pronounced decline in all parameters with increasing defect density. V_{OC} drops from 1.00 V at 10^{10} cm^{-2} to 0.80 V at 10^{18} cm^{-2}, accompanied by decreases in J_{SC} and FF, culminating in a

significant PCE reduction from 23.19% to 14.98%. This highlights that the ETL/absorber interface is more vulnerable to defect-assisted recombination, consistent with previous findings that solar cells are more sensitive to ETL-related interface defects [180]. Similarly, the GCN/absorber interface (**Fig. 48 (g,h**)) shows the highest VOC (~1.22 V) and PCE (~27.37%) at low defect densities, but a gradual performance decline occurs beyond 1012 cm-2 due to increased recombination. This sensitivity underscores the necessity of controlling defect density to fully exploit the potential of GCN. Remarkably, the ETL/GCN interface (**Fig. 48 (i,j)**) maintains a similar trend, indicating strong suppression of trap-assisted recombination by GCN at this interface. Hence, optimal Nt of 1014 cm-2 for the HTL/absorber interface and 1010 cm-2 for the ETL/absorber, GCN/absorber, and GCN/ETL interfaces were selected for the final devices as consistent with the literature [180][181].

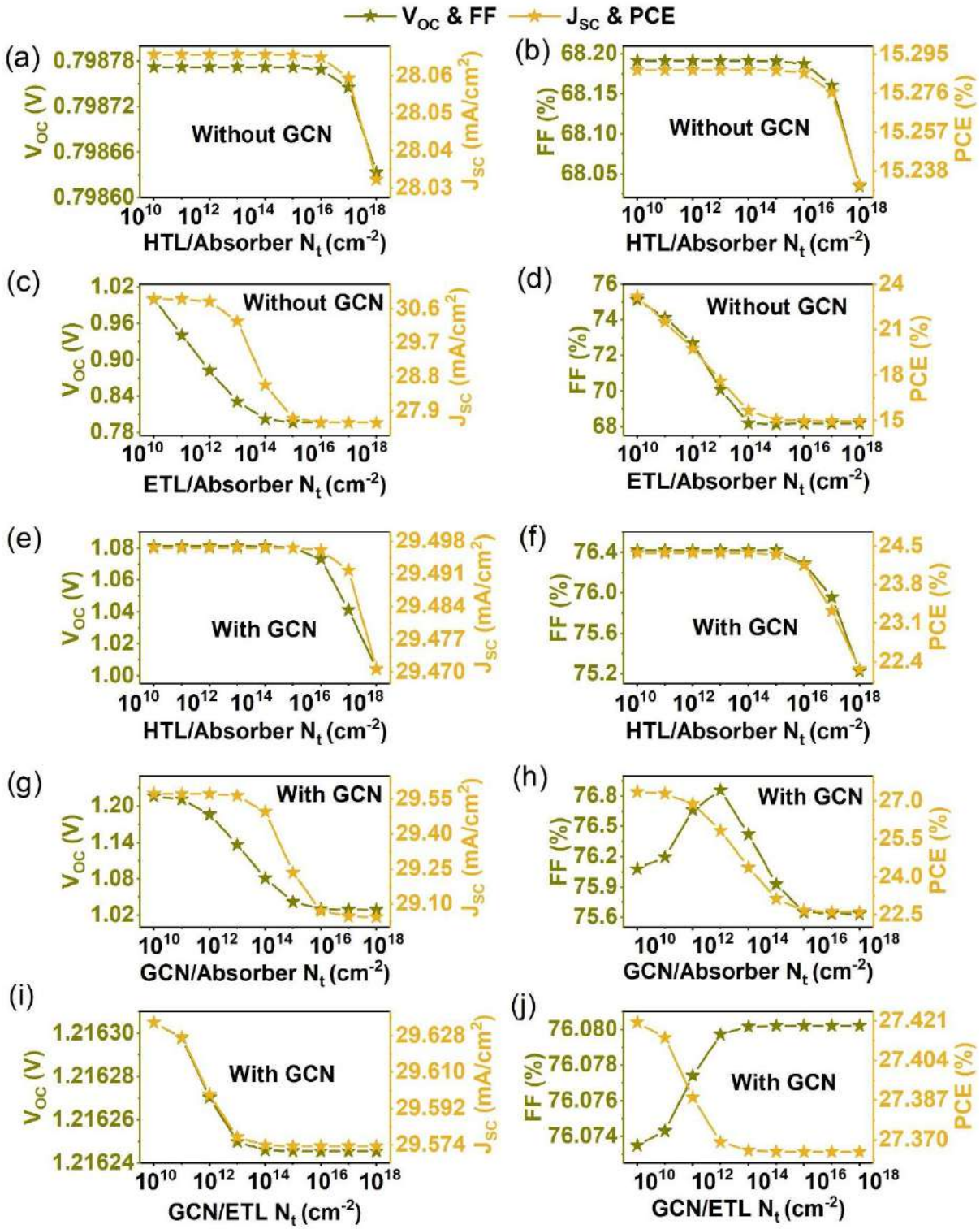

Fig. 48. Variation in PV parameters at (a,b) HTL/absorber (without GCN), (c,d) ETL/absorber (without GCN), (e,f) HTL/absorber (with GCN), (g,h) GCN/absorber, and (i,j) GCN/absorber interfaces concerning different Nt

6.3.8. Analysis of Defect Energy Level and Density on PCE

From the interface optimization results, it is evident that the ETL/absorber interface exhibits higher sensitivity to defect densities compared to the HTL/absorber interface, and optimizing defect densities below 1014 cm-2 is crucial to minimize trap-assisted recombination and maximize device efficiency. However, understanding the charge carrier dynamics involved in the GCN incorporation and interface optimization is imperial**. Fig. 49 (a)** and **(b)** presents the effect of interfacial defect energy levels on the power conversion efficiency (PCE) at the absorber/GCN and GCN/ETL interfaces for different defect densities (Nt = 1010 to 1018 cm-2). At the absorber/GCN interface, the PCE exhibits its maximum value (~27.37%) for a low defect density (≤1012cm-3) when the defect level is positioned near the valence band (−0.4 eV). A progressive decline in efficiency is observed as the defect energy level shifts toward the midgap region (0 to 0.6 eV) and the defect density increases, resulting from the formation of deep-level traps that act as non-radiative recombination centers and reduce carrier lifetime. When the defect levels approach the conduction band edge (>1.4 eV), the PCE recovers slightly and saturates, suggesting that shallow traps near or within the conduction band have minimal impact on charge transport and may even assist in electron transfer across the interface. These results are consistent with previous findings, where defect states near the valence band and midgap were shown to degrade PV performance, whereas shallow donor-like states near the conduction band exhibited negligible effects [258,259].. In contrast, the GCN/ETL interface demonstrates exceptional defect tolerance, with the PCE remaining nearly constant (~27.42%) across all defect levels and densities. This indicates efficient charge extraction and suppressed interfacial recombination, even under high Nt conditions. The stability can be attributed to the presence of shallow defect states near the conduction band that behave as benign traps, promoting electron transfer rather than recombination. Overall, while the absorber/GCN interface exhibits strong dependence on defect energy, particularly within the midgap region at the GCN/ETL interface maintains interfacial robustness and electronic compatibility, thereby ensuring minimal defect-induced losses and sustaining high device efficiency [180].

6.3.9. Electron (n) and Hole(p) Densities of Device at Intial and Optimal N_t

Fig. 49(c–f) provide deeper insight into the carrier dynamics and recombination behaviour at different for N_t at the absorber/GCN and GCN/ETL interfaces. As seen in **Fig. 49(c)** and **(d)**, the spatial distributions of electron and hole densities demonstrate that at higher N_t, the concentration of charge carriers across the absorber region and particularly near the absorber/GCN interface is substantially reduced due to enhanced trap-assisted recombination.

This depletion of carriers restricts their transport toward the electrodes, resulting in severe recombination losses at the interface. Upon optimization of N_t, the carrier densities are effectively restored and become more uniformly distributed throughout the absorber layer, indicating reduced deep-level trapping and improved carrier extraction efficiency. Similar trends have been reported in $MoSe_2$- and perovskite-based heterojunctions, where lowering interfacial trap density led to higher minority carrier concentration and improved charge collection [249,260,261].

6.3.10. SRH and Overall Recombination Behaviour of Device at Intial and Optimal Nt

Correspondingly, **Fig. 49(e)** shows a sharp reduction in the SRH recombination current density (J_{SRH}) after defect optimization, confirming the suppression of non-radiative recombination and trap-mediated carrier losses, consistent with reports on defect passivation improving diode quality and open-circuit voltage in thin-film solar cells [262]. Furthermore, **Fig. 49(f)** illustrates that the total recombination rate exhibits a pronounced peak near the depletion/interface region (~0.849 μm) for the initial N_t, which is significantly diminished following optimization. This confirms that recombination is primarily localized at the absorber/GCN interface under high defect densities and that defect passivation effectively mitigates these losses, consistent with prior analyses of interfacial recombination localization in heterojunction systems [263]. Collectively, these observations substantiate that reducing the interfacial defect density enhances carrier densities, suppresses SRH recombination, and minimizes localized recombination peaks, thereby improving charge extraction and sustaining the high PCE observed in Fig. 12(a,b).

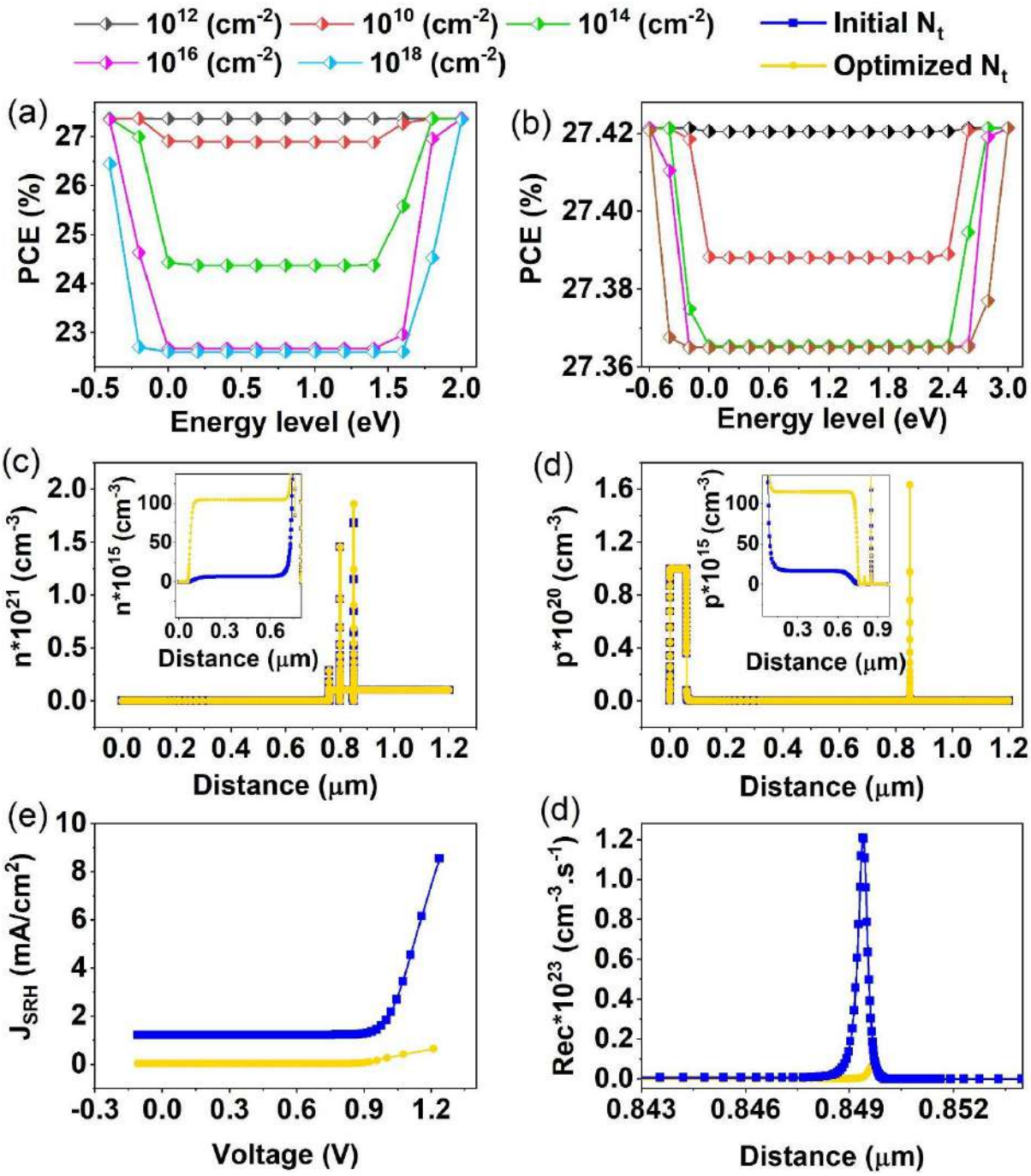

Fig. 49. Effect of defect energy level and N_t at the **(a)** Absorber/GCN and **(b)** GCN/ETL interfaces on device PCE, Variation in density of **(c,d)** electrons and holes, **(e)** SRH recombination current density (J_{SRH}) and **(f)** Total recombination rate at initial and optimized N_t.

6.3.11. Final Outcomes of Optimal Solar Cell Design

The final optimized solar cells with and without the GCN interfacial layer were analyzed through J–V characteristics, QE spectra, and energy band diagrams, as shown in **Fig.50**. The results provide both quantitative and visual evidence of the improved device physics and

performance upon the incorporation of GCN. **Fig. 50(a)** compares the J–V curves of the optimized devices. The device with GCN demonstrates a clear rightward shift in turn-on voltage and a steeper slope, indicating a significantly higher V_{OC} and improved diode quality. The V_{OC} increased from 1.00 V to 1.22 V, matching the numerically extracted values. This enhancement can be attributed to suppressed interfacial recombination, as also reflected in the reduced V_{OC} loss from 0.43 eV to 0.21 eV, when calculated against the absorber bandgap of 1.43 eV.

Table 16. Final device performance with and without GCN

Device structure	**V_{OC} (V)**	**J_{SC} (mA/cm^2)**	**FF (%)**	**PCE (%)**
FTO/CdS/$Sb_2(S,Se)_3$/Spiro-OMeTAD/Au	1	30.86	75.13	23.19
FTO/CdS/GCN/$Sb_2(S,Se)_3$/Spiro-OMeTAD/Au	1.22	29.63	76.07	27.42

Table 16 highlights the enhancement in PV parameters following optimization. The overall PCE increased to 23.19% for the device without GCN and further improved to 27.42% with the inclusion of GCN. The more pronounced knee in the JV curve of the GCN-based device indicates improved carrier extraction and lower series resistance. As shown in **Fig. 50(b)**, the QE spectrum of the GCN-modified device exhibits a broader and significantly higher response across the 350–750 nm range. The peak QE increases from 81.7% to 90.2%, indicating more efficient photon-to-electron conversion. The GCN device also shows faster onset and delayed roll-off, suggesting improved light absorption and carrier collection, especially in the visible spectrum. This improvement is consistent with enhanced interfacial energy alignment that facilitates better charge extraction as illustrated in **Fig. 50(c,d)**. To understand the effect of interfacial band alignment on the PV performance, the conduction band offset (CBO) and valence band offset (VBO) at the ETL/absorber and GCN/absorber interfaces were analyzed. The CBO is defined as the difference between the conduction band minimum (E_C) of the ETL (or interfacial layer) and that of the absorber, while the VBO is calculated as the difference between the valence band maximum (E_V) of the absorber and that of the ETL (or interfacial layer). A positive CBO denotes a spike-like barrier for electrons, whereas a negative CBO implies a cliff-like barrier. Similarly, a positive VBO indicates a spike-like barrier for holes, which is favorable for blocking hole back-injection, while a negative VBO forms a cliff-like barrier that can hinder hole extraction [183,184]. In the device without the GCN interfacial layer, the CBO at the ETL/absorber interface was +0.2928 eV, indicating a significant spike

that may partially hinder electron transport. Upon introducing the GCN interfacial layer between the ETL and absorber, the CBO at the GCN/absorber interface was reduced to +0.18 eV. This moderate spike is widely regarded as optimal, as it efficiently suppresses interfacial recombination without significantly impeding electron extraction. Correspondingly, the VBO at the ETL/absorber interface increased from +1.304 eV (without GCN) to +1.429 eV (at GCN/absorber), indicating an enhanced hole-blocking barrier. This increase in VBO further reduces the likelihood of hole backflow toward the front contact, thereby improving charge carrier selectivity and reducing recombination losses [44]. These improved energy band alignments, characterized by a more moderate CBO and a stronger VBO, contribute to the enhanced performance observed in the GCN-introduced device. The PV parameters show a marked improvement, validating the effectiveness of GCN in tuning interfacial energetics to facilitate better charge extraction and suppress losses. The results derived from the energy band diagram are consistent with theoretical expectations and previous studies emphasizing the importance of optimal interfacial offsets for efficient carrier transport and minimized recombination.

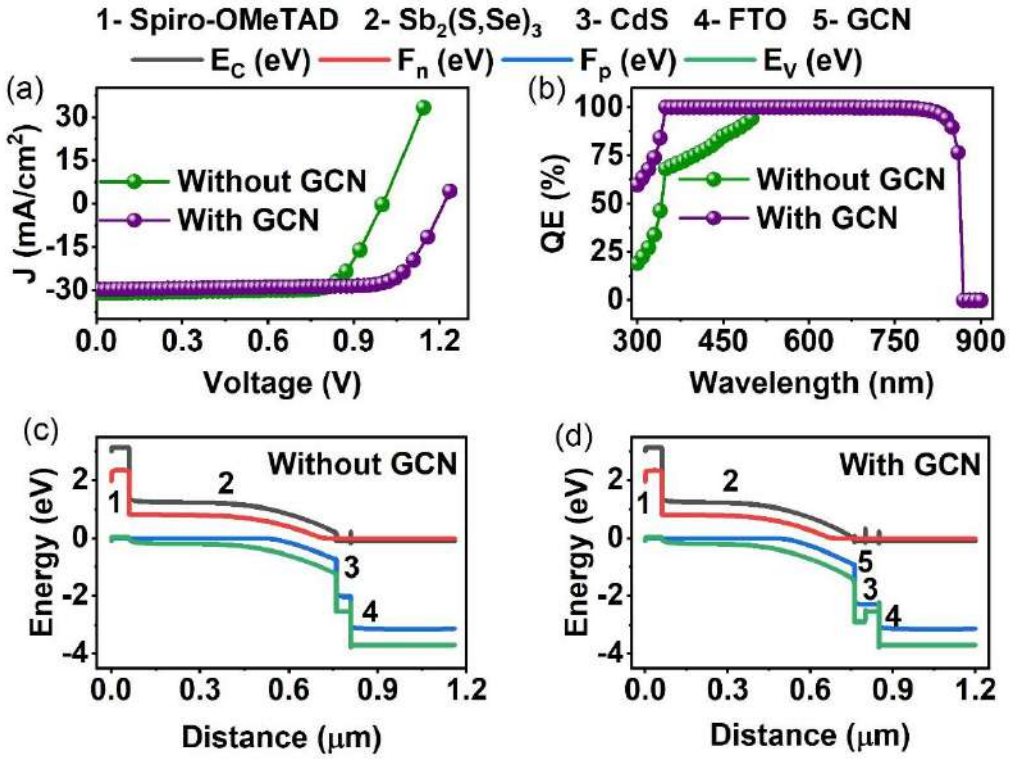

Fig. 50. (a) JV characteristic, (b) QE plot, (c,d) energy band diagrams for the devices without and with GCN

6.3.12. Effect of Temperature and Illumination Intensity

Temperature plays a critical role in defining the operational behavior and stability of solar cells, primarily by modulating carrier transport, recombination dynamics, and resistive losses. In the present study, the PV performance of the GCN-incorporated optimized device was examined under temperatures ranging from 300 K to 450 K, and the results are presented in **Fig. 51 (a,b)**. A clear monotonic decrease in V_{OC} is observed as the temperature increases, declining from 1.22 V at 300 K to 1.06 V at 450 K. This reduction in V_{OC} can be attributed to enhanced SRH recombination at elevated temperatures, which becomes increasingly dominant due to the rise in intrinsic carrier concentration and saturation current density, in accordance with the temperature dependence described by the diode equation in prior studies [195,196]. Additionally, the reduction in the semiconductor bandgap with temperature further contributes to the observed V_{OC} degradation [197]. FF and PCE also exhibit a gradual decline with increasing temperature. The FF drops from 76.07% to 69.88%, while the PCE decreases from 27.42% at 300 K to 22.74% at 450 K. This trend is linked to increased series resistance and decreased carrier mobility due to phonon scattering, as carrier mobility typically follows [199]:

$$\mu(T) \propto T^{-m} \tag{7}$$

where m > 0 for phonon-limited transport. These factors collectively degrade charge extraction efficiency, reducing both FF and PCE, consistent with previously reported results [198]. J_{SC} shows a mild increase with temperature, rising from 29.63 to 30.60 mA/cm^2. This is likely due to the narrowing of the absorber bandgap at higher temperatures, allowing for absorption of longer-wavelength photons and a marginal increase in charge carrier generation. However, the benefits of enhanced generation are counterbalanced by recombination losses, resulting in only a modest J_{SC} gain [201,202].

To assess the light intensity dependence, the device was simulated under varying illumination levels from 100 to 1000 W/m^2, and the corresponding PV parameters are illustrated in **Fig. 51 (c,d)**. As expected, J_{SC} increases linearly with illumination intensity, consistent with the proportional relationship between photon flux and photocarrier generation [204]. J_{SC} rises from 2.96 mA/cm^2 at 100 W/m^2 to 29.63 mA/cm^2 at 1000 W/m^2, validating the efficient light harvesting and charge generation capability of the optimized device. Simultaneously, V_{OC} exhibits a logarithmic increase with intensity, reaching 1.22 V at 1000 W/m^2 from 1.12 V at 100 W/m^2. This is attributed to greater quasi-Fermi level splitting under enhanced carrier generation, aligning with the dependence [203,205].. The FF shows a sharp increase from

48.52% at low intensity (100 W/m²) to around 76.5% at intensities ≥800 W/m^2, beyond which it saturates. This initial improvement stems from reduced series resistance effects and enhanced carrier transport at higher illumination, while the subsequent saturation suggests that internal resistive and recombination losses dominate, limiting further improvement [206]. Consequently, PCE follows a similar trend, increasing rapidly from 16.08% at 100 W/m^2 to a maximum of 27.45% at 900 W/m^2, beyond which it remains stable. This saturation behavior in both FF and PCE suggests that the device operates near its intrinsic efficiency limits under full sunlight, with minimal losses due to optical or external constraints [44].

Overall, the simulated GCN-based solar cell demonstrates stable and predictable performance trends under both thermal and optical stress. While elevated temperatures induce recombination and resistive losses that deteriorate V_{OC}, FF, and PCE, the device maintains relatively high performance even at 450 K. Under increasing light intensity, the PV parameters improve significantly and eventually saturate, underscoring the robustness and practical applicability of the device under real-world sunlight conditions.

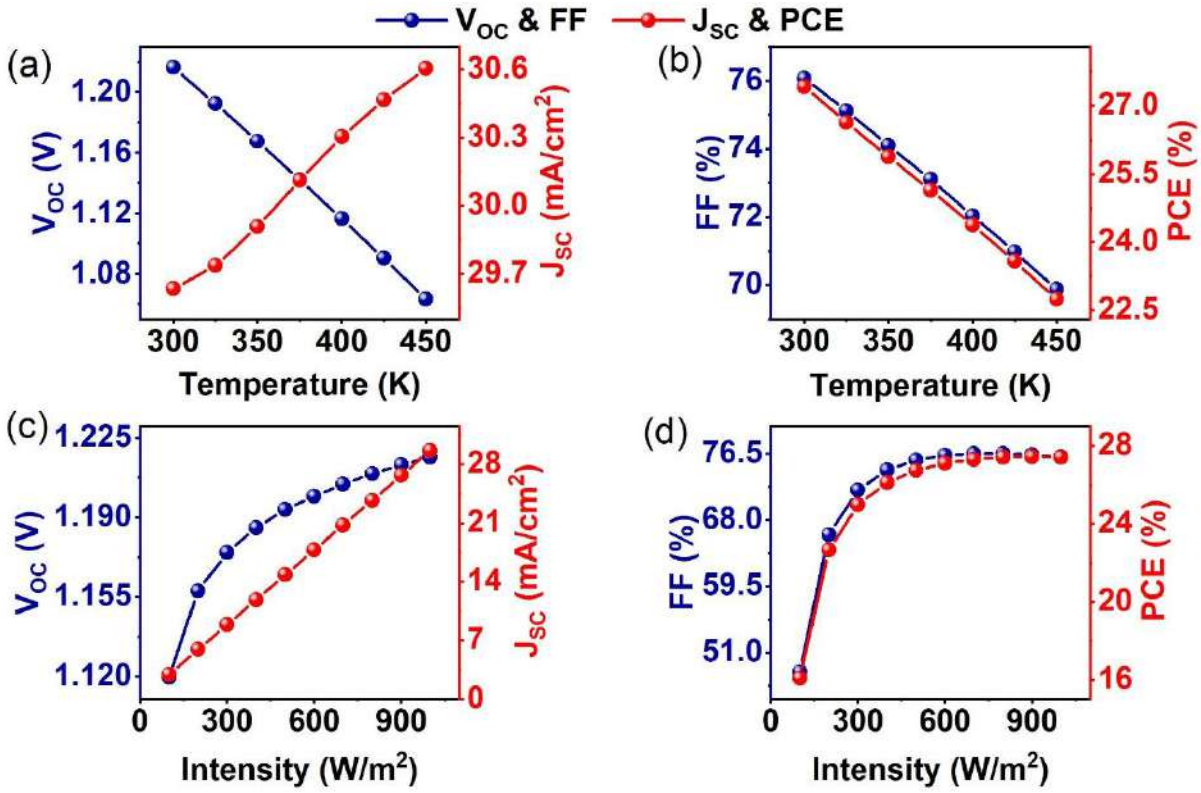

Fig. 51. Influence of (a,b) temperature and (c,d) illumination intensity on the PV parameters for the optimized device

Conclusion

This thesis systematically investigated $Sb_2(S,Se)_3$ thin-film solar cells through three major studies involving device simulation, optimization, and interfacial engineering, aimed at addressing the intrinsic limitations of conventional CdS/Spiro-OMeTAD-based architectures. A total of multiple device structures were simulated using the SCAPS-1D platform, and their performance was analyzed through electrical (J–V, C–V), optical (QE, absorption), and recombination–generation studies. Additionally, Nyquist analysis was employed to evaluate charge transfer resistance, and the influence of operating conditions such as temperature and illumination intensity was examined to assess device stability and charge dynamics under realistic conditions. Each study specifically focused on a key structural modification—hole transport layer (HTL), electron transport layer (ETL), and interfacial layer engineering—to systematically enhance device efficiency, reduce non-radiative losses, and optimize charge carrier extraction and recombination mechanisms. The outcomes are as follows:

(1) The first study explored cost-effective triazatruxene-based HTLs (CI-B2, CI-B3, TAT-H, TAT-TY1, and TAT-TY2) as replacements for the conventional Spiro-OMeTAD in $Sb_2(S,Se)_3$ solar cells. Initially, the baseline device was designed to replicate the device configuration of FTO/CdS/$Sb_2(S,Se)_3$/Spiro-OMeTAD/Au reproducing the same experimental outcomes. Later, by optimizing the thickness and carrier densities of the HTL, ETL, and absorber layers, significant efficiency improvements were achieved. In precise, on optimizing the HTL, the CI-B2, CI-B3, TAT-H, TAT-TY1, and TAT-TY2-based solar cells resulted in efficiency increases of 4.53%, 5.2%, 1.6%, 1.22%, and 0.18%, respectively, compared to the baseline efficiencies. Meanwhile, Spiro-OMeTAD showed only a slight increase, from 10.75% to 10.79%. The enhancement in PCE is attributed to enhanced charge collection at the respective contacts, as evident from the drastic increase in QE (>70%) for all the solar cells. Further optimization of the ETL led to efficiencies exceeding 12% for TAT-H and 13% for the other HTLs owing to the reduced recombination at optimal thickness (0.05 μm) and enhanced electric fields at optimal N_D (10^{20} cm^{-3}). Additionally, optimizing the absorber parameters resulted in improvements to the V_{OC} (~0.8 V), J_{SC} (27 to 29 mA/cm^2), and FF (66%–68%), stabilizing efficiencies over 15% for all solar cells pertaining to the favorable band alignments, enhanced fermi level splitting and greater light absorption. Tuning the absorber/HTL and ETL/absorber interfaces effectively minimized the non-radiative recombination at the interfaces, leading to reduced V_{OC} loss (~0.4 V), largely attributed to refined ETL/absorber interface engineering. Overall, the final efficiencies of 22.97% for Spiro-OMeTAD, 23.09% for CI-B2, 22.47% for

CI-B3, 21.08% for TAT-H, 23.24% for TAT-TY1, and 23.11% for TAT-TY2, were achieved, with CI-B2, TAT-TY1, and TAT-TY2 exceeding 23% efficiency. This work highlights the advantages of triazatruxene HTLs as a potential alternative to Spiro-OMeTAD with comparable efficiencies after meticulous optimization of each layer. Finally, the effects of operating temperature and light intensity on device behavior were systematically analyzed. Hence, the findings from this study lay the groundwork for future efforts to push these devices closer to their theoretical efficiency limits.

(2) The second study focused on implementing a Cd-free electron transport layer using STO in place of CdS to enhance both environmental compatibility and interfacial quality. The introduction of STO, with its wide bandgap (3.2 eV) and superior dielectric properties, led to reduced interface recombination (~0.12×10^{17} $cm^{-3}.s^{-1}$) and improved photogeneration rates (3.21×10^{21} $cm^{-3}.s^{-1}$). Optimization of ETL parameters revealed a favorable electric field distribution across the junction, resulting in stronger carrier drift and suppressed non-radiative losses. The reduced V_{OC} loss (~0.39 V) was attributed to a well-aligned conduction band profile characterized by a small cliff-type offset that facilitated electron extraction while preventing hole backflow. Simultaneously, the valence band spike acted as a selective barrier, further lowering interfacial recombination. These effects collectively enhanced quantum efficiency and J_{SC}, demonstrating improved absorption response and charge separation. The temperature and illumination studies further revealed stable PV operation, with V_{OC} and FF showing predictable behavior under thermal and light variation, confirming the reliability of the STO-based Cd-free configuration for future $Sb_2(S,Se)_3$ solar cells.

(3) The third study integrated an experimentally synthesized GCN interfacial layer between CdS and $Sb_2(S,Se)_3$ to improve interface energetics and stability. The GCN, prepared through thermal polymerization of urea and characterized by XRD, XPS, FESEM, and UV–Vis spectroscopy, exhibited a (002) diffraction peak at 27.4°, an indirect bandgap of 2.8 eV, and an electron affinity of 3.6 eV. These experimentally validated parameters were incorporated into SCAPS-1D simulations, ensuring physical accuracy. The incorporation of GCN improved the built-in potential (V_{bi}) to 0.8 V and reduced charge transfer resistance (625.4 to 401.3 $\Omega.cm^2$) and series resistance (3.7 to 3.5 $\Omega.cm^2$), which correlated with an improved fill factor of 76.07%. The modified energy band structure, with CBO reduced from +0.29 eV to +0.18 eV and VBO increased to +1.43 eV, enabled selective carrier transport and minimized recombination losses. These factors enhanced carrier generation (~0.20×10^{21} $cm^{-3}.s^{-1}$) and elevated QE beyond 90% across the visible region, leading to a final efficiency of 27.42%. The

illumination and temperature analyses confirmed minimal degradation and high stability under operating conditions, establishing GCN as a highly effective interfacial modifier for $Sb_2(S,Se)_3$ solar cells.

In summary, this thesis provides a clear understanding of how targeted interfacial and layer-level engineering can systematically overcome the limitations of $Sb_2(S,Se)_3$ PV devices. The implementation of triazatruxene-based HTLs improved hole transport and reduced V_{OC} losses, $SrTiO_3$ offered a Cd-free alternative with enhanced interfacial recombination control, and GCN interfacial engineering delivered superior energetics and stability. Together, these studies contribute a coherent strategy toward achieving high-efficiency (>27%) and stable $Sb_2(S,Se)_3$ solar cells, laying the groundwork for future experimental realizations and commercialization of sustainable thin-film PV technologies.

References

[1] International Energy Outlook 2023 - U.S. Energy Information Administration (EIA), (n.d.). **https://www.eia.gov/outlooks/ieo/.**

[2] AR6 Synthesis Report: Climate Change 2023, **https://www.ipcc.ch/report/ar6/syr/.**

[3] N. Kannan, D. Vakeesan, Solar energy for future world: - A review, Renewable and Sustainable Energy Reviews 62 (2016) 1092–1105. **https://doi.org/10.1016/J.RSER.2016.05.022**.

[4] Global Electricity Review 2025, Ember, **https://ember-energy.org/latest-insights/global-electricity-review-2025/**.

[5] Renewables in 2024: 5 Key Facts Behind a Record-Breaking Year, **https://www.irena.org/news/articles/2025/Apr/Renewables-in-2024-5-Key-Facts-Behind-a-Record-Breaking-Year**.

[6] L.A. Iturralde Carrera, M.G. Garcia-Barajas, C.D. Constantino-Robles, J.M. Álvarez-Alvarado, Y. Castillo-Alvarez, J. Rodríguez-Reséndiz, Efficiency and Sustainability in Solar Photovoltaic Systems: A Review of Key Factors and Innovative Technologies, Eng 2025, Vol. 6, Page 50 6 (2025) 50. **https://doi.org/10.3390/ENG6030050**.

[7] G. Masson, M. de l'Epine, I. Kaizuka, J. Okazaki, Trends in PV Applications 2025, (2025). **https://doi.org/10.69766/NCNN2417**.

[8] Market Information Mexico, (n.d.). **https://www.intersolar.mx/market-information**.

[9] Mexico deploys 1 GW of distributed solar in 2024 – pv magazine International, **https://www.pv-magazine.com/2025/02/04/mexico-deploys-1-gw-of-distributed-solar-in-2024/**.

[10] Becquerel, E. (1839) Mémoire sur les effets électriques produits sous l'influence des rayons solaires. Comptes Rendus, 9, 561-567.

[11] D.M. Chapin, C.S. Fuller, G.L. Pearson, A New Silicon p-n Junction Photocell for Converting Solar Radiation into Electrical Power, J Appl Phys 25 (1954) 676. **https://doi.org/10.1063/1.1721711**.

[12] M. Green, Solar cells: operating principles, technology, and system applications, (1981). **https://www.osti.gov/biblio/6051511**.

[13] A. Luque, S. Hegedus, Handbook of photovoltaic science and engineering, John Wiley & Sons, (2011).

[14] Best Research-Cell Efficiency Chart, Photovoltaic Research, NREL, **https://www.nrel.gov/pv/cell-efficiency**.

[15] D. Intal, A. Ebong, Thin-Film Solar Photovoltaics: Trends and Future Directions, International Symposium on High-Capacity Optical Networks and Enabling Technologies (2024) 135–142. **https://doi.org/10.1109/HONET63146.2024.10822947**.

[16] F. Liu, G. Wang, Z. Huang, J. Tian, D. Wang, Enhanced Performance of CdTe Solar Cells with $SbSe_3$ Back Contacts, Physica Status Solidi (A) Applications and Materials Science 220 (2023) 2300426, **https://doi.org/10.1002/pssa.202300426**.

[17] M.F. Rahman, M.K. Hasan, M. Chowdhury, M.R. Islam, M.H. Rahman, M.A. Rahman, S.R. Al Ahmed, A.B.M. Ismail, M. Amami, M.K. Hossain, G.A. Al-Hazmi, A qualitative Design and optimization of CIGS-based Solar Cells with Sn_2S_3 Back Surface Field: A plan for achieving 21.83 % efficiency, Heliyon 9 (12) (2023), **https://doi.org/10.1016/j.heliyon.2023.e22866.**

[18] T. Sharpton, T. Lawrence, M. Hall, Drivers and barriers to public acceptance of future energy sources and grid expansion in the United States, Renewable and Sustainable Energy Reviews 126 (2020) 109826, **https://doi.org/10.1016/j.rser.2020.109826.**

[19] B. Yu, S. Tan, D. Li, Q. Meng, The stability of inorganic perovskite solar cells: from materials to devices, Materials Futures 2 (3) (2023) 032101, **https://doi.org/10.1088/2752-5724/ACD56C.**

[20] K. Kaur, M. Kumar, Progress and prospects of CZTSSe/CdS interface engineering to combat high open-circuit voltage deficit of kesterite photovoltaics: a critical review, Journal of Materials Chemistry A 8 (41) (2020) 21547–21584, **https://doi.org/10.1039/D0TA06450E.**

[21] M. Albaladejo-Siguan, E.C. Baird, D. Becker-Koch, Y. Li, A.L. Rogach, Y. Vaynzof, Stability of Quantum Dot Solar Cells: A Matter of (Life)Time, Adv Energy Mater 11 (2021) 2003457. **https://doi.org/10.1002/AENM.202003457;ISSUE:ISSUE:DOI.**

[22] K. Sharma, V. Sharma, S.S. Sharma, Dye-Sensitized Solar Cells: Fundamentals and Current Status, Nanoscale Res Lett 13 (1) (2018) 381. **https://doi.org/10.1186/S11671-018-2760-6.**

[23] S.K. Mostaque, J. Hossain, A. Kuddus, Simulating the performance of a high-efficiency SnS-based dual-heterojunction thin film solar cell, Optical Materials Express, Vol. 11, Issue 11, pp 3812-3826 (2021). **https://doi.org/10.1364/OME.439629.**

[24] M. Rahman, G. Boschloo, A. Hagfeldt, T. Edvinsson, On the Mechanistic Understanding of Photovoltage Loss in Iron Pyrite Solar Cells, Advanced Materials 32 (26) (2020) 1905653. **https://doi.org/10.1002/ADMA.201905653;REQUESTEDJOURNAL:JOURNAL:15214095;ISSUE:ISSUE:DOI.**

[25] S. Chen, L. Wang, C. Zhou, J. Yang, A review of Cu_2O solar cell, Journal of Renewable and Sustainable Energy 15 (6) (2023). **https://doi.org/10.1063/5.0167383.**

[26] F. Kawamura, M. Imura, H. Murata, N. Yamada, T. Taniguchi, Synthesis of a Novel Rocksalt-Type Ternary Nitride Semiconductor $MgSnN_2$ Using the Metathesis Reaction under High Pressure, Eur J Inorg Chem (2020) (5) 446–451. **https://doi.org/10.1002/EJIC.201901059.**

[27] F. Ning, J. Huang, J. Kang, Cation-Disorder-Enhanced Unintentional Doping in $MgSnN_2$, Phys Rev Appl 19 (5) (2023) 054046. **https://doi.org/10.1103/PhysRevApplied.19.054046.**

[28] D. Tiwari, D. Alibhai, D.J. Fermin, Above 600 mV Open-Circuit Voltage BiI_3 Solar Cells, ACS Energy Lett 3 (8) (2018) pp 1882–1886. **https://doi.org/10.1021/ACSENERGYLETT.8B01182/SUPPL_FILE/NZ8B01182_SI_003.AVI.**

[29] Z. He, R. Yu, W. Song, Y. Gong, H. Li, Z . A. Tan, Bismuth Complex Controlled Morphology Evolution and CuSCN-Induced Transport Improvement Enable Efficient BiI3 Solar Cells, Nanomaterials 12 (18) (2022) 3121. **https://doi.org/10.3390/nano12183121.**

[30] Y.T. Huang, S.R. Kavanagh, M. Righetto, M. Rusu, I. Levine, T. Unold, S.J. Zelewski, A.J. Sneyd, K. Zhang, L. Dai, A.J. BBrittonR. L. Hoye, Strong absorption and ultrafast localisation in $NaBiS_2$ nanocrystals with slow charge-carrier recombination, Nature Communications 13(1) (2022). **https://doi.org/10.1038/s41467-022-32669-3.**

[31] S. Kalambur, R. Mouli, N.J. Choudhari, D.M. Kavya, Y. Raviprakash, Exploring the potential of Cu_2FeSnS_4: a comprehensive review on structural properties, optoelectronic features, and future prospects in earth-abundant thin film, Taylor & FrancisS Kalambur, R Mouli, NJ Choudhari, DM Kavya, Y RaviprakashCogent Engineering, 2024•Taylor & Francis 11 (2024). **https://doi.org/10.1080/23311916.2024.2322076.**

[32] J.W. Choi, B. Shin, P. Gorai, R.L.Z. Hoye, R. Palgrave, Emerging Earth-Abundant Solar Absorbers, ACS Energy Lett 7 (2022) 1553–1557. **https://doi.org/10.1021/ACSENERGYLETT.2C00516.**

[33] Ganose, Alex M., Christopher N. Savory, and David O. Scanlon. "Beyond methylammonium lead iodide: prospects for the emergent field of ns 2 containing solar absorbers." Chemical Communications 53, no. 1 (2017): 20-44. **https://doi.org/10.1039/C6CC06475B**,

[34] A. Bosio, G. Foti, S. Pasini, D. Spoltore, A Review on the Fundamental Properties of Sb_2Se_3- Based Thin Film Solar Cells, Energies 2023, Vol. 16, Page 6862 16 (2023) 6862. **https://doi.org/10.3390/EN16196862**.

[35] K. Li, R. Tang, C. Zhu, T. Chen, Critical Review on Crystal Orientation Engineering of Antimony Chalcogenide Thin Film for Solar Cell Applications, Adv Sci (Weinh) 11 (2024). **https://doi.org/10.1002/ADVS.202304963.**

[36] A. Mavlonov, T. Razykov, F. Raziq, J. Gan, J. Chantana, Y. Kawano, T. Nishimura, H. Wei, A. Zakutayev, T. Minemoto, X. Zu, S. Li, L. Qiao, A Review of Sb_2Se_3 Photovoltaic Absorber Materials and Thin-Film Solar Cells, Solar Energy 201 (2020) 227–246. **https://doi.org/10.1016/J.SOLENER.2020.03.009.**

[37] X. Chen, X. Shu, J. Zhou, L. Wan, P. Xiao, Y. Fu, J. Ye, Y.T. Huang, B. Yan, D. Xue, T. Chen, J. Chen, R.L.Z. Hoye, R. Zhou, Additive engineering for Sb_2Se_3 indoor

photovoltaics with efficiency exceeding 17%, Light: Science & Applications 2024 13:1 13 (2024) 1–15. **https://doi.org/10.1038/s41377-024-01620-0.**

[38] J. Chen, G. Li, Z. Xu, C. Xu, F. Naveed, B. Liu, Y. Zhang, R. Zhou, C. Chen, M. Wang, J. Xu, L. Li, recent-advances-and-prospects-of-solution-processed-efficient Sb_2S_3-solar-cells, Adv Funct Mater 34 (2024). **https://doi.org/10.1002/ADFM.202313676.**

[39] J.S. Eensalu, A. Katerski, E. Kärber, L. Weinhardt, M. Blum, C. Heske, W. Yang, I.O. Acik, M. Krunks, Semitransparent Sb_2S_3 thin film solar cells by ultrasonic spray pyrolysis for use in solar windows, Beilstein Journal of Nanotechnology 10 (2019) 2396–2409. **https://doi.org/10.3762/BJNANO.10.230.**

[40] K. Li, Y. Lu, X. Ke, S. Li, S. Lu, C. Wang, S. Wang, C. Chen, J. Tang, Over 7% Efficiency of $Sb_2(S,Se)_3$ Solar Cells via V-Shaped Bandgap Engineering, Solar RRL 4 (2020). **https://doi.org/10.1002/SOLR.202000220**.

[41] S. Barthwal, S. Singh, A.K. Chauhan, N.S. Prabhu, A.G. Prabhudessai, K. Ramesh, A comprehensive insight into deep-level defect engineering in antimony chalcogenide solar cells, Mater Adv 4 (2023) 5998–6030. **https://doi.org/10.1039/D3MA00479A.**

[42] X. Chen, B. Che, Y. Zhao, S. Wang, H. Li, J. Gong, G. Chen, T. Chen, X. Xiao, J. Li, Solvent-Assisted Hydrothermal Deposition Approach for Highly-Efficient $Sb_2(S,Se)_3$ Thin-Film Solar Cells, Adv Energy Mater 13 (2023) 2300391. **https://doi.org/10.1002/AENM.202300391.**

[43] X. Wang, S.R. Kavanagh, D.O. Scanlon, A. Walsh, Upper efficiency limit of Sb_2Se_3 solar cells, Joule 8 (2024) 2105–2122. **https://doi.org/10.1016/J.JOULE.2024.05.004.**

[44] V.S. George, A.D. Rasu Chettiar, S. Rajendran, H. Bencherif, P. Sasikumar, L. Marasamy, Modelling Insights of $Sb_2(S,Se)_3$ Solar Cells Using Triazatruxene Hole Transport Layers, Adv Theory Simul (2025) e00487. **https://doi.org/10.1002/ADTS.202500487**.

[45] R.E. Williams, Q.M. Ramasse, K.P. McKenna, L.J. Phillips, P.J. Yates, O.S. Hutter, K. Durose, J.D. Major, B.G. Mendis, Evidence for Self-healing Benign Grain Boundaries and a Highly Defective Sb_2Se_3-CdS Interfacial Layer in Sb_2Se_3 Thin-Film Photovoltaics, ACS Appl Mater Interfaces 12 (2020) 21730–21738. **https://doi.org/10.1021/acsami.0c03690.**

[46] S. Vadakkedath Gopi, R. Krautmann, A. Katerski, R. Josepson, D. Untila, J. Hiie, M. Krunks, I.O. Acik, N. Spalatu, Optimization of VTD Sb_2Se_3 absorber growth rate in CdS/Sb_2Se_3 thin film solar cells: A defect perspective on chloride vs non-chloride based devices, Solar Energy Materials and Solar Cells 293 (2025) 113856. **https://doi.org/10.1016/J.SOLMAT.2025.113856.**

[47] X. Xiong, C. Ding, B. Jiang, G. Zeng, B.Li, An Optimization Path for $Sb_2(S,Se)_3$ Solar Cells to Achieve an Efficiency Exceeding 20%, Nanomaterials, (2024). **https://www.mdpi.com/2079-4991/14/17/1433**.

[48] R. Kumari, M. Mamta, R. Kumar, Y. Singh, V.N. Singh, 24% Efficient, Simple ZnSe/Sb_2Se_3 Heterojunction Solar Cell: An Analysis of PV Characteristics and Defects, ACS Omega 8 (2022) 1632–1642. **https://doi.org/10.1021/ACSOMEGA.2C07211**.

[49] J. Tao, X. Hu, Y Guo, J Hong, K Li, J Jiang, S Chen, C Jing, F Yue, P Yang, C ZhangSolution-processed SnO_2 interfacial layer for highly efficient Sb_2Se_3 thin film solar cells, Nano Energy, (2019). **https://doi.org/10.1016/j.nanoen.2019.04.019**.

[50] A. Maiti, S. Chatterjee, A.J. Pal, Sulfur-Vacancy Passivation in Solution-Processed Sb_2S_3 Thin Films: Influence on Photovoltaic Interfaces, ACS Applied Energy Materials, 2019•ACS Publications 3 (2020) 810–821. **https://doi.org/10.1021/ACSAEM.9B01951.**

[51] Y. Wang, R. Tang, L. Huang, C. Qian, W. Lian, C. Zhu, T. Chen, Post-Treatment of TiO_2 Film Enables High-Quality Sb_2Se_3 Film Deposition for Solar Cell Applications, ACS Applied Materials & Interfaces, 14 (2022) 33181–33190. **https://doi.org/10.1021/ACSAMI.2C07157.**

[52] W. Wang, L. Yao, J. Dong, L. Wu, Z. Cao, L. Hui, G. Chen, J. Luo, Y. Zhang, Interface Modification Uncovers the Potential Application of SnO_2/TiO_2 Double Electron Transport Layer in Efficient Cadmium-Free Sb_2Se_3 Devices, Advanced Materials Interfaces, 2022•Wiley Online Library 9 (2022). **https://doi.org/10.1002/ADMI.202102464.**

[53] Y. Hua, P. Liu, Y. Li, L. Sun, L.Kloo, Composite hole-transport materials based on a metal-organic copper complex and spiro-OMeTAD for efficient perovskite solar cells, Solar RRL, 2018•Wiley Online Library 2 (2018). **https://doi.org/10.1002/SOLR.201700073**.

[54] Y. Shi, Y. Xue, K. Hou, G. Meng, K. Wang, R. Chi, F. Chen, H. Ren, M. Pang, C. Hao, Molecular structure simplification of the most common hole transport materials

in perovskite solar cells, RSC Advances, 2016•pubs.Rsc.Org (2016). **https://doi.org/10.1039/c6ra21448g.**

[55] L. Guguloth, K. Singh, V. Channu, K.Kumari, Enhancement in performance of ternary blend-polymer solar cells using a PEDOT: PSS–graphene oxide hole transport layer via Förster resonance energy transfer, Materials Advances, 1 (2020) 2872. **https://doi.org/10.1039/d0ma00532k**.

[56] T. Ding, N. Wang, C. Wang, X. Wu, W. Liu, Q. Zhang, W. Fan, X. Wei Sun, Solution-processed inorganic copper (I) thiocyanate as a hole injection layer for high-performance quantum dot-based light-emitting diodes, RSC Advances, 7 (2017) 26322–26327. **https://doi.org/10.1039/c7ra03433d.**

[57] N. Rahman, M.D. Haque, M.F. Rahman, M.M. Islam, M.A.N. Juthi, A.R. Roy, M.A. Akter, M.F. Islam, Assessing the performance of $MoTe_2$ based solar cell with Cu_2O hole transport layer through device simulation, Discover Materials 3 (2023) 1–17. **https://doi.org/10.1007/S43939-023-00061-7/FIGURES/1.**

[58] H. Guo, S. Huang, H. Zhu, T. Zhang, K. Geng, S. Jiang, D. Gu, J. Su, X. Lu, H. Zhang, S. Zhang, Enhancement in the Efficiency of Sb_2Se_3 Solar Cells by Triple Function of Lithium Hydroxide Modified at the Back Contact Interface, Advanced Science 10 (2023) **2304246. https://doi.org/10.1002/ADVS.202304246**.

[59] L. Zhang, M. Peng, S. Cong, Q. Yi, B. Qian, Y. Ma, H. Huang, W. Wang, Interface diffusion blocking layer for the performance improvement of substrate structured Sb_2Se_3 solar cells, Solar Energy 282 (2024) 112945. **https://doi.org/10.1016/J.SOLENER.2024.112945.**

[60] T.P. Weiss, I. Minguez-Bacho, E. Zuccalà, M. Melchiorre, N. Valle, B. El Adib, T. Yokosawa, E. Spiecker, J. Bachmann, P.J. Dale, S. Siebentritt, Post-deposition annealing and interfacial atomic layer deposition buffer layers of Sb_2Se_3/CdS stacks for reduced interface recombination and increased open-circuit voltages, Progress in Photovoltaics: Research and Applications 31 (2023) 203–219. **https://doi.org/10.1002/pip.3625**.

[61] M. Neophytou, M. De Bastiani, N. Gasparini, E. Aydin, E. Ugur, A. Seitkhan, F. Moruzzi, Y. Choaie, A.J. Ramadan, J.R. Troughton, R. Hallani, Enhancing the Charge Extraction and Stability of Perovskite Solar Cells Using Strontium Titanate ($SrTiO_3$) Electron Transport Layer, ACS Applied Energy Materials, 2 (2019) 8090–8097. **https://doi.org/10.1021/ACSAEM.9B01567**.

[62] P. Chaluvachar, G.T. Mahesha, Y.N. Sudhakar, V. Nair, D. Pai, A Review on Graphitic Carbon Nitride and Conducting Polymer Nanocomposite Electrodes for Supercapacitors, Engineering Proceedings 2023, Vol. 59, Page 154 59 (2024) 154. **https://doi.org/10.3390/ENGPROC2023059154**.

[63] J. Dong, Y. Zhang, M.I. Hussain, W. Zhou, Y. Chen, L.N. Wang, g-C_3N_4: Properties, Pore Modifications, and Photocatalytic Applications, Nanomaterials 2022, Vol. 12, Page 121 12 (2021) 121. **https://doi.org/10.3390/NANO12010121**.

[64] S.M. Sze, K.K. Ng, Physics of Semiconductor Devices, Third Edition, Physics of Semiconductor Devices, Third Edition (2006) 1–813. **https://doi.org/10.1002/0470068329**.

[65] D. Berney Needleman, Optical design guidelines for spectral splitting photovoltaic systems : a sensitivity analysis approach, (2014). **https://dspace.mit.edu/handle/1721.1/92072**.

[66] Peter. Würfel, Uli. Würfel, Physics of solar cells : from basic principles to advanced concepts, (2016) 274.

[67] Quantum Efficiency | PVEducation, (n.d.). **https://www.pveducation.org/pvcdrom/solar-cell-operation/quantum-efficiency**.

[68] B. Qi, J. Wang, Fill factor in organic solar cells, Physical Chemistry Chemical Physics 15 (2013) 8972–8982. **https://doi.org/10.1039/C3CP51383A.**

[69] B. Ehrler, E. Alarcón-Lladó, S.W. Tabernig, T. Veeken, E.C. Garnett, A. Polman, Photovoltaics reaching for the Shockley–Queisser limit, ACS Energy Lett 5 (2020) 3029–3033. **https://doi.org/10.1021/ACSENERGYLETT.0C01790.**

[70] H. Shiel, O.S. Hutter, L.J. Phillips, J.E.N. Swallow, L.A.H. Jones, T.J. Featherstone, M.J. Smiles, P.K. Thakur, T.L. Lee, V.R. Dhanak, J.D. Major, T.D. Veal, Natural Band Alignments and Band Offsets of Sb_2Se_3 Solar Cells, ACS Appl Energy Mater 3 (2020) 11617–11626. **https://doi.org/10.1021/ACSAEM.0C01477.**

[71] L. Wang, D.B. Li, K. Li, C. Chen, H.X. Deng, L. Gao, Y. Zhao, F. Jiang, L. Li, F. Huang, Y. He, H. Song, G. Niu, J. Tang, Stable 6%-efficient Sb_2Se_3 solar cells with a ZnO buffer layer, Nature Energy, 2 (2017). **https://doi.org/10.1038/NENERGY.2017.46.**

[72] W. Zajac, A. Rozycka, A. Trenczek-Zajac, Rational Design of the Electronic Structure of CdS Nanopowders, Inorg Chem 62 (2023) 10955–10964. **https://doi.org/10.1021/ACS.INORGCHEM.3C00935.**

[73] M.G. Helander, M.T. Greiner, Z.B. Wang, W.M. Tang, Z.H. Lu, Work function of fluorine doped tin oxide, Journal of Vacuum Science & Technology A: Vacuum, Surfaces, and Films 29 (2011). **https://doi.org/10.1116/1.3525641/244332.**

[74] M. DeJarld, P.M. Campbell, A.L. Friedman, M. Currie, R.L. Myers-Ward, A.K. Boyd, S.G. Rosenberg, S.P. Pavunny, K.M. Daniels, D.K. Gaskill, Surface potential and thin film quality of low work function metals on epitaxial graphene, Scientific Reports 2018 8:1 8 (2018) 1–11. **https://doi.org/10.1038/s41598-018-34595-1.**

[75] Y. Zhou, L. Wang, S. Chen, S. Qin, X. Liu, J. Chen, D.-J. Xue, M. Luo, Y. Cao, Y. Cheng, E.H. Sargent, J. Tang, Thin-film Sb_2Se_3 photovoltaics with oriented one-dimensional ribbons and benign grain boundaries, Nature Photonics, (2015). **https://doi.org/10.1038/NPHOTON.2015.**

[76] Y. Zeng, K. Sun, J. Huang, M.P. Nielsen, F. Ji, C. Sha, S. Yuan, X. Zhang, C. Yan, X. Liu, H. Deng, Y. Lai, J. Seidel, N. Ekins-Daukes, F. Liu, H. Song, M. Green, X. Hao, Quasi-vertically-orientated antimony sulfide inorganic thin-film solar cells achieved by vapor transport deposition, ACS Applied Materials & Interfaces, 2020•ACS Publications 12 (2020) 22825–22834. **https://doi.org/10.1021/ACSAMI.0C02697.**

[77] KP McKenna, Self-Healing of Broken Bonds and Deep Gap States in Sb_2Se_3 and Sb_2S_3, Advanced Electronic Materials, Wiley Online Library 7 (2021). **https://doi.org/10.1002/AELM.202000908**.

[78] L. Guo, B. Zhang, Y. Qin, D. Li, L. Li, X. Qian, F. Yan, Tunable Quasi-One-Dimensional Ribbon Enhanced Light Absorption in Sb_2Se_3 Thin-film Solar Cells Grown by Close-Space Sublimation, Solar RRL, 2 (2018). **https://doi.org/10.1002/SOLR.201800128.**

[79] R.X. Yang, K.T. Butler, A. Walsh, Assessment of hybrid organic–inorganic antimony sulfides for earth-abundant photovoltaic applications, The Journal of Physical Chemistry Letters, 6 (2015) 5009–5014. **https://doi.org/10.1021/ACS.JPCLETT.5B02555.**

[80] H. Deng, S. Yuan, X. Yang, J. Zhang, J. Khan, Y. Zhao, M. Ishaq, W. Ye, Y.B. Cheng, H. Song, J. Tang, High-throughput method to deposit continuous composition spread $Sb_2(SexS1 - x)_3$ thin film for photovoltaic application, Progress in Photovoltaics: Research and Applications, 26 (2018) 281–290. **https://doi.org/10.1002/PIP.2980.**

[81] H. Zhang, S. Yuan, H. Deng, M. Ishaq, X. Yang, T. Hou, U.A. Shah, H. Song, J. Tang, Controllable orientations for Sb_2S_3 solar cells by vertical VTD method, Progress in Photovoltaics: Research and Applications, 28 (2020) 823–832. **https://doi.org/10.1002/PIP.3278.**

[82] X. Jin, Y. Fang, T. Salim, M. Feng, S. Hadke, S.W. Leow, T.C. Sum, L.H. Wong, In Situ Growth of -Oriented Sb_2S_3 for Solution-Processed Planar Heterojunction Solar Cell with 6.4% Efficiency, Advanced Functional Materials, 30 (2020). **https://doi.org/10.1002/ADFM.202002887.**

[83] M.M. Nicolás-Marín, J.R. González-Castillo, O. Vigil-Galán, M. Courel, The state of the art of $Sb_2(S, Se)_3$ thin film solar cells: Current progress and future prospect, J Phys D Appl Phys 55 (2022). **https://doi.org/10.1088/1361-6463/AC5F32.**

[84] M. Calixto-Rodriguez, H.M. García, M.T.S. Nair, P.K. Nair, Antimony chalcogenide/lead selenide thin film solar cell with 2.5% conversion efficiency prepared by chemical deposition, Journal of Solid State Science and Technology, 2 (2013) Q69–Q73. **https://doi.org/10.1149/2.027304JSS/META**.

[85] Y.C. Choi, Y.H. Lee, S.H. Im, J.H. Noh, T.N. Mandal, W.S. Yang, S.I. Seok, Efficient Inorganic-Organic Heterojunction Solar Cells Employing $Sb_2(Sx/Se1-x)_3$ Graded-Composition Sensitizers, Advanced Energy Materials, 4 (2014). **https://doi.org/10.1002/AENM.201301680.**

[86] R. Tang, X. Wang, W. Lian, J. Huang, Q. Wei, M. Huang, Y. Yin, C. Jiang, S. Yang, G. Xing, S. Chen, C. Zhu, X. Hao, M.A. Green, T. Chen, Hydrothermal deposition of antimony selenosulfide thin films enables solar cells with 10% efficiency, Nature Energy, 5 (2020) 587–595. **https://doi.org/10.1038/S41560-020-0652-3.**

[87] X. Wang, R. Tang, C. Jiang, W. Lian, H. Ju, G. Jiang, Z. Li, C. Zhu, T. Chen, Manipulating the Electrical Properties of $Sb_2(S,Se)_3$ Film for High-Efficiency Solar Cell, Advanced Energy Materials, 10 (2020). **https://doi.org/10.1002/AENM.202002341.**

[88] Y. Zhao, S. Wang, C. Jiang, C. Li, P. Xiao, R. Tang, J. Gong, G. Chen, T. Chen, J. Li, X. Xiao, Regulating Energy Band Alignment via Alkaline Metal Fluoride Assisted Solution Post-Treatment Enabling $Sb_2(S,Se)_3$ Solar Cells with 10.7% Efficiency, Advanced Energy Materials, 12 (2022). **https://doi.org/10.1002/AENM.202103015.**

[89] S. Lu, Y. Zhao, X. Wen, D.J. Xue, C. Chen, K. Li, R. Kondrotas, C. Wang, J. Tang, $Sb_2(Se1-xSx)_3$ Thin-Film Solar Cells Fabricated by Single-Source Vapor

Transport Deposition, Solar RRL, 3 (2019). **https://doi.org/10.1002/SOLR.201800280**.

[90] H Guo, S Huang, X Ni, H Zhu, J Su, C Ma, S Jiang, H Zhang, D Gu, S Zhang, J Qiu, N Yuan, High-efficiency and stable $Sb_2(S,Se)_3$ thin film solar cells with phthalocyanine as a hole transport layer, Journal of Materials Chemistry C, (2023). **https://doi.org/10.1039/D3TC01980B**.

[91] H. Deng, Y. Zeng, M. Ishaq, S. Yuan, H. Zhang, X. Yang, M. Hou, U. Farooq, J. Huang, K. Sun, Quasiepitaxy Strategy for Efficient Full-Inorganic Sb_2S_3 Solar Cells, Advanced Functional Materials, 29 (2019). **https://doi.org/10.1002/ADFM.201901720**.

[92] K. Tsujimoto, D.C. Nguyen, S. Ito, H. Nishino, H. Matsuyoshi, A. Konno, G.R.A. Kumara, K. Tennakone, TiO_2 Surface Treatment Effects by Mg^{2+}, Ba^{2+}, and Al^{3+} on Sb_2S_3 Extremely Thin Absorber Solar Cells, The Journal of Physical Chemistry C, 116 (2012) 13465–13471. **https://doi.org/10.1021/JP208937J**.

[93] W.H. Kim, S. Woo, K.P. Kim, S.M. Kwon, D.H. Kim, Efficient TiO_2 Surface Treatment Using Cs_2CO_3 for Solution-Processed Planar-Type Sb_2S_3 Solar Cells, Nanoscale Research Letters, 14 (2019). **https://doi.org/10.1186/S11671-019-2858-5**.

[94] C Lan, J Luo, H Lan, B Fan, H Peng, J Zhao, H Sun, Z Zheng, G Liang, P Fan, Enhanced Charge Extraction of Li-Doped TiO_2 for Efficient Thermal-Evaporated Sb_2S_3 Thin Film Solar Cells, Mdpi.Materials, (2018). **https://www.mdpi.com/1996-1944/11/3/355**.

[95] M. Ishaq, S. Chen, U. Farooq, M. Azam, H. Deng, Z.H. Su, Z.H. Zheng, P. Fan, H.S. Song, G.X. Liang, High Open-Circuit Voltage in Full-Inorganic Sb_2S_3 Solar Cell via Modified Zn-Doped TiO_2 Electron Transport Layer, Solar RRL, 4 (2020). **https://doi.org/10.1002/SOLR.202000551**.

[96] S. Lu, Y. Zhao, C. Chen, Y. Zhou, D. Li, K. Li, W. Chen, X. Wen, C. Wang, R. Kondrotas, N. Lowe, J. Tang, Sb_2Se_3 Thin-Film Photovoltaics Using Aqueous Solution Sprayed SnO_2 as the Buffer Layer, Advanced Electronic Materials, 4 (2018). **https://doi.org/10.1002/AELM.201700329**.

[97] Z Chen, H Guo, C Ma, X Wang, X Jia, N Yuan, J Ding, Efficiency improvement of Sb_2Se_3 solar cells based on La-doped SnO_2 buffer layer, Solar Energy, (2019). **https://doi.org/10.1016/j.solener.2019.05.026**.

[98] J Zhou, X Zhang, H Chen, Z Tang, D Meng, K Chi, Y Cai, G Song, Y Cao, Z Hu, Dual-function of $CdCl_2$ treated SnO_2 in Sb_2Se_3 solar cells, Applied Surface Science, (2020). **https://doi.org/10.1016/j.apsusc.2020.147632**.

[99] H Sirringhaus, PJ Brown, RH Friend, MM Nielsen, K Bechgaard, BMW Langeveld-Voss, AJ Spiering, RA Janssen, EW Meijer, P Herwig, DD de Leeuw, Two-dimensional charge transport in self-organized, high-mobility conjugated polymers, Nature.Com Nature, (1999). **https://doi.org/10.1038/44359**.

[100] C. Chen, L. Wang, L. Gao, D. Nam, D. Li, K. Li, Y. Zhao, C. Ge, H. Cheong, H. Liu, H. Song, J. Tang, 6.5% Certified Efficiency Sb_2Se_3 Solar Cells Using PbS Colloidal Quantum Dot Film as Hole-Transporting Layer, ACS Energy Letters, 2 (2017) 2125–2132. **https://doi.org/10.1021/ACSENERGYLETT.7B00648**.

[101] J.A. Christians, P. V. Kamat, Trap and Transfer. Two-Step Hole Injection Across the Sb_2S_3/CuSCN Interface in Solid-State Solar Cells, ACS PublicationsJA Christians, PV KamatACS Nano, 2013•ACS Publications 7 (2013) 7967–7974. **https://doi.org/10.1021/NN403058F**.

[102] X Jin, Y Yuan, C Jiang, H Ju, G Jiang, W Liu, C Zhu, T Chen, Solution processed NiOx hole-transporting material for all-inorganic planar heterojunction Sb2S3 solar cells, Solar Energy Materials and Solar Cells, 185 (2018) 542–548. **https://doi.org/10.1016/J.SOLMAT.2018.06.017**.

[103] L. Zhang, C. Jiang, C. Wu, H. Ju, G. Jiang, W. Liu, C. Zhu, T. Chen, V_2O_5 as Hole Transporting Material for Efficient All Inorganic Sb_2S_3 Solar Cells, ACS Applied Materials & Interfaces, 10 (2018) 27098–27105. **https://doi.org/10.1021/ACSAMI.8B09843**.

[104] C. Liu, K. Shen, D. Lin, Y. Cao, S. Qiu, J. Zheng, F. Bao, Y. Gao, H. Zhu, Z. Li, Y. Mai, Back Contact Interfacial Modification in Highly-Efficient All-Inorganic Planar nip Sb_2Se_3 Solar Cells, ACS Publications 12 (2020) 38397–38405. **https://doi.org/10.1021/ACSAMI.0C10629**.

[105] Y Ma, Y Yin, G Li, W Lian, J Zhang, R Tang, H Ju, T Chen, Aqueous solution processed MoS_3 as an eco-friendly hole-transport layer for all-inorganic Sb_2 Se_3 solar cells, Chemical Communications, (2020). **https://doi.org/10.1039/D0CC05997H**.

[106] L. Yao, L. Lin, H. Liu, F. Wu, J. Li, S. Chen, Z. Huang, G. Chen, Front and Back contact engineering for high-efficient and low-cost hydrothermal derived $Sb_2(S,Se)_3$ solar cells by using FTO/SnO_2 and carbon, J Mater Sci Technol 58 (2020) 130–137. **https://doi.org/10.1016/J.JMST.2020.03.049**.

[107] H Li, L Lin, L Yao, F Wu, D Wei, G Liu, Z Huang, S Chen, J Li, G Chen, High-Efficiency $Sb_2(S,Se)_3$ Solar Cells with New Hole Transport Layer-Free Back Architecture via 2D Titanium-Carbide Mxene, Wiley Online Advanced Functional Materials, 2022•Wiley Online Library 32 (2022). **https://doi.org/10.1002/ADFM.202110335**.

[108] A. Mutlu, S. Siyahjani, G. Ltekin, Z. Gü Lay Gü Nel, C. Zafer, Enhanced Hole Mobility of p-Type Materials by Molecular Engineering for Efficient Perovskite Solar Cells, ACS Omega, 8 (2778) 27784–27793. **https://doi.org/10.1021/acsomega.3c04088**.

[109] K. Rakstys, A. Abate, M.I. Dar, P. Gao, V. Jankauskas, G. Jacopin, E. Kamarauskas, S. Kazim, S. Ahmad, M. Grätzel, M.K. Nazeeruddin, Triazatruxene-Based Hole Transporting Materials for Highly Efficient Perovskite Solar Cells, J Am Chem Soc 137 (2015) 16172–16178. **https://doi.org/10.1021/jacs.5b11076**.

[110] A. Connell, Z. Wang, Y.-H. Lin, P.C. Greenwood, A.A. Wiles, E.W. Jones, L. Furnell, R. Anthony, C.P. Kershaw, G. Cooke, H.J. Snaith, P.J. Holliman, Low cost triazatruxene hole transporting material for> 20% efficiency perovskite solar cells, Journal of Materials Chemistry C, (2019). **https://doi.org/10.1039/C8TC04231D**.

[111] J. Jing, B. Heinrich, A. Prel, E. Steveler, T. Han, I. Bulut, S. Mery, Y. Leroy, N. Leclerc, P. Leveque, M. Rosenthal, Efficient 3D charge transport in planar triazatruxene-based dumbbell-shaped molecules forming a bridged columnar phase, Journal of Materials Chemistry A, 43 (2021). **https://doi.org/10.1039/D1TA06300F**.

[112] N. Li, Y. Chen, S. Duan, G. Chen, Y. Xu, H Tong, Y. Sanehira, T. Miyasaka, A. Li, X.F Wang, Planar perovskite solar cells using triazatruxene-based hyperbranched conjugated polymers and small molecule as hole-transporting materials, Journal of Photochemistry and Photobiology A: Chemistry 389 (2020): 112228. **https://doi.org/10.1016/j.jphotochem.2019.112228**.

[113] L. Calió, C. Momblona, L. Gil-Escrig, S. Kazim, M. Sessolo, Á. Sastre-Santos, H.J. Bolink, S. Ahmad, Vacuum deposited perovskite solar cells employing dopant-free triazatruxene as the hole transport material, Solar Energy Materials and Solar Cells, (2017). **https://doi.org/10.1016/j.solmat.2017.01.037**.

[114] E. Agafonova, M. Tepliakova,DO Balakirev, IV Dyadishchev, PK Sukhorukova,SG Protasova, AV Novikov, Stars are aligned: triazatruxene hole transporting material hits the sweet spot to reach 20% efficiency of perovskite solar

cell, Solar Energy Materials and Solar Cells, (2023). **https://doi.org/10.1016/j.solmat.2022.112168.**

[115] X. Li, C. Wang, W. Lai, W. Huang, Triazatruxene-based materials for organic electronics and optoelectronics, Journal of Materials Chemistry C, (2016) **https://doi.org/10.1039/C6TC03832H**.

[116] E. Rezaee, X. Liu, Q. Hu, L. Dong, Q. Chen, J.H. Pan, Z.X. Xu, Dopant-Free Hole Transporting Materials for Perovskite Solar Cells, Solar RRL 2 (2018). **https://doi.org/10.1002/SOLR.201800200**.

[117] L.A. Illicachi, J. Urieta-Mora, J. Calbo, J. Aragó, C. Igci, I. García-Benito, C. Momblona, B. Insuasty, A. Ortiz, C. Roldán-Carmona, A. Molina-Ontoria, E. Ortí, N. Martín, M.K. Nazeeruddin, Azatruxene-Based, Dumbbell-Shaped, Donor–π-Bridge–Donor Hole-Transporting Materials for Perovskite Solar Cells, Chemistry - A European Journal 26 (2020) 11039–11047. **https://doi.org/10.1002/CHEM.202002115**.

[118] A.A. Raheem, S. Kamaraj, V. Sannasi, C. Praveen, New D–π-A push–pull chromophores as low band gap molecular semiconductors for organic small molecule solar cell applications, Organic Chemistry Frontiers, 5 (2018) 777. **https://doi.org/10.1039/c7qo00920h**.

[119] K Rakstys, S Paek, P Gao, P Gratia, T Marszalek, G Grancini, KT Cho, K Genevicius, Molecular engineering of face-on oriented dopant-free hole transporting material for perovskite solar cells with 19% PCE, Journal of Materials Chemistry A, (2017). **https://pubs.rsc.org/en/content/articlehtml/2017/ta/c7ta01718a**.

[120] N. Miyaura, A.Suzuki, Palladium-catalyzed cross-coupling reactions of organoboron compounds, Chemical Reviews, 95 (1995) 2457–2483. **https://pubs.acs.org/doi/pdf/10.1021/cr00039a007**.

[121] C. Igci, S. Paek, K. Rakstys, H. Kanda, N. Shibayama, V. Jankauskas, C. Roldán-Carmona, H. Kim, A.M. Asiri, M.K. Nazeeruddin, D–π–A-Type Triazatruxene-Based Dopant-Free Hole Transporting Materials for Efficient and Stable Perovskite Solar Cells, Solar RRL 4 (2020) 2000173. **https://doi.org/10.1002/SOLR.202000173**.

[122] D. Kil, C. Lu, J. Ji, C. Kim, H.Kim, Dopant-free triazatruxene-based hole transporting materials with three different end-capped acceptor units for perovskite solar cells, Nanomaterials, (2020). **https://www.mdpi.com/2079-4991/10/5/936**.

[123] D. Kim, S. Gwon, K. Park, E.C. Jeon, Structural and Optical Properties of $SrTiO_3$-Based Ceramics for Energy and Electronics Applications, Crystals, 2024•mdpi.Com 14 (2024). **https://doi.org/10.3390/CRYST14110942**.

[124] K. Van Benthem, C. Elsässer, R.H. French, Bulk electronic structure of $SrTiO_3$: Experiment and theory, J Appl Phys 90 (2001) 6156–6164. **https://doi.org/10.1063/1.1415766**.

[125] M. Siebenhofer, A. Viernstein, M. Morgenbesser, J. Fleig, M. Kubicek, Photoinduced electronic and ionic effects in strontium titanate, Mater Adv 2 (2021) **7583. https://doi.org/10.1039/D1MA00906K**.

[126] N. Tsvetkov, B.C. Moon, J.Y. Lee, J.K. Kang, Controlled Synthesis of Nanocrystalline Nb:$SrTiO_3$ Electron Transport Layers for Robust Interfaces and Stable High Photovoltaic Energy Conversion Efficiency in perovskite halide solar cells, ACS Applied Energy Materials 3, no. 1 (2019): 344-351. **https://doi.org/10.1021/ACSAEM.9B01592**.

[127] T. Mahmoudi, Y. Wang, Y.B. Hahn, $SrTiO_3$/$Al2O_3$-Graphene Electron Transport Layer for Highly Stable and Efficient Composites-Based Perovskite Solar Cells with 20.6% Efficiency, Advanced Energy Materials, 2020•Wiley Online Library 10 (2020). **https://doi.org/10.1002/AENM.201903369**.

[128] L.L. Rusevich, M. Tyunina, E.A. Kotomin, N. Nepomniashchaia, A. Dejneka, The electronic properties of $SrTiO_3$-δ with oxygen vacancies or substitutions, Sci Rep 11 (2021). **https://doi.org/10.1038/S41598-021-02751-9**.

[129] A. Bera, K. Wu, A. Sheikh, E. Alarousu, O.F. Mohammed, T. Wu, Perovskite Oxide $SrTiO_3$ as an Efficient Electron Transporter for Hybrid Perovskite Solar Cells, The Journal of Physical Chemistry C, 118 (2014) 28494–28501. **https://doi.org/10.1021/JP509753P**.

[130] G. Dong, Y. Zhang, Q. Pan, J.Q.-J. of P. and, undefined 2014, A fantastic graphitic carbon nitride (g-C_3N_4) material: electronic structure, photocatalytic and photoelectronic properties, Journal of Photochemistry and Photobiology C: Photochemistry Reviews 20 (2014): 33-50. **https://doi.org/10.1016/j.jphotochemrev.2014.04.002**.

[131] A. Alaghmandfard, K. Ghandi, A comprehensive review of graphitic carbon nitride (g-C_3N_4)–metal oxide-based nanocomposites: potential for photocatalysis and sensing, 12 (2022). **https://doi.org/10.3390/NANO12020294**.

[132] W.J. Ong, L.L. Tan, Y.H. Ng, S.T. Yong, S.P. Chai, Graphitic Carbon Nitride (gC_3N_4)-Based Photocatalysts for Artificial Photosynthesis and Environmental Remediation: Are We a Step Closer To Achieving, Chemical Reviews, 116 (2016) 7159–7329. **https://doi.org/10.1021/ACS.CHEMREV.6B00075**.

[133] L.L. Jiang, Z.K. Wang, M. Li, C.C. Zhang, Q.Q. Ye, K.H. Hu, D.Z. Lu, P.F. Fang, L.S. Liao, Passivated Perovskite Crystallization via g-C_3N_4 for High-Performance Solar Cells, Advanced Functional Materials, 28 (2018). **https://doi.org/10.1002/ADFM.201705875**.

[134] M. Lee, E.Y. Mei Ang, W. Toh, P.C. Wang, T.Y. Ng, S.Y. Lee, S.W. Kim, M.A. Green, X. Hao, J.S. Yun, D.H. Seo, Hybrid SnO_2/gC_3N_4 layers with plasma-induced modifications for enhanced charge transport in perovskite solar cells, Journal of Materials Chemistry A, 13 (2025) 12949–12956. **https://doi.org/10.1039/D5TA00480B**.

[135] Y. Wang, J. Zou, C. Zhao, H. Jiang, Y. Song, L. Zhang, X. Li, F. Wang, L. Fan, X. Liu, M. Wei, L. Yang, Building a Charge Transfer Bridge between gC_3N_4 and Perovskite with Molecular Engineering to Achieve Efficient Perovskite Solar Cells, ACS Applied Materials & Interfaces, 16 (2024) 13815–13827. **https://doi.org/10.1021/ACSAMI.3C19475**.

[136] M. Burgelman, J. Verschraegen, S. Degrave, P. Nollet, Modeling thin-film PV devices, Wiley Online Library 12 (2004) 143–153. **https://doi.org/10.1002/PIP.524**.

[137] S.k, Mukaddar, Optimization of efficiency of $CsPbI_2Br$ by using different electron transport and hole transport layers: A DFT and SCAPS-1D simulation, Elsevier 197 (2025). **https://doi.org/10.1016/J.MICRNA.2024.208024**.

[138] M. Mahmood, M.T. Islam, M.S. Sadek, K. Noor, MHB Baharuddin, M Ibrahim, GU Sheikh, MA Ibrahim, MS Soliman, K Sobayel, Advancing perovskite solar cells: Unveiling the superior efficiency of copper-doped Strontium Titanate as a novel ETL, Solar Energy, 2024 **https://doi.org/10.1016/j.solener.2024.112806**.

[139] X. Chen, B. Che, Y. Zhao, S. Wang, H. Li, J. Gong, G. Chen, T. Chen, X. Xiao, J. Li, Solvent-Assisted Hydrothermal Deposition Approach for Highly-Efficient $Sb_2(S,Se)_3$ Thin-Film Solar Cells, Advanced Energy Materials, 13 (2023). **https://doi.org/10.1002/aenm.202300391**.

[140] J. Liu, T. Zhang, Z. Wang, G. Dawson, W. Chen, Simple pyrolysis of urea into graphitic carbon nitride with recyclable adsorption and photocatalytic activity, J Mater Chem 21 (2011) 14398–14401. **https://doi.org/10.1039/C1JM12620B**.

[141] S. Kumari, J. Mahanta, M.K. Singh, A. Suhail, N.R. Peela, D.K. Singh, Graphitic carbon nitride-based high-performance Organic Field-Effect Transistor and photodetector, Diam Relat Mater 155 (2025) 112289. **https://doi.org/10.1016/J.DIAMOND.2025.112289**.

[142] A. Verma, N. Shrivastav, J. Madan, Optimizing Solar Energy Capture: Exploring Absorber Layer Thickness in Carbon-Nitrate-PSK Solar Cells, In 2023 3rd International Conference on Emerging Frontiers in Electrical and Electronic Technologies (ICEFEET), pp. 1-3. IEEE, 2023. **https://doi.org/10.1109/ICEFEET59656.2023.10452202**.

[143] V. Ragupathi, P. Panigrahi, N. Subramaniam, Scalable fabrication of graphitic-carbon nitride thin film for optoelectronic application, Materials Today: Proceedings, (2023). **https://doi.org/10.1016/j.matpr.2021.06.125**.

[144] A. Sunny, S.R. Al Ahmed, Numerical Simulation and Performance Evaluation of Highly Efficient Sb_2Se_3 Solar Cell with Tin Sulfide as Hole Transport Layer, Physica Status Solidi (b) 258 (2021) 2000630. **https://doi.org/10.1002/PSSB.202000630**.

[145] K. Afridi, M. Noman, S.T. Jan, Evaluating the influence of novel charge transport materials on the photovoltaic properties of MASnI3solar cells through SCAPS-1D modelling, R Soc Open Sci 11 (2024). **https://doi.org/10.1098/rsos.231202**.

[146] G.W. Kim, D. V. Shinde, T. Park, Thickness of the hole transport layer in perovskite solar cells: performance versus reproducibility, RSC Adv 5 (2015) 99356–99360. **https://doi.org/10.1039/C5RA18648J**.

[147] A. Bag, R. Radhakrishnan, R. Nekovei, R. Jeyakumar, Effect of absorber layer, hole transport layer thicknesses, and its doping density on the performance of perovskite solar cells by device simulation, Solar Energy 196 (2020) 177–182. **https://doi.org/10.1016/J.SOLENER.2019.12.014**.

[148] V.M. Le Corre, M. Stolterfoht, L. Perdigón Toro, M. Feuerstein, C. Wolff, L. Gil-Escrig, H.J. Bolink, D. Neher, L.J.A. Koster, Charge Transport Layers Limiting the Efficiency of Perovskite Solar Cells: How to Optimize Conductivity, Doping, and Thickness, ACS Appl Energy Mater 2 (2019) 6280–6287. **https://doi.org/10.1021/acsaem.9b00856**.

[149] A. Ghosh, A.A. Hassan, H.A. Alrafai, S.K.A. Abdelrahim, A comprehensive study on electron and hole transport layers for designing and optimizing the efficiency of $MoSe_2$-Based solar cells using numerical simulation techniques, Heliyon 10 (2024) 35061. **https://doi.org/10.1016/J.HELIYON.2024.E35061**.

[150] Y. Wang, S. Akel, B. Klingebiel, T. Kirchartz, Hole Transporting Bilayers for Efficient Micrometer-Thick Perovskite Solar Cells, Adv Energy Mater 14 (2024) 2302614. **https://doi.org/10.1002/aenm.202302614**.

[151] G.O. Odunmbaku, S. Chen, B. Guo, Y. Zhou, N.A.N. Ouedraogo, Y. Zheng, J. Li, M. Li, K. Sun, Recombination Pathways in Perovskite Solar Cells, Adv Mater Interfaces 9 (2022) 2102137**, https://doi.org/10.1002/ADMI.202102137**.

[152] C. Chen, Y. Yin, W. Lian, L. Jiang, R. Tang, C. Jiang, C. Wu, D. Gao, X. Wang, F. Fang, C. Zhu, T. Chen, Pulsed laser deposition of antimony selenosulfide thin film for efficient solar cells, Appl Phys Lett 116 (2020). **https://doi.org/10.1063/1.5139467**.

[153] G.K. Gupta, A. Dixit, Simulation studies on photovoltaic response of ultrathin $CuSb(S/Se)_2$ ternary compound semiconductors absorber-based single junction solar cells, Int J Energy Res 44 (2020) 3724–3736. **https://doi.org/10.1002/ER.5158**.

[154] Y. Cao, X. Zhu, H. Chen, X. Zhang, J. Zhou, Z. Hu, J. Pang, Towards high efficiency inverted Sb_2Se_3 thin film solar cells, Solar Energy Materials and Solar Cells 200 (2019) 109945. **https://doi.org/10.1016/J.SOLMAT.2019.109945**.

[155] A. Ahmed, K. Riaz, H. Mehmood, T. Tauqeer, Z. Ahmad, Performance optimization of $CH_3NH_3Pb(I_{1-x}Br_x)_3$ based perovskite solar cells by comparing different ETL materials through conduction band offset engineering, Opt Mater (Amst) 105 (2020) 109897. **https://doi.org/10.1016/J.OPTMAT.2020.109897**.

[156] R. Ranjan, N. Anand, M.N. Tripathi, N. Srivastava, A.K. Sharma, M. Yoshimura, L. Chang, R.N. Tiwari, SCAPS study on the effect of various hole transport layer on highly efficient 31.86% eco-friendly CZTS based solar cell, Scientific Reports 2023 13:1 13 (2023) 1–16. **https://doi.org/10.1038/s41598-023-44845-6**.

[157] A. Tara, V. Bharti, S. Sharma, R. Gupta, Device simulation of $FASnI_3$ based perovskite solar cell with $Zn(O_{0.3}, S_{0.7})$ as electron transport layer using SCAPS-1D, Opt Mater (Amst) 119 (2021) 111362. **https://doi.org/10.1016/J.OPTMAT.2021.111362**.

[158] A. Oktafiani, F. Wahyu Adi Nugroho, Z. Salsabila, al -, P. Kartikay, K. Mokurala, B. Sharma, M. Ali Ashraf, I. Alam, Numerical simulation of CIGS, CISSe and CZTS-based solar cells with In_2S_3 as buffer layer and Au as back contact using SCAPS 1D, Engineering Research Express 2 (2020) 035015. **https://doi.org/10.1088/2631-8695/ABADE6**.

[159] Y.H. Khattak, F. Baig, H. Toura, S. Ullah, B. Marí, S. Beg, H. Ullah, Effect of CZTSe BSF and minority carrier life time on the efficiency enhancement of CZTS kesterite solar cell, Current Applied Physics 18 (2018) 633–641. **https://doi.org/10.1016/J.CAP.2018.03.013**.

[160] J.Y. Park, R.B.V. Chalapathy, A.C. Lokhande, C.W. Hong, J.H. Kim, Fabrication of earth abundant $Cu_2ZnSnSSe_4$ (CZTSSe) thin film solar cells with cadmium free zinc sulfide (ZnS) buffer layers, J Alloys Compd 695 (2017) 2652–2660. **https://doi.org/10.1016/J.JALLCOM.2016.11.178**.

[161] CW Hong, SW Shin, MP Suryawanshi, MG Gang, J Heo, JH Kim, Chemically Deposited CdS Buffer/Kesterite Cu_2ZnSnS_4 Solar Cells: Relationship between CdS Thickness and Device Performance, ACS Applied Materials & Interfaces, (2017) 9 (2017) 36733–36744. **https://doi.org/10.1021/acsami.7b09266**.

[162] L Marasamy, R Aruna-Devi, OID Robledo, JÁC Carvayar, NEV Barragán, J Santos-Cruz, Probing the significance of RF magnetron sputtering conditions on the physical properties of CdS thin films for ultra-thin CdTe photovoltaic applications, Applied Surface Science, (2022) Elsevier (n.d.). **https://doi.org/10.1016/j.apsusc.2021.151640**.

[163] A Cantas, F Turkoglu, E Meriç, FG Akça, M Ozdemir, E Tarhan, L Ozyuzer, G Aygun, Importance of CdS buffer layer thickness on Cu_2ZnSnS_4-based solar cell efficiency, Iopscience.Iop.OrgJournal of Physics D: Applied Physics, (2018). **https://doi.org/10.1088/1361-6463/aac8d3**.

[164] I. Pintilie, Q. Sun, J. Tang, C. Zhang, Y. Li, W. Xie, H. Deng, Q. Zheng, J. Wu, S. Cheng, Efficient environmentally friendly flexible CZTSSe/ZnO solar cells by optimizing ZnO buffer layers, Materials, (2023). **https://doi.org/10.3390/ma16072869**.

[165] M.K. Hossain, G.F.I. Toki, I. Alam, R. Pandey, D.P. Samajdar, M.F. Rahman, M.R. Islam, M.H.K. Rubel, H. Bencherif, J. Madan, M.K.A. Mohammed, Numerical simulation and optimization of a $CsPbI_3$-based perovskite solar cell to enhance the power conversion efficiency, New Journal of Chemistry 47 (2023) 4801–4817. **https://doi.org/10.1039/D2NJ06206B**.

[166] M. Saadat, O. Amiri, P.H. Mahmood, Potential efficiency improvement of $CuSb(S_{1-x},Se_x)_2$ thin film solar cells by the Zn(O,S) buffer layer optimization, Solar Energy 225 (2021) 875–881. **https://doi.org/10.1016/J.SOLENER.2021.08.013**.

[167] O. Ahmad, A. Rashid, M.W. Ahmed, M.F. Nasir, I. Qasim, Performance evaluation of Au/p-CdTe/Cs_2TiI_6/n-TiO_2/ITO solar cell using SCAPS-1D, Opt Mater (Amst) 117 (2021) 111105. **https://doi.org/10.1016/J.OPTMAT.2021.111105**.

[168] N Thakur, P Kumar, R Neffati, P Sharma, Design and simulation of chalcogenide perovskite BaZr (S, Se) $_3$ compositions for photovoltaic applications,

Physica Scripta, (2023). **https://iopscience.iop.org/article/10.1088/1402-4896/accfc6/meta**.

[169] Sadanand, P.K. Singh, S. Rai, P. Lohia, D.K. Dwivedi, Comparative study of the CZTS, $CuSbS_2$ and $CuSbSe_2$ solar photovoltaic cell with an earth-abundant non-toxic buffer layer, Solar Energy 222 (2021) 175–185. **https://doi.org/10.1016/J.SOLENER.2021.05.013**.

[170] Mamta, K.K. Maurya, V.N. Singh, Efficient Sb_2Se_3 solar cell with a higher fill factor: A theoretical approach based on thickness and temperature, Solar Energy 230 (2021) 803–809. **https://doi.org/10.1016/J.SOLENER.2021.11.002**.

[171] D Saikia, J Bera, A Betal, S Sahu, Performance evaluation of an all inorganic $CsGeI_3$ based perovskite solar cell by numerical simulation, Optical Materials, (2022). **https://doi.org/10.1016/j.optmat.2021.111839**.

[172] S. Abdelaziz, A. Zekry, A. Shaker, M. Abouelatta, Investigating the performance of formamidinium tin-based perovskite solar cell by SCAPS device simulation, Opt Mater (Amst) 101 (2020) 109738. **https://doi.org/10.1016/J.OPTMAT.2020.109738**.

[173] S.Z. Haider, H. Anwar, M. Wang, Theoretical Device Engineering for High-Performance Perovskite Solar Cells Using CuSCN as Hole Transport Material Boost the Efficiency Above 25%, Physica Status Solidi (A) Applications and Materials Science 216 (2019). **https://doi.org/10.1002/PSSA.201900102**.

[174] H.S. Duan, W. Yang, B. Bob, C.J. Hsu, B. Lei, Y. Yang, The role of sulfur in solution-processed $Cu_2ZnSn(S,Se)_4$ and its effect on defect properties, Adv Funct Mater 23 (2013) 1466–1471. **https://doi.org/10.1002/ADFM.201201732**.

[175] M.K. Hossain, D.P. Samajdar, R.C. Das, A.A. Arnab, M.F. Rahman, M.H.K. Rubel, M.R. Islam, H. Bencherif, R. Pandey, J. Madan, M.K.A. Mohammed, Design and Simulation of Cs_2BiAgI_6 Double Perovskite Solar Cells with Different Electron Transport Layers for Efficiency Enhancement, Energy and Fuels 37 (2023) 3957–3979. **https://doi.org/10.1021/ACS.ENERGYFUELS.3C00181**.

[176] M.T. Islam, A.K. Thakur, Two stage modelling of solar photovoltaic cells based on Sb2S3 absorber with three distinct buffer combinations, Solar Energy 202 (2020) 304–315. **https://doi.org/10.1016/J.SOLENER.2020.03.058**.

[177] A. Mortadi, E.M. El Hafidi, H. Nasrellah, M. Monkade, R. El Moznine, Investigation of bandgap grading on performances of perovskite solar cell using SCAPS-1D and impedance spectroscopy, Solar Energy Advances 4 (2024). **https://doi.org/10.1016/J.SEJA.2024.100056**.

[178] B. Barman, S. Ingole, Analysis of Si Back-Contact for Chalcogenide Perovskite Solar Cells Based on $BaZrS_3$ Using SCAPS-1D, Adv Theory Simul 6 (2023) 2200820. **https://doi.org/10.1002/ADTS.202200820**.

[179] F. Ayala-Mató, O. Vigil-Galán, M.M. Nicolás-Marín, M. Courel, Study of loss mechanisms on $Sb_2(S_{1-x}Se_x)_3$solar cell with n-i-p structure: Toward an efficiency promotion, Appl Phys Lett 118 (2021). **https://doi.org/10.1063/5.0032867/39816**.

[180] M. Yousefi, M. Minbashi, Z. Monfared, N. Memarian, A. Hajjiah, Improving the efficiency of CZTSSe solar cells by engineering the lattice defects in the absorber layer, Solar Energy 208 (2020) 884–893. **https://doi.org/10.1016/J.SOLENER.2020.08.049**.

[181] Y. Yin, C. Jiang, Y. Ma, R. Tang, X. Wang, L. Zhang, Z. Li, C. Zhu, T. Chen, Sequential Coevaporation and Deposition of Antimony Selenosulfide Thin Film for Efficient Solar Cells, Advanced Materials 33 (2021) 2006689. **https://doi.org/10.1002/ADMA.202006689**.

[182] M. Shasti, A.M. status solidi (a), undefined 2019, Numerical Study of Cu_2O, $SrCu_2O_2$, and $CuAlO_2$ as Hole-Transport Materials for Application in Perovskite Solar Cells, Wiley Online LibraryM Shasti, A Mortezaaliphysica Status Solidi (a), 216 (2019). **https://doi.org/10.1002/PSSA.201900337**.

[183] G. Pindolia, S.M. Shinde, P.K. Jha, Optimization of an inorganic lead free $RbGeI_3$ based perovskite solar cell by SCAPS-1D simulation, Solar Energy, 236 (2022) 802–821. **https://doi.org/10.1016/J.SOLENER.2022.03.053**.

[184] P Roy, A Khare, Understanding the strategies to attain the best performance of all inorganic lead-free perovskite solar cells: Theoretical insights, International Journal of Energy Research, 46 (2022) 15881–15899. **https://doi.org/10.1002/ER.8287**.

[185] C. Walkons, R. Murshed, S. Bansal, Numerical analysis of Pb-free perovskite absorber materials: prospects and challenges, Solar RRL, 4 (2020). **https://doi.org/10.1002/SOLR.202000299**.

[186] T Minemoto, T Matsui, H Takakura, Y Hamakawa, T Negami, Y Hashimoto, T Uenoyama, Theoretical analysis of the effect of conduction band offset of window/CIS layers on performance of CIS solar cells using device simulation, solar Energy Materials and Solar Cells, (2001). **https://doi.org/10.1016/S0927-0248(00)00266-X**.

[187] Minemoto, Takashi, and Jasmeen Julayhi. "Buffer-less Cu (In, Ga) Se2 solar cells by band offset control using novel transparent electrode." *Current Applied Physics* 13, no. 1 (2013): 103-106, **https://doi.org/10.1016/j.cap.2012.06.019**.

[188] T Minemoto, M Murata, Theoretical analysis on effect of band offsets in perovskite solar cells, Solar Energy Materials and Solar Cells, (2015). **https://doi.org/10.1016/j.solmat.2014.10.036**.

[189] Mamta, R. Kumar, R. Kumari, K.K. Maurya, V.N. Singh, $Sb_2(S, Se)_3$-based photovoltaic cell with MoS_2 as a hole transport layer: a numerical investigation, Materials Today Sustainability 20 (2022) 100218. **https://doi.org/10.1016/J.MTSUST.2022.100218**.

[190] M.M. Nicolás-Marín, F. Ayala-Mato, O. Vigil-Galán, M. Courel, Simulation analysis of $Cd_{1-x}Zn_xS/Sb_2(Se_{1-x}S_x)_3$ solar cells with n-i-p structure, Solar Energy 224 (2021) 245–252. **https://doi.org/10.1016/J.SOLENER.2021.05.092**.

[191] [191] M.M. Nicolás-Marín, O. Vigil-Galán, F. Ayala-Mato, M. Courel, Analysis of Hole Transport Layer and Electron Transport Layer Materials in the Efficiency Improvement of $Sb_2(Se_{1-x} S_x)_3$ Solar Cell, Physica Status Solidi (b) 260 (2023) 2200342. **https://doi.org/10.1002/PSSB.202200342.**

[192] K. Sekar, S. Mayarambakam, Effect of Annealed and Non-Annealed Inorganic MnS Hole-Transport Layer for Efficient $Sb_2(S,Se)_3$ Solar Cells: A Theoretical Justification, Physica Status Solidi (b) 260 (2023) 2300087. **https://doi.org/10.1002/PSSB.202300087**.

[193] I. Gharibshahian, A.A. Orouji, S. Sharbati, Efficient $Sb_2(S,Se)_3$/Zn(O,S) solar cells with high open-circuit voltage by controlling sulfur content in the absorber-buffer layers, Solar Energy 227 (2021) 606–615. **https://doi.org/10.1016/J.SOLENER.2021.09.039**.

[194] S. Barthwal, S. Singh, A.K. Chauhan, R. Karuppannan, Design and Simulation of CdS-Free $Sb_2(S, Se)_3$ Solar Cells with Efficiency Exceeding 20%, ACS Sustain Chem Eng 12 (2024) 947–958. **https://doi.org/10.1021/acssuschemeng.3c06210**.

[195] ElsevierP Singh, NM Ravindra, Temperature dependence of solar cell performance—an analysis, Solar Energy Materials and Solar Cells, (2012). **https://doi.org/10.1016/j.solmat.2012.02.019**.

[196] S. Al Ahmed, A. Sunny, S. Rahman, Performance enhancement of Sb_2Se_3 solar cell using a back surface field layer: a numerical simulation approach, Solar Energy Materials and Solar Cells, (2021). **https://doi.org/10.1016/j.solmat.2020.110919**.

[197] N. Devi, K.A. Parrey, A. Aziz, and S. Datta, Numerical simulations of perovskite thin-film solar cells using a CdS hole blocking layer. Journal of Vacuum Science & Technology B, (2018). **https://doi.org/10.1116/1.5026163.**

[198] A. Ouédraogo, B. Zouma, E. Ouédraogo, L Guissou, DJ Bathiébo, Individual efficiencies of a polycrystalline silicon PV cell versus temperature, Results in Optics, (2021). **https://doi.org/10.1016/j.rio.2021.100101**.

[199] S. Shrestha, G.J. Matt, A. Osvet, D. Niesner, R. Hock, C.J. Brabec, Assessing temperature dependence of drift mobility in methylammonium lead iodide perovskite single crystals, The Journal of Physical Chemistry C, 122 (2018) 5935–5939. **https://doi.org/10.1021/ACS.JPCC.8B00341.**

[200] T. Ouslimane, L. Et-Taya, L. Elmaimouni, A Benami, Impact of absorber layer thickness, defect density, and operating temperature on the performance of $MAPbI_3$ solar cells based on ZnO electron transporting material, Heliyon, (2021). **https://doi.org/10.1016/j.heliyon.2021.e06379**.

[201] H. Shu, H. Long, H. Sun, B. Li, H. Zhang, X. Wang, Dynamic model of the short-term synaptic behaviors of PEDOT-based organic electrochemical transistors with modified Shockley equations, ACS Omega, 7 (2022) 14622–14629. **https://doi.org/10.1021/ACSOMEGA.1C06864**.

[202] K. Djessas, I. Bouchama, K. Medjnoun, A. Bouloufa, Simulation and performance analysis of superstrate $Cu(In,Ga)Se_2$ solar cells using nanostructured $Zn_{1-x}V_xO$ thin films, International Journal of Nanotechnology, 11 (2014) 854–868. **https://doi.org/10.1504/IJNT.2014.063794**.

[203] M.T. Islam, A. Kumar, A.K. Thakur, Defect density control using an intrinsic layer to enhance conversion efficiency in an optimized SnS solar cell, Journal of Electronic Materials, 50 (2021) 3603–3613. **https://doi.org/10.1007/S11664-021-08881-0**.

[204] D. Glowienka, Y. Galagan, D. Glowienka, Y. Galagan, Light intensity analysis of photovoltaic parameters for perovskite solar cells, Advanced Materials, 34 (2022). **https://doi.org/10.1002/ADMA.202105920.**

[205] A. Castro-Chong, A.J. Riquelme, T. Aernouts, L.J. Bennett, G. Richardson, G. Oskam, J.A. Anta, Illumination Intensity Dependence of the Recombination Mechanism in Mixed Perovskite Solar Cells, Chempluschem 86 (2021) 1347–1356. **https://doi.org/10.1002/cplu.202100233**.

[206] C. Proctor, T.Q. Nguyen, Effect of leakage current and shunt resistance on the light intensity dependence of organic solar cells, Applied Physics Letters 106, no. 8 (2015). **https://doi.org/10.1063/1.4913589**.

[207] J. Greulich, M. Glatthaar, S. Rein, Fill factor analysis of solar cells' current-voltage curves, Progress in Photovoltaics: Research and Applications 18 (2010) 511–515. **https://doi.org/10.1002/pip.979**.

[208] S. Ryu, D.C. Nguyen, N.Y. Ha, H.J. Park, Y.H. Ahn, J.Y. Park, S. Lee, Light Intensity-dependent Variation in Defect Contributions to Charge Transport and Recombination in a Planar $MAPbI_3$ Perovskite Solar Cell, Sci Rep 9 (2019) 19846. **https://doi.org/10.1038/S41598-019-56338-6**.

[209] K.A. Dass, M. Hossain, L.Marasamy, Highly efficient emerging $Ag_2BaTiSe_4$ solar cells using a new class of alkaline earth metal-based chalcogenide buffers alternative to CdS, Scientific Reports, (2024). **https://doi.org/10.1038/s41598-024-51711-6.**

[210] MK Hossain, GFI Toki, I Alam, R Pandey, DP Samajdar, MF Rahman, MR Islam, MHK Rubel, Numerical simulation and optimization of a $CsPbI_3$-based perovskite solar cell to enhance the power conversion efficiency, Journal of Chemistry, (2023). **https://doi.org/10.1039/D2NJ06206B.**

[211] M. Saadat, O. Amiri, P.H. Mahmood, Analysis and performance assessment of $CuSbS_2$-based thin-film solar cells with different buffer layers, The European Physical Journal Plus 2022 137:5 137 (2022) 1–12. **https://doi.org/10.1140/EPJP/S13360-022-02804-6**.

[212] A. Ahmed, K. Riaz, H. Mehmood, T. Tauqeer, Z Ahmad, Performance optimization of $CH_3NH_3Pb(I_{1-x}Br_x)_3$ based perovskite solar cells by comparing different ETL materials through conduction band offset engineering, Optical Materials, 105 (2020) 109897. **https://doi.org/10.1016/j.optmat.2020.109897**.

[213] J. Kim, M. Jin, B. Hou, M. Kim, D. Um, C.Kim, Reducing the oxygen vacancy concentration in $SrTiO_3$-δ thin films via an optimized O_2 plasma treatment for enhancing device properties, Applied Surface Science, (2023). **https://doi.org/10.1016/j.apsusc.2023.158271**.

[214] E. Zhang, M. Zhang, M. Kato, Effect of dislocations on carrier recombination and photoelectrochemical activity in polished and unpolished TiO_2 and $SrTiO_3$ crystals, Journal of Applied Physics 135, no. 4 (2024). **https://doi.org/10.1063/5.0181625**.

[215] W. Wang, Z. Cao, H. Wang, J Luo, Y Zhang, Remarkable Cd-free Sb_2Se_3 solar cell yield achieved by interface band-alignment and growth orientation screening, Journal of Materials Chemistry A, (2021). **https://doi.org/10.1039/D1TA08404F**.

[216] Y. Gao, Y. Masuda, T. Yonezawa, K. Koumoto, Preparation of $SrTiO_3$ thin films by the liquid phase deposition method, Materials Science and Engineering: B 99, no. 1-3 (2003): 290-293. **https://doi.org/10.1016/S0921-5107(02)00527-5**.

[217] G. Altuntas, M. Isik, G. Surucu, M. Parlak, O. Surucu, Exploring the Thermal Stability of Sb_2Se_3 for Potential Applications through Advanced Thermal Analysis Methods, ACS Omega, (2025). **https://doi.org/10.1021/ACSOMEGA.4C10053**.

[218] X. Ni, J. Liu, F. Xu, J. Zhang, S. Jiang, B Fang, H Guo, N Yuan, J Ding, S Zhang, Performance enhancement of $Sb_2(S,Se)_3$ solar cells through neodymium ion flow doping, Chemical Engineering Journal, (2024). **https://doi.org/10.1016/j.cej.2024.151574.**

[219] X. Wang, K. Maeda, A. Thomas, K. Takanabe, G. Xin, J.M. Carlsson, K. Domen, M. Antonietti, A metal-free polymeric photocatalyst for hydrogen production from water under visible light, Nature Materials, 8 (2009) 76–80. **https://doi.org/10.1038/NMAT2317**.

[220] F. Dong, Y. Li, Z. Wang, W.Ho, Enhanced visible light photocatalytic activity and oxidation ability of porous graphene-like g-C_3N_4 nanosheets via thermal exfoliation, Applied Surface Science, 2015•Elsevier 358 (2015) 393–403. **https://doi.org/10.1016/j.apsusc.2015.04.034**.

[221] A.F. Pérez-Torres, D.F. Hernández-Barreto, V. Bernal, L. Giraldo, J.C. Moreno-Piraján, E.A. da Silva, M. do C.M. Alves, J. Morais, Y. Hernandez, M.T. Cortés, M.A. Macías, Sulfur-Doped g-C_3N_4 Heterojunctions for Efficient Visible Light Degradation of Methylene Blue, ACS Omega 8 (2023) 47821–47834. **https://doi.org/10.1021/acsomega.3c06320**.

[222] E. Palik, Handbook of optical constants of solids, Vol. 3. Academic press, (1998).

[223] M. van Huy, D. Chi Dung, L. Hoang Hai, L. Duy Hoan, N. Tuan Hieu, O. Schneegans, Determination Of The Refractive Index Of Optical Ceramics By Using Transmission Data In The Mid-Wave Infrared Region, Journal of Science and Technique, (2020). **https://doi.org/10.56651/lqdtu.jst.v15.n04.7**.

[224] A. McNaught, A. McNaught, Compendium of chemical terminology, 1997. **http://publications.iupac.org/publications/books/author/mcnaught.html**.

[225] P. Patra, Y. Mohapatra, Dielectric constant of thin film graphitic carbon nitride (g-C_3N_4) and double dielectric Al_2O_3/g-C_3N_4, Applied Physics Letters 118, no. 10 (2021). **https://doi.org/10.1063/5.0045911**.

[226] Y. Yang, J. Chen, Z. Mao, N. An, D. Wang, BD Fahlman, Ultrathin gC_3N_4 nanosheets with an extended visible-light-responsive range for significant enhancement of photocatalysis, RSC Advances, (2017). **https://doi.org/10.1039/c6ra26172h**.

[227] S. Yan, S. Lv, Z. Li, Z.Zou, Organic–inorganic composite photocatalyst of gC_3N_4 and TaON with improved visible light photocatalytic activities, Dalton Transactions, (2010). **https://doi.org/10.1039/b914110c**.

[228] G. Shao, G. Shao, Work Function and Electron Affinity of Semiconductors: Doping Effect and Complication due to Fermi Level Pinning, Energy & Environmental Materials 4 (2021) 273–276. **https://doi.org/10.1002/EEM2.12218**.

[229] K. Bai, Z. Cui, E. Li, Y. Ding, J. Zheng, Y. Zheng, C. Liu, Adsorption of alkali metals on graphitic carbon nitride: A first-principles study, Modern Physics Letters B 34 (2020). **https://doi.org/10.1142/S0217984920503613**.

[230] H. Lu, Y. Guo, J.W. Martin, M. Kraft, J. Robertson, Atomic structure and electronic structure of disordered graphitic carbon nitride, Carbon N Y 147 (2019) 483–489. **https://doi.org/10.1016/J.CARBON.2019.03.031**.

[231] B.L. Phoon, C.W. Lai, G.T. Pan, T.C.K. Yang, J.C. Juan, Highly mesoporous g-C_3N_4 with uniform pore size distribution via the template-free method to enhanced solar-driven tetracycline degradation, Nanomaterials 11 (2021) 2041. **https://doi.org/10.3390/NANO11082041/S1**.

[232] A. Lafuente-Sampietro, K. Yoshida, S. Wang, S. Ishizuka, H. Shibata, N. Sano, K. Akimoto, T. Sakurai, Effect of the double grading on the internal electric field and on the carrier collection in CIGS solar cells, Solar Energy Materials and Solar Cells 223 (2021) 110948. **https://doi.org/10.1016/J.SOLMAT.2020.110948**.

[233] A. Crovetto, O. Hansen, What is the band alignment of $Cu_2ZnSn(S,Se)_4$ solar cells?, Solar Energy Materials and Solar Cells 169 (2017) 177–194. **https://doi.org/10.1016/J.SOLMAT.2017.05.008**.

[234] F. Dong, Z. Zhao, T. Xiong, Z. Ni, W. Zhang, Y. Sun, W.K. Ho, In Situ Construction of g-C_3N_4/g-C_3N_4 Metal-Free Heterojunction for Enhanced Visible-Light Photocatalysis, ACS Appl Mater Interfaces 5 (2013) 11392–11401. **https://doi.org/10.1021/AM403653A**.

[235] K. Gkini, I. Martinaiou, P. Falaras, A review on emerging efficient and stable perovskite solar cells based on g-C_3N_4 nanostructures, Materials 14 (2021). **https://doi.org/10.3390/MA14071679.**

[236] T. Yang, W. Zhao, X. Liu, S. Liu, Tailoring the Interfacial Termination via Dipole Interlayer for High-Efficiency Perovskite Solar Cells, Adv Energy Mater 13 (2023) 2204192. **https://doi.org/10.1002/AENM.202204192**.

[237] Y. Ma, J. Gong, P. Zeng, M. Liu, Recent Progress in Interfacial Dipole Engineering for Perovskite Solar Cells, Nanomicro Lett 15 (2023) 173. **https://doi.org/10.1007/S40820-023-01131-4**.

[238] S. Prabhu, S.K. Pandey, S. Chakrabarti, Theoretical investigations of band alignments and SnSe BSF layer for low-cost, non-toxic, high-efficiency CZTSSe solar cell, Solar Energy 226 (2021) 288–296. **https://doi.org/10.1016/J.SOLENER.2021.08.050**.

[239] Z. Liu, S. Wu, X. Yang, Y. Zhou, J. Jin, J. Sun, L. Zhao, S. Wang, The dual interfacial modification of 2D g-C3N4 for high-efficiency and stable planar perovskite solar cells, Nanoscale Adv 2 (2020) 5396–5402. **https://doi.org/10.1039/D0NA00613K**.

[240] Y. Gan, G. Qiu, C. Yan, Z. Zeng, B. Qin, X. Bi, Y. Liu, Numerical Analysis on the Effect of the Conduction Band Offset in Dion–Jacobson Perovskite Solar Cells, Energies 2023, Vol. 16, Page 7889 16 (2023) 7889. **https://doi.org/10.3390/EN16237889**.

[241] E. Von Hauff, Impedance Spectroscopy for Emerging Photovoltaics, The Journal of Physical Chemistry C 123 (2019) 11329–11346. **https://doi.org/10.1021/ACS.JPCC.9B00892**.

[242] E. Ghahremanirad, O. Almora, S. Suresh, A.A. Drew, T.H. Chowdhury, A.R. Uhl, Beyond Protocols: Understanding the Electrical Behavior of Perovskite Solar Cells by Impedance Spectroscopy, Adv Energy Mater 13 (2023) 2204370. **https://doi.org/10.1002/AENM.202204370**.

[243] C.K. Lai, Y.C. Lin, Numerical Investigation and Device Architecture Optimization of Sb_2Se_3 Thin-Film Solar Cells Using SCAPS-1D, Materials 17 (2024) 6203. **https://doi.org/10.3390/MA17246203**.

[244] S.S. Dipta, A. Uddin, G. Conibeer, Enhanced light management and optimization of perovskite solar cells incorporating wavelength dependent reflectance modeling, Heliyon 8 (2022). **https://doi.org/10.1016/J.HELIYON.2022.E11380**.

[245] J. Yang, Y. Ma, J. Yang, W. Liu, X. Li, Recent Advances in g-C_3N_4 for the Application of Perovskite Solar Cells, Nanomaterials 12 (2022) 3625. **https://doi.org/10.3390/NANO12203625**.

[246] S. Chowdhury, A.S. Najm, M. Luengchavanon, A.M. Holi, C.H. Chia, K. Techato, S. Channumsin, I.K. Salih, Investigating the Effect of Nonideal Conditions on the Performance of a Planar Sb_2Se_3-Based Solar Cell through SCAPS-1D Simulation, Energy & Fuels 37 (2023) 6722–6732. **https://doi.org/10.1021/ACS.ENERGYFUELS.2C03593**.

[247] T. Wu, J. Hu, S. Chen, Z. Zheng, M. Cathelinaud, H. Ma, Z. Su, P. Fan, X. Zhang, G. Liang, Energy Band Alignment by Solution-Processed Aluminum Doping Strategy toward Record Efficiency in Pulsed Laser-Deposited Kesterite Thin-Film Solar Cell, ACS Appl Mater Interfaces (2023). **https://doi.org/10.1021/ACSAMI.2C22174**.

[248] G. Li, Z. Li, X. Liang, C. Guo, K. Shen, Y. Mai, Improvement in Sb_2Se_3 Solar Cell Efficiency through Band Alignment Engineering at the Buffer/Absorber Interface, ACS Appl Mater Interfaces 11 (2018) 828–834. **https://doi.org/10.1021/ACSAMI.8B17611**.

[249] K.T. Arockiya-Dass, K. Sekar, L. Marasamy, Theoretical Insights of Degenerate ZrS_2 as a New Buffer for Highly Efficient Emerging Thin-Film Solar Cells, Energy Technology, 11 (2023). **https://doi.org/10.1002/ENTE.202300333**.

[250] M. Haider, C. Zhen, T. Wu, G. Liu, & H. Cheng, Boosting efficiency and stability of perovskite solar cells with nickel phthalocyanine as a low-cost hole transporting layer material, Journal of Materials Science & Technology, (2018) **https://doi.org/10.1016/j.jmst.2018.03.005**.

[251] S. Karthick, J. Bouclé, S. Velumani, Effect of bismuth iodide (BiI_3) interfacial layer with different HTL's in FAPI based perovskite solar cell–SCAPS–1D study, Solar Energy, (2021). **https://doi.org/10.1016/j.solener.2021.02.041**.

[252] S. Ravishankar, Z. Liu, U. Rau, T. Kirchartz, Multilayer capacitances: How selective contacts affect capacitance measurements of perovskite solar cells. PRX energy 1 (2022) 13003. **https://doi.org/10.1103/PRXENERGY.1.013003.**

[253] D.K. Shah, K.C. Devendra, M. Muddassir, M.S. Akhtar, C.Y. Kim, and O.BD. Yang, A simulation approach for investigating the performances of cadmium telluride solar cells using doping concentrations, carrier lifetimes, thickness of layers, and band gaps, Solar Energy 216 (2021) 259-265. **https://doi.org/10.1016/j.solener.2020.12.070.**

[254] G. Kartopu, B. L. Williams, V. Zardetto, A. K. Gürlek, A. J. Clayton, S. Jones, W. M. M. Kessels, M. Creatore, S. J. C. Irvine, Enhancement of the photocurrent and

efficiency of CdTe solar cells suppressing the front contact reflection using a highly-resistive ZnO buffer layer. Solar Energy Materials and Solar Cells 191 (2019) 78-82. **https://doi.org/10.1016/j.solmat.2018.11.002.**

[255] K. Sarkar, S. Jahan, B. Dutta, S. Chatterjee, S. Gain, S. Ghosh, Effects of very thin CdS window layer on CdTe solar cell, J. Mech. Contin. Math. Sci, 14 (2019) 14-29. **https://doi.org/10.26782/jmcms.2019.06.00002.**

[256] M. Saadat, O. Amiri, P. H Mahmood, Potential efficiency improvement of $CuSb(S_{1-x}, Se_x)_2$ thin film solar cells by the Zn (O, S) buffer layer optimization, Solar Energy, 225 (2021): 875-881, **https://doi.org/10.1016/j.solener.2021.08.013.**

[257] M. Rai, L.H. Wong, L. Etgar, Effect of perovskite thickness on electroluminescence and solar cell conversion efficiency, The Journal of Physical Chemistry Letters, 11 (2020) 8189-8194. **https://doi.org/10.1021/ACS.JPCLETT.0C02363.**

[258] Y. Chen, Y. Wang, R. Wang, X. Hu, J. Tao, G.E. Weng, C. Zhao, S. Chen, Z. Zhu, J. Chu, H. Akiyama, Importance of Interfacial Passivation in the High Efficiency of Sb_2Se_3 Thin-Film Solar Cells: Numerical Evidence, Applied Energy Materials, 3 (2020) 10415-10422. **https://doi.org/10.1021/ACSAEM.0C01203.**

[259] F. Izadi, A. Ghobadi, A. Gharaati, M. Minbashi, A. Hajjiah, Effect of interface defects on high efficient perovskite solar cells, Optik 227 (2021) 16606. **https://doi.org/10.1016/j.ijleo.2020.166061.**

[260] W. Shen, Y. Dong, F. Huang, Y.B. Cheng, J. Zhong, Interface passivation engineering for hybrid perovskite solar cells, Materials Reports: Energy 1 (2021) 100060. **https://doi.org/10.1016/J.MATRE.2021.100060.**

[261] T.S. Sherkar, C. Momblona, L. Gil-Escrig, J. Ávila, M. Sessolo, H.J. Bolink, L.J.A. Koster, Recombination in perovskite solar cells: significance of grain boundaries, interface traps, and defect ions, ACS Energy Letters, 2 (2017) 1214-1222. **https://doi.org/10.1021/ACSENERGYLETT.7B00236.**

[262] C.H. Ng, K. Hamada, G. Kapil, M.A. Kamarudin, Z. Wang, Q. Shen, K. Yoshino, T. Minemoto, S. Hayase, Reducing trap density and carrier concentration by a Ge additive for an efficient quasi 2D/3D perovskite solar cell, Journal of Materials Chemistry A, 8 (2020) 2962-8. **https://doi.org/10.1039/C9TA11989B.**

[263] R. Tang, W. Hu, C. Hu, C. Duan, J. Hu, G. Liang, Effective non-radiative interfacial recombination suppression scenario using air annealing for antimony

triselenide thin-film solar cells, Materials, 17 (2024)13. **https://doi.org/10.3390/ma17133222.**